Search for heavy resonances decaying via a vector-like quark

and

Interconnection technology for the Phase I Upgrade of the CMS experiment

Zur Erlangung des akademischen Grades eines

DOKTORS DER NATURWISSENSCHAFTEN (Dr. rer. nat.)

von der Fakultät für Physik des
Karlsruher Instituts für Technologie (KIT)
genehmigte

DISSERTATION

von

M.Sc. Simon Kudella
aus Karlsruhe

Zusammenfassung

Die vorliegende Dissertation wurde im Rahmen des CMS-Experiments am LHC verfasst. Im Vordergrund stand dabei die Suche nach neuartigen Elementarteilchen in hochenergetischen Proton-Proton-Kollisionen, sowie die Entwicklung einer Bump-Bonding-Verbindungstechnik zur Produktion von hybriden Siliziumpixelmodulen.

Die Existenz sowohl von schweren bosonischen Resonanzen als auch schweren vektorartigen Quarks wird von vielen Modellen jenseits des Standardmodells der Teilchenphysik vorhergesagt. Diese Dissertation präsentiert die Suche nach solchen bosonischen Resonanzen und deren Zerfall in Top-Quarks und schwere vektorartige Top-Quark-Partner in einem vollhadronischen Endzustand. Zur Identifikation der charakteristischen Zerfallsprodukte einer solchen Resonanz werden dabei dedizierte Substrukturalgorithmen verwendet, welche die charakteristischen Jets eines solchen Zerfalls identifizieren. Darüber hinaus wurde eine datengetriebene Methode zur Abschätzung des QCD-Multijetuntergrundes entwickelt. Die Analyse von $35.9\,\mathrm{fb}^{-1}$ an Daten, die im Jahr 2016 durch das CMS-Experiment aufgezeichnet wurden, erlaubte es modellunabhängige Limits auf den Wirkungsquerschnitt für die Produktion von bosonischen Resonanzen und deren Zerfall über ein vektorartiges Quark aufzustellen. Die Ergebnisse wurden in zwei Modellen für Physik jenseits des Standardmodells interpretiert. Auf diese Weise konnte der Parameterraum für Modelle, welche die Existenz verzerrter Extradimensionen vorhersagen, eingeschränkt werden.

Der Silizium-Pixeldetektor des CMS-Experiments stellt eine zentrale Komponente des Detektorsystems dar und ermöglicht eine präzise Teilchenspurrekonstruktion sowie die Unterscheidung verschiedener Wechselwirkungsvertizes. Die erwartete erhöhte instantane Luminosität, die durch den LHC in den nächsten Jahren bereitgestellt wird, erfordert den Austausch des kompletten Pixeldetektors. Am KIT wurde ein Teil der notwendigen Detektormodule für den neuen Pixeldetektor hergestellt. Dabei erlaubte die Verwendung einer am KIT entwickelten Bump-Bonding-Verbindungstechnik eine detaillierte Qualitätskontrolle. Durch eine Optimierung des Bump-Bonding-Prozesses und mehrere Qualitätskontrollen konnte eine zuverlässige stabile Verbindung erzielt werden. Weitere Qualitätssicherungsmaßnahmen erlaubten kurze Bearbeitungszeiten und eine exzellente Verbindungsqualität.

Abstract

The existence of heavy bosonic resonances as well as vector-like quarks is predicted by many models beyond the Standard Model of Particle Physics. In this thesis, the search for such bosonic resonances decaying via a top quark and its vector-like partner is presented, with special focus on the fully-hadronic final state. The characteristic substructures of hadronic jets produced by such resonances were analyzed using elaborate jet identification algorithms. Furthermore, a data-driven background estimation method was developed in order to estimate the background contribution by QCD-multijet events. The search was performed using $35.9\,\mathrm{fb}^{-1}$ of data collected by the CMS at the LHC in 2016. Model-independent cross section times branching ratio limits are derived. The results are also interpreted in models featuring warped extra-dimensions, constraining the parameter space for resonance masses between $1.6\,\mathrm{TeV}$ and $2.5\,\mathrm{TeV}$.

A crucial component of the CMS experiment is its silicon pixel detector which allows to distinguish different interaction vertices and is crucial for track reconstruction and many jet identification techniques. Due to the expected increase in the instantaneous luminosity provided by the outstanding performance of the LHC, a complete overhaul and replacement of the CMS pixel detector was required. As one of the production centers for pixel detector modules, KIT developed a bump bonding interconnection technology process that allowed full control over the production quality. The bump bonding process was optimized in order to provide a strong and reliable interconnection, and several quality assurance tests were introduced to monitor the production quality during the production period. By following the philosophy of frequent quality tests, short turn-around times and frequent quality feedback, the KIT production line achieved an excellent module production quality.

Contents

Where do I begin?...
Where do I start?...

Andy Williams

1
Introduction

High-energy particle physics focuses on the most fundamental principles describing nature and our universe at the elementary scale. The current knowledge about elementary particles and their interactions is summarized and incorporated into a single theoretical framework, the Standard Model of Particle Physics (SM). Since its introduction in the 1960s, the SM has been subsequently refined, expanded and adapted in order to provide simple and precise explanations and predictions of phenomena of nature. Nevertheless, several observations prove that the description of nature based on the SM cannot be complete. For this reason, a large number of theoretical models predict the existence of physics beyond the SM. Today, many experiments are dedicated to the search for physics beyond the SM.

Over the last century, the controlled acceleration and collision of elementary and composite particles has been a prime tool to investigate the fundamental properties and constituents of matter and their interactions. The large energy released in a high-energy particle collision allows the creation of different stable and unstable elementary particles. By identifying and precisely measuring the decay products, the initial interaction processes can be reconstructed and probed to gain insight into the fundamental laws of physics.

In order to identify all decay products created in a high-energy particle collision, highly complex particle detector systems are designed and built, fitting the particular requirements of their research program. The correct particle reconstruction and identification requires the development of complex and elaborate reconstruction algorithms. The design, construction, and execution of a modern high-energy particle physics experiment require deep understanding of the physical and technological approaches. At the same time, a good overview of the challenges that are related to the fabrication of the most basic detector components, the event reconstruction and the physical interpretation of data is needed.

The most powerful particle collider to date is the Large Hadron Collider (LHC) at the Conseil Européen pour la Recherche Nucléaire (CERN) near Geneva in Switzerland. It collides protons with an unprecedented energy of $13\,\mathrm{TeV}$ at four interaction points. The Compact Muon Solenoid (CMS) experiment is located at one of these interaction points. The work presented in this thesis was performed at the Institute of Experimental Particle Physics (ETP) and the Institute for Data Processing and Electronics (IPE) of the Karlsruhe Institute of Technology (KIT) as part of the CMS collaboration, and can be divided into two major parts. These two parts are dedicated to the construction of the new semiconducting CMS pixel detector and to the analysis of data in a search for physics beyond the SM using modern particle identification techniques.

Chapter 2 covers an introduction into the SM, its limitations and deficits, and two possible models approaching these limitations. Furthermore, an overview of the LHC and the physical and technical challenges arising from a hadron collider experiment is given in Chapter 3, before introducing the CMS detector systems.

The first part of this thesis focuses on the search for heavy bosonic resonances decaying via a vector-like quark. Heavy bosonic resonances are hypothetical heavy spin-1 particles which could be produced in the proton-proton collisions provided by the LHC. Vector-like quarks, on the other hand, are hypothetical heavy spin-1/2 particles that are similar to SM quarks, but couple non-chirally to the weak force. Heavy bosonic resonances and vector-like quarks are predicted by many models beyond the SM and provide a possible solution to several of its problems, such as the observed lightness of the Higgs boson or observed absence of large amounts of anti-matter in the universe. A possible decay mode of heavy bosonic resonances is the decay into a SM particle and a vector-like quark. This analysis focuses on a fully-hadronic final state with a signature of three individual characteristic particle jets with large transverse momentum.

After introducing some basic object and event reconstruction techniques, jet identification algorithms that analyze the substructure of complex hadronic jets are described in more detail in Chapter 4. In Chapter 5, the event selection criteria and event reconstruction are introduced. Since the contribution of QCD-multijet background events is difficult to simulate, a new data-driven background estimation method was developed. The $35.9\,\mathrm{fb}^{-1}$ of data, collected by the CMS experiment in 2016, are analyzed to search for excesses compatible with heavy bosonic resonances decaying via a vector-like quark. The results are interpreted in two different models and limit the parameter range of models that predict the existence of such heavy bosonic resonances decaying via a vector-like quark. Finally, an outlook on possible improvements to increase the sensitivity of this analysis is given.

The second part of this thesis is dedicated to the *Phase I Upgrade* of the CMS pixel detector. The CMS pixel detector is the innermost sub-detector system of the CMS experiment and is used to provide precise tracking information in order to distinguish the trajectories of charged particles very close to the interaction point. The tracking information of the CMS pixel detector system is a crucial input for jet identification and reconstruction techniques and allows to distinguish interaction vertices at high particle rates. So far, the CMS pixel detector has performed very well at the instantaneous luminosity it was designed for. However, the instantaneous luminosity delivered by the LHC exceeded the design value by 50 % in 2016 and is expected to be further increased up to twice the design value within the next years. These conditions would result in an increased particle flux inside the detector and an intolerable reduction of the tracking performance requiring a complete replacement of the CMS pixel detector with an upgraded version in spring 2017 as part of the so-called CMS Phase I Upgrade. The production of hybrid silicon pixel detector modules for the upgraded CMS pixel detector at KIT is at the center of the second part of this thesis.

After a brief introduction into the basics of semiconductors and their usage as particle detectors in Chapter 6, an overview of the special requirements of a pixelated semiconductor particle detector is given. Special focus is set on the bump bonding interconnection technology required to assemble hybrid pixel detector systems. In Chapter 7, the design and technology changes in the Phase I Upgrade of the CMS pixel detector are addressed as well as the expected detector performance. Chapter 8 is dedicated to the pixel detector module production, performed at KIT in 2015 and 2016. After introducing the KIT module

assembly line, the material selection processes are described in detail. A cautious selection of components is crucial for the entire production sequence in order to ensure a high production quality. Furthermore, a detailed description of the bump bonding interconnection process established at KIT is given. The bump bonding interconnection technology processes were used to establish a mechanical and electrical high density interconnection between the pixel cells of the silicon sensor and the corresponding readout electronics. By performing parts of the bump bonding process at IPE, KIT had direct control over the process quality. A series of production quality assurance tests were developed to monitor the module assembly, and to allow immediate reaction to potential quality issues. These production quality assurance test are introduced, before summarizing the final production results.

2

Theoretical motivation

In the first chapter of this thesis, a very brief introduction to the SM, its basic concepts and limitations, as well as potential extensions to the SM is given. These basics are useful for the remainder of this thesis, but especially for the first part described in Sections 4 and 5.

After a first phenomenological description of the SM, the concept of symmetry breaking and the Higgs mechanism is briefly described. Then, an overview of the SM problems and approaches to solve these is given. Special focus is put on vector-like quarks. Finally, two example models beyond the SM are introduced that predict the existence of heavy bosonic resonances and vector-like quarks.

2.1 The Standard Model of Particle Physics

The SM is a quantum field theory model to describe the fundamental physics of elementary particles. It quantitatively describes three of the four know elementary forces of nature: the electromagnetic, the weak and the strong force. The fourth force, however, the gravitational force that dominates the interaction between massive large-scale structures, like planets, stars and galaxies within our universe, is not included in the SM. Based on the most basic principles and interactions defined by the SM, larger and more complex macroscopic systems can be described.

2.1.1 Phenomenological Overview

The SM has been developed and subsequently refined over the last hundred years. In 2012, the ATLAS and CMS collaborations at the LHC discovered a Higgs-boson-like particle, the last remaining particle predicted by the SM, and thereby completed the SM [CMS12b; ATL12]. Within the SM, three fundamental forces are mediated by five gauge bosons, while the Higgs field gives mass to all massive particles. The electromagnetic force is mediated by photons, coupling to the electric charge of a particle. Similarly, gluons act as the interaction carriers of the strong force, coupling the *color charge* of a particle. The weak interaction is transmitted by three heavy bosons, the $W^{\pm}$ and Z bosons that interact with the *hyper charge* and weak isospin. All particles that interact with the Higgs boson are massive.

Besides the bosons, twelve fermions and their corresponding anti-partners (opposite charges) are included in the SM. An overview of the particles content of the SM is given in Figure 2. The fermions can be separated into quarks and leptons, both organized in three
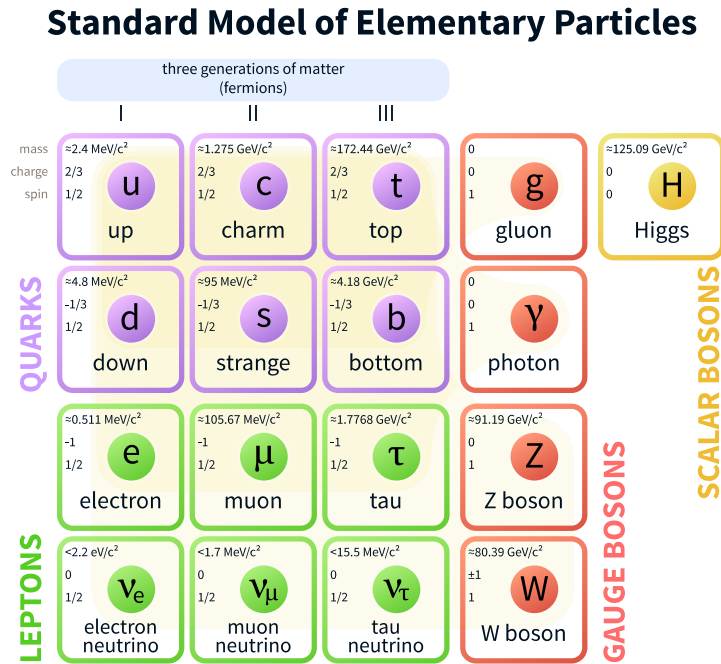
Figure 2.1: Particles of the Standard Model of Particle Physics. Overview of the elementary particles of the Standard Model of Particle Physics categorized into bosons and fermions and organized by particle generation [Wik18].

generations with increasing particle masses. Each lepton and quark generation consists of a pair of particles that forms a weak isospin doublet. While quarks are subject of the electromagnetic, weak and strong force, leptons are only subject of the electromagnetic and weak force. Only up-type leptons (*electrons*, *muons* and *tau leptons*) are electrically charged. The corresponding *neutrinos* are electrically neutral, have no color charge and therefore only interact weakly. Since some of the bosons also carry electric, color, or weak charge, very complex multi-loop processes containing fermion and boson loops are possible.

Although all elementary interactions are mediated by bosonic mediators, the strength, range and characteristics of the individual interactions differ vastly. However, the electromagnetic and the weak force can be described as two very different low-energy manifestations of a single unified interaction mechanism. The spontaneous breaking of this electroweak symmetry can be described by the Higgs mechanism (see Section 2.1.2). In Quantum Chromodynamics (QCD) the strong interaction between quarks and gluons can be described, which results in bound composite objects like hadrons and nuclei. Since gluons are massless and interact with each other due to their color charge, the effects of confinement and asymptotic freedom can be observed. Due to confinement, no free color charged particles can be observed in nature, but only color neutral bound states of color charged particles. Asymptotic freedom, on the other hand, enables the probing of the elementary constituents of protons and neutrons in deep inelastic scattering processes, since the strong force becomes weaker at high energies. Despite the large differences of these interactions, a unified interaction mechanism uniting all three of these interactions is imaginable and pursued by theoretical particle physics.

In the SM, a large range of particle masses is realized. While photons, gluons and neutrinos are considered massless, most quarks and leptons have particle masses in the range of several keV/c^2 to few GeV/c^2. However, W, Z, and Higgs bosons show particle masses in the range of approximately $80\,\mathrm{GeV/c^2} - 125\,\mathrm{GeV/c^2}$ [Par16]. With a particle mass of $m_\mathrm{top} \approx 172\,\mathrm{GeV/c^2}$, the top quark is the heaviest particle of the SM [Par16; Spa16]. The top quark almost exclusively decays into a W boson and a bottom quark via a weak decay and its short lifetime of $\tau_\mathrm{top} < 10^{-24}\,\mathrm{s}$ allows no hadronization and no bound states including a top quark [HL06; Par16].

With its center-of-mass energy of $\sqrt{s} = 13\,\mathrm{TeV}$, the LHC is capable of producing large amounts of all SM particles. Although even the production of Higgs bosons in association with top anti-top pairs is kinematically possible and detectable, the majority of interactions is dominated by light flavor QCD production processes [CMS18l]. However, the LHC also has the potential to produce hypothetical new heavy particles that are not considered by the SM.

Unit conventions   Beside the International System of Units (SI), a few additional non-SI units are common within the high-energy physics (HEP) community to describe physical quantities. The *electronvolt* (eV) is a common unit to measure energies in atomic and subatomic systems and corresponds to an energy of $1\,\mathrm{eV} \approx 1.6 \times 10^{-9}\,\mathrm{J}$. Furthermore, a common convention of HEP is to set the speed of light as well as the Planck constant $\hbar$ to unity:

$$c = \hbar = 1. \tag{2.1}$$

As a consequence, also masses and momenta are expressed in units of electronvolts. Furthermore, the particle interaction *cross sections* of a physical process is an important variable defining the probability for a subatomic particle interaction. The cross section is typically expressed in the non-SI unit *barn* which corresponds to $1\,\mathrm{b} = 10^{-28}\,\mathrm{m^2}$. To both of these units, electronvolt and barn, standard SI-unit prefixes are applied to indicate multiples and fractions of the units (e.g. $1\,\mathrm{pb} = 10^{-12}\,\mathrm{b}$, $1\,\mathrm{GeV} = 10^9\,\mathrm{eV}$, etc.).

2.1.2 Gauge symmetry and symmetry breaking

The SM is a complex mathematical construct based on few general assumptions. Its complete description would exceed the scope of this thesis. Still, a very brief introduction into the basic concept of gauge symmetry is given at the example of a $\mathcal{U}(1)$ symmetry. Furthermore, the concept of symmetry breaking is illustrated at the example of the Higgs mechanism.

The SM is based on the principle of interactions arising from imposing local gauge invariance (gauge symmetry, see e.g. [Pes15]). In this principle, the action is invariant under local gauge transformations $\Omega(x)$ of any fermion field $\psi(x)$:

$$\psi(x) \to \psi'(x) = \Omega(x)\psi(x). \tag{2.2}$$

Here, $\Omega(x)$ corresponds to an element of a given representation of a symmetry group. In order to fulfill the invariance under such a local gauge transformation, additional fields are required and the simple derivatives ∂_μ[1] in the SM Lagrangian need to be replaced by covariant derivatives D_μ including the additional fields.

---

[1]For the remainder of this chapter, the covariant Einstein notation is used: $x_\mu x^\mu = \sum_{\mu,\nu=0}^{3} x_\mu \eta^{\mu\nu} x_\nu$ with $\eta_{\mu\nu}$ representing the Minkowski metric and x_μ representing a covariant vector within this metric [Min08].

For example, in order to achieve invariance under the $\mathcal{U}(1)$ symmetry, which corresponds to a gauge transformation $e^{i\phi(x)}$, an additional field $A_\mu(x)$ and a covariant derivative

$$D_\mu = \partial_\mu + i g_{\text{charge}} A_\mu(x) \tag{2.3}$$

need to be introduced. The additional gauge field $A_\mu(x)$ can be interpreted as the photon field with g_{charge} representing its coupling to electrically charged fermions. The gauge field $A_\mu(x)$ itself transforms as:

$$A_\mu(x) \to A'_\mu(x) = A_\mu(x) - \frac{1}{g_{\text{charge}}} \partial_\mu \phi(x). \tag{2.4}$$

The SM is a $\mathcal{U}(1)_Y \times \mathcal{SU}(2)_L \times \mathcal{SU}(3)_C$ gauge group, with many different internal degrees of freedom. Strong interactions are represented by the $\mathcal{SU}(3)_C$, while electroweak interactions are represented by the $\mathcal{U}(1)_Y \times \mathcal{SU}(2)_L$ subgroup which represent a single interaction. Within the gauge symmetry ansatz presented before, all gauge bosons are required to be massless [Nam60; Gol61]. However, experimentally the W/Z gauge bosons of the weak interaction show large masses [UA183a; UA283b; UA183b; UA283a]. This property can be incorporated in a gauge invariant way by a symmetry that is spontaneously broken by the so called Higgs mechanism [EB64; Hig64a; Hig64b; Hig66; Kib67; GHK64]. This results in W/Z bosons with mass. For a more extensive and complete description, the reader is referred to [Djo08].

In the Higgs mechanism, a weak-isospin doublet commonly referred to as *Higgs doublet* $\phi = (\phi_1, \phi_2)$, with two complex components is introduced. The Lagrangian of the Higgs doublet is invariant under $\mathcal{U}(1) \times \mathcal{SU}(2)$ transformations. In addition, a potential:

$$V(\phi) = \mu^2 \phi^\dagger \phi + \lambda (\phi^\dagger \phi)^2, \ \text{with } \mu^2 < 0, \lambda > 0 \tag{2.5}$$

is introduced. For $\mu^2 < 0$ and $\lambda > 0$, the potential $V(\phi)$ shows a non-vanishing degenerate minimum at:

$$\phi^\dagger_{\text{min}} \phi_{\text{min}} = -\frac{\mu^2}{2\lambda} = \frac{1}{2} v^2. \tag{2.6}$$

None of these energy ground states satisfies the $\mathcal{U}(1) \times \mathcal{SU}(2)$ symmetry. This is referred to as a spontaneously broken symmetry [GSW62]. Figure 2.2 illustrates the shape of the Higgs potential for the simplified case of a $\mathcal{U}(1)$ symmetry. However, the concept of spontaneous symmetry breaking can still be illustrated.

With no loss of generality, the vacuum state can be chosen electrically neutral as:

$$\phi = \frac{1}{\sqrt{2}} \begin{pmatrix} 0 \\ v \end{pmatrix} \tag{2.7}$$

Pertubative fluctuations around the vacuum expectation state can be interpreted as one massive boson (describing radial excitations and later one interpreted as the Higgs boson), and three massless Goldstone bosons (describing the non-radial degrees of freedom). The selection of a suitable gauge eliminates the Goldstone bosons and results in a Higgs field that can be written as:

$$\phi = \frac{1}{\sqrt{2}} \begin{pmatrix} 0 \\ v + H(x) \end{pmatrix}. \tag{2.8}$$
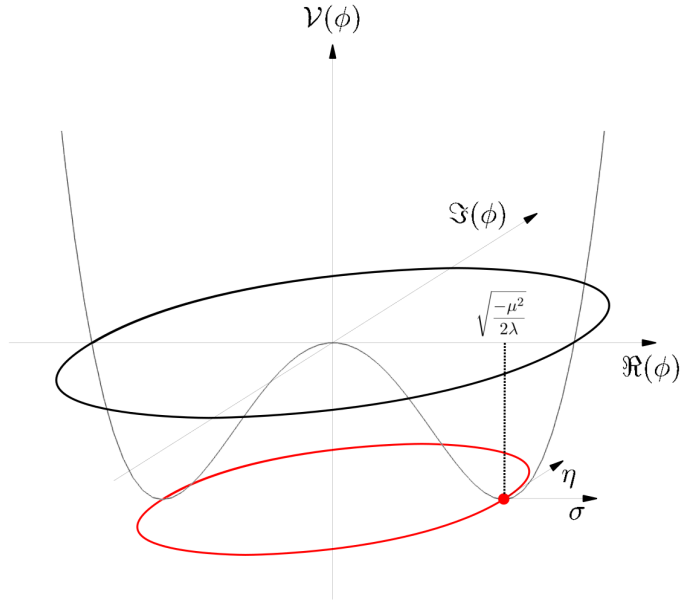
Figure 2.2: Illustration of Higgs potential. Symmetric Higgs potential $V(\phi)$ for a complex scalar Higgs field. The degenerate ground states are indicated by the red circle [Woz17].

The selected gauge also results in massive W and Z bosons as well as a a photon mass term equal to zero. In total the following boson masses are generated by the Higgs mechanism:

$$m_{\mathrm{W}^\pm} = \frac{1}{2}vg_2, \quad m_{\mathrm{Z}} = \frac{1}{2}v\sqrt{g_1^2 + g_2^2}, \quad m_\gamma = 0, \quad m_{\mathrm{H}} = \sqrt{2\lambda}\,v, \tag{2.9}$$

with g_1 and g_2 corresponding to the couplings to fermions that arise from the $\mathcal{U}(1)_{\mathrm{Y}} \times \mathcal{SU}(2)_{\mathrm{L}}$ symmetry.

But not only the W and Z bosons are influenced by the presence of the Higgs field ϕ. Yukawa coupling of fermions to the Higgs field can be interpreted as mass terms for the fermions. Furthermore, a coupling between the Higgs boson and the fermions $m_f = \frac{vG_f}{\sqrt{2}}$ follows:

$$\mathcal{L}_{\mathrm{Yukawa}} = \bar{\psi}_{\mathrm{f,L}}\phi\psi_{\mathrm{f,R}} + \mathrm{h.c.} = -m_f\bar{\psi}_{\mathrm{f,L}}\psi_{\mathrm{f,R}} - \frac{m_f}{v}H\bar{\psi}_{\mathrm{f,L}}\psi_{\mathrm{f,R}} + \mathrm{h.c.} \tag{2.10}$$

From theses calculations follows that the Higgs boson couples proportional to the masses of fermions and quadratically to the masses of massive vector bosons with coupling constants:

$$g_{Hff} = \frac{m_f}{v} \text{ and } g_{HVV} = \frac{2m_V^2}{v}. \tag{2.11}$$

A comparison between SM predictions and measurements on the Higgs coupling is shown in Figure 2.3.

2.2 Physics beyond the Standard Model

Although the SM is successfully used to describe interactions between the known particles at low energy scales, several experimental observations prove that the SM is not capable of completely describing all processes within our universe.
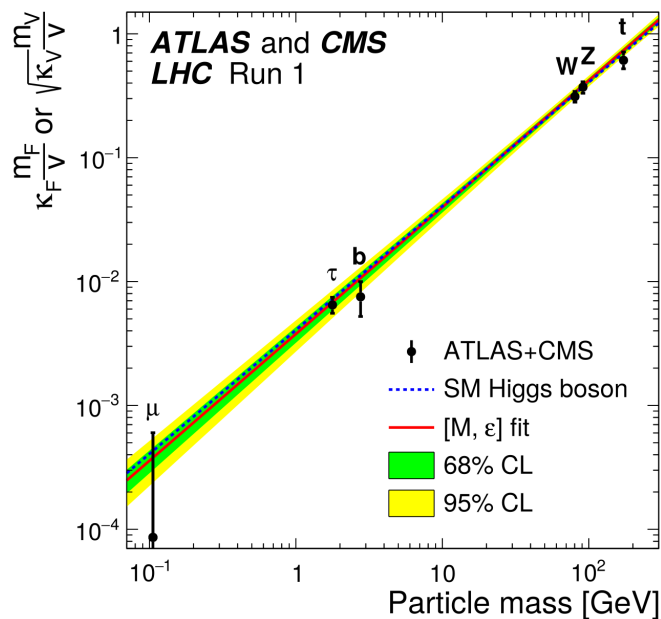
Figure 2.3: Higgs coupling to particles of the Standard Model of Particle Physics.
Coupling strength between Standard Model particles and the Standard Model Higgs boson as a function of the particle mass [CMS16c].

2.2.1 Limitations of the Standard Model of Particle Physics

The most obvious limitation of the SM is that gravity cannot be included so far. Although gravity can be well described by theory of General Relativity (GR), it uses a completely different approach and cannot be formulated as a re-normalizable quantum field theory. The inclusion of the SM and a theory of gravity in a single unified theoretical model is very challenging. So far, the most promising approaches are represented in String Theory and Loop Quantum Gravity [BN90; Rov11]. The effects of quantum gravity are expected to become significant at the Planck scale (10^{19} GeV) or in black holes. Besides this, several cosmological observations and measurements of cosmological quantities indicate the existence of an unknown invisible type of matter called Dark Matter (DM) [Clo+06]. Such cosmological observations are for example: the rotational velocities of spiral galaxies, comparisons between the visible and invisible matter distributions in galaxy clusters, the distribution of matter in large scale structures as well as temperature fluctuation in the cosmic microwave background [Ken87; Bra+08; Blu+84; Hu01]. The DM contribution to the total energy density within our universe is estimated to be five times more than the 5 % of baryonic matter described by the SM. Within the SM, no candidates for DM that are compatible with the large-scale structures observed in the universe exist, requiring the existence of an additional sector of particle physics. Several experiments are dedicated to the search for suitable DM particle candidates, using particle colliders, rare event searches and astronomic telescopes [Fox+12; Ang+08; Aha+06; Ber+17].

Another discrepancy between the SM and the cosmological model is visible in the prediction of the value of the cosmological constant Λ, also called *dark energy*. Using distant supernovae and anisotropies in the cosmic microwave background, the dark energy was measured to account for 70 % of the univers' energy [Per+97; Spe+03]. However,

the predicted value of the cosmological constant from the SM is overestimated by up to 100 orders of magnitude [CST06; Lim04].

The SM can also not explain why the universe consists of matter and almost no anti-matter [DK03]. This asymmetry requires several unique conditions at the early stage of the universe, also know as Sakharov criteria [Sak98]. One of the Sakharov criteria is the existence of CP violating processes that favor matter over anti-matter. Although the SM provides a CP-violating complex phase within the Cabibbo-Kobayashi-Maskawa (CKM) matrix, the resulting CP-violation is much too small to cause the matter anti-matter asymmetry observed in our universe [HL06]. A potential new source of CP-violation within the SM could lie in the Pontecorvo-Maki-Nakagawa-Sakata (PMNS) matrix in the leptonic sector [Whi16].

Within the SM, neutrinos are expected to be massless. However, neutrino oscillation experiments have measured mass differences for the different neutrinos flavors, requiring neutrinos to have a mass [Ahm+02; Fuk+98]. So far, only the differences between the neutrino masses are known, but a series of experiments is dedicated to the measurement of the absolute neutrino mass [Gas+17; Fer+15]. In addition, several experiments are dedicated to question, whether neutrinos are Dirac particles, as predicted by the SM, or Majorana particles and therefore their own anti-particles. Majorana neutrinos would include the existence of lepton-number violating processes as well as additional CP-violating complex phases [Poc15; XZ13].

Besides these experimental observations that cannot be explained by the SM, a detailed look at the SM brings up theoretical issues within the SM as well. Assuming the SM would be the correct theory up to the Planck scale, it could still neither explain the values of the particle masses, the existence of flavor, the number of particle generations nor the large differences in the strength of the fundamental forces. These and other free parameters within the SM suggest that the SM itself is a low energy manifestation of a higher broken symmetry. A theoretical model that unifies the electroweak and the strong force into a single symmetry is typically referred to as Grand Unified Theory (GUT). This unification into a GUT is expected at energies of 10^{16} GeV.

Another problem with the SM arises from radiative corrections to the Higgs boson mass. Since the Higgs boson is a scalar particle, radiative corrections to its mass are quadratically divergent as a function of the energy cut-off Λ [Giu08]:

$$m_{\mathrm{H}} = m_{\mathrm{H,pole}} - \frac{3}{8\pi^2}y_{\mathrm{top}}^2\Lambda^2 + \frac{1}{16\pi^2}g^2\Lambda^2 + \frac{1}{16\pi^2}\lambda^2\Lambda^2. \tag{2.12}$$

The energy cut-off Λ marks the energy scale up to which the SM is considered to provide a correct description of nature. y_{top}, g and λ correspond to the couplings of the top quark and the W/Z bosons to the Higgs boson as well as to the Higgs boson self-coupling loop. Already at cut-off energies of 10 TeV, the corrections become very large and require a very unnatural fine tuning of parameters or a more complete theory. This issue is typically referred to as the *little hierarchy problem.* The problem of fine tuning becomes even more drastic when considering additional radiative corrections caused by the particles expected at the GUT scale. In order to explain the value of the Higgs boson mass, an extreme fine tuning of parameters is required. This is typically referred to as the *big hierarchy problem.*

These and other problems of the SM are surmounted by the number of theoretical models addressing some of these issues. In this thesis, two of the most common approaches to address the hierarchy problems are briefly described: composite-Higgs models and models including extra dimensions. Both of these theories predict the existence of heavy bosonic

resonances as well as vector-like quarks. Although the analysis presented as part of this thesis is designed as a model independent search, these two models are used as benchmark models.

2.2.2 Vector-like quarks

One of the most natural extensions of the SM is the implementation of an additional fourth heavy quark generation. It seems natural to assume the most basic scenario in which the new quarks couple to SM bosons the same way as SM fermions: coupling to strong force proportional to g_s, coupling to photon proportional to electric charge and chiral V-A coupling to weak force. Since no such fourth generation has been observed yet, the quark masses would have to be much larger than the top quark mass. The mass of this fourth generation of heavy quarks would be created by the Higgs mechanism. But since these additional heavy quarks would show a large Yukawa coupling to the Higgs boson, they would significantly modify the fermionic loops in Higgs production and decay processes. For example, the dominant production process for Higgs bosons at the LHC is the fusion of two highly energetic gluons via a top-quark loop. The decay $H \rightarrow \gamma\gamma$ on the other hand is only possible due to fermion and W boson loops. An additional heavy quark would therefore increase the Higgs boson production from gluon fusion as well as the decay branching ratio into two photons [CMS16c]. For this reason, precise measurements of the Higgs boson production and decay modes exclude the existences of such a fourth generation of heavy quarks.

As a modification to the concept of a fourth quark generation, one could assume that the fourth quark generation does not show a chiral coupling $(V - A)$, but instead a vector-like coupling structure (V) [Agu+13; Sim+13]. This would not only allow the left- and right-handed components of these so called vector-like quarks (VLQs) to couple alike, it would also allow a Dirac mass term $m\bar{\psi}\psi$ without the Higgs mechanism. This way, the existence of VLQs would not be in contradiction with the Higgs boson measurements.

In general, VLQs could mix with the SM quarks and therefore have a direct impact on several SM parameters like the Z boson decay branching ratios. Furthermore, VLQs would result in a forward-backward asymmetry in the Z boson decay as well as in the existence of flavor changing neutral currents (FCNCs) at tree-level. While some of these measured parameters constrain the VLQ parameter sector, others favor VLQs, like the forward-backward asymmetry of the Z boson decay observed at LEP [ADM16]. Furthermore, the existence of VLQs would include additional processes of CP-violation. VLQs are also predicted by many theories beyond the SM that include the Higgs boson as a pseudo-Goldstone boson as well as by theories of partial compositness of flavor. For more details on VLQs, the reader is referred to [Agu+13].

Considering requirements like a re-normalizable Lagrangian and well defined quantum numbers, seven potential isospin multiplet representations of VLQs are possible:

$$
\begin{aligned}
& \mathrm{T_{L,R}} \ \mathrm{B_{L,R}} && \text{(singlets)}, \\
(\mathrm{X,T})_{\mathrm{L,R}} \ (\mathrm{T,B})_{\mathrm{L,R}} \ & (\mathrm{B,Y})_{\mathrm{L,R}} && \text{(doublets)}, \\
(\mathrm{X,T,B})_{\mathrm{L,R}} \ & (\mathrm{T,B,Y})_{\mathrm{L,R}} && \text{(triplets)}.
\end{aligned}
\tag{2.13}
$$

The vector-like X quark has an electric charge of $5/3\,e$, the T quark of $2/3\,e$, the B quark of $-1/3\,e$ and the Y quark of $-2/3\,e$. A mass scale of:

$$
m_{\mathrm{T}} \geq m_{\mathrm{X}}, \quad m_{\mathrm{B}} \geq m_{\mathrm{Y}}
\tag{2.14}
$$
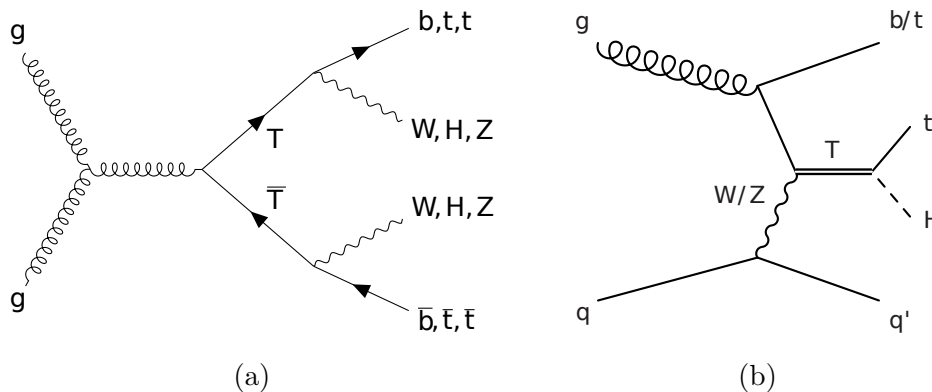
Figure 2.4: Vector-like quark production processes. Leading order Feynman diagrams for two representative processes for the pair production (a) and single production (b) of vector-like quarks at a hadron collider [CMS17l; CMS17m].

is defined by the mixing with other quark generations while the mass ratio between T quark and B quark is model dependent. More complicated representations are theoretically possible when assuming the existence of even more VLQs (e.g in a fifth quark generation) but are not further addressed here.

In general, mixing of the VLQs with all SM quarks and all other VLQs is possible. Due to the constraints from measurements of the SM mixing angles, a mixing with the third generation of the SM quarks is favored. In combination with the mass scale limitations, the following FCNC and charged current (CC) decays of VLQs are dominant:

$$
\begin{aligned}
&\text{T} \rightarrow \text{W}^+\text{b}/\text{Zt}/\text{Ht},\\
&\text{B} \rightarrow \text{W}^-\text{t}/\text{Zb}/\text{Hb},\\
&\text{X} \rightarrow \text{W}^+\text{t},\\
&\text{Y} \rightarrow \text{W}^-\text{b}.
\end{aligned}
\tag{2.15}
$$

At the LHC, VLQs can be produced in a pair production, by coupling to a gluon mediator, similar to the top quark-antiquark pair production process. Additionally, single VLQs can be produced in an electroweak process including a W/Z boson. The exact electroweak coupling for the single VLQ production is model dependent. Figure 2.4 shows two possible production processes at a hadron collider. The dominant production process depends on the mass of the VLQ. At low energies, VLQ pair production via the strong force is dominant, while at high energies VLQs are dominantly produced in electroweak processes. Some VLQ production cross sections at the LHC with a center-of-mass energy of $\sqrt{s} = 13\,\text{TeV}$ are shown in Figure 2.5.

Direct searches at the LHC exclude the existence of VLQs in a mass range of approximately $800\,\text{GeV}$ to $1300\,\text{GeV}$, depending on the signal hypothesis and final state considered [CMS17l; CMS17m; CMS17n; CMS17o; CMS18m]. Nevertheless, the existence of VLQs is predicted by many theories beyond the SM that also predict the existence heavy bosonic resonances. If VLQs can be produced by such a heavy resonance, probing for much heavier VLQs would be possible. Two of these theories beyond the SM are briefly introduced in the following sections.
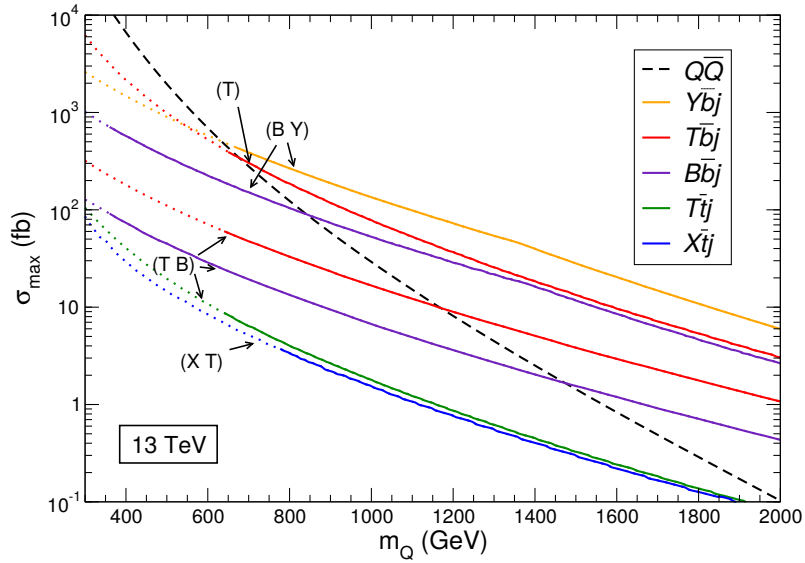
Figure 2.5: Production cross section for vector-like quarks. Maximum production cross section for vector-like quarks singlets and doublets at the LHC at a center-of-mass energy of $\sqrt{s} = 13\,\text{TeV}$ as a function of the vector-like quark mass [Agu+13].

2.2.3 Composite-Higgs theories

A possible solution to the little and big hierarchy problem would be that the Higgs boson is not a fundamental scalar particle. Instead, the Higgs boson would be a composition of two other elementary constituents arising from a higher gauge symmetry. From a historical point of view, this concept of compositeness was very successful after the discovery of the pion in 1947 [Bjo+50]. Originally, the pion was considered to be an elementary mediator of the nuclear interactions between protons and nucleons. Later, the pion was identified as a composite of two elementary quarks, and one of many composite mediators. Nevertheless, the pion plays a central role in low energy chiral perturbation theory of QCD. Here, the pion appears as a would-be Goldstone boson of the spontaneously broken chiral symmetry.

In a composite-Higgs model, instead of the Higgs mechanism, a chiral condensation in a QCD-like interaction would break the electroweak symmetry, resulting in a vector boson mass compatible with the measurements. Such additional QCD-like forces are referred to as *technicolor* [FS81; EL80; DS79].

Although this approach seems very promising, several problems arise when applying it to the SM. While the Higgs mechanisms role to break electroweak symmetry could replaced by a technicolor approach, its role to give fermions their mass via Yukawa coupling cannot be replaced. Also, precision measurements of FCNCs strongly constrain the parameter range for a basic technicolor theory. Finally, the discovery of the Higgs boson makes the realization of a basic technicolor impossible since it does not provide any Higgs boson candidate with such a low mass. However, a modification to an *extended technicolor* model would still be possible and was investigated extensively in the past years [APS04; CS06; Bel+14; LP17].

An alternative approach to the basic technicolor models is the *little composite-Higgs model*, which again includes the Higgs boson as a Goldstone boson arising from an additional strong force [GP75; Ark+02; ACG01; ST05]. Different than before, the new force is not introduced explicitly but as the result of a broken new global symmetry. If the new global symmetry is broken explicitly, a Goldstone boson compatible with the measured

light Higgs boson is provided. In order to provide a substructure compatible with the SM at low-energies while avoiding the quadratic Higgs boson mass divergences, the new global symmetry group G has to provide a very complex group structure. For many models, a so called *collective symmetry breakdown* is assumed. In this scenario, the G symmetry contains two copies of the SM $\mathcal{SU}(2) \times \mathcal{U}(1)$:

$$G \supset H_1 \times H_2 = [\mathcal{SU}(2) \times \mathcal{U}(1)] \times [\mathcal{SU}(2) \times \mathcal{U}(1)]. \tag{2.16}$$

For each subgroup copy H_i, a Goldstone scalar field is introduced. While some of the degrees of freedom are used to give the vector bosons their mass, the remaining degrees of freedom form Higgs bosons. The G symmetry group is required to be constructed in such a way that the Higgs boson mass corrections are protected by the global symmetry, even if part of the symmetry is broken. Several additional massive gauge bosons are predicted with a mass similar to the scale of the symmetry breaking. These additional gauge bosons are typically referred to as heavy bosonic resonance (HBR) or Z' and W'. Furthermore, an additional quark sector with massive quarks is predicted that cancel out top quark loop corrections to the Higgs boson mass. These new heavy fermions could be VLQs. In some models, the concept of *partial compositeness* is implemented, which allows mixing between SM fermions and their heavy partners [Per07]. With the SM fermions coupling to the new physics sector proportional to their mass, the HBR preferably decay into the heaviest fermions. The heaviest fermions available are SM top quarks as well as new heavy fermions from the new composite sector, depending on the mass scale realized.

Effective little-Higgs model In [GL14] an example minimal composite-Higgs model is described in the form of a simplified low-energy effective Lagrangian. Simulated signal events based on this model have been used to interpret the results of chapter 5. The exemplary minimal composite-Higgs model is based on a global $G = \mathcal{SO}(5) \times \mathcal{U}(1)_X$ symmetry that is spontaneously broken into $H = \mathcal{SO}(4) \times \mathcal{U}(1)_X \propto \mathcal{SU}(2)_L \times \mathcal{SU}(2)_R \times \mathcal{U}(1)$. It features several HBRs

$$\rho^{\pm}_{L/R}, \ \rho^{0}_{L/R} \tag{2.17}$$

as well as a VLQ sector that can be organized as

$$\Psi = \frac{1}{\sqrt{2}} \begin{pmatrix} i\text{B} - i\text{X}_{5/3} \\ \text{B} + \text{X}_{5/3} \\ i\text{T} + i\text{X}_{2/3} \\ -\text{T} + \text{X}_{2/3} \end{pmatrix} \tag{2.18}$$

with Ψ corresponding to a quadruplet of VLQs, and $\text{X}_{2/3}$ corresponding to a second top-like VLQ. Within an $\mathcal{SU}(2) \times \mathcal{U}(1)$, the quadruplet Ψ decomposes into two doublets $\Psi_1 = (\text{T}, \text{B})$ and $\Psi_2 = (\text{X}_{5/3}, \text{X}_{2/3})$.

This model focuses on the phenomenological description of heavy vector resonances, and their interactions with top quarks and the top quark partners. Special focus is put on the decay of a neutral ρ^{0}_L resonance into top quarks and vector-like top quark partners. In this particular case, the decay of $\text{T} \to \text{Zt}/\text{Ht}$ is favored with a decay branching ratio of $\text{Zt}/\text{Ht} = 50\,\%/50\,\%$. However, modifications in the model allow decays $\text{T} \to \text{Wb}$ as well, motivating searches in all possible decay channels.

Typical benchmark model parameters are used, ensuring compatibility with constraints from SM precision measurements, while exposing the resonance to decays into VLQs.
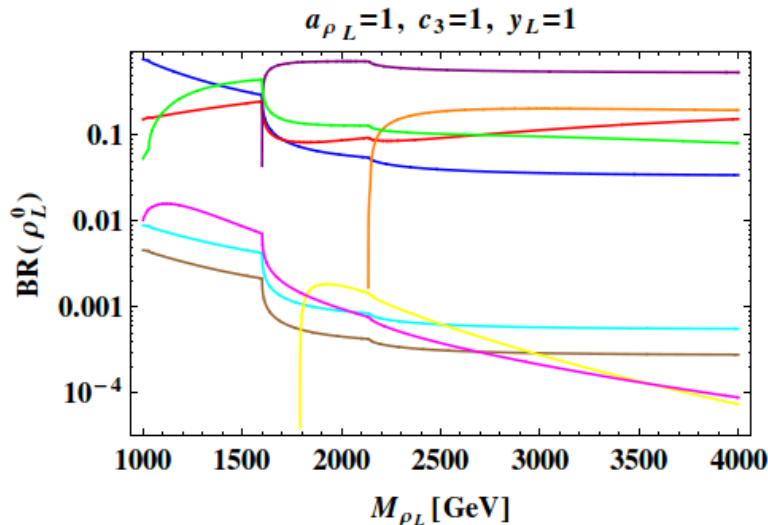
Figure 2.6: Decay of composite-Higgs resonance. Decay branching ratios as a function of the resonance mass for $m_\Psi = 800\,\text{GeV}$, $g_{\rho_{L^0}} = 3$, $c_2 = c_3 = y_L = 1$. Decay modes: WW+ZH (blue), $t\bar{t}+b\bar{b}$ (red), l^+l^- (brown), $u\bar{u} + d\bar{d}$ (cyan), $X_{5/3}\bar{X}_{5/3} + X_{2/3}\bar{X}_{2/3}$ (purple), $T\bar{T} + B\bar{B}$ (orange), $X_{2/3}\bar{T}$ (yellow), $X_{2/3}\bar{t}$ (magenta), and $T\bar{t} + B\bar{b}$ (green) [GL14].

The interaction strength between the HBR and the heavy vector-like top partners c_3, the interaction strength between the top quark and its heavy partners c_2, and the Yukawa coupling y_L are set to $y_L = c_2 = c_3 = 1$. The coupling of the vector resonances to the composite sector is set to $g_{\rho_L} = 3$. Figure 2.6 shows the expected decay branching ratios of a ρ_L resonance for the assumed model parameters and a VLQ mass of $m_\Psi = 800\,\text{GeV}$. While the decay into third generation SM particles dominates at resonance masses $m_{\rho_L^0} \approx m_\Psi$, the decay into pairs of VLQs becomes dominant for $m_{\rho_L^0} > 2m_\Psi$. In the intermediate regime $m_\Psi < m_{\rho_L^0} < 2m_\Psi$, the decay into a top quark and a vector-like top quark becomes dominant.

2.2.4 Extra dimension theories

Another approach involving topologies similar to HBRs and VLQs are models involving extra dimensions (EDs). EDs were originally introduced by Kaluza and Klein shortly after the publication of Einstein's theory of General Relativity [Kal21; Kle26]. One of the most prominent and appealing features of ED models is the possible solution to the gauge hierarchy problem of the large difference in the strength between gravity and other forces. The most basic assumption of ED models is that there are more than the four dimensions assumed by GR. Instead, there are $D = 4 + \delta$ dimensions with gravity interacting in $D - 1$ of these dimensions. With the additional dimension, Newton's law has to be modified from:

$$F(r) = -G_N \frac{m_1 m_2}{r^2} = -\frac{1}{M_{Pl}} \frac{m_1 m_2}{r^2} \tag{2.19}$$

for the classical $D = 4$ scenario, with G_N corresponding to Newton's gravitational constant and M_{Pl} corresponding to the Planck mass, to:

$$F(r) = -G_D(r) \frac{m_1 m_2}{r^2} = -\frac{1}{M_D^{2+\delta}} \frac{m_1 m_2}{r^{2+\delta}}. \tag{2.20}$$

Here, M_D represents the energy scale of the gravitational theory in $D = 4 + \delta$ dimensions. The masses of two particles at a distance r from each other is given by m_1 and m_2. In order to fulfill the original intent of solving the hierarchy problem, M_D should be in the range of the electroweak scale ($\approx 1\,\mathrm{TeV}$). With increasing distance r, the gravitational interaction within the EDs would therefore saturate to a constant value corresponding to a scale of $R \propto 1/M_D$. This way, the large r limit ($r \gg R$) would be compatible with Newton's law in a four dimensional geometry:

$$\frac{1}{M_{\mathrm{Pl}}^2} \frac{m_1 m_2}{r^2} = \frac{1}{M_D^2} \frac{1}{(M_D R)^\delta} \frac{m_1 m_2}{r^2}. \tag{2.21}$$

For small distances ($r \ll R$), however, Newton's law would be violated since the gravitational force would increase proportional to $r^{-(2+\delta)}$. The saturation distance scale R depends on the number of ED and is expected to be in the range of $1\,\mathrm{mm}$. Using small-scale precision measurements of the gravitational force, ED of $\delta < 3$ are already excluded. However, models featuring many EDs, *compactified* EDs, large EDs, or *warped* EDs are still possible. The basic phenomenology of compactified ED models and warped ED models is introduced here. For a more detailed introduction, the reader is referred to [Usa17; RS99a; RS99b].

Compactified extra dimension models Assuming that SM particles are restricted to the known four dimensions of GR and only gravity and gravitons propagate within the EDs, the highest multidimensional space can be referred to as *bulk* while subspaces are referred to as *branes*. Depending on model, groups of particles are limited to certain branes while others have access to the full bulk.

In a simplified model with only one ED, the energy of a free particle would be defined as:

$$E = \sqrt{\vec{p}^2 + p_{\mathrm{ED}}^2 + m^2} = \sqrt{\vec{p}^2 + m_{\mathrm{KK}}^2} \tag{2.22}$$

with $\vec{p}$ the particle momentum in our known three dimensions, m the particle mass, and p_{ED} the corresponding to the momentum in the ED. The manifastation of p_{ED}^2 in our known three dimensions is absorbed in the KK mass m_{KK}. If the ED is infinite and available to the particle, p_{ED} is represented by a continuous spectrum of particle masses. If the ED is compactified, the additional degree of freedom results in an infinite number of quantized additional mass terms or particle excitations. This KK tower of excitations can be interpreted as a spectrum of particles of different mass visible in the three dimensional subspace. For a $\delta = 1$ theory with a compactified ED that has periodic boundary conditions, the space within the ED can be described by $0 \leq \tau \leq R$. The metric of a 5D space without gravity can therefore be written as:

$$ds^2 = dX^M \eta_{MN} dX^N = dx^\mu \eta_{\mu\nu} dx^\nu - d\tau^2, \tag{2.23}$$

with $\eta_{\mu\nu}$ corresponding to the Minkowski metric. As a result, an infinite KK tower of particles is created as excitations of the 4D mass m_0:

$$m^2 = m_0^2 + \frac{n^2}{R^2}. \tag{2.24}$$

Similar calculations can be performed for δ additional dimensions as well as for additional fermion and gluon fields, resulting in even more KK particles. So far, no evidence for such compactified EDs has been found. However, the particle excitations within the additional dimension depend on its size. Therefore, scenarios with very compact EDs are still possible. For more details on the calculations, see [Usa17].

Warped extra dimension models   Another common type of ED models does not assume compactified EDs but focuses instead on EDs with a warped spatial geometry [RS99b; RS99a]. The ED is defined to contain only vacuum energy similar to the vacuum energy of our universe typically referred to as dark energy. This results in a five dimensional metric η_{MN} that can be described as:

$$ds^2 = dX^M \eta_{MN} dX^N = e^{-2\sigma(\tau)} g_{\mu\nu} dx^\mu dx^\nu - d\tau^2, \tag{2.25}$$

with $e^{-2\sigma(\tau)}$ defining the *warp factor* of the ED $\eta_{\mu\nu}$ as the metric tensor of the Minkowsky metric. The metric shows a structure similar to the metric of a vacuum-energy dominated universe, expanded by a fifth dimension. Here, $\sigma(\tau)$ can be interpreted as the vacuum energy of the fifth dimension. Although matter cannot penetrate the fifth dimension, it can be assumed to be localized to two branes at $\tau_1 = 0$ and $\tau_2 = \pi R$ within the multidimensional bulk. In this scenario, the Einstein equations are only fulfilled for $\sigma(\tau) = k|\tau|$ resulting in two different metrics within the two branes:

$$(ds_4(\tau_1))^2 = \eta_{\mu\nu} dx^\mu dx^\nu \tag{2.26}$$

and

$$(ds_4(\tau_2))^2 = e^{-2k\pi R} \eta_{\mu\nu} dx^\mu dx^\nu. \tag{2.27}$$

This corresponds to two 4D Minkowski metrics with a zero cosmological constant. They only differ in the strength of the gravitational interaction. While the first brane can be considered as the *Planck brane* describing physics at the Planck scale, the second is often referred to as the *TeV brane*, representing the physics at the TeV scale. At the TeV scale the gravitational interaction is suppressed by the warp factor $e^{-2k\pi R}$. Considering a 4D Higgs boson at the TeV brane, the action can be written as:

$$S_{\text{Higgs}} = \int d^4x \sqrt{-\det(g^{\mu\nu}(\tau_2))} \left[g^{\mu\nu}(\tau_2) \partial_\mu H \partial_\nu H - \lambda(|H| - v_0^2)^2 \right] \tag{2.28}$$

with H describing the Higgs field, $g^{\mu\nu}(\tau_2)$ defining the metric at the TeV brane, and λ and v_0^2 corresponding to the Higgs self-coupling and the vacuum expectation value. Since the metric at the TeV brane is warped, it can be replaced by $g_{\mu\nu}(\tau_2) = s^{-2k\pi R} g_{\mu\nu}(\tau_1)$. By re-normalizing the Higgs field, the vacuum expectation value $v_0 \approx M_{\text{Planck}}$ as well as all mass parameters of the bulk theory are scaled down to the TeV brane by several orders of magnitude due to a factor $e^{-2k\pi R}$. The quadratic self-coupling of the Higgs boson is retained by this scaling. In such a scenario, also known as Randall-Sundrum (RS1) scenario, the hierarchy problem can be avoided by considering many SM parameters as scaled-down versions of their counterparts at the Planck scale [BCV12].

In typical ED models, additional particles to the SM particle spectrum are expected. Besides gravitons that can penetrate the bulk, so called radions are expected which correspond to a scalar field created by quantum excitations in the ED. Additional predictions strongly depend on the model. However, in order to address the little hierarchy issue, one can loosen the constraints on the SM particles and allow them to propagate through the multidimensional bulk. As a result, KK modes of these SM particles are present. The heavy fermion partners of the top quark that arise from KK excitations can be used to cancel top contributions to the quadratic divergences of the Higgs boson mass. Besides this, a majority of these models predicts the existence of KK excitations of the gluon at the TeV scale [Aga+08]. Also very common is the prediction of a mass-dependent coupling of the KK excitation of the gluon to fermions. This motivates searches for KK gluons decaying into top quarks or the corresponding heavy KK partners of the top quark.

Although the analysis presented in this thesis as part of Chapter 5 is designed as a model-independent search, its results are interpreted in an RS1 model and constrain the parameter range of the first KK gluon excitation [Aga+08].

Effective theory for warped extra dimensions A phenomenologic description of the lightest KK gluon excitation arising from warped EDs at a hadron collider is provided in [BCV12]. The description is limited to the lightest spin-1 and spin-1/2 resonances with a special focus on the decay of a KK gluon G* into an SM particle and a heavy fermion partner. Although designed for KK gluons, the model can be used as a benchmark for many theories beyond the SM that include heavy spin-1 resonances decaying into SM fermions or the heavy fermion partners arising from the model. Here, only a brief introduction to this model is given.

Based on the partial-compositeness paradigm already described in Section 2.2.3, the heavy particles within this theory arise from a new strong sector that couples to SM particles via a linear mixing term. Due to a strong coupling of the G* to heavy SM fermions and their heavy fermion partners, the G* dominantly decays into heavy SM particles and their heavy fermion partners. This allows the creation of an effective theory based on a global symmetry $\mathcal{SU}(3)_C \times \mathcal{O}(4) \times \mathcal{U}(1)_X$, with $\mathcal{O}(4) \supset \mathcal{SO}(4) \propto \mathcal{SU}(2)_L \times \mathcal{SU}(2)_R$. The model contains two sectors, a composite sector containing the Higgs boson $\mathcal{H}$ and an elementary sector. Within the composite sector, a heavy gluon G* exists and transforms as $(\mathbf{8}, \mathbf{1}, \mathbf{1})_0$ under $\mathcal{SU}(3)_C \times \mathcal{SU}(2)_L \times \mathcal{SU}(2)_R \times \mathcal{U}(1)_X$[2]. Further a set of VLQs is comprised:

$$\mathcal{Q} = (\mathbf{3}, \mathbf{2}, \mathbf{2})_{2/3} = \begin{pmatrix} T & T_{5/3} \\ B & T_{2/3} \end{pmatrix}, \qquad \widetilde{T} = (\mathbf{3}, \mathbf{1}, \mathbf{1})_{2/3},$$

$$\mathcal{Q}' = (\mathbf{3}, \mathbf{2}, \mathbf{2})'_{-1/3} = \begin{pmatrix} B_{-1/3} & T' \\ B_{-4/3} & B' \end{pmatrix}, \quad \widetilde{B} = (\mathbf{3}, \mathbf{1}, \mathbf{1})_{-1/3}. \tag{2.29}$$

Other composite states could theoretically be present as well but are not further considered here. The model contains thirteen free parameters in addition to the Higgs boson mass and the Higgs self-coupling: four composite VLQ masses in the fermionic sector, four mass mixing terms, two composite Yukawa couplings and two gauge couplings, one for elementary and one for composite particles. The mixing with the third generation of SM particles is assumed to be dominant.

Since in this model the masses of the SM particles are created by Yukawa couplings, SM measurements can be used to constrain the models parameter range. Furthermore, the parameter range is reduced by assuming the Yukawa coupling to be equal for all composites, and the top-like and bottom-like VLQs masses to be the same. Five free parameters remain: the mass of the top-like VLQ m_T, the mass of the heavy resonance M_{G^*}, the Yukawa coupling for composites $Y_{comp.}$, the gauge sector mixing angle $\tan \theta_3$, and the mixing angle between top quark and vector-like top partner $\sin \varphi_{tR}$.

For the interpretation of the results of Chapter 5, the parameter range is reduced to a scenario where the G* decays via a top quark and a heavy VLQ T. Furthermore, a branching ratio of 50 %/25 %/25 % is selected for the decay of the T quark into Wb/Zt/Ht,

---

[2]In this notation, the first element of $(\mathbf{C},\mathbf{L},\mathbf{R})_X$, corresponds to the transformations under the $\mathcal{SU}(3)_C$ symmetry, the second element nominates the transformation under the assumed $\mathcal{SU}(2)_L$ symmetry, and the third element corresponds to the transformation under $\mathcal{SU}(2)_R$ symmetry. The index corresponds to the charge of the particle defined by the transformation under the $\mathcal{U}(1)_X$ symmetry. For example, particles with charge $2e$ transforming as octets under $\mathcal{SU}(3)_C$ are referred to by as $(\mathbf{8}, ...)_2$.

since it is commonly assumed by the literature [Agu+13]. The other free parameters are selected to be $\tan\theta_3 = 0.44$, $\sin\varphi_{\mathrm{tR}} = 0.6$ and $Y_{\mathrm{comp.}} = 3$ in order to provide an enhanced decay into a VLQ and an SM top quark. The model also predicts the existence of another top-like VLQ $T_{5/3}$ with charge 5/3 that has a mass lower than the vector-like top partner T. The existence of additional VLQs has an impact on the G^* decay width for $2m_{T_{5/3}} \gtrsim M_{G^*}$ and is considered in the theoretical prediction.

The presence of a G^* would theoretically introduce new sources of FCNCs in the top quark T quark interaction. However, these effects are strongly suppressed by off-shell effects of both the HBR and the VLQ. The FCNCs therefore lie beyond the sensitivity of current measurements [Par16]. Therefore, the model is used here to estimate the production cross section, decay branching ratios and resonance width as a function of the resonance mass (see Figure 2.7 and Figure 2.8). In general, the production cross section scales quadratically with $\tan\theta_3$. With increasing resonance masses, more decay channels become available, resulting in an increase of the resonance width. The dominant decay channel strongly depends on the resonance mass. While the G^* decay into SM particles dominates the low mass range, the decay into two VLQs becomes dominant at the high mass range. In the intermediate range, the HBR resonance dominantly decays into an SM particle and its vector-like counterpart. This intermediate range is at the focus of the analysis described in Chapter 5. As shown in Figure 2.7, the potential presence of a top-like VLQ $T_{5/3}$ results in an increased decay width Γ_{G^*} at $M_{G^*} \gtrsim 2m_{T_{5/3}}$. This requires analyses searching for such HBRs decaying via a top quark and a heavy VLQ T to be also sensitive to large resonance widths up to $\Gamma_{G^*}/M_{G^*} \approx 30\,\%$.

(a)

(b)
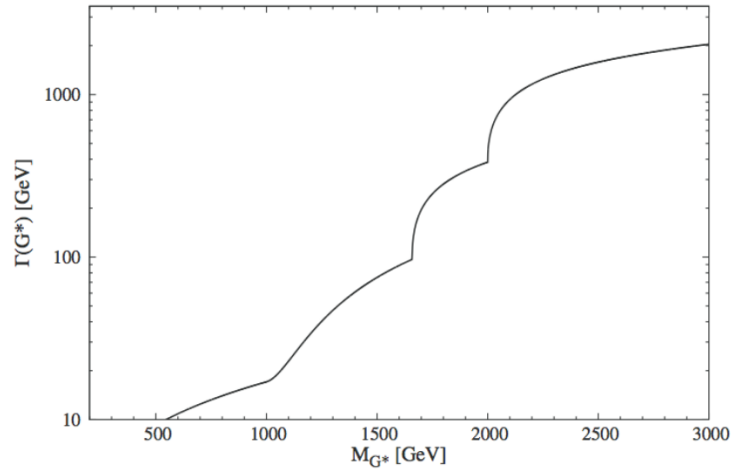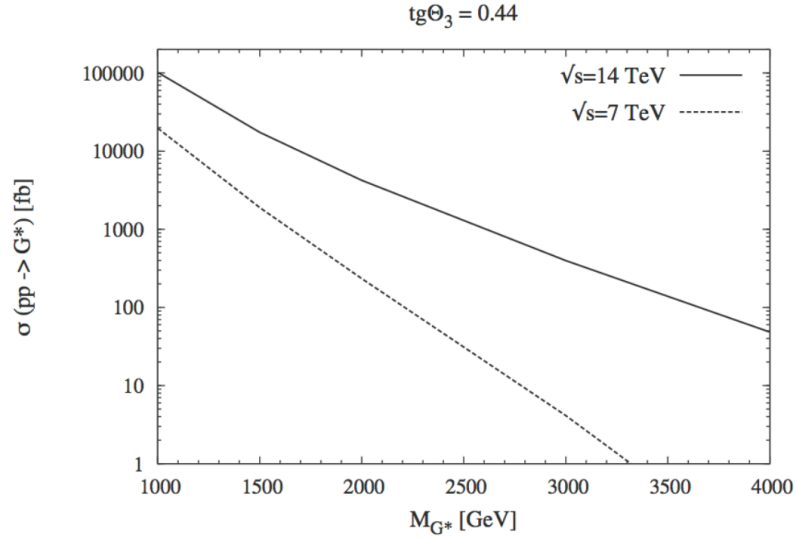
Figure 2.7: Production cross section and resonance width of Kaluza-Klein gluon. Production cross-section for a heavy Kaluza-Klein gluon at the LHC for different center-of-mass energies (a) as a function of the Kaluza-Klein gluon mass. Resonance width as a function of the Kaluza-Klein gluon mass (b). Benchmark parameters $\tan\theta_3 = 0.44$, $\sin\varphi_{tR} = 0.6$, $Y_{comp.} = 3$, and $m_T = 1\,\text{TeV}$ were assumed [BCV12].
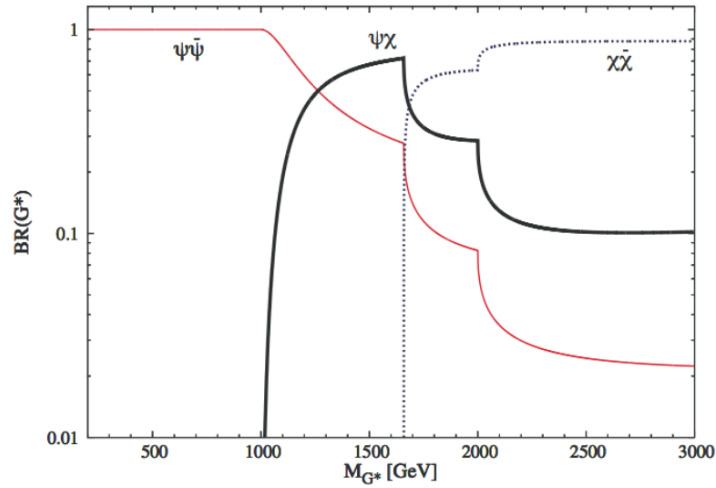
(a)
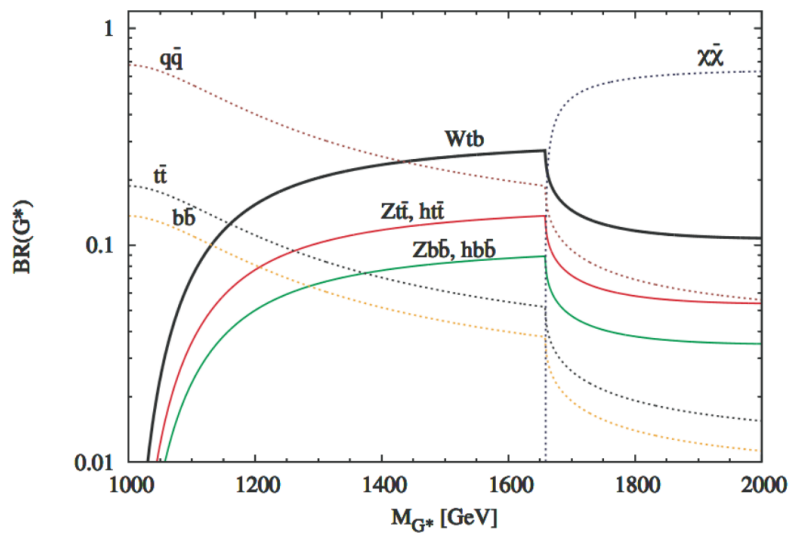
(b)

Figure 2.8: Decay branching ratios of Kaluza-Klein gluon. Decay fractions for Kaluza-Klein gluon decay into pairs of SM particles $\psi\bar{\psi}$, pairs of vector-like quarks $\chi\bar{\chi}$, or into an SM particle and its corresponding vector-like heavy partner $\chi\bar{\psi}$ as a function of the Kaluza-Klein gluon mass (a). Breakdown of decay branching ratios with SM final states (b). Benchmark parameters $\tan\theta_3 = 0.44$, $\sin\varphi_{\mathrm{tR}} = 0.6$, $Y_{\mathrm{comp.}} = 3$, and $m_{\mathrm{T}} = m_\chi = 1\,\mathrm{TeV}$ were assumed [BCV12].

I fell into a burning ring of fire.
I went down down down, and the flames went higher.
And it burns, burns, burns,
the ring of fire, the ring of fire.

Johnny Cash

3

The Compact Muon Solenoid Experiment at the Large Hadron Collider

This chapter is dedicated to the CMS experiment at the LHC and the technical challenges of a HEP experiment at a hadron collider. To begin with, a quick overview of the LHC acceleration complex and the experiments located at the LHC is given. Then the technical and physical challenges arising for high-energy physics experiments at a hadron collider are explained. Besides a brief introduction into the physics goals and the general design concept, a brief description of the CMS subdetector systems and the data readout and processing structures is given.

3.1 The Large Hadron Collider accelerator complex

The LHC is currently the most powerful particle collider available for high-energy physics. Located in a subterranean tunnel of 27 km circumference across the Franco-Swiss border near Geneva, it is designed to accelerate and collide protons, as well as heavy ions. Built by the CERN, the goal of the LHC is the detailed investigation of the high-energy domain of particle physics and the search for physics beyond the SM. Furthermore, it can be operated with heavy ions (typically lead ions) and can be used to study QCD matter states at extreme particle densities as well as to investigate the properties of the strong interaction [Brü+04].

In general, two major variables define the performance of a particle collider: the center-of-mass energy, and the luminosity provided. For a collider with symmetrical beam energies – like the LHC – the center-of-mass energy is given by the sum of the particle energies of the beams $\sqrt{s} = 2 \times E_{\text{particle}}$. For proton-proton collisions, the LHC is designed to provide center-of-mass energies of up to 14 TeV. In heavy ion runs, a maximum center-of-mass energy of 2.7 TeV per nucleon can be achieved.

The instantaneous luminosity, on the other hand, is defined by the rate of interactions $\dot{N}$ created in a process with a certain production cross-section σ

$$\mathcal{L} = \frac{\dot{N}}{\sigma}. \tag{3.1}$$

Assuming the particle beams hit each other at approximately 180°, the instantaneous luminosity of a collider can be estimated as

$$\mathcal{L} = \frac{n_{\text{bunches}} \cdot N_1 \cdot N_2 \cdot f}{\sigma_x \cdot \sigma_y} \tag{3.2}$$
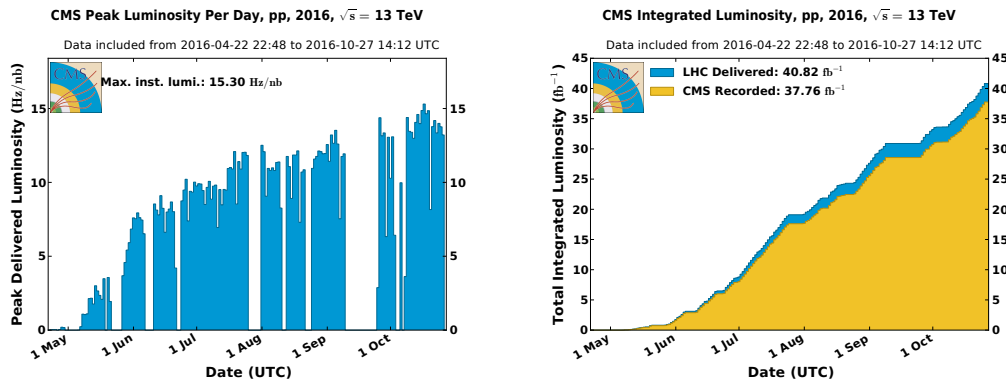
Figure 3.1: Luminosity of 2016 proton-proton run. Peak instantaneous luminosity delivered by the LHC (left) and integrated luminosity collected by CMS (right) [CMS17i].

with n_bunches defining the number of pairs of colliding bunches in the collider and N_1 and N_2 defining the number of particles in the colliding bunches. The frequency with which the particles circulate in the collider is given by f. The width of the transverse particle distribution within a bunch is described by σ_x and σ_y, assuming a Gaussian shape. The LHC is designed to provide an instantaneous luminosity of $\mathcal{L}_\text{design} = 1 \times 10^{34}\,\text{cm}^{-2}\text{s}^{-1}$ at a center-of-mass energy of up to $14\,\text{TeV}$ [Brü+04]. Assuming a total proton-proton interaction cross-section of $7 \times 10^{-28}\,\text{cm}$, an event rate of approximately 7×10^8 events/s is expected [ATL16a]. During the proton-proton collision runs of 2016, peak luminosities of up to $\mathcal{L}_\text{peak,2016} = 1.5 \times 10^{34}\,\text{cm}^{-2}\text{s}^{-1}$ were achieved [CMS17i]. As described in Section 3.4, the instantaneous luminosity is expected to further increase within the upcoming years.

Since the basic principles of physics are typically considered as time independent, the statistical precision can be increased by integrating over all events of a full data set. The integrated luminosity is therefore defined as

$$L = \int \mathcal{L} dt = \frac{N_\text{process events}}{\sigma_\text{process}} \tag{3.3}$$

and can be used to estimate the total number of events expected for a certain physics process $N_\text{process events}$ in dependence of its total cross-section σ_process. Figure 3.1 illustrates the peak luminosity as well as the integrated luminosity provided in the proton-proton collision run of 2016, which has been used in the analysis part of this thesis. Despite the gradual increase in the instantaneous luminosity delivered by the LHC, a good data collection efficiency was achieved by the CMS experiment.

At the LHC, a sequence of several stages is used to accelerate and collide particles. In the acceleration process, the particle bunches are accelerated using drift tubes with oscillating electro-static fields and cavity resonators driven by radio-frequency electromagnetic waves, which are coupled into the cavity resonator longitudinally to the beam direction. Depending on the strength of the electric field required, the cavity resonators are made of superconducting materials (typically NbTi-alloys) or conductive metals (typically copper). Magnetic dipole fields are used to bend the beam into circular trajectory. Depending on the particle momentum, superconducting or normally conducting magnets are used to provided the necessary magnetic fields. Focusing of the particle beams are focused using quadrupole magnets arranged in a so called FODO (Focussing, nOthing, Defocussing, nOthing) structure. The FODO structure consists of two quadrupole magnets arranged at
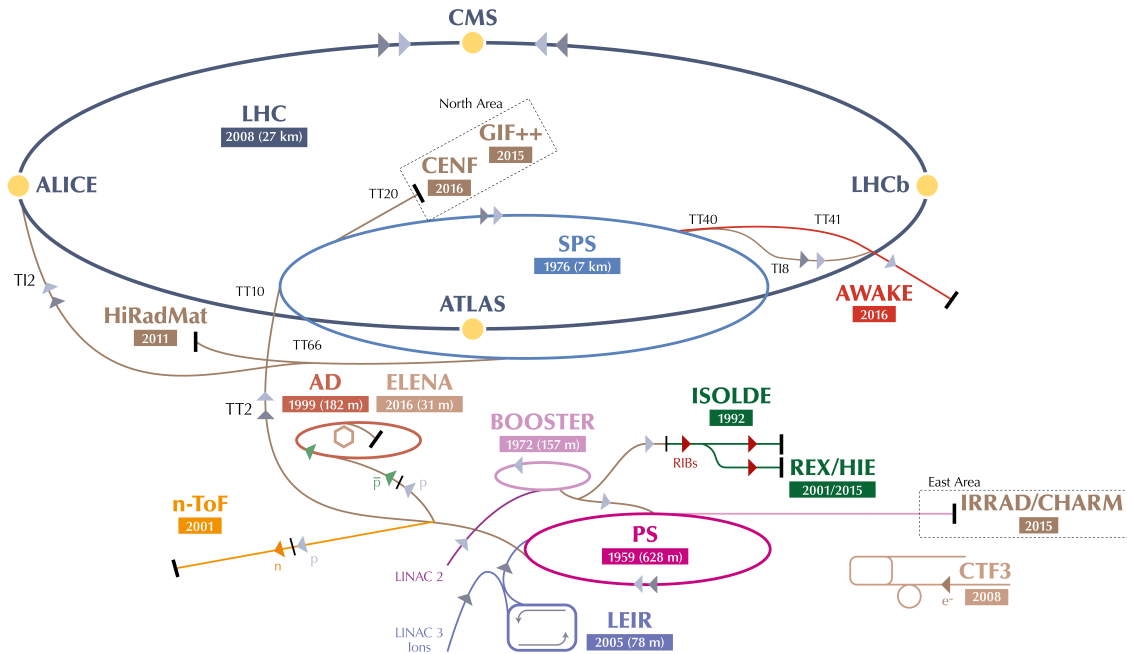
Figure 3.2: CERN accelerator complex. Overview of the acceleration facilities at CERN. For protons, the acceleration process is performed by LINAC 2, Booster, PS, SPS and LHC. For heavy ions, the acceleration stages are LINAC 3, LEIR, PS, SPS and LHC (modified from [Mob16]).

a certain distance and rotated by 90° towards each other around the beam axis. Although both quadrupole magnets are always focusing in one direction of the beam cross-section and defocussing in the other, the arrangement in a FODO structure results in an overall focusing in both directions. The beam focusing in FODO structures is referred to as strong focusing [Bet46]. Further beam manipulations and corrections can be performed by higher order and kicker magnets.

Figure 3.2 illustrates the accelerator complex at CERN. Since the focus of this thesis is placed on proton-proton collisions, the acceleration process of protons is described exemplarily, beginning with the acceleration in a linear accelerator (LINAC 2). In 100 µs pulses, the electrons of highly pure hydrogen gas molecules are stripped off using a so called duoplasmatron. This leaves only protons that are then pre-accelerated in the Radio Frequency Quadrupole (RFQ) before being injected into the LINAC 2. In the strong electric field between the drift tubes of the LINAC, which are driven by a klystron, the protons are accelerated up to an energy of 50 MeV. The second acceleration stage is provided by the Proton Synchrotron Booster (PSB), where the protons are split up into four parallel accelerator rings and compressed into bunches [Han13]. When the protons leave the PSB to be injected into the Proton Synchrotron (PS), they have an energy of 1.4 GeV. The PS forms the second circular accelerator stage and is used to increase the particle energy to 25 GeV. It also increases the number of bunches and defines the final time between two bunches of 25 ns. The PS is followed by the Super Proton Synchrotron (SPS) where the protons are further accelerated to an energy of 450 GeV. Up to this point, normally conducting materials are sufficient to provide the required electric and magnetic fields. The final acceleration of the proton bunches is performed inside the LHC, were eight superconducting resonator cavities increase the particle energy in every beam by 0.5 MeV

per particle turn around the collider. Up to 2808 bunches with approximately 10^{11} protons each can be circulated within the storage ring of the LHC resulting in a bunch-crossing rate of 40 MHz. In total, 1232 superconducting dipole magnets and 392 additional quadrupole magnets are used to bend the beam trajectory and to focus the beam. The superconducting materials is cooled using supra-fluid helium at a temperature of 1.9 K [Brü+04]. Supra-fluid helium has the advantage of no internal friction and high thermal conductivity, ensuring a good heat dissipation [LP70]. At four positions around the LHC collider, the two particle beams intersect and the particles collide.

The heavy ion acceleration process mainly differs in the starting point. After a first acceleration within the LINAC 3, the ions are fed into the Low Energy Ion Ring (LEIR), which is the heavy ion counterpart to the PSB before being transmitted into the PS, the SPS and finally the LHC. For more technical details on the LHC, the reader is referred to [EB08; Brü+04].

In total, the LHC houses seven major experiments at four interaction points around the collider:

- **A Toroidal LHC ApparatuS (ATLAS):** ATLAS is a multi-purpose detector to investigate the characteristics of the Higgs boson and the process of electroweak symmetry breaking. Further it is used to search for physics beyond the SM, and can be used to investigate heavy ion collisions provided by the heavy ion runs of the LHC [ATL08].

- **Compact Muon Solenoid (CMS):** Similar to ATLAS, CMS is a multi-purpose detector experiment with a similar physics program. By operating two similar though not identical experiments at the LHC, an additional redundancy is provided in physics analysis and is used to increase the confidence in physical measurements [CMS08].

- **A Large Ion Collider Experiment (ALICE):** The ALICE experiment puts special focus on the investigation of heavy ion collisions at the LHC and the search for high matter density effects like the quark-gluon plasma. Its detector components are designed to cope with the very high particle track densities created in heavy ion particle collisions. In addition, ALICE can be used as a general-purpose detector similar to CMS and ATLAS [ALI08].

- **Large Hadron Collider beauty (LHCb):** Specialized on the precise measurements of CP-violations and rare B-hadron decays, the LHCb experiment has a unique asymmetric design with a special focus on a precise tracking in the forward region [LHC08a].

- **Large Hadron Collider forward (LHCf):** The physics goal of the LHCf experiment is the investigation of hadron interactions in the forward region of the ATLAS detector. The measurements provide an important calibration input for high energetic cosmic ray experiments [LHC08b].

- **Total Elastic and Diffractive Cross Section Measurement (TOTEM):** Similar to the LHCf experiment, the TOTEM experiment is located in the forward region of the CMS detector. Its main tasks are to measure the total proton-proton interaction cross section in luminosity independent measurements and to search for exotic particles produced in the forward direction [TOT08].

- **Monopole and Exotics Detector at the LHC (MoEDAL):** Located in the LHCb cavern, the MoEDAL experiment is designed to detect highly ionizing particles [Mit17].

3.2 Physics at hadron colliders

A hadron is defined as a composite particle held together by the strong force, and therefore is not elementary, unlike leptons. This has several consequences when operating an experiment at a hadron collider. Since a hadron is a composition of several elementary particles that are in constant interaction, several complex and coupled elementary interactions are possible in a single proton-proton collision. In addition, the actual momentum of an interacting hadron constituent, also known as a *parton*, is unknown.

Protons are the most common representative of hadrons and are also used in the collision at the LHC. At low energies, protons can be considered as a composition of three valence quarks. However with increasing energy, the presence of other partons – gluons and so called *sea quarks* – becomes more and more relevant. The probability density to find a parton i with momentum $x_i \cdot p_{\mathrm{proton}}$, where p_{proton} is the momentum of the proton and x the momentum fraction carried by the parton ($x \in \mathbb{R}, [0,1]$), can be given as function $f_i(x_i, Q^2)$ called Parton Density Function (PDF). Here, Q^2 defines the energy scale of the interaction. As a result, the actual energy of a scattering process, occurring between two elementary partons of the colliding hadrons, is statistically distributed with an average value lower than center-of-mass energy. Furthermore, energy of a scattering process strongly depends on the partons participating in the process. Since the effective center-of-mass energy at parton level is statistically distributed, a large energy range can be investigated simultaneously and without changing the particle beam energies. On the other hand, also the energy fraction available hard scattering process statistically distributed.

The majority of proton-proton collisions is dominated by long-distance interactions resulting in a small momentum transfer. The collision products for these interactions are scattered at small angles with a small transverse momentum ($< 0.5\,\mathrm{GeV}$) and escape the detector undetected. Although these forward scattering processes are at the center of the investigations of the TOTEM and LHCf experiments, they are not of interest for the CMS and ATLAS experiments. The CMS and ATLAS physics programs focus on *hard scattering processes* with a large momentum transfer resulting in decay products with high transverse momenta. The large momentum transfer in hard scattering processes allows the production of massive particles that are used in searches for physics beyond the SM. Figure 3.3 shows an illustration of a hard scattering process.

The cross-section for a hard scattering process can be described by:

$$\sigma(p_1, p_2) = \sum_{i,j \in \mathrm{partons}} \int_0^1 f_i^{\mathrm{H1}}(x_i, \mu_{\mathrm{F}}^2) f_j^{\mathrm{H2}}(x_j, \mu_{\mathrm{F}}^2)\, \hat{\sigma}_{ij}(x_1 p_1, x_2 p_2, \alpha_{\mathrm{S}}(\mu_{\mathrm{R}}^2), \mu_{\mathrm{R}}^2)\, dx_1 dx_2. \quad (3.4)$$

The parton level cross-section $\hat{\sigma}$ is defined by the physical process considered, and can be calculated as a function of the effective center-of-mass energy $\hat{s} = x_1 x_2 s$ and the running coupling constant α_{S} of the strong interaction. The renormalization scale μ_{R} defines the energy scale of the process and is used for the pertubative calculation of the parton level cross-section and α_{S}. The PDFs of the interacting partons f_i^{H1} and f_j^{H2} can be considered as universal and process-independent. Typically, the PDFs are derived from deep inelastic scattering processes [Lai+97]. The factorization scale μ_{F} can be considered as the scale that separates the high-energy short-distance physics of the hard scattering process and
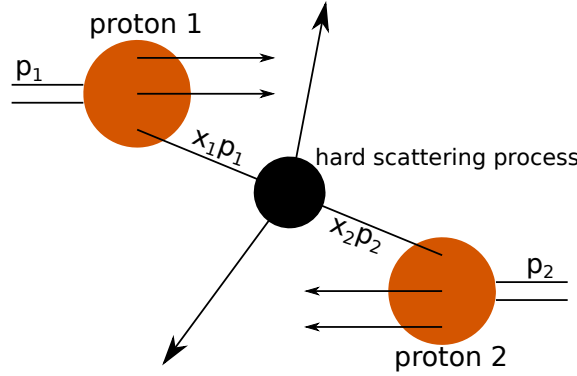
Figure 3.3: Hard scattering process at a proton-proton collider. Graphical representation of a generic hard scattering process with undefined final states at a proton-proton collider like the LHC.

the low-energy long-distances physics. Using Equation (3.2), the cross-section for different hard scattering processes as well as the total interaction cross-section for proton-proton interactions can be calculated as a function of the collider's center-of-mass energy. An overview of the SM cross-sections at hadron colliders is given in Figure 3.4.

In addition, radiative effects allow the production of additional particles in form of initial and final state radiation before and after the actual hard scattering process. Since all other partons in a hadronic collision may interact and radiate particles that influence the hard scattering process, collisions at hadron colliders can be extremely complicated, as illustrated in Figure 3.5. The additional activity in a hadronic collision created by other partons and radiative processes is referred to as Underlying Event (UE). The UE cannot be fully disentangled from the hard scattering process of interest, since the confinement requirement of the strong interactions creates a color connection between the hard scattering process of interest and the UE.

Furthermore, since a single bunch in a LHC proton beam contains $\mathcal{O}(10^{11})$ protons each, typically several proton-proton interactions occur simultaneously. The decay products of the additional collisions that cannot be fully distinguish from the ones created in the main hard scattering process are referred to as pileup (PU). Pileup created by additional collisions in a single bunch-crossing are commonly referred to as *in-time pileup*, while particle remnants from a previous or a subsequent bunch-crossing are referred to as *out-of-time pileup*. In case of in-time pileup, several collision vertices can be identified and are typically referred to as *primary vertices*. Additional so-called *secondary vertices* arise from the decays of unstable particles with a measurable decay length[1] (e.g. τ-leptons and hadrons containing bottom quarks). The number of additional pileup interactions can be estimated as

$$N_{\mathrm{PU}}^{\mathrm{true}} = \frac{\mathcal{L} \cdot \sigma_{\mathrm{inel.\ pp}}}{n_{\mathrm{bunches}} \cdot f} - 1 \tag{3.5}$$

with $\mathcal{L}$ the instantaneous luminosity, $\sigma_{\mathrm{inel.\ pp}}$ the total inelastic proton-proton interaction cross-section, n_{bunches} the total number of bunches per beam and f the frequency with which the bunches circulate the collider.

---

[1]The decay length is defined of flight as the distance an unstable particle before decaying.

proton - (anti)proton cross sections
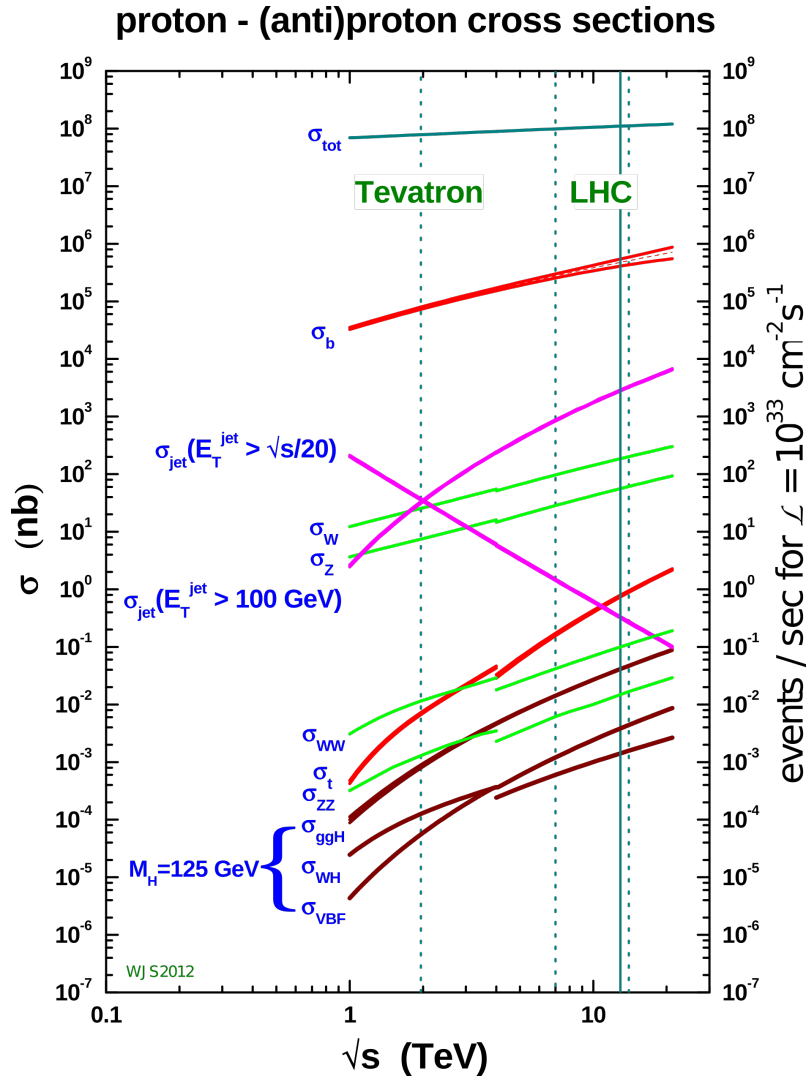
Figure 3.4: Standard Model cross sections at the LHC. Calculated interaction cross-sections in proton-(anti)proton collisions as a function of the center-of-mass energy $\sqrt{s}$ according to the Standard Model of Particle Physics [Sti18].
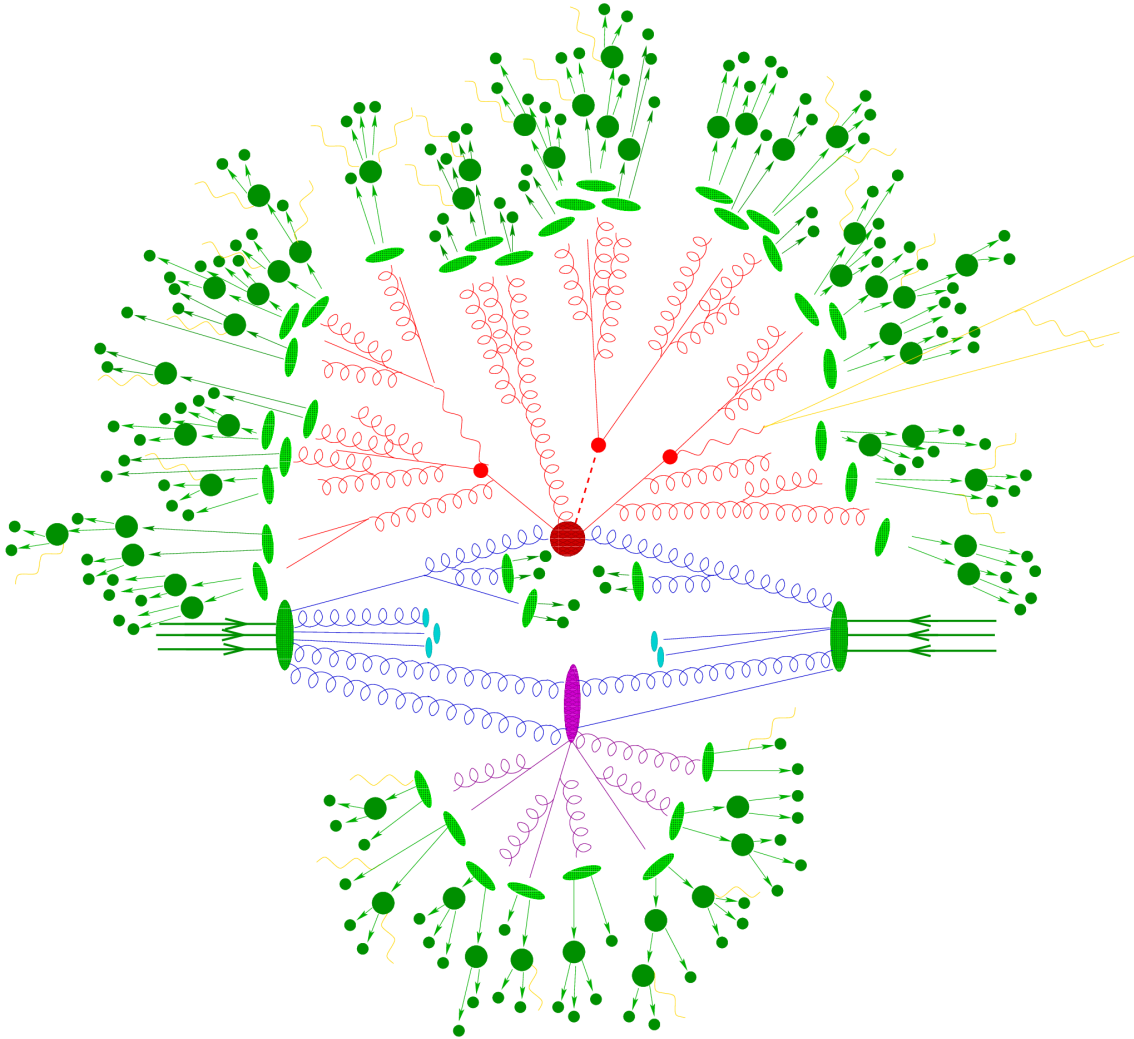
Figure 3.5: Simulated proton-proton collision. Graphical representation of a simulated hadronic collision including: the main interaction (red blob), the initial partons (blue lines), the final interaction products (red lines), and initial and final state radiation. The secondary interaction of the underlying event is represented in purple with its own interaction process, as well as initial state and final state radiation. The transition from partons to hadrons is represented (light green). Decays of the hadrons created in the event are illustrated by dark green blobs [Höc15].

We can summarize that, although a hadron collider can provide high center-of-mass energies, collisions at a hadron collider are extremely complex and include a large number of particles. Therefore detectors with precise and highly granular tracking systems and calorimeters are required to distinguish the decay products as well as possible.

3.3 The Compact Muon Solenoid experiment

Designed in the 1990s, the main goals of the CMS experiment are the investigation of electroweak symmetry breaking and the detailed investigation of the Higgs boson properties, as well as physics at the TeV scale in general. Furthermore, the CMS experiment searches for new physics beyond the SM like Super-symmetry (SUSY), heavy vector bosons, extra-dimensions. During LHC operation in the heavy ion mode, the CMS experiment also provides data about strong interactions in the high particle density state provided by heavy ion collisions.

The CMS detector is a general purpose detector located at the interaction point number five at the northern part of the LHC storage ring. In order to investigate all physics projects mentioned above, the CMS detector is designed to reconstruct all decay products of an event as good as possible. In the design of the detector, a special focus was set on the following requirements [CMS08]:

- Good muon identification, momentum resolution, mass resolution ($< 1\%$ at a particle momentum $p = 100\,\mathrm{GeV}$) and the ability to determine the muon charge for particle momenta up to $p \approx 1\,\mathrm{TeV}$.

- Good momentum resolution and track reconstruction for charged particles in the inner tracker, to allow b and τ tagging.

- Good electromagnetic energy resolution at high granularity for di-photon and di-electron signals ($\approx 1\%$ at $p = 100\,\mathrm{GeV}$) with good vertex localization. Also wide geometric coverage, allowing π^0 rejection and photon-lepton isolation.

- Good jet and missing energy resolution, requiring a highly segmented hadron calorimeter with wide geometric coverage.

- Fast front-end electronics providing a detector signal detection at collision rates of up to 40 MHz.

As most high energy physics particle detectors, the CMS detector is designed in a cylindrical shape housing a barrel region and an endcap region, and shows an onion-like inner substructure. Within the detector, every part has been designed to meet the requirements defined by the CMS physics program. In total, the CMS detector is about 21.6 m long, has a diameter of about 14.6 m, and has a total mass of about 14 000 t. Figure 3.6 gives an overview of the the CMS detector layout.

The basic concept of a detector in high-energy physics is to measure the energies of all particles as well as the trajectories of all charged particles created in the hard scattering process. In order to reconstruct the event fully, a solid angle coverage of nearly 4π is required. Inside the CMS detector, a large superconducting solenoid creates a strong magnetic field, bending the trajectories of charged particles and allowing an identification of the charge sign and the measurement of the particle momentum. Furthermore, the primary vertex the charged particle originates from, can be reconstructed to distinguish the

CMS DETECTOR

Total weight   : 14,000 tonnes
Overall diameter : 15.0 m
Overall length   : 28.7 m
Magnetic field   : 3.8 T

STEEL RETURN YOKE
12,500 tonnes

SILICON TRACKERS
Pixel (100x150 μm) ~16m² ~66M channels
Microstrips (80x180 μm) ~200m² ~9.6M channels

SUPERCONDUCTING SOLENOID
Niobium titanium coil carrying ~18,000A

MUON CHAMBERS
Barrel: 250 Drift Tube, 480 Resistive Plate Chambers
Endcaps: 468 Cathode Strip, 432 Resistive Plate Chambers

PRESHOWER
Silicon strips ~16m² ~137,000 channels

FORWARD CALORIMETER
Steel + Quartz fibres ~2,000 Channels

CRYSTAL
ELECTROMAGNETIC
CALORIMETER (ECAL)
~76,000 scintillating PbWO₄ crystals

HADRON CALORIMETER (HCAL)
Brass + Plastic scintillator ~7,000 channels

Silicon
Tracker

Electromagnetic
Calorimeter

Hadron
Calorimeter

Superconducting
Solenoid

Iron return yoke interspersed
with muon chambers

2T

——— Muon   ——— Electron   ——— Charged hadron (e.g. pion)
- - - Neutral hadron (e.g. neutron)   ····· Photon

Figure 3.6: Overview of the CMS detector layout. Sketches of the CMS detector and its sub-detector systems (top). Furthermore, the trajectories and detector signals caused by different particle types are illustrated in a slice through the central region of the CMS detector (bottom) [CMS18d; CMS16a].

charged particle contributions from the main hard scattering process and pileup. Probably the most important design decision of the CMS detector was to place the whole tracker as well as all calorimeters inside the superconducting solenoid. Hence, the collision products do not lose energy to the solenoid before being detected in the calorimeters. The innermost component of the CMS detector is a large all-silicon tracking system to measure precisely the trajectories of all charged particles. Outside the solenoid, only the muon system is housed. Muons can be considered minimal ionizing as they traverse all calorimeters without creating a relevant signal and can be detected outside the solenoid.

During operation at the LHC high particle fluxes are expected, requiring a large number of readout channels, of the order of $\mathcal{O}(10^8)$, to distinguish the collision products. To be able to handle the large data volume created by $40\,\mathrm{M}$ collisions every second, a potent trigger system is required. The trigger system reduces the amount of data that is read out and stored by several orders of magnitude.

In a hadron collider, the actual momentum of the parton participating in a hard scattering process is unknown. Since the event cannot be fully reconstructed due to particles escaping collinearly with the beam, the boost of the rest frame of the scattering process along the beam axis with respect to the laboratory frame is unknown. However, the transverse fraction of the parton momentum can be considered negligibly small. Therefore the total sum of all transverse momenta is expected to vanish. For this reason, a convenient coordinate system has been established for proton-proton collisions.

The origin of the coordinate system is centered at the nominal collision point of the experiment with the z-axis parallel to the beam line, the y-direction pointing vertically upwards, and the x-direction pointing towards the center of the LHC storage ring. In spherical coordinates, the azimuth angle φ is defined within the xy-plane starting from the x-axis, while the polar angle is measured from the z-axis. The polar angle θ is typically expressed in terms of the pseudorapidity η, which is defined as

$$\eta = -\ln\left(\tan\frac{\theta}{2}\right). \tag{3.6}$$

The pseudorapidity is identical with the high energy limit of the rapidity y, defined as

$$y = \frac{1}{2}\ln\left(\frac{E + p_\mathrm{z}}{E - p_\mathrm{z}}\right). \tag{3.7}$$

Transverse quantities like the transverse momentum and energy are calculated from the components in the xy-plane

$$p_\mathrm{T} = \sqrt{p_\mathrm{x}^2 + p_\mathrm{y}^2}, \ E_\mathrm{T} = \sqrt{E_\mathrm{x}^2 + E_\mathrm{y}^2} \tag{3.8}$$

and are invariant under Lorentz boosts along the z-axis, same as differences in y.

In the following sections a more detailed insight into the different detector components of the CMS detector is given. Quantities like the pseudorapidity η, the distance from the beam pipe r, the azimuth angle φ and the distance from the nominal collision point in z-direction is further used to describe the geometry of the CMS detector components.

3.3.1 Solenoid magnet and muon system

The central part of the CMS detector is formed by a superconducting solenoid made of NbTi-alloy and cooled to approximately $4\,\mathrm{K}$ using liquid helium. The solenoid can be operated with currents of up to $19.14\,\mathrm{kA}$ providing $3.8\,\mathrm{T}$ in its inner volume. The

superconducting solenoid of the CMS detector is not only outstanding due to the strong and relatively homogeneous magnetic field it creates, but also due to its large outer dimensions of $12.5\,\text{m}$ length and $6.3\,\text{m}$ in diameter, providing much space in its inner volume that can be equipped with detector components. Outside the solenoid, an iron yoke is installed to return the magnetic field and to house the muon systems. Furthermore, the iron yoke absorbs hadrons from the collision and the calorimeters and thereby suppresses the hadronic background in the muon system. The magnetic field strength in between the iron yoke reaches $1.8\,\text{T}$ in the barrel region and $2.5\,\text{T}$ in the forward region.

The CMS muon system is implemented in between the slabs of the iron yoke. The main purpose of the muon detector system is the fast identification of muons and a precise measurement of the momenta and the timing information. In the final reconstruction, the detector information of the muon system is combined with the tracking information of the inner tracker to achieve an optimum momentum resolution. Nevertheless, the standalone muon momentum measurement of the muon system is an important part in the trigger system.

Since the muon detector system covers a large area, great emphasis has been put into the design of a cheap, durable, and easy-to-build detector system. In the end, several gas detector concepts were combined into the muon tracking system. In the barrel region ($|\eta| < 1.3$), where the neutron induced background is low and the magnetic field is very homogeneous, four layers of rectangular Drift Tubes (DTs) were installed. Three of the drift tube layers house readout wires parallel to the beam direction. The fourth is installed perpendicular to the z-axis to provide a z-measurement. In the forward region, $0.9 < |\eta| < 2.4$, Cathode Strip Chambers (CSCs) are used. Since the cathode of these multi-wire projection chambers is segmented orthogonally to the wires, every CSC provides two-dimensional spatial resolution, allowing to deal with the higher muon rates in the forward region. Both, the barrel and the forward region are complemented by Resistive Plate Chambers (RPCs) integrated into the muon system structure. Although RPCs provide a poor spatial resolution ($0.8\,\text{cm} - 1.2\,\text{cm}$), they show a very fast detector response and an exceptional time resolution of approximately $3\,\text{ns}$, which is used to provide a precise bunch crossing timing for the detector. The tracking resolution has been measured to be approximately $80\,\mu\text{m} - 400\,\mu\text{m}$ for the DTs in the barrel region and $40\,\mu\text{m} - 150\,\mu\text{m}$ for the CSCs in the endcap regions [CMS13c].

3.3.2 Calorimeters

In the CMS detector, the calorimeters are housed inside the superconducting solenoid. Two calorimeters are installed, each specialized on the detection of a certain group of particles.

The outer part of the calorimeter system is formed by the Hadronic Calorimeter (HCAL), designed to determine the energy of strongly interacting particles by initiating hadronic and electromagnetic showers based on particle-nucleus interactions [CMS97b]. For the HCAL, a good hermiticity is essential to collect reliably most of the transverse energy of an event. The transverse energy can be used to derive the Missing Transverse Energy (MET) of an event, which is defined as the part of momentum in the transverse plane that has not been detected. Missing transverse energy is typically created by neutrinos or long-lived particles predicted by physics beyond the SM, that leave the detector without any interaction. Since hadronic showers can be very complex and extensive and since space within the solenoid is limited, a sampling calorimeter design has been selected for the HCAL. The sampling calorimeter design relies on alternating layers of absorber material initiating a hadronic shower, and sensitive scintillator material creating a signal. Depending on the η-region,

different absorber materials, scintillator materials and readout techniques are used to fit the requirements of the environment in the corresponding detector region.

In total, the HCAL consists of four sub-detector systems. The Hadron Barrel (HB) detector system in the barrel region ($|\eta| < 1.5$) has a thickness of approximately $1.2\,\mathrm{m}$ and is equipped with absorber layers made of non-magnetic brass ($70\,\%$ copper and $30\,\%$ tin). Plastic scintillators form the sensitive layers and are read out by Hybrid Photo Diodes (HPDs). The Hadron Endcap (HE) detector system is constructed similarly and extends the coverage up to $|\eta| < 3$. In the very forward region outside the muon system, the Hadron Forward (HF) detector system is installed to further extend the coverage up to $|\eta| < 5.2$. To cope with the increased particle fluxes in the forward region, steel has been selected as absorber material equipped with quartz fiber Cherenkov detectors as sensitive material layers. The Cherenkov light is read out via photomultiplier tubes, which can be operated in the reduced magnetic field in the forward region. The HCAL is completed by the Hadron Outer (HO) detector, a tailcatcher system installed in the barrel region outside the solenoid. It is designed to detect tails of the high energetic showers inside the HB system that would otherwise not be fully detected. The HO detector system consists of two scintillator layers read out via Silicon Photomultipliers (SiPMs) [CMS97b].

Inside the HCAL, the Electromagnetic Calorimeter (ECAL) is installed [CMS97a]. The ECAL is designed to detect electromagnetically interacting light particles and to measure their total energy. An electromagnetically interacting light particle (electron, positron or photon) hitting one of the 83000 lead tungstate ($PbWO_4$) crystals of the homogeneous ECAL creates a compact electromagnetic shower that is read out via photo-detectors. The amount of light produced in the electromagnetic shower is directly proportional to the total energy of the original particle.

Lead tungstate has been selected due to its radiation hardness, high density, its short radiation length ($X_{\mathrm{rad}} = 8.9\,\mathrm{mm}$) and its fast response time comparable with the time between two bunch crossings of $25\,\mathrm{ns}$ at the LHC. The surface of the lead tungstate crystals is polished in order to allow total reflection and maximize the signal readout efficiency. All crystals in the barrel-endcap design of the ECAL are shaped in a truncated pyramidal shape, and point towards the nominal interaction point with a small offset to avoid an alignment of the particle trajectories with the cracks between the crystals. In the barrel region ($|\eta| < 1.479$), the lead tungstate crystals are $23\,\mathrm{cm}$ long (corresponding to $25.8\,X_0$), have a front surface of $22\,\mathrm{mm} \times 22\,\mathrm{mm}$ and are read out by Avalanche Photo Diodes (APDs). In the endcap region ($1.479 < |\eta| < 3$), the crystals have a length of $22\,\mathrm{cm}$ (corresponding to $\approx 25.8\,X_0$), a front surface of $28\,\mathrm{mm} \times 28\,\mathrm{mm}$ and are read out by Vacuum Phototriodes (VPTs). To identify photons originating from π^0 decays, the endcap region is equipped with a pre-shower detector system. The pre-shower system consist of a $20\,\mathrm{cm}$ thick bulk of lead to initiate electromagnetic showers, and silicon strip detector to measure the hit position where the shower was created [CMS97a].

3.3.3 Silicon Tracker

Another unique feature of the CMS detector is its all-silicon tracker [Kar+97; CMS08]. At the LHC, the tracker has to distinguish and track the trajectories of more than 1000 particles from 20 primary vertices for every bunch crossing. This should be performed with maximum precision while keeping the amount of material as low as possible to avoid multiple scattering, photon conversions or the emission of bremsstrahlung radiation. To cope with the high particle rates, a detector technology with high granularity, fast signal readout and high radiation tolerance is required. To deal with these demands, CMS decided
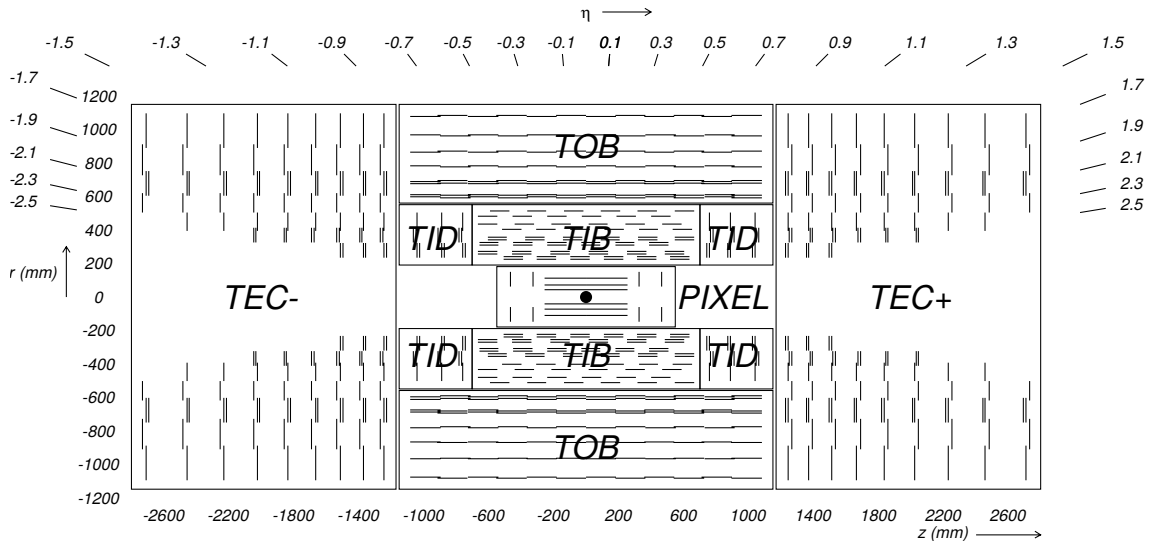
Figure 3.7: Layout of the CMS silicon tracker. Cross-section of CMS silicon tracker, showing the different subdetector systems of the inner tracker. Stereo modules are indicated by double line [CMS12a].

to use an all-silicon tracker with a total active area of over $200\,\mathrm{m}^2$. The working principle of a silicon particle detector is described in Section 6.2.2. Therefore, the description of the CMS silicon tracker in this section is limited to the detector geometry and performance.

Similar to the rest of the CMS detector, the silicon tracker is built in a cylindrical barrel-endcap design and has a total length of $5.8\,\mathrm{m}$ and a diameter of $2.5\,\mathrm{m}$, providing coverage up to $|\eta| < 2.5$. It can be separated into the silicon microstrip detector and the silicon pixel detector. In total, the silicon tracker consists of up to 10 microstrip detector layers provided by four subdetector systems (Tracker Outer Barrel (TOB), Tracker EndCap (TEC), Tracker Inner Barrel (TIB) and Tracker Inner Disk (TID)) and up to three pixel detector layers provided by two additional subdetector systems (Barrel Pixel Detector (BPIX) and Forward Pixel Detector (FPIX)). An overview of the CMS silicon tracker is given in Figure 3.7.

The TOB and TEC form the outermost silicon tracking systems and are built from six layers in the barrel region and nine disks each in endcap at a radius of $55\,\mathrm{cm} < r < 110\,\mathrm{cm}$. The $20\,\mathrm{cm}$ long silicon microstrips are implemented in sensors of $500\,\mathrm{\mu m}$ thickness and have a pitches between $122\,\mathrm{\mu m}$ and $183\,\mathrm{\mu m}$ in the barrel region. In the endcap region (TEC), the average pitch within a module ranges from $97\,\mathrm{\mu m}$ to $184\,\mathrm{\mu m}$. Depending on the pitch, the microstrip detector modules provide a single hit resolution between $23\,\mathrm{\mu m}$ and $40\,\mathrm{\mu m}$. Inside the TOB, within a radius of $20\,\mathrm{cm} < r < 55\,\mathrm{cm}$, the TIB and TID silicon tracking systems are located. Four layers in the barrel region and three disks in the endcap region house microstrip detector modules equipped with $320\,\mathrm{\mu m}$ thick silicon sensors and a microstrip length of $10\,\mathrm{cm}$. In the barrel region the microstrips have pitches between $80\,\mathrm{\mu m}$ and $120\,\mathrm{\mu m}$. In the endcap region the average pitch within a module ranges from $100\,\mathrm{\mu m}$ to $141\,\mathrm{\mu m}$. In the first two tracking layers of every microstrip subdetector system and in the fifth layer of the TEC, the strip detector modules are mounted back to back with additional detector modules. The additional modules are mounted at a stereo angle of $100\,\mathrm{mrad}$ and allow the measurement of a second coordinate. This way these stereo modules can provide an additional measurement of the point where a particle penetrates the layer (z in the

barrel region and r in the endcap region). Overall, the microstrip subdetector systems provide at least nine layers in the acceptance region ($|\eta| < 2.5$) [CMS08].

In total, approximately 9.3 M readout channels are individually wire bonded to their corresponding front-end electronics to be read out every 25 ns. The large number of readout channels comes at cost of a large power consumption (150 kW), requiring a powerful tetradecaflourohexane (C_6F_{14}) cooling system. The cooling system is designed for an operation at $-20\,°C$ in order to dissipate the heat created by the detector modules [CMS08].

The innermost part of the silicon tracker is formed by the CMS silicon pixel detector [CMS08; Erd00]. Other than the microstrip detector, the pixel detector is equipped with a pixelated module structure providing a two-dimensional hit position information. Due to its high granularity, the pixel detector is capable to distinguish particle trajectories even at the high particle densities close to the interaction point. In early 2016, the CMS pixel detector underwent a major upgrade. A more detailed description of the CMS pixel detector, its performance and the upgrade of pixel detector is given in Chapter 7. Since the data used for the analysis presented as part of this thesis was collected using the original pixel detector, a very short sketch of its geometry is given here.

In the barrel region, the original pixel detector was equipped with three detector layers at radii of 44 mm $< r <$ 102 mm. Each of the detector layers had a length of 530 mm [CMS08]. Additional endcap disks in the forward region, at $z = \pm 345$ mm and $z = \pm 465$ mm, covered radii of 60 mm $-$ 150 mm. The whole pixel detector covered a pseudorapidity range of $|\eta| < 2.5$. The pixel cells were implemented in silicon sensors with a thickness of 285 μm and had a size of 100 μm $\times$ 150 μm providing a single hit resolution of 10 μm. Overall, the original pixel detector had a sensitive area of about 1.06 m^2 that was read out via approximately 66 M readout channels. The heat created by the pixel detector was dissipated using a cooling system based on tetradecaflourohexane (C_6F_{14}), similar to the cooling system of the silicon microstrip tracker.

The total material budget of the whole inner tracker extends from 0.4 X_{rad} at $|\eta| = 0$ up to 1.8 X_{rad} at $|\eta| \approx 1.4$, where the barrel and endcap regions overlap [CMS08].

3.3.4 Trigger system and data processing structures

At an instantaneous luminosity of 1×10^{34} cm^{-2}s^{-1}, about $\mathcal{O}(10^9)$ inelastic collision events are expected every second. As described in Section 3.2, high energy physics collision events at hadron colliders can be very complex. At the LHC, not only the storage of $\mathcal{O}(10^9)$ events per seconds, with a data size of 2 MB each, would be impossible. In addition, the readout of the full detector is not possible at such high rates. Technically, only a few hundred events per second can be stored offline for detailed analyses. Since the majority of events are dominated by soft proton-proton scattering processes, which are not interesting for the CMS physics program, a two-stage triggering system has been introduced, reducing the stored number of events by about seven orders of magnitude [CMS17c]. This way, only the potentially interesting events are stored offline.

The first trigger level (L1) is designed to analyze each bunch crossing on a coarse-grain scale and to take a trigger decision within less than 3.2 μs. The L1-trigger is designed to reduce the trigger rate to $\mathcal{O}(100\,\text{kHz})$. To do so, only the detector responses of the muon system and the calorimeter systems are read out. In the mean time, the detector signals of the silicon tracker are stored within its front-end electronics. The L1-trigger is implemented within fast electronics (Field-Programmable Gate Arrays (FPGAs) and Application-Specific Integrated Circuits (ASICs)). If the L1 trigger decision is positive,
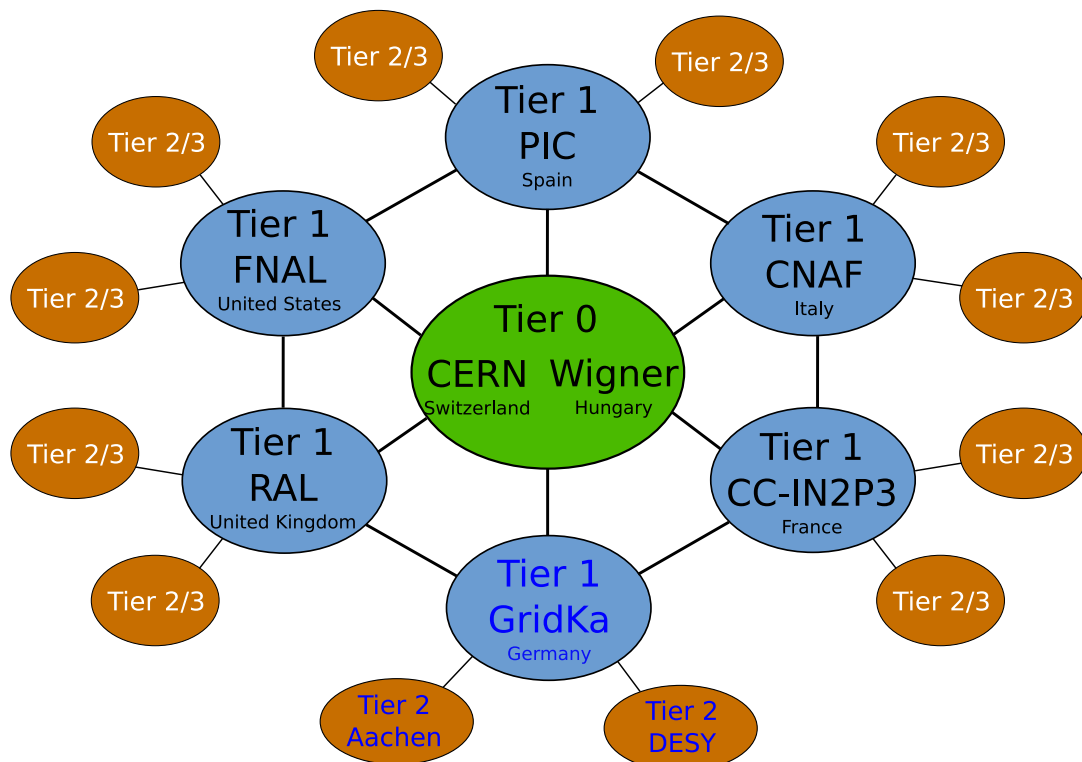
Figure 3.8: Illustration of Worldwide LHC Computing Grid. Distributed computing process flow of data collected in CMS [Cas17].

the whole detector is read out and the event information is forwarded to the next trigger stage. If not, the detector signals are discarded.

The high-level trigger (HLT) forms the second trigger stage and is designed to further reduce the trigger rate to $\mathcal{O}(100\,\mathrm{Hz})$. The HLT is implemented in a software system running on a farm of over 22000 Central Processing Unit (CPU) cores, allowing a flexible adaption of the trigger design. Internally, the HLT is organized in three levels. While the first level only exploits information from the muon system and the calorimetric systems, the second level also uses hit information of the pixel detector. In the third level, the full event information is made available. This allows more sophisticated trigger decisions based on partial event reconstructions.

Nevertheless, large amounts of data (more than $5000\,\mathrm{TB/a}$) and Monte-Carlo event simulations need to be processed in complex event reconstructions before a detailed analysis is possible. Most of the CMS member institutions have local computing clusters available to process their data. But to avoid that every institution performs its own reconstruction and to maximize the available processing power, the LHC community employed a distributed computing system called Worldwide LHC Computing Grid (WLCG). In the WLCG, the processing and storage resources of all contributers are combined in order to provide maximum flexibility in the distributed data processing while maximizing the CPU utilization.

The WLCG is organized in several stages, called *Tiers*. Figure 3.8 illustrates the general structure of the WLCG. The *Tier 0* computing centers, located at CERN and at the Wigner data center in Budapest, provide the basic full event reconstruction and raw data
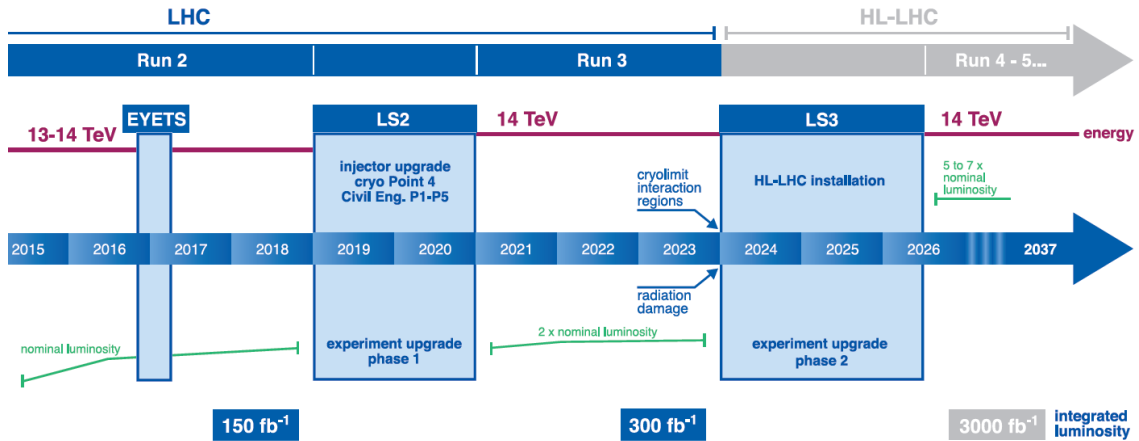
Figure 3.9: Proposed timeline for upgrades of the LHC. Over the next years, the luminosity of the LHC will be gradually increased by several upgrades. In the end, until 2037, an integrated luminosity of about $3000\,\mathrm{fb}^{-1}$ is targeted (modified from [RSS16]).

storage before distributing the data among the *Tier 1* centers. In the Tier 1 centers, a copy of the data is stored which can later on be reprocessed with improved reconstruction algorithms or up-to-date calibrations if needed. Furthermore, the Tier 1 centers are used to generate simulated events for physics analysis. Finally, the *Tier 2* centers are used for end-user analyses and event simulations. For more details in the computing infrastructure, the reader is referred to [Bir+14; Rob12].

3.4 Upgrade plans

The LHC and the experiments at the LHC were originally designed for maximum luminosity of $\mathcal{L} = 1 \times 10^{34}\,\mathrm{cm}^{-2}\mathrm{s}^{-1}$. In recent years, the excellent performance of the LHC and its experimental setups motivated further increases in its luminosity and center-of-mass energy. The current timeline proposed for upgrades of the LHC and the experiments located at the LHC is shown in Figure 3.9.

As a first step already started in 2015, the instantaneous luminosity of the LHC is being gradually increased until it reaches twice its design value. Under these conditions, the LHC is planned to be operated until 2023. In a second step, the LHC will be upgraded to the High-Luminosity LHC (HL-LHC), providing five to seven times the design luminosity. During its whole operation period, the LHC is expected to provide an integrated luminosity of about $3000\,\mathrm{fb}^{-1}$.

The increased amount of data will allow detailed investigations of the Higgs boson properties and its coupling to SM particles, as well as the study of the Higgs boson self coupling. Furthermore, the potential coupling of the Higgs boson to particles beyond the SM will be able to be probed. Since the energy of hard scattering process is statistically distributed, the statistical significance of high-energetic hard scattering processes can be improved by increasing the integrated luminosity. This way a more detailed investigation of physics at the highest energies is possible. With a larger amount of data, it will be possible to extend the energy range of searches for heavy gauge bosons by several TeV [CMS17p].

With the planned improvements in the LHC performance, also new challenges to the detector systems arise, requiring upgrades in the detector systems. So far, two upgrade

phases are planned to keep up with the LHC performance. The first upgrade phase is planned for 2019/2020 (Phase I Upgrade) to handle the doubled design luminosity, and the second for 2024 to 2026 (Phase II Upgrade) to prepare for the HL-LHC. In this section, only a very brief sketch of the planned detector upgrades will be given. For a detailed description of the Phase I Upgrade and the Phase II Upgrade of CMS, the reader is referred to [CMS12a; Man+12; CMS11; TA13] and [Con+15].

CMS Phase I Upgrade   The Phase I Upgrade scheduled to be subsequently performed between 2015 and 2020 will be dedicated to smaller improvements in the beam monitoring systems, luminosity measurements systems as well as in the CMS infrastructure and facilities. In addition, the increased particle rates expected from the increased instantaneous luminosity and the radiation damage of the detector components will be tackled.

The CMS pixel detector is the detector component that is affected most by the increased LHC performance and was already completely replaced with an upgraded version in the Extended Year End Technical Shutdown (EYETS) in 2017. Not only the radiation damage dealt to the pixel detector required the replacement, also an improved front-end electronics was needed to handle the increase in the instantaneous luminosity of the LHC. Furthermore, the number of detector layers had been increased in the upgraded version and the support and cooling system was replaced with a more powerful version. By performing the Phase I Upgrade of the pixel detector in the EYETS 2017, CMS can fully exploit the continuous increase in the instantaneous luminosity while maintaining a high data quality [CMS12a]. The Phase I Upgrade of the pixel detector will be described in more detail in Chapter 8.

The readout of the hadronic calorimeter will be upgraded by replacing all remaining HPDs with SiPMs, in order to enhance the readout performance at the presence of a magnetic field. Furthermore, the SiPMs will provide additional timing information that can be used to suppress background, and the calorimeter trigger will be improved by better back-end electronics [Man+12].

By installing additional CSCs and RPCs, the muon momentum resolution is expected to be improved. So far, this has not been an issue but with increasing luminosity, the contribution of poorly reconstructed muons is expected to increase the overall trigger rate. Furthermore, the readout electronics will be exchanged to improve the rate capability of the muon system [CMS11].

With the increased luminosity, the L1 trigger rate will be increased above $100\,\mathrm{kHz}$. To stay within the $100\,\mathrm{kHz}$, the L1 trigger thresholds implemented on hardware level need to be adapted. Furthermore, the Data Acquisition (DAQ) bandwidth will be increased to handle the larger data volume due to more complex events. The access to the detector will also be used to exchange electronic parts that are not commercially available any more. In addition, the HLT processor farm will be equipped with more powerful CPU cores [TA13].

CMS Phase II Upgrade   With the upgrade to the HL-LHC and an instantaneous luminosity of up to $\mathcal{L} = 7.5 \times 10^{35}\,\mathrm{cm^{-2}s^{-1}}$, the requirements for the CMS detector will be further increased. Up to 140 primary vertices, unprecedented particle rates and radiation damages will require major changes in the CMS detector systems performed as part of the Phase II Upgrade between 2024 and 2026 [Con+15; RSS16].

Three major reasons require a complete overhaul and replacement of the CMS silicon tracker. First, the radiation damage accumulated will reach a level that cannot be managed by the current silicon tracker, requiring the design of more radiation tolerant silicon sensors and readout electronics. Second, the granularity of the current system is not sufficient to be able to distinguish tracks at the expected particle rates. To reduced the detector

occupancy and to improve vertex resolution in the z-direction, modules with so called macro-pixels will be installed. Furthermore, the size of pixels in the pixel vertex detector will be reduced by a factor of six. Finally, to keep the trigger rates reasonably low without increasing the trigger thresholds too much, the silicon tracker itself has to contribute to the L1 trigger decision. Therefore, new types of detector modules will be used, each consisting of two silicon sensors. By comparing the hit positions of a particle traversing these two sensors with the expected curvature of the particle trajectory within the magnetic field, an estimation of the particle momentum can be performed on module level. This way, the silicon tracker will be able to select particles with a momentum larger than e.g. 2 GeV, thus reducing the amount of data being transferred out of the detector per bunch crossing. The possibility to combine the trigger information of several tracker modules allows a basic track reconstruction at the level of the L1 trigger. The technical implementation of such track triggers is currently under investigation [Abb11; Cie+17; Agg+17].

The calorimeters in the forward region of the CMS detector will not only suffer from radiation damage, but also will not be able to cope with the high particle fluxes expected at the HL-LHC. The ECAL as well as the HCAL in the forward region will be replaced by a High Granularity Calorimeter (HGC), a fast sampling calorimeter system using silicon layers as sensitive material. In the electromagnetic part of the HGC, tungstate and copper will be used as absorber materials, while the hadronic section will rely on absorber layers made of brass. The fast readout and the high granularity of the HGC allow a detailed shower reconstruction to cope with the expected high track density [Con+15].

In the forward region of the muon system $(1.5 < |\eta| < 2.4)$, the CSCs will not be able to meet the challenges in terms of momentum resolution and background. The momentum resolution of the muon chamber will therefore be improved by replacing the CSCs with GEM detector chambers. Furthermore, additional GEM detector chambers will be installed outside the the endcap calorimeter HE, providing muon detection coverage up to $|\eta| \approx 3$ [Con+15].

Similar to the Phase I Upgrade, the bandwidth of the trigger and DAQ system will have to be increased in order to cover the increased data volume caused by more complex events at higher pileup. In addition, the trigger latency will be increased from 3.4 µs to 12.8 µs. Further on, all computing and processing steps will have to be upgraded in order to be capable of handling a 15 times larger bandwidth while providing 30 times more processing power [Con+15].
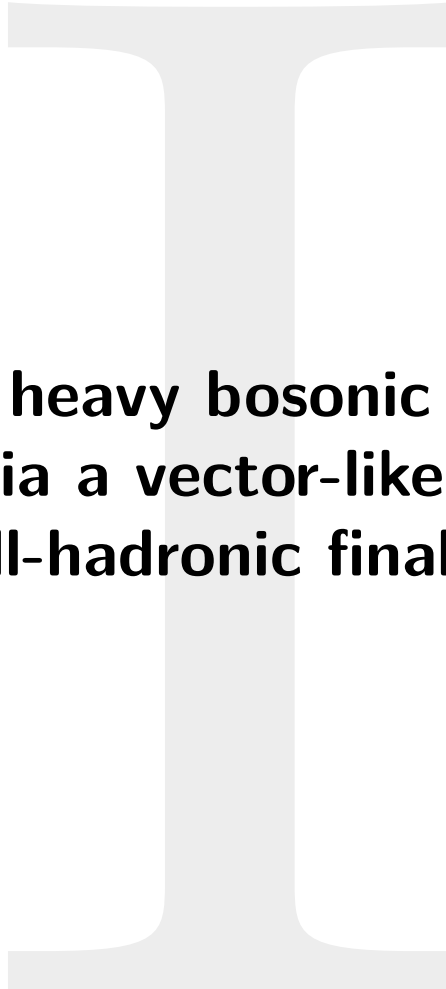
Search for heavy bosonic resonances decaying via a vector-like quark into the all-hadronic final state

Outline

Within our universe, several observations indicate the existence of physics beyond the SM. The CMS experiment at the LHC is one the experiments searching for physics beyond the SM in high-energy proton-proton collisions. The first part of this thesis is dedicated to such a search for physics beyond the SM. Focus is put on the search for heavy bosonic resonances (HBRs) that are predicted by many models beyond the SM and are potentially produced in the proton-proton collisions of the LHC. The analysis presented in the first part of this thesis searches for the decay of such a HBR via a VLQ into the all-hadronic final state. First, a brief introduction into the particle identification techniques that are used to identify the decay products of the HBR is given. Then, the analysis is described in detail. Focus is set on the development of a new data-driven background estimation technique to predict the QCD-multijet background. Finally, the results of the analysis of data collected during the LHC run II in 2016 are presented and interpreted. The analysis was performed at the Institute of Experimental Particle Physics (ETP) at KIT as part of the CMS experiment and in close cooperation with the University of Hamburg.

4

Object reconstruction and identification

The following chapter presents the methods, algorithms and selections used to reconstruct and identify particle signatures for the analysis described in this thesis. After a brief introduction of the basic strategy pursued by the CMS experiment, some relevant particle object reconstruction methods are briefly explained. Since the analysis presented in this thesis is performed in the fully-hadronic final state that only considers hadronic jets to reconstruct the event, special focus is put on jet identification algorithms.

4.1 Particle flow

For most analyses by the CMS experiment, the Particle Flow (PF) approach is used to identify and reconstruct collision product candidates [CMS17h]. The algorithm exploits detector features like the high position and momentum resolution of the CMS silicon tracker, as well as the excellent energy resolution of the ECAL. This way it can provide an excellent high-level physics objects reconstruction efficiency while minimizing the impact of non-linearities in the energy resolution of the calorimeters, as well as pileup (PU) effects. As a general idea of the PF approach, the signals of all detector components are combined to follow the path of a particle through the detector. This way, particles can be categorized into five particle candidate categories: muons, electrons, photons, charged hadrons, and neutral hadrons. The PF concept of single particle identification is illustrated in Figure 4.1 for the example of a single hadronic jet. Since one can distinguish the different single particle candidates, individual energy calibrations can be performed to improve the overall detector resolution.

The particle reconstruction is performed in several iterative steps. In an initial step, intermediate detector objects like particle tracks, calorimeter clusters and muon chamber segments are reconstructed. The particle track reconstruction is performed by iteratively running a combinatorial Kalman-Filter algorithm [Kal60]. This algorithm uses the pixel detector hit information as a seed to reconstruct an initial track that is then further extended by consecutively considering more layers of the silicon tracker. Using additional filters and ECAL information, radiative energy losses of a particle, such as bremsstrahlung emission off an electron as well as particle interactions with the detector material can be considered. Furthermore, the high reconstruction efficiency can be exploited to identify photon conversions into electron-positron pairs within the detector. In addition, particle tracks of the inner tracker can be combined with track segments in the muon system. These
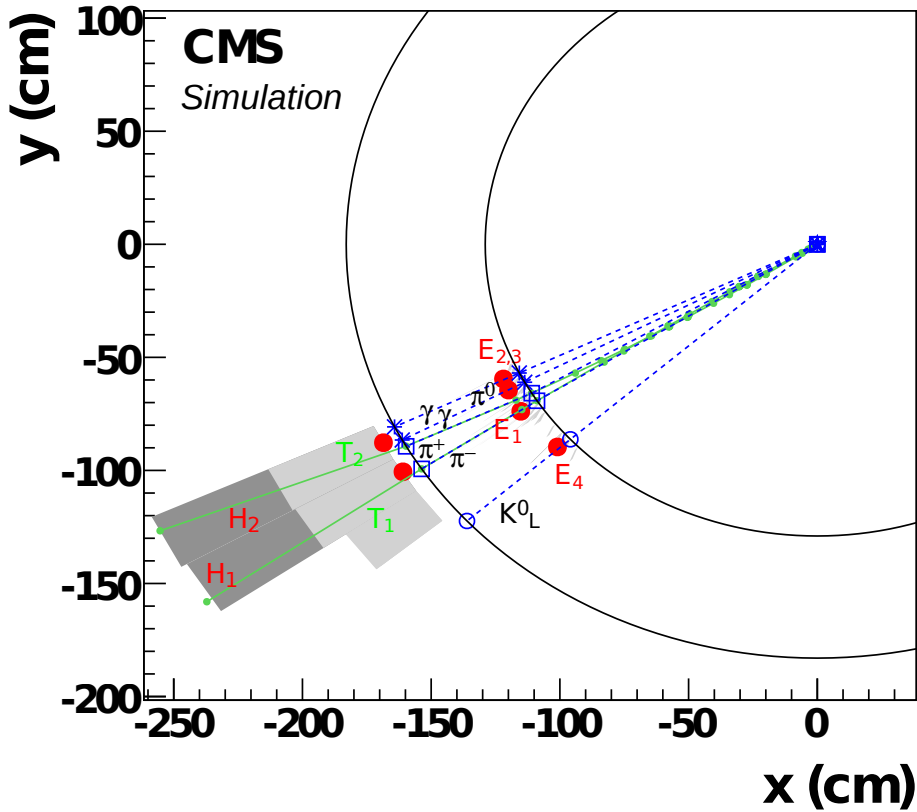
Figure 4.1: Single particle identification within a hadronic jet. Simulation of a hadronic jet and the detector response created by its constituents. The calorimeter responses of the hadronic (dark grey, H_i) and the electromagnetic (light grey, E_i) calorimeters can be combined with the tracker information (green dots, T_i), to reconstruct PF particles (blue lines). Here the PF particles can be identified as photons as well as neutral and charged hadrons [CMS17h].

track segments are derived by combining the tracking information of several muon system cells that were hit.

On the calorimeter side, several calorimeter cells are clustered into *topological clusters*. Starting from a cell with a detector signal larger than all its neighboring cells as a seed, all cells sharing at least one corner with the cells belonging to the cluster are combined into a single cluster. Finally each cluster is fitted with a Gaussian distribution to derive the deposited energy, position and resolution.

A central part of the PF algorithm is the link concept that can be used to create links between the reconstructed particle tracks of the silicon tracker, the muon system and the reconstructed calorimeter clusters. Therefore the particle tracks are matched to the calorimeter clusters as well as to the muon systems creating PF candidates. With all relevant detector information assigned to the corresponding PF candidates, dedicated algorithms, selections and identification techniques can be used to subsequently identify the PF candidates. High-level physics objects like isolated leptons, jets and MET can be reconstructed by combining several of these PF candidates. In addition, part of the PF objects are made available to the HLT allowing to use sophisticated algorithms in order to improve the trigger performance. For more information on the PF approached used in CMS, the reader is referred to [CMS17h].

Using all reconstructed particle tracks compatible with the interaction point of the LHC, the interaction vertices are reconstructed. Groups of tracks close to each other are identified using the *Deterministic Annealing* algorithm [Ros98]. The position of the vertices is derived via an adaptive vertex fit of the groups of tracks [WFV07]. Based on the vertex positions and the clusters of physics objects that are defined later on, the vertex with the largest square sum of the transverse momenta of physics object clusters is identified as the primary vertex.

4.2 Lepton and photon identification

Since the analysis presented in this thesis focuses on the all-hadronic final state, leptons are not used in the event reconstruction and only play a minor role. However, events containing leptons originating from the primary interaction vertex are vetoed for this analysis. Hence, a correct lepton identification is still required. In addition, the identification of leptons plays an important role in the reconstruction sequence of the PF approach. For this reasons, a brief introduction of the lepton identification is given in this section.

Muons   In general, muons provide a very clear signature within the detector. Since they are minimum ionizing particles at the relevant energies, they deposit almost no energy within the calorimeters and traverse the hole detector almost unhindered. Therefore, the particle identification process within the PF approach is typically initiated with the muon reconstruction.

Only if a muon track within the tracker can be linked to a muon track within the outer muon system, the PF candidate is considered as a *global muon*. A global muon that is well separated from other activity within the detector is referred to as an *isolated muon*. In order to be considered well-separated, the energy deposition inside the calorimeters as well as the sum of the transverse momenta of all particle tracks within a cone of $\Delta R = 0.4$ around the global muon track are required to be less than $10\,\%$ of the muon momentum. For $p_\mathrm{T} < 200\,\mathrm{GeV}$, the muon momentum is reconstructed from the particle trajectory within the tracker only, avoiding the impact of multiple scattering of the muon within the calorimeters and the solenoid. Otherwise ($p_\mathrm{T} \geq 200\,\mathrm{GeV}$), several trajectories including different segments of the muon system are fitted and the one with the smallest χ^2 is selected [CMS12c]. The PF particle candidates used to identify and reconstruct the muons are removed from the set of PF particle candidates and are not considered for the remaining object identifications.

In addition to this basic muon reconstruction, offline selections are applied to avoid the reconstruction of fake muons. These selections depend on the application and consider the overall χ^2 of the fitted track, the fraction of valid tracker hits, the compatibility with the muon system segments as well as kinks in the particle trajectory [CMS18a]. For the analysis presented as part of this thesis, muons are required to have $p_\mathrm{T} > 30\,\mathrm{GeV}$, $|\eta| < 2.4$ and need to fulfill certain quality criteria that aim at suppressing fake or misreconstructed muons. These requirements are typically referred to as a so called *medium muon ID* [CMS18a]. Since events containing muons are vetoed in this analysis, no data-simulation correction factors are applied.

Electrons and Photons   As a next step in the PF approach, electrons, positrons and isolated photons are reconstructed. The typical electron/positron reconstruction is induced by a *seed* crystal within the ECAL, that shows at least $1\,\mathrm{GeV}$ ($0.18\,\mathrm{GeV}$) of transverse energy deposited in the barrel (endcap) region. After clustering neighboring crystals

into a so called supercluster, suitable charged particle tracks are identified. By using superclusters for the energy measurement, energy losses from bremsstrahlung can be recovered. The particle tracks are required to have at least five hits in the silicon tracker. By combining the energy measurement in the ECAL with the momentum derived from the particle trajectory within the silicon tracker, an improved energy resolution of the estimated electron momentum at the interaction vertex can be achieved [CMS06].

ECAL energy clusters that cannot be linked to any charged particle trajectory are interpreted as photons. The energy of the photon is directly derived from the ECAL response. Several correction factors are applied to consider shower containment within the ECAL crystals and energy losses within the tracker [CMS15]. Also identified as photons are topologies where a electron-positron pair is created within the tracker, but cannot be traced back to a vertex. Such topologies are assumed to be created by photon conversions in the tracker material. The original photon is then reconstructed from the electron-positron pair. Again, the PF components used to identify and reconstruct electrons and photons are removed from the selection and are not considered for the remaining object identifications.

Additional offline selections are used to improve the electron identification and to discriminate against other particles mimicking an electron signature. These selections are implemented into a multivariate classifier that combines characteristic properties such as: the relative energy deposition within ECAL and HCAL, the cluster shape within the ECAL, the number of hits within the silicon tracker, the quality of the track fit, as well as kinematic variables. For this analysis, electrons are required to fulfill quality criteria referred to as *loose electron ID* that correspond to an average electron identification efficiency of $\epsilon \approx 90\%$ [CMS18j]. Furthermore, electrons have to fulfill $p_T > 30\,\text{GeV}$ and $|\eta| < 2.4$. With all events containing such electrons being vetoed, no additional data-simulation correction factors are applied to the electron selection. Isolated photons were not considered for this analysis.

4.3 Hadronic jet clustering

At a hadron collider, jets are created copiously by strongly interacting particles. In the hadronic showering process, the energy of the original particle is distributed among all jet particles. In order to estimate the energy of the original particle, all particles of the showering process need to be clustered into a single jet.

At the LHC, the energy composition of a typical hadronic jet can be estimated as: 65% charged hadrons, 25% photons, and 10% neutral hadrons [CMS17f]. Although a hadronic jet could generally be reconstructed from low-level objects like calorimeter clusters, the usage of PF candidates provides superior performance. The improvement in the jet energy resolution using PF jets instead of jets reconstructed from the calorimeters only is illustrated in Figure 4.2. For this reason, PF jets are the standard within the CMS experiment, exploiting the good particle track resolution of the silicon tracker.

PF jets are clustered from the remaining PF candidates (after removing muons, electrons, positrons, photons, as well as charged hadrons from PU vertices) using different jet-clustering algorithms. The most common jet clustering algorithms for experiments at the LHC are the anti-k_T (AK) algorithm and the Cambridge-Aachen (CA) algorithm [Cat+93; Dok+97]. Both clustering algorithms are members of the class of sequential recombination algorithms and can be used to cluster the four-vectors of all PF candidates. Their basic working principle is briefly described here.
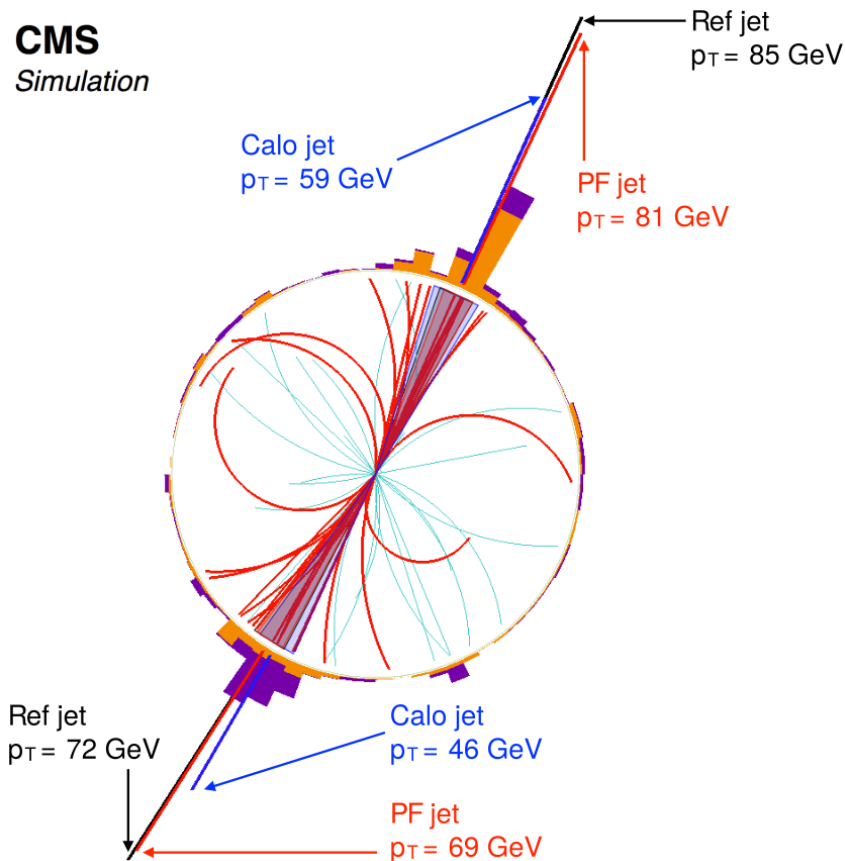
Figure 4.2: Comparison between Particle Flow jets and calorimeter jets. Simulated hadronic di-jet event with generator level hadronic jets (Ref jet), jets reconstructed from single Particle Flow candidates (PF jet) as well as jets reconstructed from the calorimeter response only (Calo jet). Using PF components, improves the jet energy resolution compared to jets reconstructed from the calorimeter response only [CMS17h].

For both clustering algorithms, the distance between two entities (e.g. PF candidates or proto-jets) i and j is defined as:

$$d_{ij} = \min(k_{\mathrm{T},i}^{2p}, k_{\mathrm{T},j}^{2p}) \frac{\Delta_{ij}^2}{R^2} \tag{4.1}$$

with $\Delta_{ij}^2 = (y_i - y_j)^2 + (\phi_i - \phi_j)^2$, and y_i corresponding to the rapidity (for $E_i \gg m_i$, the pseudo-rapidity η_i is typically used instead), ϕ_i to the azimuthal angle, and $k_{\mathrm{T},i}$ to the transverse momentum of entity i. The two jet clustering parameters p and R define the behavior of the clustering. The radius parameter R is related to the jet size in the $\eta \times \varphi$-plane. The distance between entity i and the beamline is defined as:

$$d_{iB} = k_{\mathrm{T},i}^{2p}, \tag{4.2}$$

and is used as termination condition for the algorithm. For every iteration of the clustering, both distances are computed for all entities i and pairs of entities ij, and the minimum distance is identified. If d_{iB} is identified as the minimum distance, the corresponding entity i is defined as a jet and removed from the collection. If the minimum distance is a d_{ij} distance, both entities i and j are merged into a new proto-jet by adding two four-vectors.

By iteratively repeating this procedure until no entities are left, all PF candidates are clustered into jets.

A radius parameter of $R = 0.4$ is selected as the standard within the CMS experiment and is suitable for the clustering of jets originating from light quarks. However, reconstruction of boosted hadronically decaying heavy particles like W, Z, or Higgs bosons or top quarks require a larger radius parameter of $R = 0.8$. A jet clustering algorithm with $p = -1$ is called anti-k_{T} algorithm, while for $p = 0$ the algorithm is called Cambridge-Aachen. A jet clustering algorithm with $p = 1$ is called k_{T} algorithm, which is only used in very specific applications. While the anti-k_{T} algorithm first merges the most energetic components of a jet before including softer components, the CA algorithm does not use momentum information for the clustering of particles emitted under small angles. It therefore first clusters softer particles before combining the more energetic clusters. Since anti-k_{T} jets typically show a more regular shape and their energy is therefore calibrated more easily, they are the standard jet selection within the CMS experiment. Still, CA jets find large usage in substructure algorithms used to identify boosted heavy particles, since they are computationally more performant when reversing the clustering history. From here on, jets clustered with the anti-k_{T} algorithm and a jet cone size of $R = 0.4$ and $R = 0.8$ are referred to as AK4-jets and AK8-jets, respectively.

In order to reject fake jets, badly reconstructed jets or jets created by detector noise, *jet-IDs* are provided by the CMS collaboration to correctly identify hadronic jets [CMS18i]. These jet-IDs consider the fractions of charged hadrons, neutral hadrons, charged electromagnetically interacting particles and neutral electromagnetically interacting particles within a jet. Furthermore, the number of constituents as well as the fraction of muons within a jet are considered.

For this analysis, a *loose jet-ID* has been selected for AK4-jets and AK8-jets, which corresponds to a reconstruction efficiency $\epsilon > 98\%$ and a background rejection $> 90\%$. In addition, jets are required to fulfill $|\eta| < 2.4$ as well as $p_{\mathrm{T}}(\mathrm{AK4\text{-}jet}) > 75\,\mathrm{GeV}$ and $p_{\mathrm{T}}(\mathrm{AK8\text{-}jet}) > 150\,\mathrm{GeV}$.

Pileup subtraction   With the primary interaction vertex known, particle tracks originating from pileup can be removed from the event reconstruction. This procedure of removing charged hadrons not originating from the primary vertex is called Charged Hadron Subtraction (CHS) [Kro+14; CMS14c]. However, neutral hadrons do not create tracks within the tracker and therefore cannot be unambiguously assigned to vertices. To compensate the neutral hadron contribution originating from pileup, maps of average pileup neutral energy density are derived from minimum bias events. Using these maps, the expected neutral hadron contribution from pileup can be subtracted from every jet as a function of its position, orientation in η and ϕ, as well as its transverse momentum and area.

Jet calibration   In order to provide a homogeneous detector response in data and event simulations, a series of correction factors is applied to the reconstructed jets [CMS17f]. The corrections are applied by scaling the four-momenta of the jets as a function of p_{T} and η. An illustration of the jet energy correction (JEC) workflow is given in Figure 4.3.

The first step of the correction sequence, typically called L1, rejects noise and performs the neutral pileup subtraction based on the jet area and is applied to reconstructed jets from data and simulations using so called random cones (RCs, see CHS procedure above). Next, the detector response is corrected as a function of η and p_{T} by applying the so called L2-relative and L3-absolute corrections to data as well as to simulated jets. The
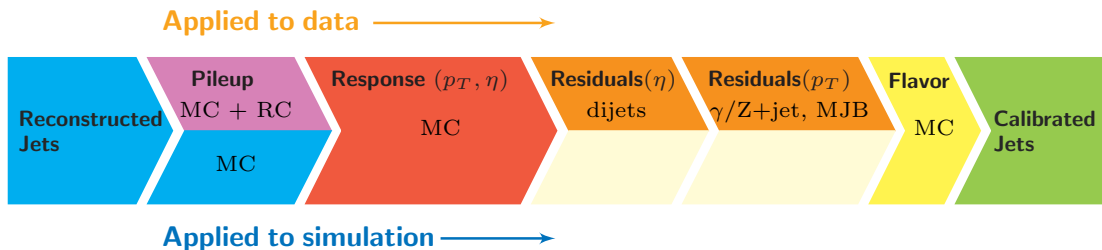
Figure 4.3: Workflow schematic of jet energy correction procedure. Several stages of correction are applied to simulations (MC) as well as data. Residual deviations between simulations and data are corrected by re-scaling data. Flavor dependent corrections that require information about the initial particle flavor are applied to simulations [CMS18h].

correction factors are derived from simulated events by matching the PF candidates to the generator level particles. In a third step, any residual deviations between data and simulations are considered in the so called L2L3-residual corrections, which are applied to the reconstructed jets in data only. The correction factors are derived from data-simulation comparisons in di-jet events, Z+jets and γ+jets events as a function of η and p_{T}.

Since simulated events showed to have a better jet energy resolution (JER) than data, the jet energy resolution of simulated events is corrected to fit the JER observed in data. The smearing factors are derived from comparisons between data and simulations of di-jet, γ+jets, and multijet background (MJB) events. For the JEC as well as the JER, systematic uncertainties are assigned.

4.4 b-jet identification

In high-energy physics, bottom quarks play an important role since they provide access to important SM processes, as well as to potential physics beyond the SM. At the LHC, bottom quarks an important tool to reconstruct top quarks and Higgs bosons which dominantly decay into bottom quarks. Jets originating from the hadronization of bottom quarks (b-jets) show several characteristics that allow to distinguish them from jets produced by the hadronization of light quarks or gluons.

The most prominent feature of b-jets is the presence of a secondary vertex well separated from the primary vertex. Such a secondary vertex arises from the delayed decay of a B-meson. The relatively long life time of B-mesons ($\tau_{\mathrm{B\text{-}meson}} \approx 1.5 \cdot 10^{-12}\,\mathrm{s}$) is attributed to weak decays of the bottom quark that are suppressed via the CKM matrix. At the LHC, B-meson decay lengths of $\beta \cdot \gamma \cdot \mathrm{c} \cdot \tau_{\mathrm{B\text{-}meson}} \approx 3\,\mathrm{mm}$ are typical [ATL16b]. As a consequence, the reconstructed particle tracks of the B-meson decay products show a higher impact parameter (IP) value. The IP is defined as the minimum distance of the linearized particle trajectory from the primary vertex. Figure 4.4 illustrates the secondary vertex characteristic of a b-jet. In addition to the secondary vertex, hadronic jets created by bottom quark decays often show an increased jet mass (reconstructed from its PF constituents), as well as the production of leptons with a large transverse momentum relative to the jet axis, that originate from electroweak decays of the bottom quark. However, jets originating from charm quark hadronizations show similar characteristics and therefore are more difficult to distinguish from b-jets than up quark, down quark, strange quark or gluon jets [CMS13a].
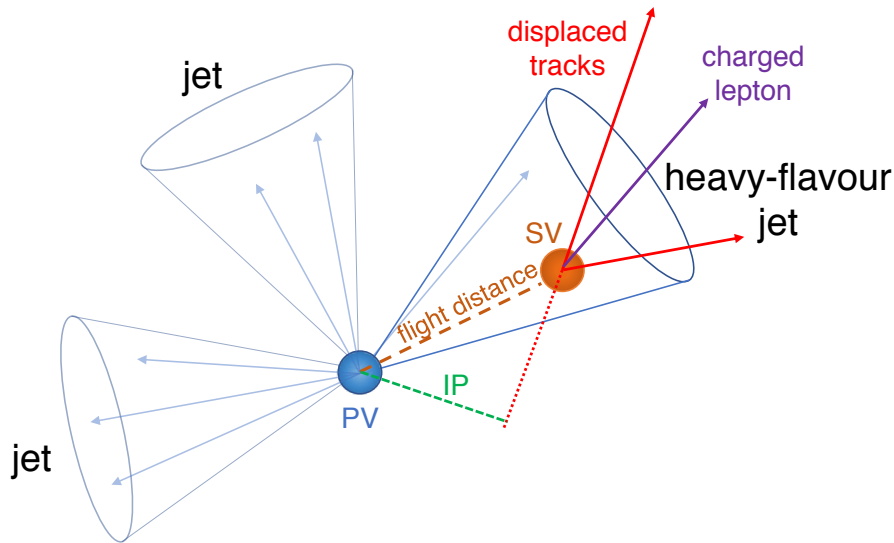
Figure 4.4: Secondary vertex in a b-jet. Illustration of an event with a secondary vertex (SV) due to a B-meson decay. The distance between the primary vertex (PV) and the SV can be exploited to identify jets originating from the hadronization of b-quarks [CMS18f].

Within the CMS experiment, version 2 of the Combined Secondary Vertex (CSV) algorithm is most commonly used to identify b-jets [CMS16b]. The CSV algorithm uses the inclusive vertex finder (IVF) algorithm to reconstruct primary and secondary vertices from all particle tracks in the event. Then, a boosted decision tree (BDT) is used to combine all event variables into a final classification. The output of the CSV algorithm, assigned individually to every jet, can take values from zero to one, with larger values corresponding to more b-jet-like jet characteristics.

More improved b-tagging algorithms have been developed by the CMS experiment as well. These algorithms combine several b-tagging algorithms or use deep neural networks (DNNs) and are expected to further increase the b-tagging performance [CMS16b; CMS17d].

In general, the CSV b-tagging algorithm can be applied to any kind of PF jet. Within CMS however, it is typically used on AK4-jets. Still, b-tagging can be applied to $R = 0.8$ cone size jets and even on so called *subjets* within such a large cone size jets. A subjet is a smaller cluster of jet constituents within the large cone size jet. This allows improvements in the identification of hadronically decaying boosted Higgs bosons, W/Z bosons and top quarks. The usage of subjet b-tagging is further described in the upcoming section.

Several working points for the CSV b-tagging algorithm are provided by the CMS experiment. The working points are derived as compromises between maximizing the b-tagging efficiency while minimizing the mis-tagging rate with which light quark and gluon jets are wrongly identified as b-jets. For this analysis, a *medium working point* (output of CSV algorithm CSV_v2 > 0.8484) was selected, corresponding to an average b-tagging efficiency of $\epsilon \approx 68\,\%$ and a mis-identification rate of approximately $1\,\%$ [CMS18f].

So-called Scale Factors (SFs) are applied to simulated jets as a function of the jet p_{T}, η as well as its flavor composition, in order to match the b-tagging performance on simulations to the performance observed in data. The scale factors are derived from data-simulation comparisons using a tag-and-probe technique in dileptonic, semileptonic

2 light-quark jets & 1 b-jet   2 light-quark jets & 1 b-jet   1 W-jet & 1 b-jet   1 t-jet with b-subjet
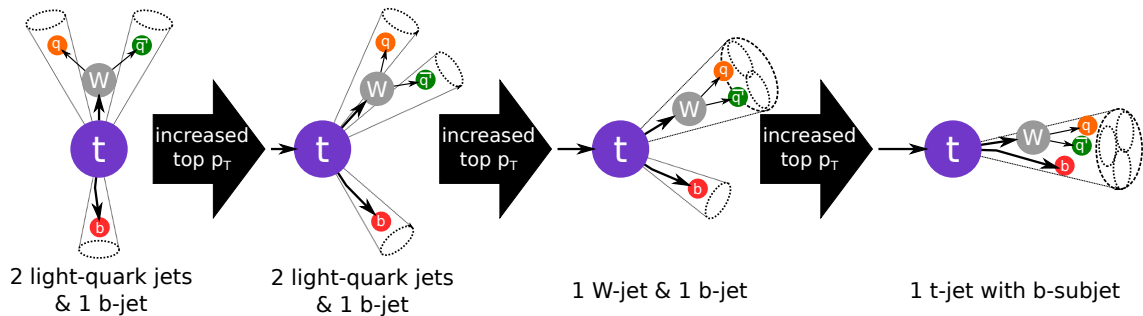
Figure 4.5: Schematic illustration boosted heavy particle regime. With increasing transverse momentum, the angular separation between the top decay products is reduced. At high top momenta, the decay particles are merged into as single jet with large cone size.

top quark-antiquark pair production events and inclusive multijet events [CMS18f]. For every jet, a CSV weight is assigned to the event in order to correct the efficiency differences between data and simulation. Several systematic uncertainties arise from the statistical precision, JECs, as well as bottom quark, charm quark and light flavor impurities in the corresponding control regions at the derivation of the SFs [CMS18f].

4.5 Boosted heavy particle jet-identification

When analyzing events with very large center-of-mass energies – as done in the analysis presented as part of this thesis – even heavy particles like W/Z bosons, Higgs bosons or top quarks can have a large Lorentz-boost. For hadronically decaying heavy particles with small Lorentz boost, the decay products are reconstructed as individual jets, that can be well separated (e.g. $t \rightarrow bW \rightarrow bq\bar{q}' \rightarrow 3$ jets). With increasing Lorentz-boost, the angular separation of the heavy particle decay products decreases until they cannot be well separated anymore (e.g. $t \rightarrow bW \rightarrow bq\bar{q}' \rightarrow 1$ large jet). Instead, all heavy particle decay products are clustered into a single *fat-jet*, e.g. an AK8-jet. An illustration of this concept is given in Figure 4.5 for the example of a hadronic top quark decay. Depending on the mass of the heavy particle, the *boosted regime* is reached at momenta of $p_\mathrm{T}(\text{AK8-jet}) \approx 200\,\text{GeV}$ for W bosons and $p_\mathrm{T}(\text{AK8-jet}) \approx 400\,\text{GeV}$ for top quarks.

The behavior of boosted heavy particles can also be exploited in order to identify jets originating from boosted heavy particles and in order to distinguish them from QCD-multijet background. To do so, the large mass of the boosted particles is exploited since it leaves a characteristic footprint in the substructure of the fat-jet. By using dedicated algorithms to analyze the substructure of a fat-jet, the boosted decaying particle creating the jet can be identified and the jet can be *t/W/Z/H-tagged*.

4.5.1 Substructure algorithms

The most prominent jet characteristic of a boosted heavy particle clustered into single fat-jet is its large jet mass. But due to their large area, jets with a large cone-size $R = 0.8$ are more likely to contain additional soft particles originating from the Underlying Event, pileup, initial state or final state radiation than the standard $R = 0.4$ jets. In order to remove such soft particles and to improve the jet mass resolution, so-called jet grooming algorithms are used. Some jet grooming algorithms are also able to return *subjets*, smaller

size structures that can be clustered within the fat-jet and can be associated with the single decay products. To do so, the fat-jet can either be reclustered or the clustering process can be subsequently reversed. By introducing certain requirements that need to be fulfilled during the clustering, soft jet constituents not originating from the decay of the heavy particle of interest can be removed. The final jet is then reconstructed from the remaining subjets.

Within the CMS experiment, two jet grooming algorithms are common: the *pruning* algorithm and the *soft-drop* algorithm [EVW10; Lar+14]. Both algorithms are used in this thesis and therefore are briefly introduced.

Jet pruning   Pruning is a grooming technique that performs a re-clustering of a fat-jet while suppressing soft and wide-angle radiation [EVW09]. For this, several predefined requirements need to be fulfilled. For any clustering step fulfilling either

$$\frac{\min(p_{\mathrm{T},i}, p_{\mathrm{T},j})}{p_{\mathrm{T},p}} < z_{\mathrm{cut}} \tag{4.3}$$

or

$$\Delta R_{i,j} > D_{\mathrm{cut}}, \tag{4.4}$$

the softer of the two objects is removed instead of being merged into the proto-jet. Here, $p_{\mathrm{T},i}$ corresponds to the transverse momentum of a recombination object i relative to the proto-jet p. The transverse momentum of the original jet is given by p_{T}, while z_{cut} defines a predefined threshold. $\Delta R_{i,j}$ corresponds to the angular separation between the two recombination objects with D_{cut} as the selection threshold.

The re-clustering is typically performed using the CA jet clustering algorithm. In general, the selection of a suitable $\Delta R_{i,j}$ value depends on the mass and the momentum of the jet. Therefore, the $\Delta R_{i,j}$ selection is typically scaled proportional to the jet mass and anti-proportional to the transverse momentum of the jet. In this analysis, the jet pruning was used to identify W-jets using a selection of $\Delta R_{i,j} = 0.5 \cdot m_{\mathrm{jet}}/p_{\mathrm{T,jet}}$ and $z_{\mathrm{cut}} = 0.1$ in accordance with the CMS W-tagging recommendation [CMS18q]. ater on, the jet mass after pruning m_{Pruning} is used as a variable to select jets created by boosted heavy particles [EVW09]. An illustration of the removal of soft wide-angle radiation with the pruning algorithm is given in Figure 4.6.

Soft-drop declustering   The soft-drop algorithm, on the other hand, reverses the clustering process of a fat-jet in order to remove wide-angle soft radiation. In every de-clustering step, the current mother jet j is split into two daughter subjets j_i and j_j. If they pass the soft-drop condition

$$\frac{\min(p_{\mathrm{T},i}, p_{\mathrm{T},j})}{p_{\mathrm{T},i} + p_{\mathrm{T},j}} > z_{\mathrm{cut}} \cdot \left(\frac{\Delta R_{ij}}{R_{\mathrm{jet}}}\right)^{\beta}, \tag{4.5}$$

the daughter subjet with the larger transverse momentum is redefined as the new mother jet j and the declustering is re-iterated. The other daughter jet is discarded. On the other hand, if the mother jet j cannot be further declustered since none of its daughter pairs passes the soft-drop condition, j is considered as the final soft-drop-jet. In the soft-drop condition, $p_{\mathrm{T},i}$ corresponds to the transverse momentum of subjet i, ΔR_{ij} corresponds to the angular separation between the two subjets and R_{jet} corresponds to the jet radius used in the clustering process. While z_{cut} works as a threshold on the declustering, β
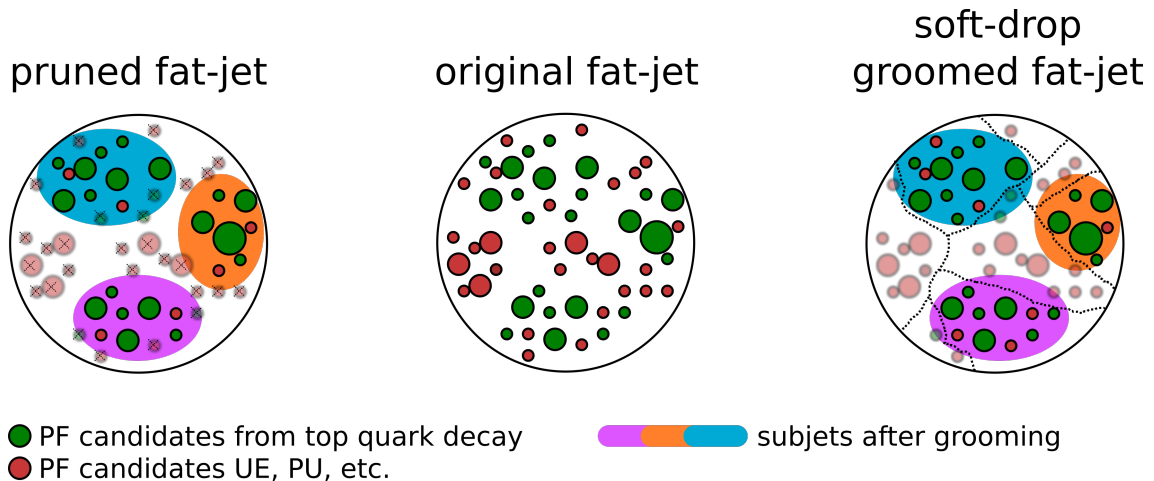
Figure 4.6: Schematic illustration of jet grooming algorithms. View in η-ϕ plane of a fat-jet created by a boosted top quark decay before and after removal of soft wide-angle radiation from the fat-jets. Either the pruning or the soft drop algorithm is applied as jet grooming technique. Particles originating from pileup, the Underlying Event (red), or initial and final state radiation are removed by the grooming. The subjets created by the grooming technique are illustrated in pink, cyan and orange.

defines the influence of the angular separation between the subjets. An illustration of the soft wide-angle radiation removal using the soft-drop declustering algorithm is given in Figure 4.6.

In this analysis, the soft-drop declustering algorithm is used to identify jets originating from the hadronic decays of boosted top quarks. The parameters defining the soft-drop condition are chosen as $\beta = 0$ and $z_{\mathrm{cut}} = 0.1$ in accordance with the CMS recommendation [CMS18c]. In this setup, the soft-drop declustering algorithm behaves very similar to the modified mass-drop tagger (mMDT) [But+08]. The jet mass after soft-drop declustering m_{SoftDrop} is used as a variable to select jets created by boosted heavy particles later on [Lar+14]. An illustration of the removal of soft wide-angle radiation with the soft-drop declustering algorithm is given in Figure 4.6.

A second characteristic observable for fat-jets created by the hadronic decay of boosted heavy objects is the jet shape. In order to measure the consistency of a jet shape with the shape of a jet with N or fewer subjets, the N-subjettiness variable τ_N is introduced [TT11; TT12a]. It can be interpreted as the deviation of the energy flow from N probed subjets and is defined as:

$$\tau_N = \frac{1}{d_0} \cdot \sum_{i\,\in\,\mathrm{const.}} p_{\mathrm{T},i} \min\{\Delta R_{1,i}, \Delta R_{2,i}, \Delta R_{3,i}, ..., \Delta R_{N,i}\} \tag{4.6}$$

with

$$d_0 = \sum_{i\,\in\,\mathrm{const.}} p_{\mathrm{T},i} R_0, \tag{4.7}$$

where N represents the total number of subjet axes that are considered, $R_{X,i}$ corresponds to the angular separation between a fat-jet constituent i and a subjet axis X. The sum is calculated from all constituents i clustered into a fat-jet. The parameter d_0 acts as a

normalization factor of τ_N and R_0 represents the radius parameter used to cluster the fat-jet.

In a scenario with $\tau_N \approx 0$, all fat-jet constituents are perfectly aligned with the N subjet axes and the fat-jet consists of N or fewer subjets. On the other hand, $\tau_N \gg 0$ corresponds to a scenario in which a majority of jet constituents is not aligned with the subjets and the fat-jet would consist of more than N subjets. The identification of the N subjet axes is a key step of the N-subjettiness algorithm. Theoretically, the ideal way to derive the N subjet axes would be to minimize τ_N over all possible orientations of the N subjet axes [TT12b]. Since this is computationally very intensive, the subjet axes are typically determined using the exclusive k_T algorithm [Cat+93]. In the exclusive k_T algorithm, the k_T algorithm (see Section 4.3) used to cluster the fat-jet constituents is stopped once N subjets are clustered.

In most applications, a defined number of subjets is expected instead of a minimum number of subjets, depending on the particle expected to create the fat-jet. In this case, the usage of the ratio $\tau_N/\tau_{N-1} = \tau_{N,N-1}$ is more suitable. Typical N-subjettiness ratios are τ_{21} for the identification of fat-jets created by the hadronic decays of W/Z bosons or Higgs bosons, or τ_{32} for the identification of fat-jets created in the hadronic decays of top quarks.

Since the N-subjettiness is calculated from all jet constituents, it can be considered independent of the jet clustering algorithm. N-subjettiness therefore provides a suitable secondary variable to be combined with a groomed jet mass measurement in order to improve the identification of jets originating from boosted heavy particles.

4.5.2 W-/Z-/H-jet tagging

Heavy SM bosons such as W bosons, Z bosons and Higgs bosons are expected to decay into two light standard model particles. Therefore, the N-subjettiness ratio τ_{21} is expected to be a potent variable to identify hadronic jets created by the decay of a boosted heavy SM boson. The expected mass of the groomed fat-jet depends on the particle hypothesis. For W bosons, a jet mass close to $m(\mathrm{W}) \approx 80.4\,\mathrm{GeV}$ is expected while for Z bosons and Higgs bosons the expected jet masses are $m(\mathrm{Z}) \approx 91.2\,\mathrm{GeV}$ and $m(\mathrm{H}) \approx 125.1\,\mathrm{GeV}$, respectively. In recent years, many developments on the identification of jets created in hadronic decays of heavy SM bosons were made [PSS10; SS11; CMS13b]. Here, the focus is set on the identification of W-boson jets since they play a major role in the analysis presented in this thesis.

Within the CMS experiment, a combination of the N-subjettiness and the pruned jet mass is used to identify AK8-jets created in the hadronic decays of boosted W bosons. In order to be considered as a W-boson jet, the AK8 fat-jet is required to have a transverse momentum larger than $200\,\mathrm{GeV}$, and has to fulfill a pruned jet mass requirement of $65\,\mathrm{GeV} < m_{\mathrm{Pruning}} < 105\,\mathrm{GeV}$. Two working points for W-boson tagging are provided by the CMS experiment as a compromise between tagging efficiency and misidentification rate. A high W-boson jet purity is provided by a N-subjettiness selection of $\tau_{21} < 0.45$, while a selection of $0.45 < \tau_{21} < 0.75$ provides a lower W-boson jet purity. Both of these selections were used as part of this thesis (see Chapter 5). W-tagging efficiencies of $\epsilon \approx 80\,\%$ and $\epsilon \approx 20\,\%$ were observed for the high and low purity selections [CMS17e]. The misidentification rate of non-W jets falsely identified as W-boson jets was measured to be in the range of approximately $2\,\% - 5\,\%$, depending on the transverse momentum of the jet.

For both W-boson jet tagging purity selections, data-to-simulation correction factors are applied. The data-simulation scale factors are derived from semi-leptonic top quark-

antiquark pair production events with a boosted W-boson topology. The systematic uncertainties on these scale factors are propagated to estimate the systematic uncertainty on the W-boson jet tagging.

Although the pruned jet is used to decide if the fat-jet created by a boosted W boson, the original AK8 fat-jet is used for further event reconstruction. This way, a correct consideration of all JECs and JERs in the kinematic event reconstruction can be ensured.

In general, the jet pruning algorithm provides the possibility to analyze the subjets derived from the fat-jet. Therefore, subjet b-tagging can be exploited to increase the tagging performance. Depending on the boosted particle hypothesis, a double subjet b-tagging or a double subjet b-tagging veto can be useful. For a hadronically decaying boosted Higgs boson, the fat-jet is expected to have two b-tagged subjets, since the Higgs boson dominantly decays into a bottom quark-antiquark pair [But+08]. The Z boson tends to decay into down-type quarks. Therefore, a double subjet b-tagging requirement can be used to increase the signal-to-background ratio. W-boson jets, on the other hand, are expected to have no b-tagged subjets, since the decay into bottom quarks is suppressed by the CKM matrix. Although this thesis focuses on the identification of hadronically decaying boosted W bosons, no subjet b-tagging veto was applied in order to retain the sensitivity to boosted Z bosons and Higgs bosons, which are created in a different final state of the analysis presented as part of this thesis.

4.5.3 t-jet tagging

For top quarks, the decay into a bottom quark and a W boson is dominant ($> 99\%$). In case of a hadronic top quark decay, the W boson further decays into a pair of light quarks (t→bW→bq$\bar{\text{q}}$'). All three final state quarks are expected to create individual subjets within a single fat-jet.

Within the CMS experiment, several top-tagging algorithms are available [PS12; CMS09; Kas+15]. For this thesis, the CMS Top Tagger algorithm has been used, which combines selections on the mass of the soft-drop groomed jet as well as on the N-subjettiness ratio τ_{32} [CMS14a]. For this tagger, the constituents of an AK8 fat-jet are reclustered using the Cambridge-Aachen clustering algorithm in order to apply the modified mass-drop tagger (mMDT), implemented as the soft-drop declustering algorithm described in Section 4.5.1. A *loose working point* corresponding to an average tagging efficiency of $\epsilon \approx 30\% - 70\%$, depending on the transverse momentum of the jet, and a misidentification rate of approximately 6% has been selected [CMS16d]. A transverse momentum larger than $400\,\text{GeV}$ is required for the AK8 fat-jet, together with a soft-drop jet mass of $105\,\text{GeV} < m_{\text{SoftDrop}} < 220\,\text{GeV}$ after grooming. The N-subjettiness ratio is required to be $\tau_{32} < 0.81$.

Similar to the W-boson jet tagging, correction factors are applied to compensate for deviations between data and simulations. These data-simulation scale factors are derived from top quark-antiquark pair production events with boosted top quark topologies. The uncertainties on the scale factors are assigned to the systematic uncertainties on the tagging of boosted top quark jets.

Again, the reclustered and groomed fat-jet is only used to identify a jet created by the hadronic decay of a top quark. For the further event reconstruction, the original AK8 fat-jet is used.

Since top quarks dominantly decay via bottom quarks, subjet b-tagging can be used to increase the signal purity and suppress QCD-multijet background. Therefore, the

CSV b-tagging algorithm is applied to every subjet derived in the soft-drop declustering algorithm. Scale factors are applied to compensate differences between data and simulation. As shown in [Rie17], the CSV output of the subjets is well compatible with the CSV of a matched AK4-jet. Therefore, the same data-simulation scale factors as described in Section 4.4 are used.

4.6 Event simulation

For most analyses, a precise simulation of collision events is a crucial aspect, since the simulated events are used e.g. to tune the event selection, estimate the background of SM processes, and estimate the expected shape of potential signal processes. Furthermore, simulated events, where the true quantities are known, are used to develop new object reconstruction methods, estimate the detector performance and to design new detector components. Since the generation of simulated events is not at the focus of this thesis, only a brief introduction into event simulations is given here. For a more excessive description, the reader is referred to [Wil16].

In general, the equations of motion that are derived from the Lagrangian cannot be solved analytically. However, in most applications an exact calculation is not necessary. Instead, a solution is derived using perturbation theory, which is possible at large enough momentum transfer, such that the couplings are small. In many applications, taking into account the first few orders is sufficient. However, with increasing precision, the number of possible *Feynman diagrams* that need to be considered rapidly increases, making higher-order calculations complex and computationally intensive. In addition, loop contributions of virtual particles, whose momenta are not constraint, result in divergent integrals. This problem can be solved using the *renormalization* technique that sets a cut-off on contributing loop momenta and absorbs all remaining divergences into the non-physical parameters of theory, such as coupling constants. As a result, the coupling constants depend on the energy scale of the considered process, but all observables remain finite.

In HEP, collision events are typically generated using Monte Carlo (MC) methods to sample from multi-dimensional probability distributions of certain physical processes. Based on these draws, a certain physics process is simulated. In general, the correct simulation of all physics processes and the correct consideration of all correlations of physics parameters is a technically difficult and computationally intensive task. The event simulation is therefore typically performed in several consecutive independent steps. These are illustrated in Figure 4.7.

As a first step, the differential cross section of the hard scattering process is calculated using a matrix element (ME) generator to compute all relevant matrix elements corresponding to the Feynman diagrams [Alw+11]. At a hadron collider like the LHC, the momentum distribution of the incoming partons is taken into account using PDFs. In this first step, also the emission of initial-state radiation can be considered.

As a second step, the parton showering describes the production of additional particles created in initial and final state radiation processes empirically. While hard large-angle radiation can be calculated by the ME generator, dedicated parton showering algorithms are required to consider soft small-angle radiation. To avoid any double counting in the intermediate range where the parton showering could be calculated by the ME generator and the parton showering algorithm, a matching algorithm is typically applied to remove overlapping emissions [Man+07]. By merging all color-charged final-state partons into color-neutral hadrons, the particle hadronization is simulated [And+83]. In this third step,
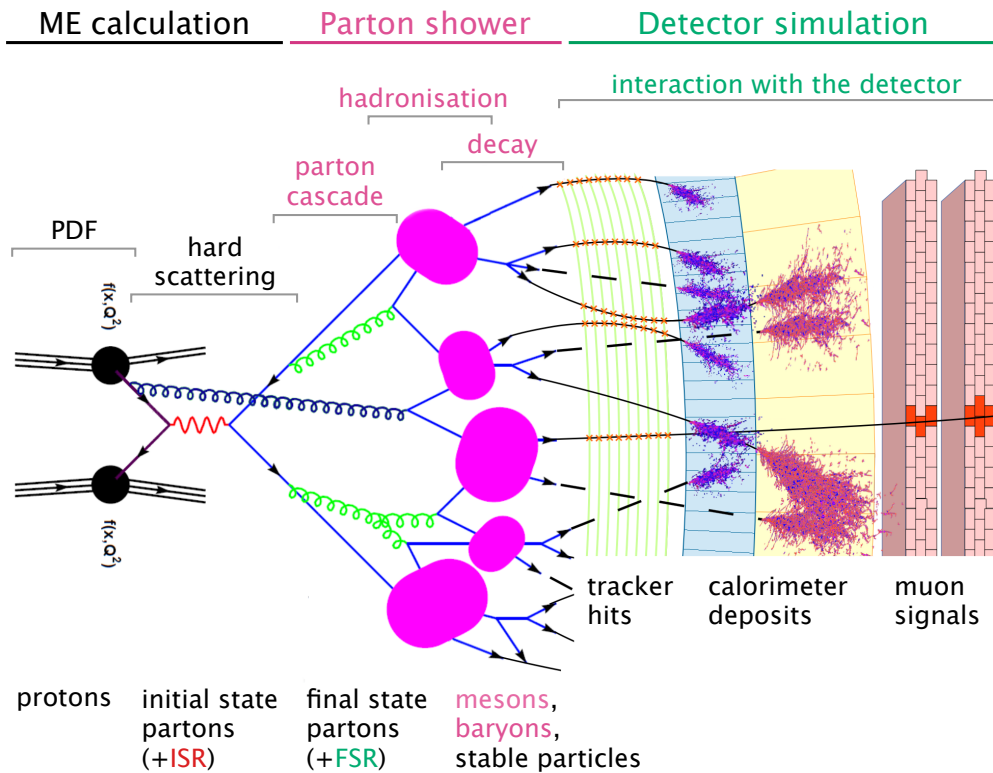
Figure 4.7: Illustration of event simulation procedure. Subsequent steps of event simulation at a hadron collider experiment (from left to right). The initial colliding protons are depicted by the parallel black lines, corresponding to the three valence quarks of the proton. The momentum distribution of the partons in the initial state are described by the PDFs. The hard scattering process, described by the Feynman diagram, is pictured in red and blue. Initial and final state radiation is depicted in dark blue and light green, while the parton showering hadronization is visualized in bright blue and magenta. Furthermore, the decay of unstable particles is illustrated. Finally, the interaction of the decay particles with the detector components is illustrated on the very right (from [Bar15], modified from [Goe14]).

the CMS experiment considers the contribution of particles originating from the UE as well as from PU by adding particles from low-energy proton-proton interactions to the event. Furthermore, the decay of unstable hadrons is simulated according the known life times, decay channels and branching ratios.

In the fourth and final step, the detector, its interaction with the stable decay particles and its electric response is simulated. The detector simulation requires detailed knowledge of the material distributions within the detector. For the CMS experiment the detector simulation is performed using the GEANT4 framework [Ago+03].

5

Heavy bosonic resonances decaying via a vector-like quark

In our universe, a series of observations provide evidence for the existence of physics beyond the SM. Many of the models developed to explain these effects predict the existence of additional heavy bosonic particles and vector-like quarks (VLQs) that could be detected at the LHC.

In this chapter, a search for such heavy bosonic resonances (HBRs) using data taken with the CMS detector is described. After a short motivation and overview of the current scientific status, the expected signature of an HBRs decay via VLQs are described. Then, the selection criteria as well as the event reconstruction are specified. Special focus is set on the background estimation performed and the systematic uncertainties arising from the background prediction. Finally, the data is analyzed and the results of this analysis are interpreted.

5.1 Motivation and general analysis approach

Both the ATLAS and CMS experiments conduct a broad programme to search for heavy resonances or for VLQs produced [ATL18; CMS18b]. While the majority of searches is focused on the decay of these heavy resonances or VLQs into SM particles, only a few are dedicated to the search for a heavy resonance decaying into pairs of VLQs, which subsequently decay into SM particles. So far, only few analyses focus on the kinematic range where an HBR dominantly decays into a single VLQ and a single SM particle [CMS17k]. Depending on the mass of the heavy resonance and the VLQ as well as the coupling parameters, this decay could be dominant. Furthermore, a dominant decay into an SM top quark and a top-like VLQ is predicted. As described in Chapter 2, such decays are typical for theoretical models based on extra dimension or a composite-Higgs boson. The HBR is further on referred to as Z′ boson and the top-like VLQ is referred to as a T quark. In many models including VLQs, the T quark dominantly decays into third-generation SM quarks and an SM boson. This leaves three possible decay modes: T → Wb, T → Zt and T → Ht. A tree-level Feynman diagram of the process of an HBR decay via a VLQ, as considered in this analysis, is shown in Figure 5.1.

Two model independent analyses are currently performed within the CMS collaboration to probe the parameter range were a neutral spin-1 HBR decays into a top quark and a top-like VLQ with charge $q = 2/3e$. One of the analyses focuses on a semi-leptonic final state, while the analysis presented as part of this thesis is dedicated to the fully-hadronic
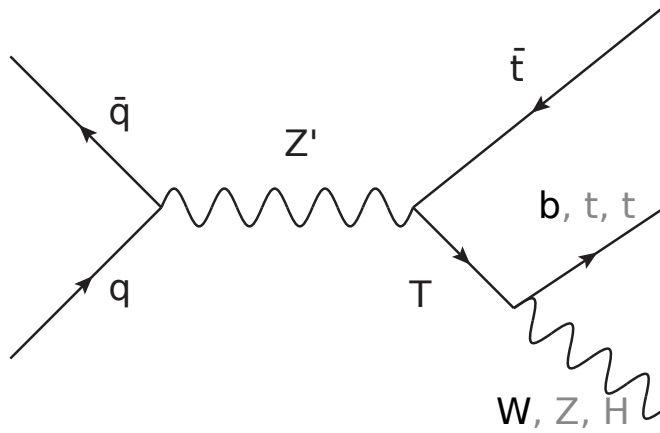
Figure 5.1: Feynman diagram of heavy bosonic resonance. The production and decay of a heavy bosonic resonance (Z′) considered in this analysis at tree-level [Usa17].

final [Ben18]. While the semi-leptonic analysis within CMS is dedicated to the T → Zt and T → Ht decay channel, this analysis is optimized for the T → Wb decay channel. Nevertheless, both analyses are sensitive to the other decay channels and are designed to be complementary to each other. Furthermore, both analyses are assigned to different final states, facilitating an easy combined analysis later on. Since this analysis focuses on the all-hadronic final state, which is not sensitive to the charge of T quark or its SM decay products, the following considerations are equally applicable to $\overline{\mathrm{T}}$ quarks and their decay products.

In many parts, the analysis presented in this thesis follows the strategy of a former analysis performed on the LHC run II dataset from 2015 [Usa17; CMS17k]. Although the general approach is similar, several modifications and improvements in the background estimation were performed to improve the robustness of the background estimation and to reduce the impact of systematic uncertainties.

5.2 Simulated events and data sets

This analysis is designed as a model independent search. However, in order to develop and perform the analysis and to estimate the background, several MC-simulated samples of signal and background processes were used. Two sets of Z′ → Tt signal samples were generated based on the little-Higgs model and the warped extra-dimensions models that are already described in Chapter 2. They are used as potent benchmark models in order to develop the analysis strategy and to interpret the results. In the following, the data and MC simulation samples used for this analysis are described.

All data sets and simulated samples were processed using version 8.0 of the Compact Muon Solenoid Software (CMSSW) framework. The run II data set from 2016 with a total integrated luminosity of $L = 35.9\,\mathrm{fb}^{-1}$ at a center-of-mass energy of $\sqrt{s} = 13\,\mathrm{TeV}$ has been analyzed. For all signal and background MC simulations, the center-of-mass energy was set to $\sqrt{s} = 13\,\mathrm{TeV}$, the simulated events were tuned to fit the data and normalized to the total integrated luminosity.

SM top-quark event simulation   Several SM processes that contain top quarks are considered. The SM top quark-antiquark pair production ($t\bar{t}$) background is simulated using version 2 of the POWHEG Box framework at next-to-leading order precision [Ali+10]. The simulated events are normalized to the next-to-next-to leading order (NNLO) production cross-section calculation of $\sigma_{t\bar{t}} = 831.76\,\text{pb}$ [CFM13; CM14; CMS18k]. Single top quark/anti-top quark production via the tW-channel is generated using the POWHEG Box framework and is normalized to a NNLO cross-section of $71.7\,\text{pb}$ [Kid10; CMS18n]. Single top quark/anti-top quark production processes via the s-channel and the t-channel are simulated using the MadGraph5_aMCatNLO framework and are normalized to an approximate NNLO total production cross-section of $\sigma_s = 11.36\,\text{pb}$ and $\sigma_t = 216.99\,\text{pb}$ [Alw+14; Ali+11; Kan+15; CMS18n]. All samples use Pythia 8.2 to simulate the parton showering process [Sjö+15]. The `CUETP8M1` parton showering tune was used for the single top-quark production in the s-channel [SCR14]. For all other top quark backgrounds, the `CUETP8M2T4` parton showering tune was used [CMS14d; SCR14].

QCD-multijet simulation   Two MC simulation samples were available to investigate QCD-multijet events. The events of the first set are generated using the Pythia 8.2 framework for both hard interaction and parton showering. In the second set, the hard interaction process is simulated using the MadGraph5_aMCatNLO framework while the parton showering has been simulated using Pythia 8.2 and the `CUETP8M1` parton showering tune. The MadGraph5_aMCatNLO based sample was mainly used to develop a data-driven background estimation method for this analysis and to derive systematic uncertainties, while the Pythia 8.2 based set was used for cross-checks only.

Although the MadGraph5_aMCatNLO based QCD-multijet sample provided a basic background prediction, a data-driven background estimation is still necessary to provide a reliable QCD-multijet background prediction at high energies and high jet-multiplicities (see Section 5.5).

Signal samples based on the little-Higgs model   Based on the little-Higgs model mentioned in Section 2, a set of simulated signal samples was produced for different signal hypotheses. The MadGraph5_aMCatNLO framework was used to generate the hard interaction process. Together with the MadSpin framework, the helicity were correctly propagated through the decay products [Art+13]. Pythia 8.2 were used for the simulation of the parton showering process.

For all signal hypotheses, a narrow resonance width of $1\,\%$ had been assumed for the neutral spin-1 resonance (Z′) decaying into a top quark and a top-like heavy VLQ. The width of the T quark had been fixed to $1\,\text{MeV}$. Both widths are selected to be below the detector resolution, and are selected consistent with the signal samples that were produced for $Z' \to t\bar{t}$ analyses [Usa17]. For all signal hypotheses, dedicated samples for all possible T-quark decays ($T \to Wb$, $T \to Zt$ and $T \to Ht$) had been generated, allowing an investigation of the analysis sensitivity dependent on the decay branching ratio $BR(T \to Wb/Zt/Ht)$.

A wide kinematic range with several different signal hypotheses and Z′ boson masses from $1.5\,\text{TeV}$ to $2.5\,\text{TeV}$ and T-quark masses from $0.7\,\text{TeV}$ to $1.5\,\text{TeV}$ is investigated. The kinematic range of these samples is illustrated in Figure 5.2. By allowing only mass combinations that fulfill $0.5 \cdot m(Z') \le m(T) \le m(Z') - m(t)$, the most interesting kinematic range for a Z′ boson decaying into an SM particle and a heavy VLQ had been selected (see Figure 2.8). For more details on the event generation, the reader is referred to [Usa17], where the signal samples have already been used.
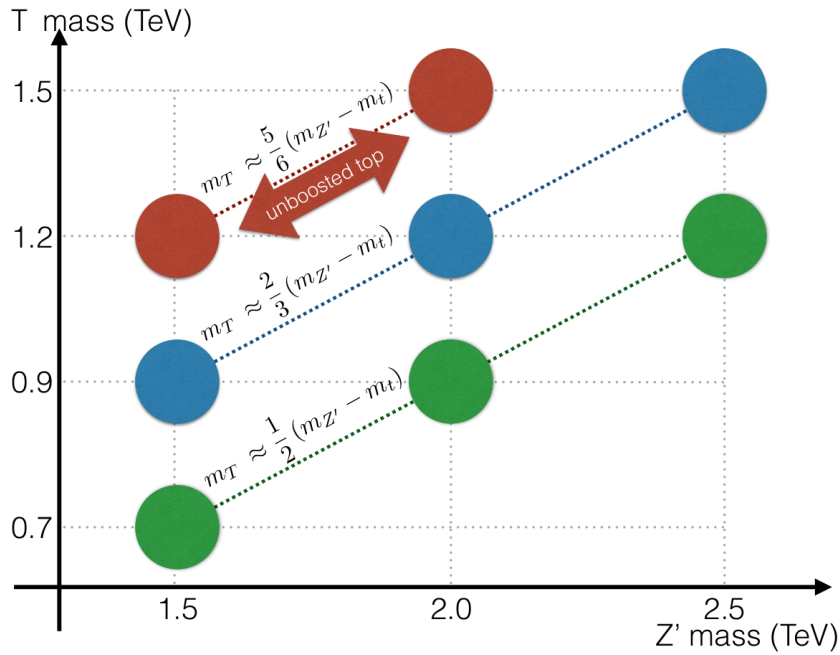
Figure 5.2: Schematic of particle masses for little-Higgs model. Overview of little-Higgs model signal samples available for this analysis. For each $m(Z')$ and $m(T)$ combination, individual signal samples for every T quark (also often referred to as T') decay channel $T \rightarrow Wb/Zt/Ht$ were available [Usa17].

Signal samples based on warped extra-dimensions model In addition, a second set of signal samples was produced to further extend the kinematic range that can be investigated and to allow a more detailed investigation of the parameter range. This second set of signal samples is based on the extra-dimension model described in Section 2. Similar to the signal samples based on the little-Higgs model, a combination of MadGraph5_aMCatNLO, MadSpin and Pythia 8.2 has been used to simulate hard scattering processes and the parton showering in combination with the `CUETP8M2T4` parton showering tune. A schematic overview of the signal samples based on the warped extra-dimensions model is given in Figure 5.3.

Again, a narrow width of $1\,\%$ was chosen for both the Z' boson and the T quark. In order to also study possible wide resonances, every signal sample was also produced with an increased resonance width of $30\,\%$. A dedicated generator level study showed that a wide resonance is indistinguishable from a T quark with a large width [Ben18]. Hence, it was sufficient to generate samples with a wide Z'-resonance in order to also cover the scenario of a T quark with a large decay width. The T quarks were produced left-handed as well as right-handed. Similar to the little-Higgs model, the T-quark mass was selected to be $0.5 \cdot m(Z') \leq m(T) \leq m(Z') - m(t)$, while the Z' mass-range was extended to up to $4\,\text{TeV}$. Additional narrow width mass points were added to scan the Z' mass-range of $1.5\,\text{TeV}$ to $3\,\text{TeV}$ in more detail. The masses of the T quark cover a range of $0.8\,\text{TeV}$ to $3\,\text{TeV}$. Signal samples were produced for every T-quark decay channel to allow a model independent analysis.
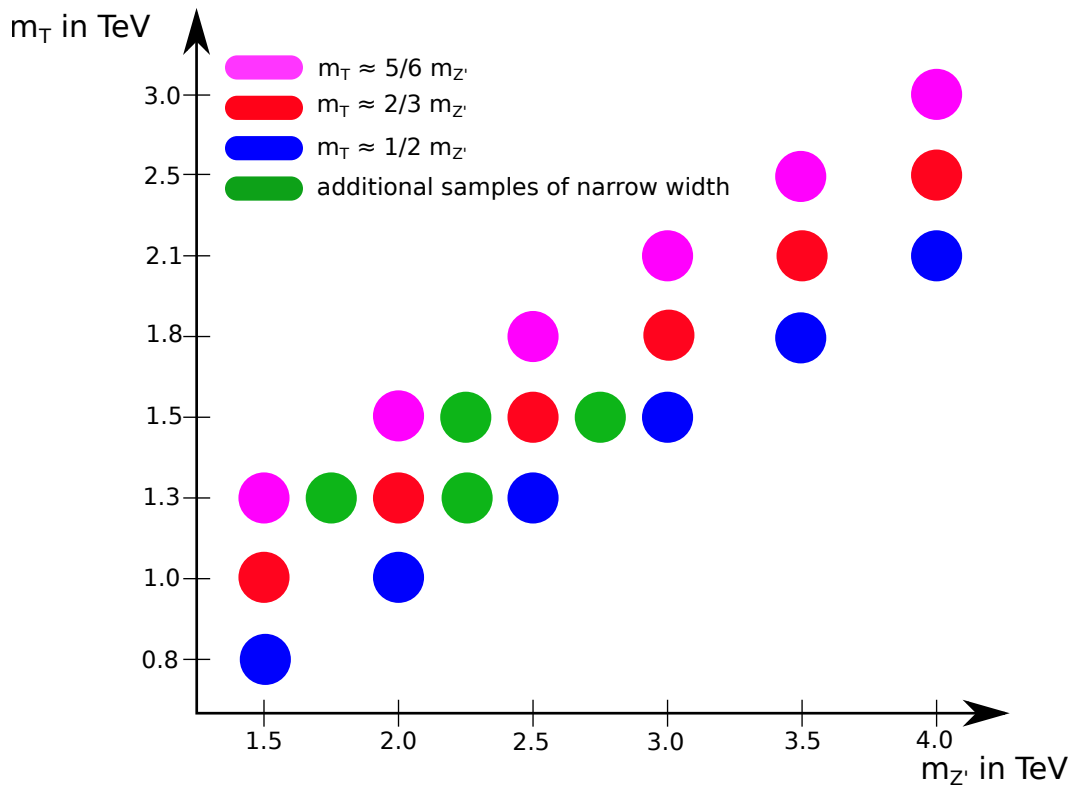
Figure 5.3: Particle masses considered for warped extra-dimension model. Overview of masses considered in warped extra-dimension model signal samples available for this analysis. For every $m(Z')$ and $m(T)$ combination, individual signal samples were produced for every T-quark decay channel $T \rightarrow Wb/Zt/Ht$. Intermediate mass point samples (green) were only available for narrow resonance widths. The axes in this illustration are not scaled linearly.

5.3 Event selection

This section is dedicated to the signature of an HBR decaying via a VLQ and a top quark. Furthermore, possibilities to exploit these signatures experimentally to identify the signal while suppressing background processes are discussed.

The main characteristic of an HBR is its large mass relative to the masses of SM particles and the large energy released during its decay into SM particles. This results in a large momentum and a strong boost of the SM decay particles. However, in this analysis, the Z' boson dominantly decays into a top quark and a heavy T quark. Due to its large mass, the T quark cannot be considered as boosted, and its SM decay products show a relatively angular separation. Since the T-quark mass is still large compared to masses of SM particles, the decay products of the T-quark decay can be considered boosted.

The boost of the top quark originating from the $Z' \rightarrow Tt$ decay strongly depends on the mass difference between the Z' boson and the T quark. Still, it is boosted, considering that $m(Z') - m(T) \gg m(t)$ is fulfilled for most of the probed parameters space. These considerations were verified in a series of generator-level investigations performed using the little-Higgs model signal as benchmarks. Since this analysis focuses on the T-quark decay into a W boson and a bottom quark, the investigations were limited to top quarks, W bosons and bottom quarks. A selection of results from these generator-level studies are
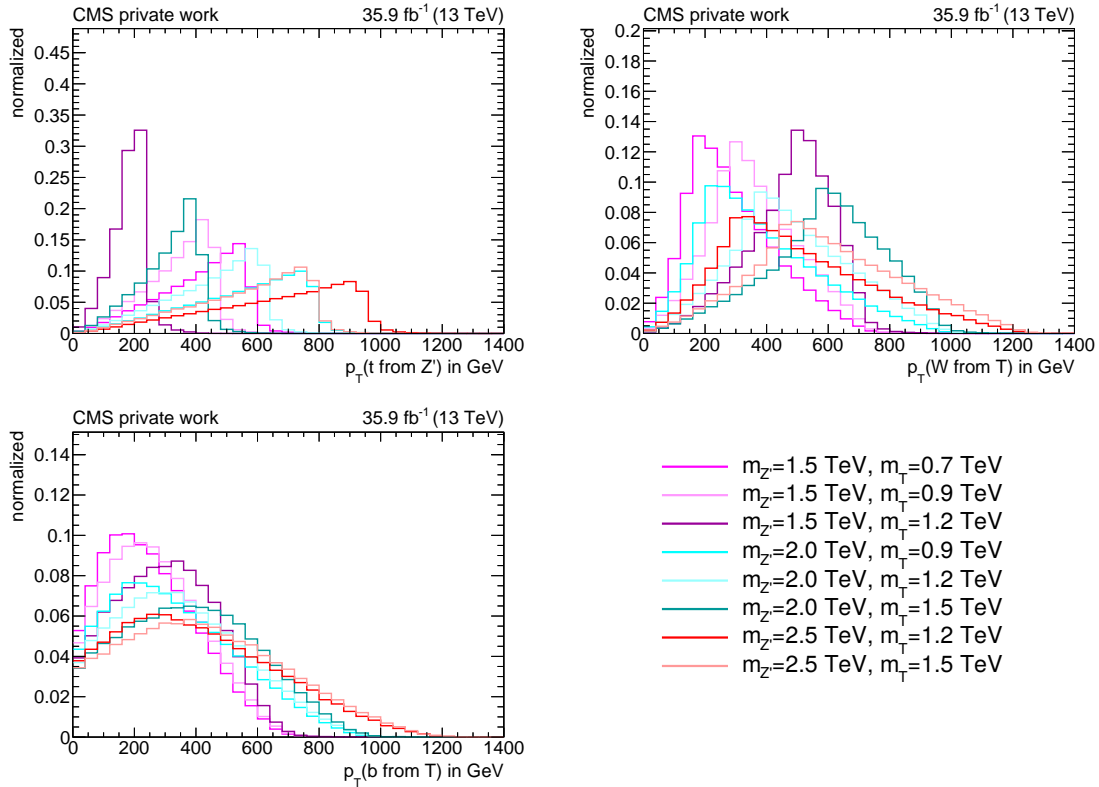
Figure 5.4: Transverse momentum distributions at generator level. Generator level transverse momenta for different SM decay particles of little-Higgs model signal hypotheses. The $Z' \to tT \to tWb$ decay channel was assumed.

shown in Figure 5.4 and Figure 5.5: For the majority of signal hypotheses, the top quarks, W bosons and bottom quarks feature a angular separation of $\Delta R > 1.5$. Furthermore, the bottom quarks created in the T-quark decay have a large transverse momentum of $p_T(b) > 100\,\text{GeV}$. For most signal hypotheses, the W bosons is boosted as well with a transverse momentum $p_T(W) > 200\,\text{GeV}$. As expected, the transverse momenta of the top quarks strongly depend on the mass difference between the Z' boson and the T quark. Nevertheless, for the majority of the signal hypotheses, a significant fraction of the top-quarks have a transverse momentum of $p_T(t) > 400\,\text{GeV}$.

The large transverse momenta of the decay products open up the possibility to use jet-substructure algorithms in order to identify the jets created by the SM decay products. In this way, the QCD-multijet background processes can be reduced. In order to identify the SM decay products and to fully reconstruct the Z' system, this analysis focuses on tri-jet events containing a top-tagged fat-jet, a W-tagged fat-jet and an additional resolved b-tagged jet.

5.3.1 Signal event selection and reconstruction

Since the kinematic spectrum of the potential signal processes is very large, and since the T quark has several potential decay channels, the event selection is chosen as loose as possible to target the general event signature. Events have to fulfill the following selection criteria in order to be considered as a signal candidate:
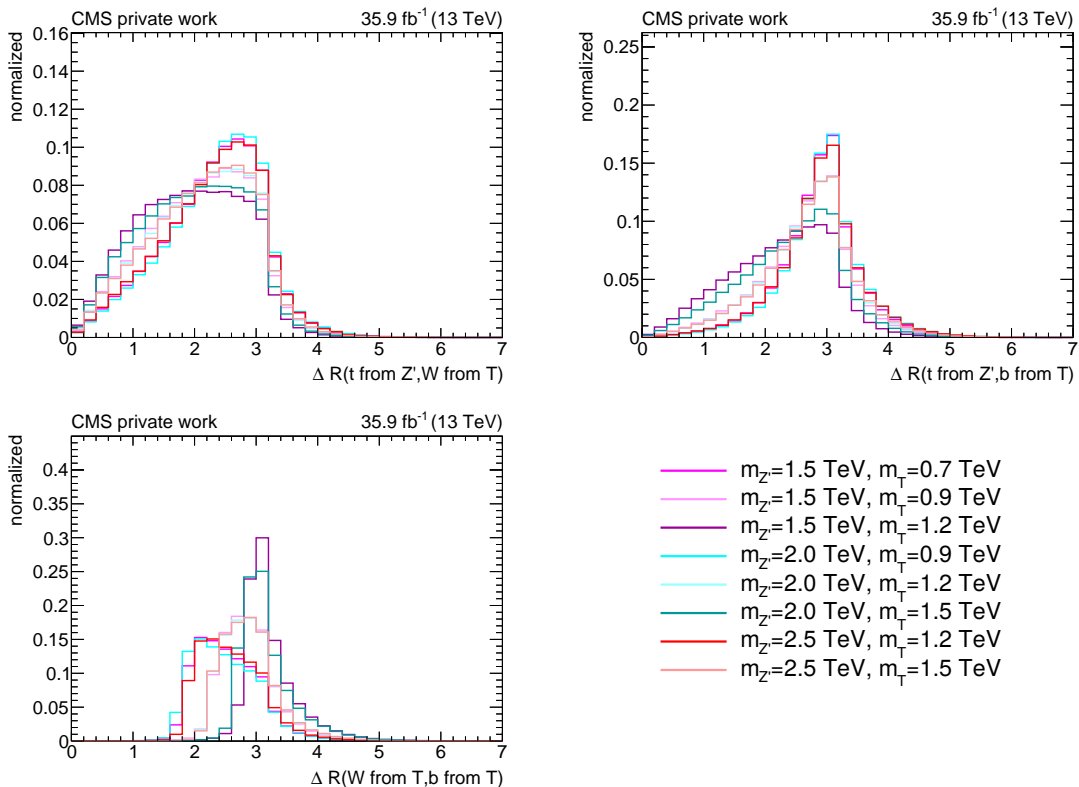
Figure 5.5: Angular separation at generator level. Generator level ΔR between SM decay particles of different little-Higgs model signal hypotheses.

- at least three resolved AK4-jets with $p_\mathrm{T} > 75\,\mathrm{GeV}$ and $|\eta| < 2.4$;

- no isolated leptons (ensuring no overlap with the semi-leptonic analysis [Ben18]);

- a large energy deposition in form of hadronic jets, requiring the scalar sum of the transverse momenta of all AK4-jets with a transverse momentum $p_\mathrm{T} > 75\,\mathrm{GeV}$, $\sum p_\mathrm{T} = H_\mathrm{T}$ to be larger than $1000\,\mathrm{GeV}$. The H_T selection also ensures full trigger efficiency as described in Section 5.3.2.

- at least one t-tagged AK8 fat-jet ($\tau_{32} < 0.81$, $105\,\mathrm{GeV} < m_{\mathrm{SoftDrop}}(\mathrm{AK8}) < 205\,\mathrm{GeV}$) with $p_\mathrm{T}(\text{t-jet}) > 400\,\mathrm{GeV}$ and $|\eta| < 2.4$;

- at least one W-tagged AK8 fat-jet ($\tau_{21} < 0.45$, $65\,\mathrm{GeV} < m_{\mathrm{Pruning}}(\mathrm{AK8}) < 105\,\mathrm{GeV}$) with $p_\mathrm{T}(\text{W-jet}) > 200\,\mathrm{GeV}$ and $|\eta| < 2.4$ that shows good angular separation from the top-tagged jet of $\Delta R(\text{t-jet,W-jet}) > 1.6$;

- at least one additional b-tagged AK4-jet ($\mathrm{CSV\_v2}(\text{b-jet}) > 0.8484$) with a transverse momentum $p_\mathrm{T}(\text{b-jet}) > 100\,\mathrm{GeV}$, $|\eta| < 2.4$, and good angular separation from the top-tagged jet $\Delta R(\text{t-jet, b-jet}) > 1.2$, as well as from the W-tagged jet, $\Delta R(\text{W-jet, b-jet}) > 1.2$.

A complete event reconstruction is pursued. Therefore, the tagged W-jets and tagged b-jets are used to reconstruct a T-quark candidate by adding the respective four-vectors, and the Z' candidate is reconstructed using the t-tagged fat-jet. Since this analysis searches for
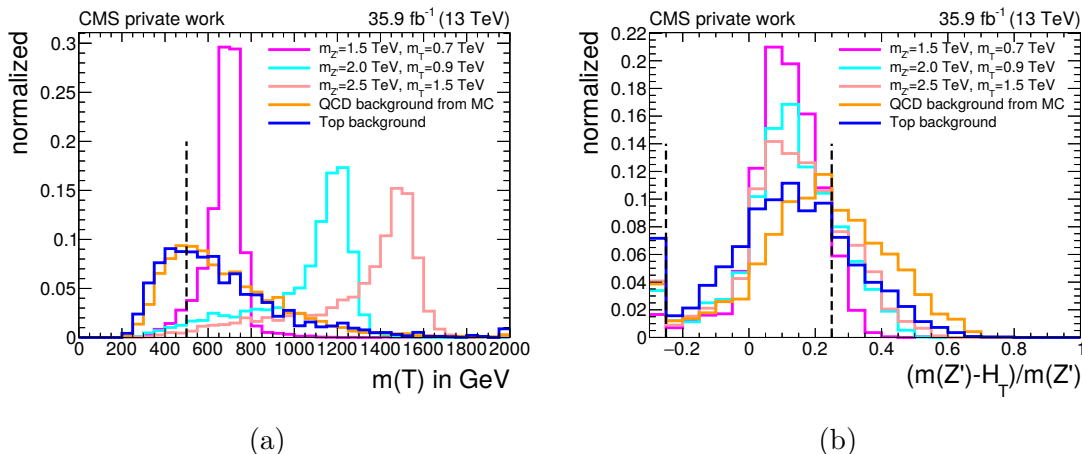
Figure 5.6: Selection of reconstructed objects. Signal and background distribution of reconstructed T-quark mass (a) and Z' (b) for the background processes as well as a three example signals.

a heavy bosonic resonance, the reconstructed Z' mass is used as the final observable. In order to distinguish the reconstructed particle mass from the generator level particle mass used in the simulation, the reconstructed particle masses are referred to as $m(Z')$ or $m(T)$. The generator level particle masses are referred to as $m_{Z'}$ and m_T.

The production of top quark-antiquark pairs ($t\bar{t}$) may result in an identical signature, i.e. represents an irreducible background: a t-tagged fat-jet, a W-tagged fat-jet and a b-tagged jet. To suppress background from $t\bar{t}$-production as well as from QCD-multijet events, the reconstructed mass of the T-quark candidate is required to be much larger than the top-quark mass ($m(T) > 500\,\text{GeV} \gg m(t)$). Figure 5.6 motivates this selection by illustrating the reconstructed T-quark mass-distribution for the major backgrounds and some exemplary signal hypotheses. The expected QCD-multijet background is suppressed further by selecting only events with a reconstructed Z' mass similar to the H_T ($|m(Z') - H_T| < 0.25 \cdot m(Z')$). This selection is motivated by the fact that QCD-multijet processes do not create real heavy boosted objects but a large number of particles that can fake heavy boosted objects. Therefore, the H_T is expected to significantly differ from the reconstructed mass of the Z' candidate. Figure 5.6 shows the expected distribution of $(m(Z') - H_T)/m(Z')$ for three exemplary signal hypotheses and the two major backgrounds; QCD-multijet background and $t\bar{t}$-production. To further avoid any residual trigger inefficiencies, the reconstructed Z' mass is required to be larger than 1000 GeV as described in Section 5.3.2. The event selection criteria on reconstructed objects can be summarized as:

- reconstructed T-quark mass $m(T) > 500\,\text{GeV}$;

- reconstructed Z' mass $m(Z') > 1000\,\text{GeV}$;

- reconstructed Z' mass similar to H_T ($|m(Z') - H_T| < 0.25 \cdot m(Z')$).

As mentioned in Section 4.5, the top-tagging efficiency can be further increased by requiring one of the subjets to be b-tagged. This possibility has been exploited to create two analysis categories. The first category with increased signal purity requires at least one b-tagged subjet with CSV_v2(subjet) > 0.8484 within the top jet, and is called 2 b-tag category below. Events not fulfilling this requirement enter the 1 b-tag category. A schematic illustration of a signal-like event is given in Figure 5.7.
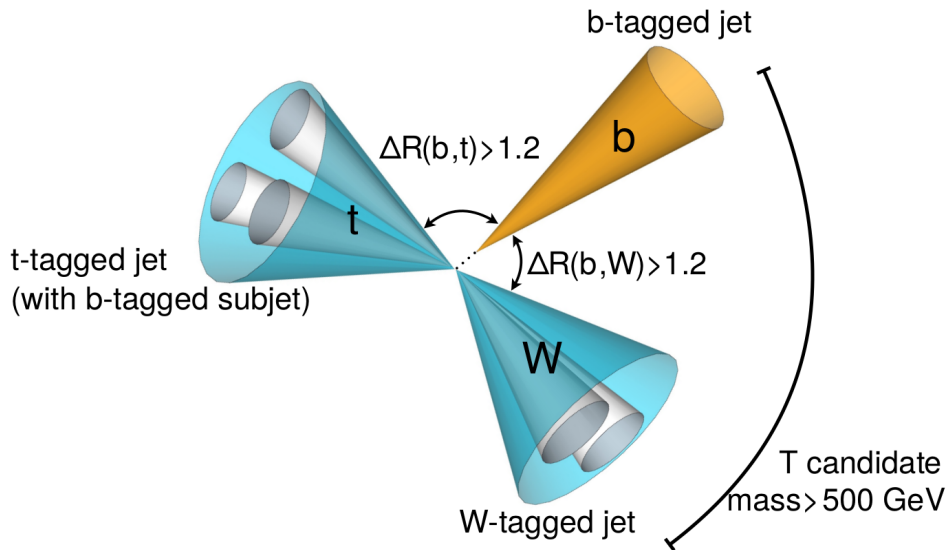
Figure 5.7: Schematic signal event topology. Signal-like tri-jet event with t-tagged, W-tagged and b-tagged jets (modified from [Usa17]).

In general, an event can have several t-jet, W-jet and b-jet candidates, resulting in a multitude of potential T-quark and Z′-boson candidates that can be reconstructed. This analysis is designed to consider all possible reconstruction combinations that fulfill the selection requirements. In case of multiple t, W or b jets, only the combination based on the jets with the largest transverse momenta is selected. This strategy was slightly modified in order to provide a data-driven background estimation as described in Section 5.5. Based on the little-Higgs model signal samples, an average signal selection efficiency of approximately 0.87 % was achieved in the 2 b-tag category, and approximately 0.80 % in the 1 b-tag category. A more detailed listing of the resulting signal efficiencies as a function of the signal hypothesis is given in Appendix A.1.

5.3.2 Trigger efficiency

Since this analysis is searching for heavy resonances in the fully-hadronic final state, large momentum transfers and jets with a large transverse momentum are expected. The ideal trigger choice reflects a compromise between the physics signature investigated and the bandwidth available. For analyses that look for such heavy resonances a combination of three high-level triggers to pre-select events is recommended by the CMS experiment [Maj17]. An event has to fulfill at least one of the three trigger conditions to be considered for this analysis. The first trigger, internally referenced as `HLT_PFHT900`, requires the sum over the transverse momenta of all particle-flow AK4-jets to be larger than 900 GeV. Since this trigger showed some trigger inefficiencies at high center-of-mass energies, the second and third triggers are used to collect events, with a logical OR in the trigger decision, to compensate the inefficiencies. The second trigger (`HLT_PFHT800`) is similar to the first but with a lower threshold, but is pre-scaled to fulfill the bandwidth requirements. The third trigger (`HLT_PFJet450`) requires at least one particle flow AK4-jet with a transverse momentum larger than 450 GeV.

However, the analysis trigger selection is not necessarily 100 % efficient, since events enter several stages of reprocessing after the trigger decision. This typically results in a *trigger turn-on* behavior. By loosening the selection criteria and defining so called pseudo signal regions (PSRs), a comparison of the analysis trigger with a reference trigger was used to investigate the analysis trigger efficiency turn-on and to measure the trigger efficiency on data as well as on MC simulations. Four PSRs were defined to derive the trigger efficiency:

1. Two AK8 fat-jets with $p_\mathrm{T}(\text{AK8-jet}) > 150\,\text{GeV}$ and $|\eta| < 2.4$ as well as one AK4-jet with $p_\mathrm{T}(\text{AK4-jet}) > 75\,\text{GeV}$ and $|\eta| < 2.4$.

   This corresponds to a selection similar to the signal region, but with lower thresholds on the transverse momenta of the jets, no tagging requirements, and no selections on the reconstructed T-quark mass and the reconstructed Z$'$-mass.

2. Same requirements as PSR 1, but in addition one of the AK8-jets is required to fulfill the t-tagging requirements on the jet mass and the N-subjettiness. The other AK8-jets is required to fulfill the W-tagging requirements on the jet mass and the N-subjettiness, while the AK4-jet has to be b-tagged (see Sections 4.4 and 4.5).

3. Same requirements as PSR 1, but tighter selections on the transverse momenta of the jets: One AK8-jet with $p_\mathrm{T}(\text{AK8-jet}) > 400\,\text{GeV}$, one AK8-jet with $p_\mathrm{T}(\text{AK8-jet}) > 200\,\text{GeV}$, and one AK4-jet with $p_\mathrm{T}(\text{AK4-jet}) > 10\,\text{GeV}$.

4. Same requirements as PSR 2, but tighter selections on the transverse momenta of the jets: One t-tagged AK8 fat-jet with $p_\mathrm{T}(\text{AK8-jet}) > 400\,\text{GeV}$, one W-tagged AK8 fat-jets with $p_\mathrm{T}(\text{AK8-jet}) > 200\,\text{GeV}$, and one one b-tagged AK4-jet with $p_\mathrm{T}(\text{AK4-jet}) > 10\,\text{GeV}$.

Two reference triggers were used, the `HLT_PFHT650` trigger that is similar to the first analysis trigger but uses a lower threshold, and the `HLT_Mu50` trigger that requires at least one muon with a transverse momentum $p_\mathrm{T} > 50\,\text{GeV}$. Although both of these reference triggers cannot be considered as fully unbiased with respect to the analysis triggers, they are both biased in a different way. Therefore, the efficiency is measured independently with both of the reference triggers and the two results are used to derive a conservative uncertainty.

The trigger efficiency is measured as a function of H_T by calculating the ratio of events passing the analysis trigger and the reference trigger, and events passing only the reference trigger.

$$\epsilon_{\mathrm{Trigger}}^{\mathrm{PSR}}(H_\mathrm{T}) = \frac{N_{\mathrm{events}} \text{ in PSR passing analysis triggers and reference trigger}}{N_{\mathrm{events}} \text{ events in PSR passing reference trigger}} \quad (5.1)$$

The trigger efficiency in PSR 4 as a function of H_T is shown in Figure 5.8. PSR 4 has been selected as an example since it is the most signal-like PSR and resembles most closely the trigger behavior in the signal region. For all PSRs, the analysis trigger can be considered fully efficient for $H_\mathrm{T} > 1000\,\text{GeV}$.

To further check for any remaining trigger inefficiencies as a function of the reconstructed Z$'$ mass, the trigger efficiencies were re-derived as a function of $m(\text{Z}')$ with the $H_\mathrm{T} > 1000\,\text{GeV}$ selection applied. The trigger efficiency in PSR 4 as a function of $m(\text{Z}')$ is shown in Figure 5.9. Similar as before, the trigger can be considered as fully efficient for $m(\text{Z}') > 1000\,\text{GeV}$.

(a)   (b)
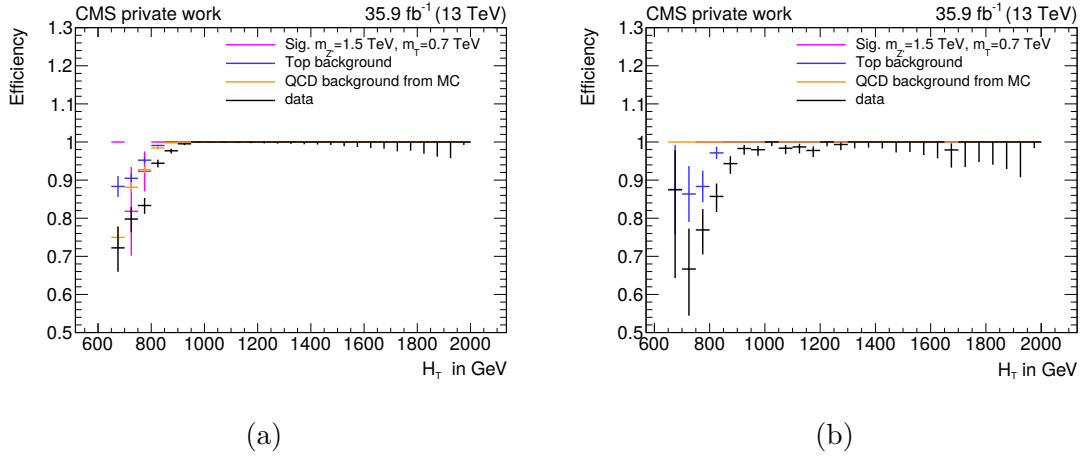
Figure 5.8: Trigger efficiency as a function of H_T. Trigger efficiency of the analysis trigger in pseudo signal region 4 as a function of H_T, using the `HLT_PFHT650` reference trigger (a) and the `HLT_Mu50` reference trigger (b).

(a)   (b)
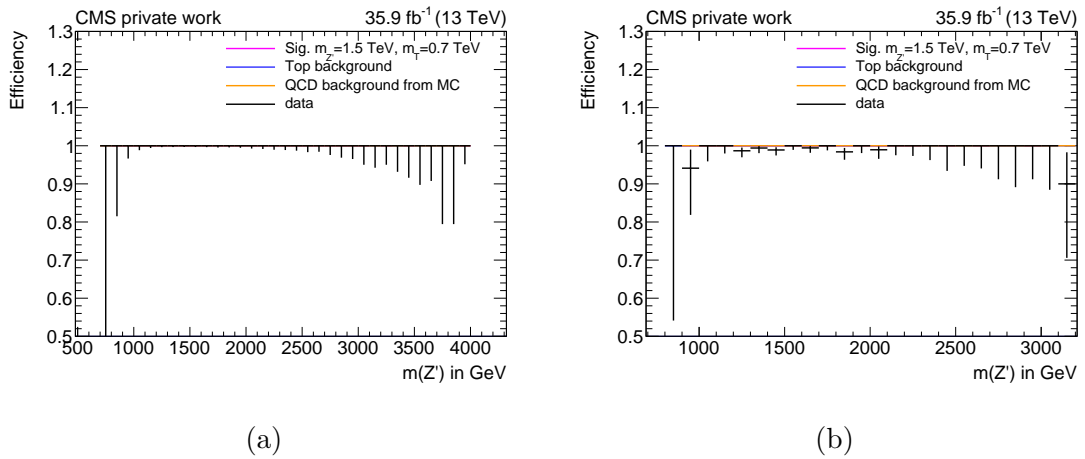
Figure 5.9: Trigger efficiency as a function of Z' mass. Trigger efficiency of the analysis trigger in pseudo signal region 4 as a function of $m(Z')$ for $H_T > 1000\,\text{GeV}$, using the `HLT_PFHT650` reference trigger (a) and the `HLT_Mu50` reference trigger (b).

For both reference triggers, the trigger efficiency distributions of the analysis trigger in all PSRs were fitted with an error-function:

$$f(x) = \frac{a}{2}\left(\operatorname{erf}\left(\frac{x-b}{c}\right) + 1\right),\tag{5.2}$$

in order to derive an uncertainty on the measured trigger efficiency. The systematic uncertainty on the trigger efficiency was conservatively estimated from the largest deviations from a fully efficient trigger ($\max\{1 - a_{\text{PSR 1, HLT\_PFHT650}}, 1 - a_{\text{PSR 2, HLT\_PFHT650}}\}$). Since the trigger efficiency as a function of H_{T} can not be considered uncorrelated from the trigger efficiency as a function of $m(\text{Z}')$, the final trigger uncertainty was calculated as the linear sum of the two largest deviations, $1\,\% + 0.6\,\% = 1.6\,\%$.

5.4 Background sources

Several background processes enter the signal regions of this analysis. They can be divided into two categories: background processes containing top quarks, and QCD-multijet backgrounds containing lighter quarks faking the presence of top-quarks. The backgrounds are shortly described in this section.

Top quark background   The most relevant process, in terms of production cross-section and background contribution, is top quark-antiquark pair production ($t\bar{t}$). Furthermore, single top quarks can be produced in several processes (s-channel, t-channel, tW-channel, see Section 5.2). The MC simulation of top quark production processes at next-to-leading order calculations had been proven to be sufficiently precise in many different analyses [CMS18l; Ben18; Wil16]. For this reason, the background containing top quarks was estimated from the prediction based on MC simulations. To ensure a correct description of the background process, a series of simulation-to-data correction factors are applied to the MC-prediction. The correction factors come with systematic uncertainties that are described in Section 5.6. In the following, all background processes containing top quarks are referred to as *Top background*.

QCD-multijet background   The large number of particles created in a QCD-multijet event can fake the decay of a boosted top quark or W boson. Combined with a large production cross-section ($\mathcal{O}(10\,\text{mb})$), QCD-multijet production becomes the dominant background process of this analysis.

QCD-multijet events are challenging to simulate, especially in the high momentum transfer and high multiplicity region investigated in this analysis ($m_{\text{Z}'} \approx 1\,\text{TeV} - 4\,\text{TeV}$, $N_{\text{jets}} = 3-8$). Figure 5.10 shows a comparison between data and the simulated background prediction for some characteristic variables. A large deviation between data and background prediction is visible, caused by the insufficiently accurate prediction of the QCD-multijet background production rate. Even the prediction of the QCD-multijet background shape from MC simulations proved to be challenging, as indicated by Figure 5.11. The MC-simulated QCD-multijet background is normalized to the difference between data and the Top background prediction in order to fit the QCD-multijet background rate to data. Especially for high jet multiplicities, large deviations between the shape of the distribution predicted by MC simulations and the shape of the distribution measured in data are visible.

Since the prediction from simulated events can neither be used to estimate the shape nor the rate of the QCD-multijet background, the development of a data-driven background estimation method was at the core of this analysis and is described in more detail in the
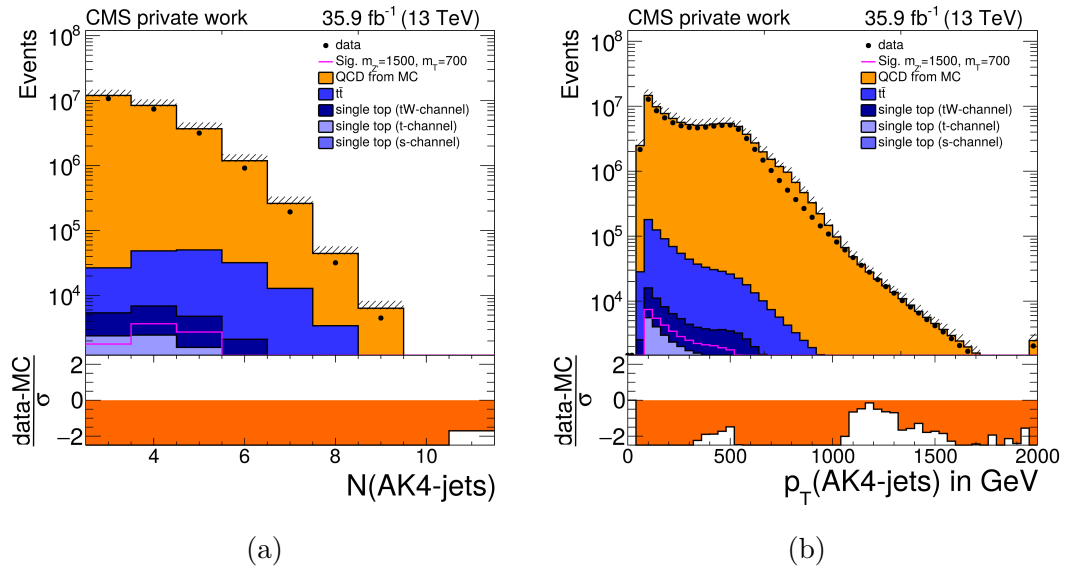
Figure 5.10: Data-MC comparison for basic variables. Comparison between data and the background prediction from MC simulations for the number of AK4-jets with $p_T > 75\,\text{GeV}$ and $|\eta| < 2.4$ (a) and their transverse momenta $p_T(\text{AK4-jets})$.
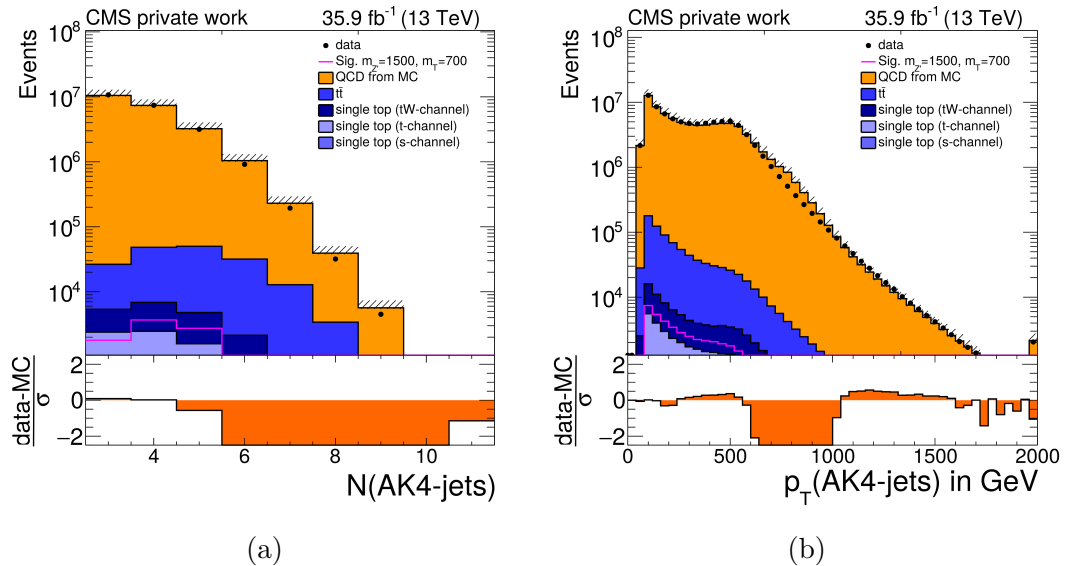
Figure 5.11: Data-MC shape comparison for basic variables. Comparison between data and the background prediction from MC simulations for the number of AK4-jets with $p_T > 75\,\text{GeV}$ and $|\eta| < 2.4$ (a) and their transverse momenta $p_T(\text{AK4-jets})$ (b). The MC-simulated QCD-multijet is normalized to $(\text{data} - \text{Top background})$ in order to fit to the event rate observed in data.

following section. The data-driven background estimation was developed and validated using the QCD-multijet sample based on the MadGraph5.2 framework as well as on data. For the remainder of this thesis, the simulated QCD-multijet predictions were normalized to the QCD-multijet rate derived from the comparison plots on basic variables. Therefore, the average deviation between the number of events observed in data and number of events predicted from the Top background MC simulations was taken as the QCD-multijet event rate. This allows a more realistic estimation of the QCD-multijet background.

5.5 Data-driven QCD-multijet background estimation

The prediction of the QCD-multijet background by a data-driven background estimation method is very common and almost unavoidable in most analyses in fully-hadronic final states. Within HEP, a large variety of different background estimation methods are established. For this analysis, a selection of data-driven background estimation techniques were investigated in order to identify the most suitable background estimation technique [Zie17; Fel17; Usa17]. The studies showed that, depending on the background estimation technique, any variables derived from MC simulations can have a large impact on the predicted rate and shape of the background. Therefore, the general strategy of this analysis was to accept a reduction in the large statistical precision of the LHC run-II data-set in order to minimize the amount of information derived from MC simulations. Additional focus was set on robustness and simplicity as well as the possibility to validate the method on data. The developed method, termed *bin-by-bin ABCD method*, can be considered a variation of the *Matrix Method* that is used by many experiments at the Tevatron or the LHC [Jun18].

The method is described in the following. After introducing the general concept, the technical implementation is described. Furthermore, several closure tests were performed to verify the background estimation technique and to derive systematic uncertainties.

5.5.1 Bin-by-bin ABCD method

The method relies on the assumption that two event variables of a process are uncorrelated. The two event variables *var*1 and *var*2 can be used to categorize all events of a process into four categories. In the following, these four categories are referred to as region A, region B, region C, and region D in order to distinguish them from the two analysis categories (2 b-tag and 1 b-tag). A possible realization of the event categorization based on *var*1 and *var*2 is visualized in Figure 5.12. If *var*1 and *var*2 are uncorrelated for a certain background process, the relationship between the number of events in the four regions follows

$$\frac{N_A}{N_B} = \frac{N_C}{N_D}, \tag{5.3}$$

where N_X defines the number of events in region X. If *var*1 and *var*2 also separate signal from background process events, a signal region can be defined and the number of background events in the signal region can be estimated as

$$N_A = N_B \cdot N_C / N_D. \tag{5.4}$$

This way, the ABCD method is typically used to estimate the rate of the QCD-multijet background in the signal region.

However, in addition to the rate of the QCD-multijet background, its shape needs to be estimated from data as well. In order to minimize the amount of information derived
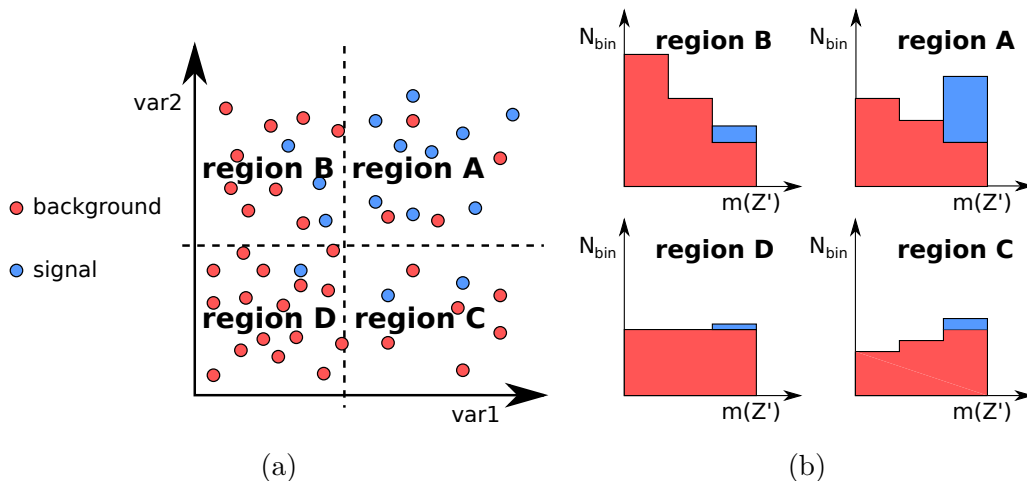
Figure 5.12: Basic concept of ABCD method. Possible realization of an event categorization based on two variables that can be considered as uncorrelated for the background process (a). By performing the ABCD method for every mass bin of Z′, the method can be extended to the bin-by-bin ABCD method (b).

from MC simulation, the ABCD method was modified to the *bin-by-bin ABCD method*. For the bin-by-bin ABCD method, the correlation between the two variables $var1$ and $var2$ is required to be independent of the analysis observable $m(\mathrm{Z}')$, allowing to apply Equation (5.3) to every bin i of the Z′ mass distributions:

$$N_{\mathrm{Reg.\,A}}^{\mathrm{QCD}}(i) = \frac{N_{\mathrm{Reg.\,B}}^{\mathrm{QCD}}(i) \cdot N_{\mathrm{Reg.\,C}}^{\mathrm{QCD}}(i)}{N_{\mathrm{Reg.\,D}}^{\mathrm{QCD}}(i)}. \tag{5.5}$$

This way, a shape dependence of the $m(\mathrm{Z}')$ distribution on $var1$ or $var2$ is predicted from the corresponding sideband regions. A visualization of the bin-by-bin ABCD method is given in Figure 5.12.

The selection of a suitable variable combination can be performed on MC simulations, assuming that the MC simulation correctly considers all variable correlations. Let us assume a suitable combination of two uncorrelated variables to estimate both the QCD-multijet rate and shape in the signal region can be found in MC simulations. Then, the applicability to data is still not necessarily provided. It could be possible that hidden correlations between the two variables exist that have not been considered correctly in the event simulation. Such a hidden correlation might result in wrong predictions of the background and possibly in a false claim of a signal presence.

In order to check whether the assumptions derived from MC simulations are still feasible for data, a third variable $var3$ can be used to create a background enriched validation region that can be used to check the variable correlations on data. By using a third variable, the ABCD method can be extended by four additional regions E, F, G, and H as illustrated in Figure 5.13. The additional variable $var3$ has to separate signal from background, but also has to have impact on the correlation between $var1$ and $var2$.

A commonality of many data-driven background estimation methods is the impact of a potential signal presence in the sideband regions on the background estimation. Since no single event variable can provide a perfect separation between signal and background,
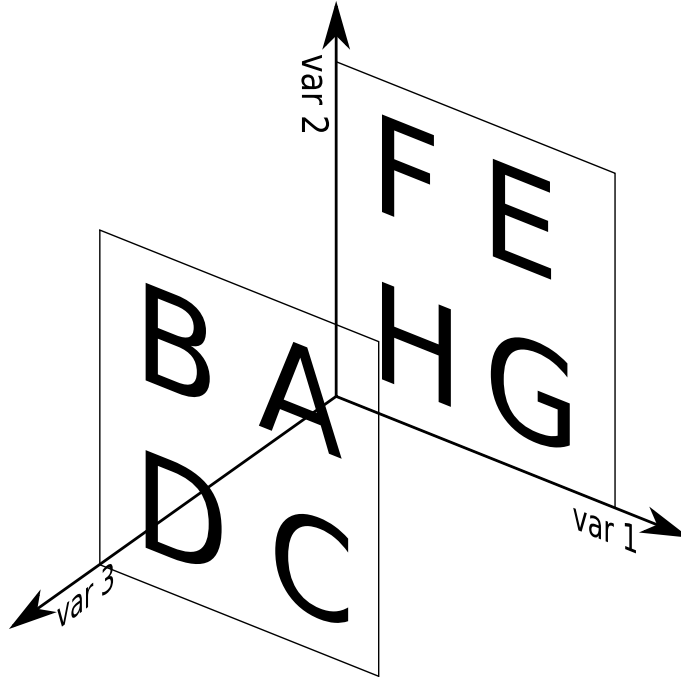
Figure 5.13: Extension of ABCD method by control region.   Possible extension of ABCD method by control regions in EFGH plane.

the presence of signal events in one of the sideband regions, which is used to estimate the background in the signal regions, is unavoidable. Depending on how the signal events are distributed among the signal and sideband regions, the signal in the sideband regions causes an over- or underestimation of the background in the signal region. In a worst-case scenario, the distribution of signal events among the regions is indistinguishable from the distribution of background events among the regions. In this case, the two variables would lose their discrimination power and the analysis would lose its sensitivity.

In an analysis with a large kinematic range and different final state topologies – like the one presented in this thesis – the impact of the signal on the background estimation might vary strongly depending on the signal hypothesis, and might become non-negligible. For example: the transverse momentum of the top-jet is not a suitable variable for the method since its discrimination power depends on the Z′-mass and the T-quark mass of the signal hypothesis. In order to correctly consider the impact of the signal onto the background estimation, the background estimation method was integrated into final fit model, as described in Section 5.7.

5.5.2 Variable selection and sideband definition

In order to use the bin-by-bin ABCD method to estimate the QCD-multijet background while keeping the possibility to validate the method in a control region, several conditions need to be fulfilled by the selected combination of variables:

1. neither linear nor higher-order correlations between $var1$ and $var2$ exist in the parameter space considered for the analysis, thus allowing a prediction of the background rate.

Furthermore, the correlation between the variables $var1$ and $var2$ has to be independent of the selection of a sub-parameters space (e.g. a certain $m(Z)'$ range), to enable shape predictions via the bin-by-bin ABCD method.

2. the correlation between $var1$ and $var2$ is independent of $var3$, allowing the creation of control regions in data;

3. discrimination power for all signal hypotheses;

4. sufficient statistical precision in sideband regions in order to provide a precise background prediction.

All requirements to the selected combination of variables need to be fulfilled for both signal categories (2 b-tag and 1 b-tag). To provide sideband regions with a similar kinematic range as the signal regions as well as sufficient statistical precision in the sidebands, special focus was set on jet identification variables. As a first step, MC simulations were used to search for suitable variable combinations [Fel17]. Although the following tests can be used to select the potentially most suitable variable combination for the bin-by-bin ABCD method, the final validation of the variable selection is provided by the closure tests on simulations as well as data, as described in Section 5.5.3.

The Pearson correlation coefficient can be used to identify linear correlations between two variables [Pea95]:

$$\rho_{\text{Pearson}} = \frac{\text{cov}(X, Y)}{\sigma_X \sigma_Y} \tag{5.6}$$

with σ_X and σ_Y denoting to the standard deviations of two variable populations X and Y, and $\text{cov}(X, Y)$ corresponding to their covariance. Furthermore, the Spearman correlation coefficient can be used to identify non-linear correlations [Spe04]:

$$\rho_{\text{Spearman}} = \frac{\text{cov}(\text{rg}(X), \text{rg}(Y))}{\sigma_{\text{rg}(X)} \sigma_{\text{rg}(Y)}}, \tag{5.7}$$

where $\text{rg}(X)$ denotes to the rank of a value X within a statistical population. This way, the compatibility with non-linear monotonic correlation can be estimated.

Both correlation coefficients were used to identify potential variable combinations. Table 5.1 shows the correlation coefficients of selected promising variable combinations. A more visual way to identify correlations between two variables are so-called *profile plots*. Here, the average value of $var1$ is calculated in bins of $var2$. For two uncorrelated variables, the average value of $var1$ is expected to be independent of $var2$. Hence, in case of no correlations the distribution is expected to be flat, while a linear or non-linear correlation would result in trends or variations in the profile. Figure 5.14 shows two example profile plots for correlated and uncorrelated variables. In addition, the correlations were quantified using correlation coefficients in dependence of the reconstructed Z'-mass. This way the variable combination was checked for major changes in the variable correlations in dependence of the reconstructed Z'-mass. In addition, the dependence of the variable correlation on the reconstructed Z'-mass was quantified using correlation coefficients.

In order to check whether the correlations between $var1$, $var2$ and the reconstructed Z'-mass are independent of a third variable $var3$, all correlation tests described before were performed with an applied $var3$ selection (ABCD plane) and an inverted $var3$ selection (EFGH plane).

Table 5.1: Correlations of variable combinations. Selection of possible variable combinations considered for the ABCD background estimation with the corresponding Pearson and Spearman correlations coefficients for both analysis categories (2 b-tag and 1 b-tag).

variable combination	Pearson		Spearman	
$var1$, $var2$	2 b-tag	1 b-tag	2 b-tag	1 b-tag
CSV_v2(b-jet), τ_{32}(t-jet)	0.02	0.0005	0.09	0.08
CSV_v2(b-jet), m_{SoftDrop}(t-jet)	-0.03	-0.006	-0.1	-0.015
CSV_v2(b-jet), m_{Pruning}(W-jet)	-0.02	-0.019	-0.23	-0.14
CSV_v2(b-jet), τ_{21}(W-jet)	-0.012	-0.008	-0.026	-0.008
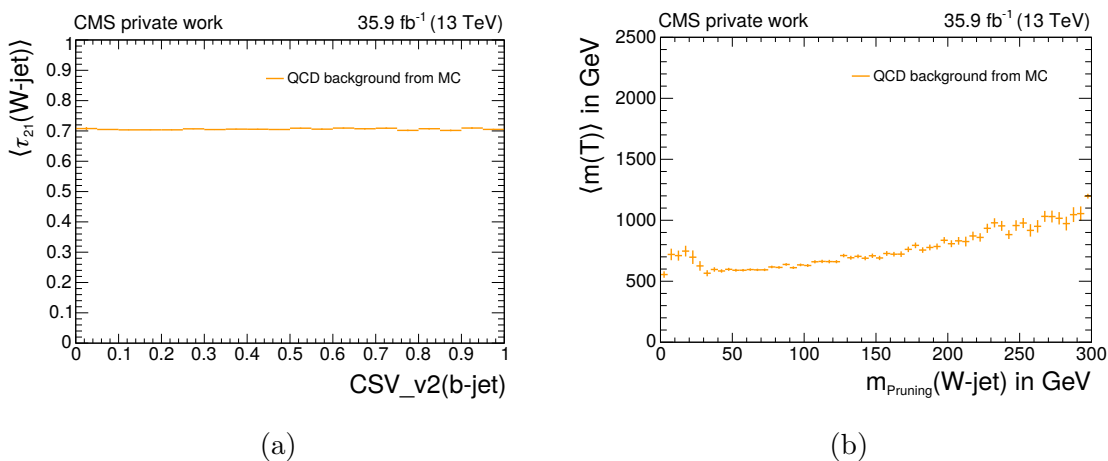
Figure 5.14: Exemplary profile plots. Profile plots derived from QCD-multijet MC simulations showing the average $\langle \tau_{21}(\text{W-jet}) \rangle$ as a function of CSV_v2(b-jet) in the 2 b-tag category (a), as well as the average $\langle m(\text{T}) \rangle$ as a function of m_{Pruning}(W-jet) in the 1 b-tag category (b).

The impact of signal contamination presence on the background estimation was tested by comparing the signal event distributions among the regions of the ABCD method and performing the ABCD method with and without the presence of a signal in the sideband region. If, for any signal hypothesis, the impact of the signal contamination on the background estimation surmounted the actual number of events in the signal region, the variable combination was considered to be not suitable.

Table 5.2 lists a selection of variable combinations that were tested for their suitability for this analysis. Based on the requirements on the variable correlations and the discrimination power of the variables, the following combination of variables has been selected for the bin-by-bin ABCD method in this analysis:

- $var1$: CSV_v2-output of bottom-jet candidate;

- $var2$: N-subjettiness τ_{21} of W-jet candidate;

Table 5.2: Overview of ABCD variable candidates. Variable combinations tested for their suitability for the bin-by-bin ABCD method. Variable combinations are required to show small correlation coefficients in the ABCD plane as well as in the EFGH plane. Furthermore, their discrimination power is required to be independent of the signal hypothesis. If a requirement is fulfilled for the background estimation, the corresponding variable combination is marked with a ✔, otherwise it is marked ✘.

| variable combination | small correlations | | S/B independent of | |
$var1$, $var2$, $var3$	ABCD	EFGH	sig. kin.	T decay
CSV_v2(b-jet), τ_{32}(t-jet), τ_{21}(W-jet)	✔	✔	✘	✔
CSV_v2(b-jet), m_{SoftDrop}(t-jet), τ_{21}(W-jet)	✘	✘	✘	✔
CSV_v2(b-jet), m_{Pruning}(W-jet), τ_{21}(W-jet)	✘	✘	✔	✘
CSV_v2(b-jet), τ_{21}(W-jet), m_{Pruning}(W-jet)	✔	✔	✔	✔

- $var3$: pruned jet mass m_{Pruning} of W-jet candidate.

The selection of $65\,\mathrm{GeV} < m_{\mathrm{Pruning}} < 105\,\mathrm{GeV}$ is optimized to identify W-jets. In case of a signal hypothesis where the T-quark decays into an SM top quark and a Higgs boson, the boosted Higgs boson is expected to create fat-jets with a pruned jet mass of $100\,\mathrm{GeV} < m_{\mathrm{Pruning}} < 150\,\mathrm{GeV}$. In such a scenario, the signal events are expected to be assigned to the regions E, F, G, and H instead of regions A, B, C and D. Although the bin-by-bin ABCD method is only performed in the ABCD plane, and therefore is not expected to be influenced by a signal presence in the EFGH plane, the potential signal presence when performing a validation of the method in the EFGH plane in data needs to be taken into account. At this point, the CMS strategy of performing two dedicated analyses each focusing on another decay channel can be exploited. With the semi-leptonic analysis setting strong limits on the signal hypotheses with a T $\rightarrow$ Ht decay, the impact of a potential signal presence in the EFGH plane on the validation of the bin-by-bin ABCD method, can be estimated to be negligibly small [Ben18].

In case there is more than one bottom-jet candidate or W-jet candidate, an ambiguity arises in the event reconstruction and the assignment of the event to a region of the ABCD method. Therefore, Figure 5.15 shows which of the potential W-jet or b-jet candidates available in an event is the first one (in orders of p_{T}) that fulfills the W-tagging or b-tagging requirements, respectively. For over $90\,\%$ of the signal events, the first jet candidate is the jet that has been W-tagged/b-tagged. Therefore, it is sufficient to reconstruct and thus distribute the events to the regions based on the tagging behavior of the W-jet and b-jet candidates with the largest transverse momentum. In addition, by only considering the W-jet and b-jet candidates with the largest transverse momentum, any residual correlations to the total number of jets in an event is suppressed, making the bin-by-bin ABCD method more robust against potential correlations between the selection variables and the number of jets in an event.

Finally, the assignment of events to the signal and sideband regions of both analysis categories can be defined. After applying all event selection criteria described in Sec-

(a)

(b)

(c)

(d)
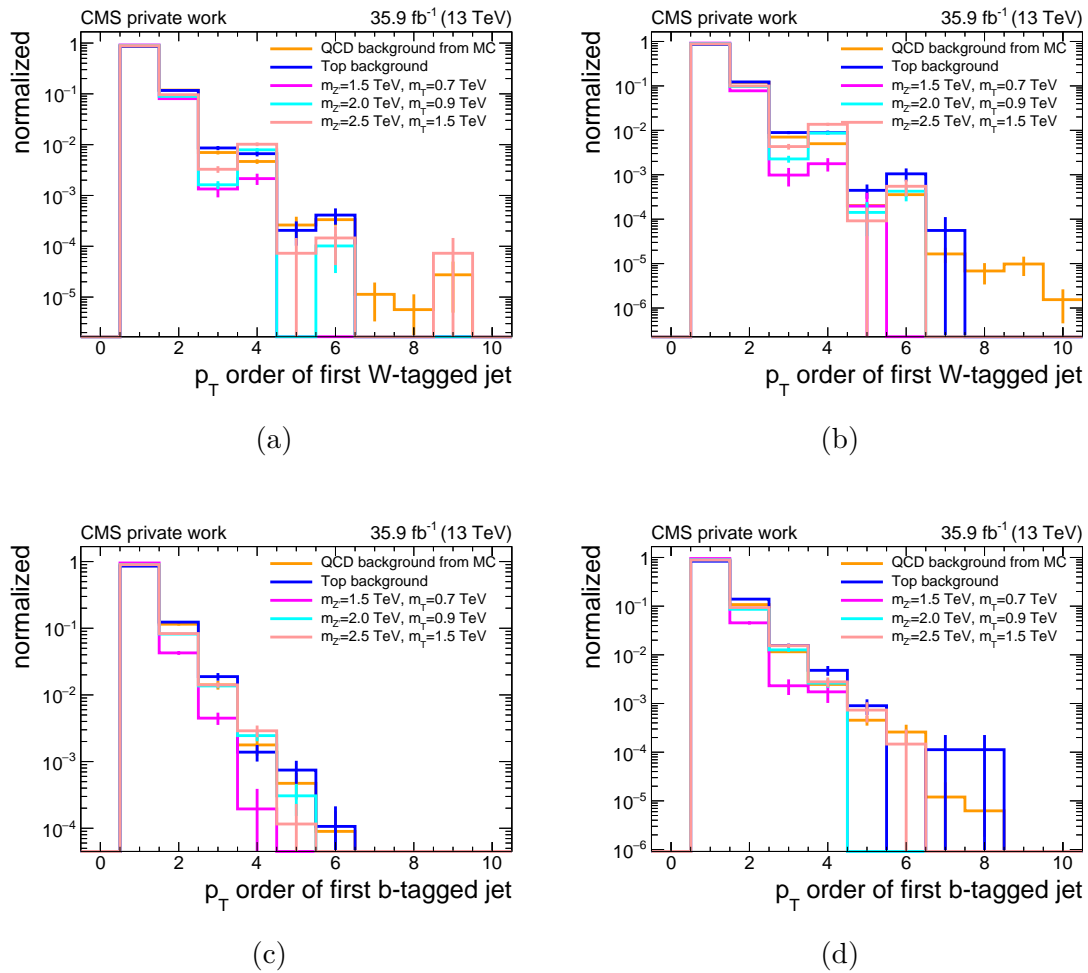
Figure 5.15: First W-tagged/b-tagged jet candidates in order of transverse momentum. Normalized distribution of first jet candidates being W-tagged/b-tagged as function of the order of the transverse momenta of the jets. (a): first W-tagged jet in the 2 b-tag analysis category, (b): first W-tagged jet in the 1 b-tag analysis category, (c): first b-tagged jet in the 2 b-tag analysis category, (d): first b-tagged jet in the 1 b-tag analysis category.

Table 5.3: Event categorization into ABCD regions. Based on the characteristics of the W-jet candidate and the b-jet candidate with the largest transverse momenta, events are assigned to a signal or sideband region.

region	τ_{21}(W-jet)	CSV_v2(b-jet)	m_{Pruning}(W-jet) in GeV
A (signal)	< 0.45	> 0.8484	> 65 && < 105
B (sideband)	≥ 0.45	> 0.8484	> 65 && < 105
C (sideband)	< 0.45	≤ 0.8484	> 65 && < 105
D (sideband)	≥ 0.45	≤ 0.8484	> 65 && < 105
E (sideband)	< 0.45	> 0.8484	≤ 65 || ≥ 105
F (sideband)	≥ 0.45	> 0.8484	≤ 65 || ≥ 105
G (sideband)	< 0.45	≤ 0.8484	≤ 65 || ≥ 105
H (sideband)	≥ 0.45	≤ 0.8484	≤ 65 || ≥ 105

tion 5.3.1, except for the W-tagging and b-tagging of the corresponding jet-candidates, the event is assigned to one of eight regions. The assignment to one of the eight regions is based on the characteristics of the W-jet candidate and b-jet candidate with the largest transverse momentum. Only W-jets with m_{Pruning}(W-jet) > 40 GeV and τ_{21}(W-jet) < 0.75 were considered, in order to respect the SFs provided centrally by the CMS experiment to avoid phase spaces where a reliable simulation of the variable correlations cannot be ensured any more. Table 5.3 summarizes the selection criteria of the different ABCD-regions of an analysis category.

5.5.3 Validation of background estimation method on simulations and data

In order to validate the selected variable combination, a consistency check, also referred to as *closure test* was performed using MC simulations and data. For this, the background in a signal region is compared to the background predicted from the sideband regions in order to check whether the data-driven background estimation method is able to consistently predict the background distribution in the signal region.

In case of the bin-by-bin ABCD method, a closure test is performed by calculating the bin-by bin ratio (region A · region D)/(region B · region C) of the QCD-multijet background distributions present in the different regions for every $m(Z')$ bin according to Equation (5.5). The closure test was considered successful if a linear function fitted to the bin-by-bin ratio is compatible with $y = 1$ within the statistical precision. Furthermore, a χ^2-test was performed on the bin-by-bin ratio to quantify its compatibility with $y = 1$, respectively [Pea00]. A compatibility of 97 % and 48 % was observed for the 2 b-tag and the 1 b-tag categories. The compatibility test as well as the bin-by-bin closure show a good compatibility with the assumption of a closure. This confirms that the bin-by-bin method can be used to estimate the QCD-multijet background in the signal region.

To further check whether the assumptions on the variable correlations are applicable to data, the closure tests were repeated in the EFGH plane for QCD-multijet MC simulations

(a)   (b)
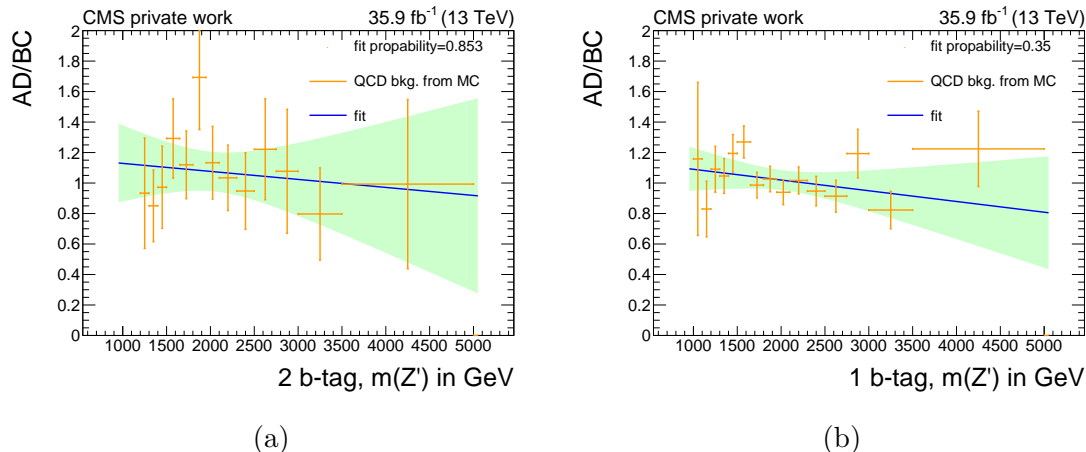
Figure 5.16: Bin-by-bin ABCD closure with QCD-multijet simulation. Results of the two closure tests performed in the ABCD plane of the 2 b-tag (a) and the 1 b-tag (b) analysis categories using simulated QCD-multijet background events. The ratio of the $m(Z')$ distribution in region A predicted by the ABCD method and the $m(Z')$ distribution obtained directly from the simulation is shown. A linear function is fitted to the bin-by-bin ratio. The shaded area depicts the 1σ confidence interval, propagating the uncertainties to the fitted parameters.

as well as for data. The data in the EFGH plane not only contains QCD-multijet events but also Top background contributions for which the assumptions of minor correlation between $CSV\_v2(b\text{-jet})$ and $\tau_{21}(W\text{-jet})$ do not apply. For this reason, the simulated Top background prediction was subtracted from data in order to only consider the QCD-multijet fraction of the data events. Figures 5.17 and 5.18 show the bin-by-bin closure tests performed in MC simulations and data, respectively. For these closure tests in the EFGH plane, a re-binning into wider $m(Z')$ bins was performed to reduce the fluctuations due to a limited statistical precision. Similar to the ABCD plane, the compatibility with an ideal closure ($y = 1$) was calculated to be 58 % in the 2 b-tag category and 96 % in the 1 b-tag category on MC simulations, and 19 % in the 2 b-tag category and 49 % in the 1 b-tag category on data.

All closure tests verify the compatibility with the assumption of an ideal closure and the method can be considered to work consistently within the given precision. The closures tests performed on data in the EFGH plane showed some trends in the fitted slopes and some offsets from $y = 1$ that can be caused by residual correlations between the two variables that were not visible before. In order to consider potential remaining correlations, visible as offsets and trends in the fitted slopes, systematic uncertainties on the background estimation method are assigned, as discussed in Section 5.6.1.

In addition, the bin-by-bin ABCD method was tested for its robustness against variations in the selection cuts separating the signal regions from the background regions. Therefore, bin-by-bin closure tests were performed using simulated QCD-multijet events with both selections $CSV\_v2(b\text{-jet}) > 0.8484$ and $\tau_{21}(W\text{-jet}) < 0.45$ tightened and loosened independently of each other by 5 % and 10 %[1]. Since a tightening of the selection criteria

---

[1] In case of the b-tagging requirement, a tightening corresponds to an increase in the cut on the $CSV\_v2(b\text{-jet})$, while a loosening of the selection corresponds to a decrease in the $CSV\_v2(b\text{-jet})$ cut value. In case of the N-subjettiness criterion on the W-jet, the selection is tightened by decreasing the $\tau_{21}(W\text{-jet})$ and loosened by increasing the cut criterion value.
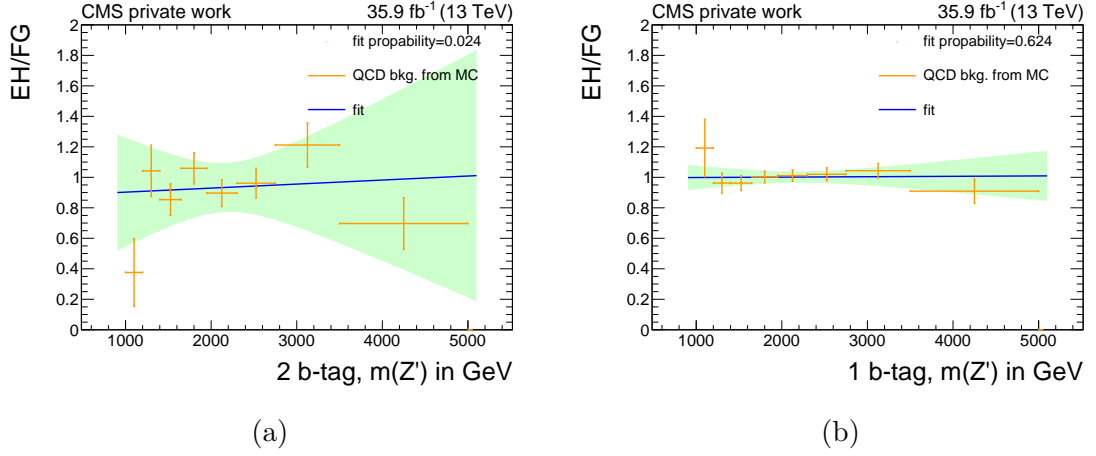
Figure 5.17: Bin-by-bin EFGH closure on QCD-multijet simulation. Results of the two closure tests performed in the EFGH plane of the 2 b-tag (a) and the 1 b-tag (b) analysis categories using simulated QCD-multijet background events. The ratio of the $m(Z')$ distribution in region A predicted by the ABCD method and the $m(Z')$ distribution obtained directly from the simulation is shown. A linear function is fitted to the bin-by-bin ratio. The shaded area depicts the 1σ confidence interval, propagating the uncertainties to the fitted parameters.
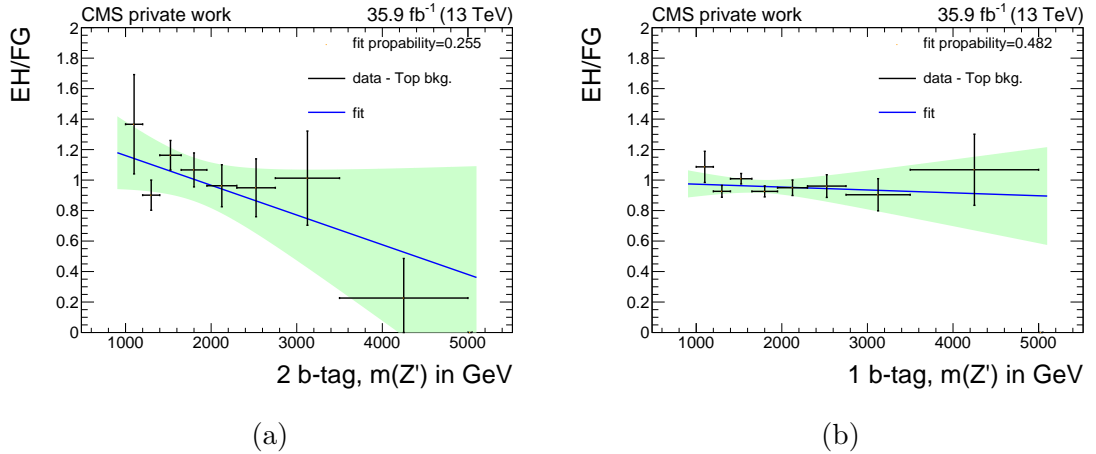
Figure 5.18: Bin-by-bin EFGH closure on data. Results of the two closure tests performed in the EFGH plane of the 2 b-tag (a) and the 1 b-tag (b) analysis categories using events from data after subtracting the simulated Top background. The ratio of the $m(Z')$ distribution in region A predicted by the ABCD method and the $m(Z')$ distribution obtained directly from the simulation is shown. A linear function is fitted to the bin-by-bin ratio. The shaded area depicts the 1σ confidence interval, propagating the uncertainties to the fitted parameters.

Table 5.4: Compatibility of varied bin-by-bin closures. Results of two compatibility checks (χ^2 test) performed on the bin-by-bin closures tests with varied selection criteria. The compatibility with an ideal closure assumption and with the linear fit derived from the nominal bin-by-bin closure were tested.

variable	category	10 % looser	5 % looser	nom.	5 % tighter	10 % tighter
		χ^2 compatibility with closure assumption in %				
τ_{21}(W-jet)	2 b-tag	50	59	60	77	46
τ_{21}(W-jet)	1 b-tag	22	9	16	28	37
CSV_v2(b-jet)	2 b-tag	74	64	60	67	60
CSV_v2(b-jet)	1 b-tag	37	45	16	34	15
		χ^2 compatibility with nominal linear fit in %				
τ_{21}(W-jet)	2 b-tag	88	91	93	62	26
τ_{21}(W-jet)	1 b-tag	76	29	28	46	63
CSV_v2(b-jet)	2 b-tag	79	76	93	92	52
CSV_v2(b-jet)	1 b-tag	56	44	28	52	33

by up to 10 % can result in strong statistical fluctuations due to the limited statistical precision of the simulated samples, a re-binning into larger bin-widths was performed for these tests. Again, the compatibility with the assumption of an ideal closure ($y = 1$) was tested for every variation of the selection criteria. Furthermore, the compatibility of the varied bin-by-bin closures with the linear fit performed on the nominal closure was tested, to check for potential trends arising from variation in the selection criteria. Table 5.4 summarizes the results of these compatibility checks. The figures illustrating the varied bin-by-bin closure tests are added in Appendix A.2.

The compatibility checks show no major variations when varying the selection criteria. The bin-by-bin ABCD method is therefore considered sufficiently robust against such variations.

5.6 Uncertainties of analysis

In this section, the uncertainties that were assumed for this analysis are listed and shortly introduced. The systematic uncertainties can be categorized into systematic uncertainties arising from the data-driven background estimation of the QCD-multijet background and systematic uncertainties originating from experimental uncertainties as well as theoretical uncertainties on the simulated Top background and signal samples. Additional uncertainties arise from the limited number of MC events of the simulated background and signal samples.

All systematic uncertainties, including the uncertainties arising from the limited statistical precision of the simulated background and signal samples are considered in the final fit using nuisance parameters, as described in Section 5.7.

5.6.1 Uncertainties of the bin-by-bin ABCD method

Although the bin-by-bin ABCD method with the selected variable combination was shown to work consistently within the statistical precision, systematic uncertainties were derived to consider potential biases. The method is based on two assumptions: minor correlation between $var1$ and $var2$, and minor dependency of this correlation from the reconstructed mass of the heavy bosonic resonances Z'. Nevertheless, it could be possible that, below the limited statistical precision, residual correlations are hidden. Therefore, systematic uncertainties were assigned to take into account these residual correlations.

A residual correlation between $var1$ and $var2$ is expected to result in a rate deviation between the predicted QCD-multijet background in the signal region and the actual QCD-multijet background. Such a rate deviation would be visible as an offset from $y = 1$ in the bin-by-bin closure tests. On the other hand, any dependence of the correlation between $var1$ and $var2$ on $m(Z')$ is expected to create a trend in the background prediction. This would be visible as a trend in the linear fit to the bin-by-bin closure test. For both effects, systematic uncertainties were derived from the closure tests performed in the ABCD plane using QCD-multijet MC simulations as well as from closure tests performed in the EFGH plane using data. Designed to cover the maximum possible variations, both uncertainties were derived by the linear functions fitted in Figures 5.16 and 5.18. By selecting a parameterization of

$$f(x) = 1 + a_0 + a_1 \cdot (x - \overline{x}), \tag{5.8}$$

for the linear function, with $\overline{x}$ corresponding to the average bin center of the reconstructed Z' mass bins, the slope and the rate parameters a_0 and a_1 were constructed to be uncorrelated [Bar93].

- **Systematic rate uncertainty of the bin-by-bin ABCD method:** For each analysis category, the rate uncertainty of a closure test is derived as a symmetrical uncertainty $\sigma_{\text{rate}} = |a_0|$. Conservatively, the larger of two deviations derived from the ABCD plane in QCD-multijet MC simulations and from the EFGH plane in data is used as a prior rate uncertainty for the final statistical analysis.

- **Systematic shape uncertainty of the bin-by-bin ABCD method:** Similar to the rate uncertainty, the shape uncertainty is derived independently for both analysis categories. The shape uncertainty is derived from the slope of the linear fit as a symmetric uncertainty $\sigma_{\text{shape}} = |a_1|$. Again the larger of the two slopes derived from the ABCD plane and the EFGH plane is selected as a prior uncertainty for the final statistical analysis.

The systematic uncertainties on the ABCD method derived from MC and data are listed in Table 5.5. Both uncertainties are used in the final fit to modify the required bin-by-bin ratio for the QCD-multijet background according to Equation (5.13).

For a data-driven background estimation method like the bin-by-bin ABCD method, also the statistical precision due to the limited number of events in the sideband regions needs to be correctly propagated into the signal region. By implementing the bin-by-bin ABCD method into the final fit model, the statistical precision is considered correctly.

Table 5.5: Systematic uncertainties of the bin-by-bin ABCD method. Values of fit parameters in Equation (5.8) derived from closure test performed in the ABCD plane using QCD-multijet MC simulations and the EFGH plane using data. For each uncertainty, the larger of the two closure deviations is selected.

par.	ABCD unc.	ABCD plane	EFGH plane	selected
a_0	rate (2 b-tag)	0.10	0.05	ABCD on MC
a_1	shape (2 b-tag)	$5.3 \cdot 10^{-5} \cdot m(\mathrm{Z}') \frac{1}{\mathrm{GeV}}$	$2.0 \cdot 10^{-4} \cdot m(\mathrm{Z}') \frac{1}{\mathrm{GeV}}$	EFGH on data
a_0	rate (1 b-tag)	0.048	0.041	ABCD on MC
a_1	shape (1 b-tag)	$7.0 \cdot 10^{-5} \cdot m(\mathrm{Z}') \frac{1}{\mathrm{GeV}}$	$1.9 \cdot 10^{-5} \cdot m(\mathrm{Z}') \frac{1}{\mathrm{GeV}}$	ABCD on MC

5.6.2 Theoretical and experimental uncertainties

A series of uncertainties arises for the simulated background and signal processes. The origins of these uncertainties stem from theoretical calculations, deviations between data and simulation and the experimental methods used to derive physics parameters used in the analysis. Depending on its type, a systematic uncertainty can have an impact on the normalization of a process (rate uncertainty), or an impact on the shape and the rate of a process (rate and shape uncertainty). An overview of the systematic uncertainties and the processes they apply to is given in Table 5.6.

- **Factorization and re-normalization scale:** shape and rate uncertainty originating from the selected energy scale of the interaction process μ_R, and the selected energy scale separating the hard scattering from the showering process μ_F. The nominal values $\mu_{X,\mathrm{avg.}}$ of both scales were varied up to $\mu_{X,\mathrm{up}}$ and down to $\mu_{X,\mathrm{down}}$ by a factor two, respectively. An envelope of six variation combinations ($\mu_{R,\mathrm{up}} + \mu_{F,\mathrm{up}}$, $\mu_{R,\mathrm{down}} + \mu_{F,\mathrm{down}}$, $\mu_{R,\mathrm{avg.}} + \mu_{F,\mathrm{up}}$, $\mu_{R,\mathrm{avg.}} + \mu_{F,\mathrm{down}}$, $\mu_{R,\mathrm{up}} + \mu_{F,\mathrm{avg.}}$, $\mu_{R,\mathrm{down}} + \mu_{F,\mathrm{avg.}}$) was considered as up and down variation. The uncertainties were considered to be correlated among all signal and background regions, but applied independently to the $t\bar{t}$ background and to the signal process, since MC-simulated events are calculated with different MC generators. For minor backgrounds, like single-top production processes, this uncertainty can be neglected.

- **PDF:** shape and rate uncertainty originating from uncertainties in the selected PDF set `NNPDF_3.0` and its impact on the shape as well as on the acceptance of the process [Bal+15]. The uncertainty is estimated by re-weighting the simulated events according to 100 replica sets of the PDF set and calculating the Root Mean Square (RMS) for every event. For the signal processes, only the PDF impact on the shape was considered. The PDF impact on th acceptance of the process was neglected.

  For the $t\bar{t}$-production background, the `NNPDF30_nlo_as_2600` PDF parameterization was used. For the little-Higgs model signal samples, the `NNPDF30_nlo_as_0118` PDF parameterization was used. The systematic uncertainties on the PDFs of the warped extra-dimensions model were derived via the LHA framework based on the `NNPDF30_nlo_as_0130` PDF parameterization [Buc+15]. The uncertainties were considered to be correlated among all signal and sideband regions, but uncorrelated

for signal process and Top background, since MC-simulated events are calculated with different MC generators. PDF uncertainties on minor single-Top background were neglected.

- **t$\bar{\text{t}}$ cross-section:** 2 % rate uncertainty arising from the t$\bar{\text{t}}$-production cross-section calculations under the assumption of a top quark mass of 172.5 GeV [CMS18k]. Uncertainties on the production cross-sections of single-top production processes were neglected due to the smallness of single-top contributions. It is considered to be correlated among all signal and background regions of all Top background and signal processes.

- **Trigger efficiency:** 1.6 % rate uncertainty arising from the uncertainty of the efficiency measurement of the selected analysis trigger, as derived in Section 5.3.2. The systematic uncertainty on the trigger efficiency is applied to the Top background as well as to the signal samples, and considered to be correlated among all signal and background regions of all Top background and signal processes.

- **Luminosity:** 2.5 % rate uncertainty derived from LHC luminosity measurements as derived in [CMS17a]. Applied to the Top background as well as to the signal samples and considered to be correlated among all signal and background regions of all Top background and signal processes.

- **Pileup:** shape and rate uncertainty arising from the predicted pileup contributions. Derived by varying the assumed pileup cross-section from the nominal value of 69.2 mb by ± 4.6 % to 66.0 mb and to 72.4 mb [CMS18p]. Applied to the Top background as well as to the signal samples and considered to be correlated among all signal and background regions of all Top background and signal processes.

- **Jet energy calibration:** shape and rate uncertainty originating from the jet energy calibration uncertainties ([CMS18h], similar to [CMS17g]). Applied to the Top background as well as to the signal samples and considered to be correlated among all signal and background regions of all Top background and signal processes, as well as among AK4-jets, AK8-jets and their subjets.

- **Jet energy resolution:** shape and rate uncertainty originating from the jet energy resolution uncertainties ([CMS18g], similar to [CMS17g]). Applied to the Top background as well as to the signal samples and considered to be correlated among all signal and background regions of all Top background and signal processes, as well as among AK4-jets, AK8-jets.

- **Top-tagging scale factors:** shape and rate uncertainty originating from the scale factors used to compensate differences between the top-tagging efficiencies in simulations and data. Applied to Top background and to the signal samples if a top-tagged jet can be matched ($\Delta R < 0.8$) to a simulated top quark. Considered to be correlated among all signal and sideband regions of all Top background and signal processes [CMS18c].

- **W-tagging scale factors:** shape and rate uncertainty originating from the scale factors to compensate differences between the W-tagging efficiencies in simulations and real data. Different scale factors and uncertainties for the regions with high purity τ_{21}(W-jet) < 0.45 and the regions with low purity τ_{21}(W-jet) > 0.45, that are considered to be anti-correlated. Applied to Top background and to the signal samples if a jet is W-tagged [CMS18r; CMS13b].

Table 5.6: Overview of systematic uncertainties. Sources of systematic uncertainties, prior size, type and processes they are applied to. The quoted average relative uncertainty that is calculated from the average deviation in the $m(Z')$ bins of all regions of one category, is listed. The uncertainty range describes the average relative uncertainty observed in the signal and background processes considered. The number of nuisance parameters assigned to the uncertainty in the final fit (see Section 5.7) is quoted as (X NP).

			avg. rel. pre-fit unc.	
Uncertainty	Type	Process	2 b-tag	1 b-tag
ABCD rate (2 NP)	rate	QCD	$10\,\%$	$5\,\%$
ABCD shape (2 NP)	shape	QCD	$14\,\%$	$5\,\%$
fac. & ren. scale (2 NP)	rate & shape	Top & Sig.	$0.3\,\% - 17\,\%$	$0.2\,\% - 17\,\%$
PDF (2 NP)	rate & shape	Top & Sig.s	$2\,\% - 17\,\%$	$2\,\% - 19\,\%$
$t\bar{t}$ cross-section	rate	$t\bar{t}$	$2\,\%$	$2\,\%$
Trigger efficiency	rate	Top & Sig.	$1.6\,\%$	$1.6\,\%$
Luminosity	rate	Top & Sig.	$2.5\,\%$	$2.5\,\%$
Pileup	rate & shape	Top & Sig.	$1\,\% - 8\,\%$	$1\,\% - 7\,\%$
Jet energy cal.	rate & shape	Top & Sig.	$6\,\% - 12\,\%$	$6\,\% - 12\,\%$
Jet energy res.	rate & shape	Top & Sig.	$1\,\% - 6\,\%$	$1\,\% - 6\,\%$
t-tagging	rate & shape	Top & Sig.	$0.6\,\% - 4\,\%$	$0.6\,\% - 4\,\%$
W-tagging	rate & shape	Top & Sig.	$8\,\% - 9\,\%$	$8\,\% - 9\,\%$
b-tagging (8 NP)	rate & shape	Top & Sig.	$0\,\% - 2\,\%$	$0\,\% - 2\,\%$

- **B-tagging scale factors on AK4-jets and on subjets of AK8 top-jet:** shape and rate uncertainty originating from the scale factors to compensate differences between the b-tagging efficiencies in simulations and data. In total, eight individual contributions consider the impact of the jet energy scale uncertainties, the heavy- and light-flavor contaminations in the control samples used to derive the SFs as well as the limited statistical precision in the control samples used to derive the scale factors [CMS18f]. All b-tagging uncertainties are applied to the Top background and the signal samples and are considered to be correlated across all AK4-jets and top-jet subjets of all signal and sideband regions of all Top background and signal processes.

- **Statistical precision of simulated distributions:** The number of events in the simulated background and signal samples results in statistical fluctuations of the nominal predictions. This is taken into account by assigning a dedicated nuisance parameter to everyin in $m(Z')$ of the Top background and the signal process.

A visualization of the shape impact of the different systematic uncertainties on the Top background is given in Appendix A.3.

With the bin-by-bin ABCD method being used to estimate the QCD-multijet background, the impact of systematic uncertainties that affect the Top background in all signal and sideband regions in the same way are expected to have a reduced impact on the final sensitivity. This can be explained by the fact that such an uncertainty causes a similar under or over estimation of the QCD-multijet background in all four regions. Since the ABCD method uses ratios of these regions, the impact is reduced. On the other hand, uncertainties affecting the Top background in a non-uniform way are expected to have an increased impact on the final analysis sensitivity since they affect numerator and denominator of the ABCD ratio differently.

5.7 Statistical analysis of data

In order extract a potential signal, taking into account all systematic and statistical uncertainties in a single fit, the Higgs-Combine Tool version 6.3.1 was used [ATL11; CMS18e]. Within the Higgs-Combine Tool, various parameter estimation techniques are implemented. The most important ones that were used for this analysis are briefly introduced here.

Maximum likelihood estimation   The most powerful test-statistic to perform a hypothesis test at a confidence level α is given by the profile likelihood ratio:

$$q_\mu = -2 \ln \frac{\mathcal{L}(\vec{\theta}_\mu | \vec{x}, \mu)}{\mathcal{L}(\vec{\theta}_{\max} | \vec{x}, \mu_{\max})} \,, \quad 0 \le \mu_{\max} \le \mu \,, \tag{5.9}$$

of the binned likelihood function

$$\mathcal{L}(\vec{\theta}_\mu | \vec{x}, \mu) = \text{Poisson}\left(\vec{x} | \mu \cdot s(\vec{\theta}_\mu) + b(\vec{\theta}_\mu)\right) \cdot p(\vec{\theta}_0 | \vec{\theta}_\mu). \tag{5.10}$$

according to the Neyman-Pearson lemma [NP33]. Here, $\vec{x}$ represents the data, $\vec{\theta}$ corresponds to a set of nuisance parameters describing the systematic uncertainties and $\mu = \mu_{\text{obs}}/\mu_{\text{hypothesis}}$ represents the signal strength modifier. The signal and background yields are represented by s and b. The set of nuisance parameters $\vec{\theta}_\mu$ depends on the signal strength modifier μ. The probability density function p represents the degree of belief that the set of nuisance parameters $\vec{\theta}_\mu$ is compatible with a default value $\vec{\theta}_0$ that is derived in an independent measurement. The numerator of Equation (5.9) corresponds to the maximum likelihood at a given μ, with $\vec{\theta}_\mu$ representing the corresponding nuisance parameters. The denominator of Equation (5.9), on the other hand, corresponds to the global maximum of the likelihood function. In a maximum likelihood estimation (MLE), the parameter values of a fit hypothesis that are most compatible with the data are derived from a multi-parametric fit model by maximizing the profile likelihood ratio test statistic [Le 90].

Every nuisance parameter θ_i follows an a-priori statistical distribution P defined by the prior uncertainties of the independent measurement $\vec{\theta}_0$. In the MLE, the nuisance parameters can be varied from their nominal value, but every pull results in a reduced likelihood. This way, the MLE derives the parameter values for which the data is most probable. This allows a decision on which relative signal strength and which parameter combination is the most likely given in the data and whether it is significantly different from $\mu = 0$. MLEs are typically performed under the hypothesis of no signal presence, *background-only*, and under a *signal+background* hypothesis with $\mu \neq 0$.

Limits   Assuming no signal is found, upper limits on the signal strength can be set. To do so, a series of MLEs is performed under the assumption of different signal strengths μ as well as for the assumption of a background-only hypothesis. By scanning the assumed signal strength μ, the probability (p-value) to find the observed test statistic q_μ^{obs} or a larger one can be calculated as a function of the signal strength:

$$p_\mu = P(q_\mu \geq q_\mu^{\mathrm{obs}} | \mu). \tag{5.11}$$

By comparing the calculated p-value of the signal+background hypothesis of a given μ with the p-value of the background-only hypothesis, a measure of the significance of the test can be given as:

$$\mathrm{CL_s}(\mu) = \frac{p_\mu}{1 - p_{\mu=0}}. \tag{5.12}$$

The upper limit on the cross-section at a 95 % confidence level (CL) can then be defined as the signal strength μ_{95} with $\mathrm{CL_s}(\mu_{95}) = 0.05$.

Expected limits can be approximated using asymptotic formulae [Cow+11]. The median of the distribution is referred to as the expected limit, with the $\pm 1\sigma (2\sigma)$ uncertainties corresponding to the 16 % and 84 % (2.5 % and 97.5 %) quantiles. For more information on the calculation of upper limits, the reader is referred to [Mor15].

Two major technical issues arise when using a data-driven background estimation like the one used in this analysis. First, depending on the signal hypothesis, the signal presence in the sideband regions is not negligible and its impact on the data-driven background estimation needs to be considered correctly. Second, the statistical distributions of data and background in the sideband regions as well as their systematic uncertainties need to be correctly propagated into the signal region[2]. Both of these issues can be addressed by integrating the bin-by-bin ABCD method into the final fit.

Therefore, all signal and sideband regions are fitted simultaneously. The QCD-multijet background contribution is kept floating for all $m(\mathrm{Z}')$-bins in all signal and sideband regions, only constrained by Equation (5.13)

$$1 + \theta_{\mathrm{rate}} \cdot \sigma_{\mathrm{rate}} + \theta_{\mathrm{shape}} \cdot \sigma_{\mathrm{shape}} \cdot (m(\mathrm{Z}') - \overline{m(\mathrm{Z}')}) = \frac{N_{\mathrm{Reg.\,A}}^{\mathrm{QCD}}(m(\mathrm{Z}')) \cdot N_{\mathrm{Reg.\,D}}^{\mathrm{QCD}}(m(\mathrm{Z}'))}{N_{\mathrm{Reg.\,B}}^{\mathrm{QCD}}(m(\mathrm{Z}')) \cdot N_{\mathrm{Reg.\,C}}^{\mathrm{QCD}}(m(\mathrm{Z}'))} \tag{5.13}$$

and

$$N_{\mathrm{Reg.\,X}}^{\mathrm{data}}(m(\mathrm{Z}')) = \mu \cdot N_{\mathrm{Reg.\,X}}^{\mathrm{Signal}}(m(\mathrm{Z}')) + \sum_{\mathrm{Backgrounds}} N_{\mathrm{Reg.\,X}}^{\mathrm{process}}(m(\mathrm{Z}')) \tag{5.14}$$

for each $m(\mathrm{Z}')$-bin. The nuisance parameters assigned to the rate and shape uncertainties σ_{rate} and σ_{shape} of the bin-by-bin ABCD method (as derived in Section 5.6.1) are given by θ_{rate} and θ_{shape}. The relative signal strength μ is used to scale the assumed signal hypothesis. Dedicated ABCD nuisance parameters are assigned to both analysis categories. Table 5.7 lists all the nuisance parameters considered for this analysis.

---

[2]When subtracting the Poisson distributed Top background from data, the resulting QCD-multijet background is not Poisson distributed anymore, but Skellam distributed [Ske46].

Table 5.7: Nuisance parameters of fit model. Listed are all uncertainties assumed for the final fit as well as the corresponding nuisance parameters.

systematic unc.	nuisance parameters
fac. & ren. scale	$\theta_{\text{renfac\_env\_BKG}}, \theta_{\text{renfac\_env\_Sig}}$
PDF	$\theta_{\text{PDF\_BKG}}, \theta_{\text{PDF\_Sig}}$
$t\bar{t}$ cross-section	θ_{ttbarXS}
Trigger efficiency	θ_{Trigger}
Luminosity	θ_{Lumi}
Pileup	θ_{PU}
Jet energy cal.	θ_{JES}
Jet energy res.	θ_{JER}
t-tagging	θ_{ttag}
W-tagging	θ_{Wtag}
b-tagging	$\theta_{\text{CSVCErr1}}, \theta_{\text{CSVCErr2}}, \theta_{\text{CSVHF}}, \theta_{\text{CSVLF}}$
	$\theta_{\text{CSVLFStat1}}, \theta_{\text{CSVLFStat2}}, \theta_{\text{CSVHFStat1}}, \theta_{\text{CSVHFStat2}}$
ABCD rate	$\theta_{\text{ABCD\_rate\_1\_b-tag}}, \theta_{\text{ABCD\_rate\_2\_b-tag}}$
ABCD shape	$\theta_{\text{ABCD\_shape\_1\_b-tag}}, \theta_{\text{ABCD\_shape\_2\_b-tag}}$
MC stat.	$\theta_{\text{SigMC\_A\_2b-tag\_stat\_bin1}}, ..., \theta_{\text{TopMC\_D\_1b-tag\_stat\_bin15}}$ (240 in total)

5.7.1 Validation tests of the final fit

Since the integration of the bin-by-bin ABCD method into the final fit results in a complex fit model, a series of fit tests were performed to verify the fit model. As this analysis uses a data-driven background estimation which is implemented within the final fit, it is necessary to clearly distinguish between the different types of *pseudo data* that were used for the fit tests:

- **Asimov data**: pseudo data generally created as the sum over the expected contributions of all backgrounds and, if desired, signals for every $m(Z')$-bin. Since a data driven method is used, the expected contribution of the QCD-multijet background is unknown. Therefore, the expected QCD-multijet background in the regions B, C and D is defined to be equal to the prediction from QCD-multijet MC simulations. The QCD-multijet background in region A, on the other hand, is calculated using Equation (5.13). As a result, the *Asimov data* set perfectly fulfills the condition of Equation (5.13).

- **Simulated background data**: pseudo data created as the sum of all simulated background processes. Different than in Asimov data, the *simulated background data* set does not fulfill Equation (5.13) by definition. It therefore provides a single more realistic pseudo data set including the residual fluctuations observed in the bin-by-bin

closure tests of Section 5.5.3 as well as statistical fluctuations. Similar to the Asimov data, a signal can be injected into the pseudo data set. The simulated background data can be used to estimate the robustness of the fit model against fluctuations or residual correlations between the variable combination used for the bin-by-bin ABCD method.

For both pseudo data sets, the fit model was tested with and without the presence of a signal using a MLE. The simulated signal events were normalized to production cross-section of $1\,\text{pb}$ corresponding to a relative signal strength of $\mu = 1$.

The validation tests of the final fit were performed for all available signal hypotheses. As an example, the results of a representative signal hypothesis ($m_{Z'} = 2000\,\text{GeV}$, $m_T = 1200\,\text{GeV}$, $\text{BR}(T \rightarrow \text{Wb}/\text{Zt}/\text{Ht}) = 50\,\%/25\,\%/25\,\%$) are shown here. The fit results are visualized by *pull plots*, which show the difference of parameter values at the global maximum of the likelihood function with respect to their a-priori values and uncertainties, normalized to ther prior values.

For Asimov data without signal presence, the MLE converged for the background-only hypothesis as well as for the signal+background hypothesis without any nuisance parameter being pulled (see Figure 5.19). The fitted signal strength is compatible with the injected signal strength $\mu^{\text{fit}}_{\text{no sig.}} = -1.7 \cdot 10^{-7} \pm 0.07$ (injected $\mu^{\text{inject}}_{\text{with sig.}} = 0$) and $\mu^{\text{fit}}_{\text{with sig.}} = 1.0 \pm 0.04$ (injected $\mu^{\text{inject}}_{\text{with sig.}} = 1.0$). In case a signal is present, the MLE is required to pull nuisance parameters away from their nominal value in order to fit the background-only hypothesis to the data. A signal+background hypothesis, on the other hand, does not require any pulls in order to fit the data. Both results verify that the fit model is consistent and capable of distinguishing signal from background. Furthermore, the pull plots show which uncertainties can be constrained by the fit and which nuisance parameters are most sensitive to a signal presence.

For simulated background data without a signal, the MLE converged with only few nuisance parameters being pulled (see Figure 5.20). Since most of the nuisance parameters are pulled similarly for the background-only as well as the signal presence hypothesis, no signal strength μ significantly different from zero is fitted and no signal is claimed. The fitted signal strength shows only a minor deviation from the injected signal strength $\mu^{\text{fit}}_{\text{no sig.}} = 0.1 \pm 0.08$ (injected $\mu^{\text{inject}}_{\text{with sig.}} = 0$). The deviation can be explained by fluctuations in Z'-mass bins where such a signal is expected, and by the residual deviations in the closure test that were observed in simulated QCD events. Again, for simulated background data with an injected signal, more and stronger pulls of the nuisance parameters are needed by the MLE to fit the background-only hypothesis. For the signal+background hypothesis the nuisance parameters are pulled less and a signal strength compatible with the assumed signal strength is fitted. The fitted signal strength is compatible with the injected signal strength $\mu^{\text{fit}}_{\text{with sig.}} = 0.94^{+0.22}_{-0.18}$ (injected $\mu^{\text{inject}}_{\text{with sig.}} = 1$). This shows that even for a non-perfect bin-by-bin ABCD-closure, the analysis is sensitive to a signal presence and can extract the injected signal without biases.

The nuisance parameter correlation matrices are given in Appendix A.4 and show no unexpected correlations among nuisances parameters assigned to the different systematic uncertainties. The strongest correlations can be observed between the W-tagging uncertainty, the rate uncertainties on the bin-by-bin ABCD method, and the signal strength parameter μ. These correlations between the nuisance parameters can be explained since they all affect the ABCD method in a similar way. A pull on the rate nuisance parameters of the ABCD method results in an underestimation of the QCD-multijet background in the signal region and therefore gives space to fit a signal strength $\mu \neq 0$. Depending on the
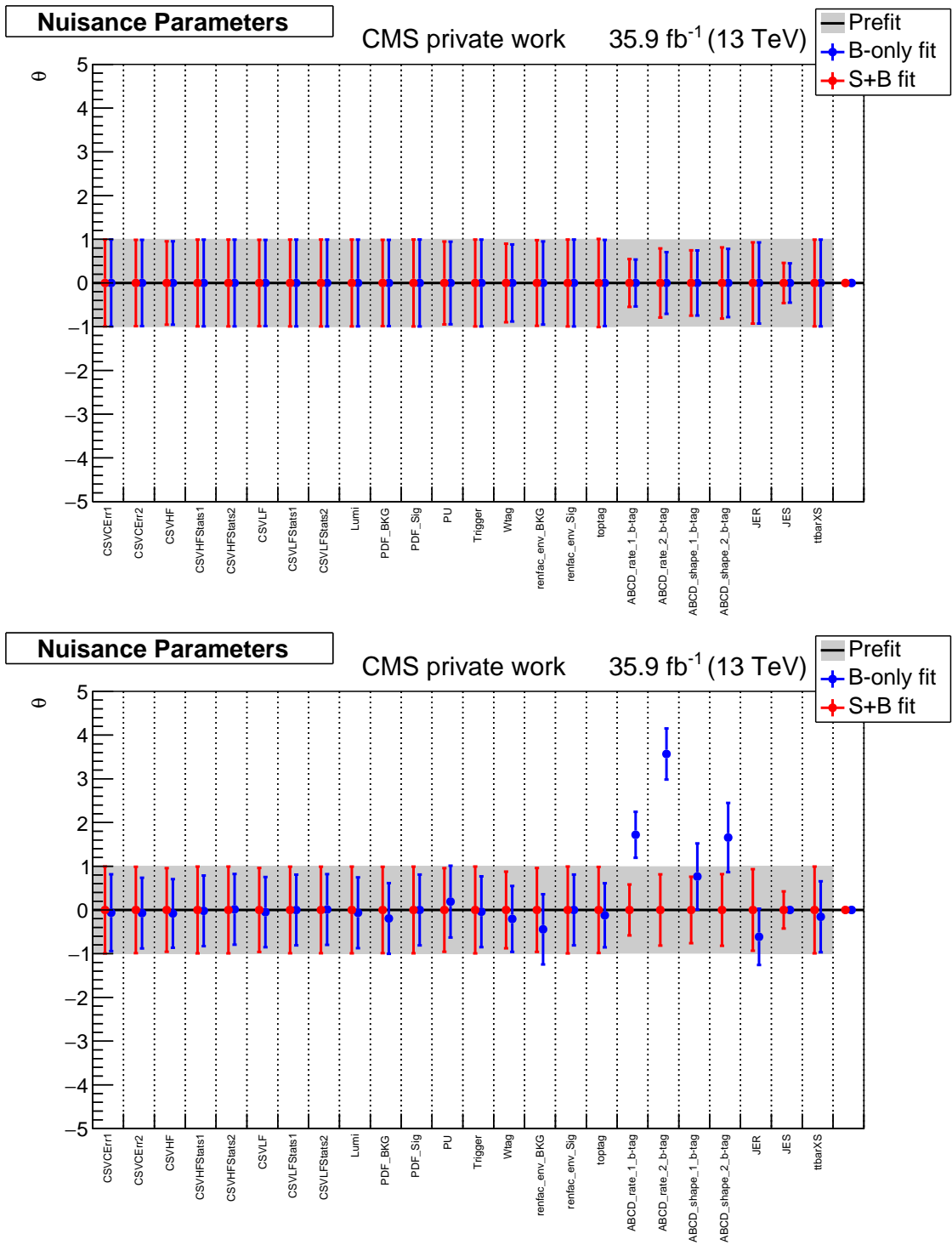
Figure 5.19: Nuisance parameter pulls of Asimov data. Difference between pre-fit and post-fit nuisance parameter values and their uncertainties relative to the pre-fit value for the maximum likelihood estimation of a signal hypothesis of $m_{Z'} = 2000\,\mathrm{GeV}$, $m_T = 1200\,\mathrm{GeV}$, $\mathrm{BR}(T \to \mathrm{Wb/Zt/Ht}) = 50\,\%/25\,\%/25\,\%$. Top: Asimov data derived from backgrounds only, bottom: signal injected into Asimov data with a cross-section of $1\,\mathrm{pb}$ ($\mu = 1$).
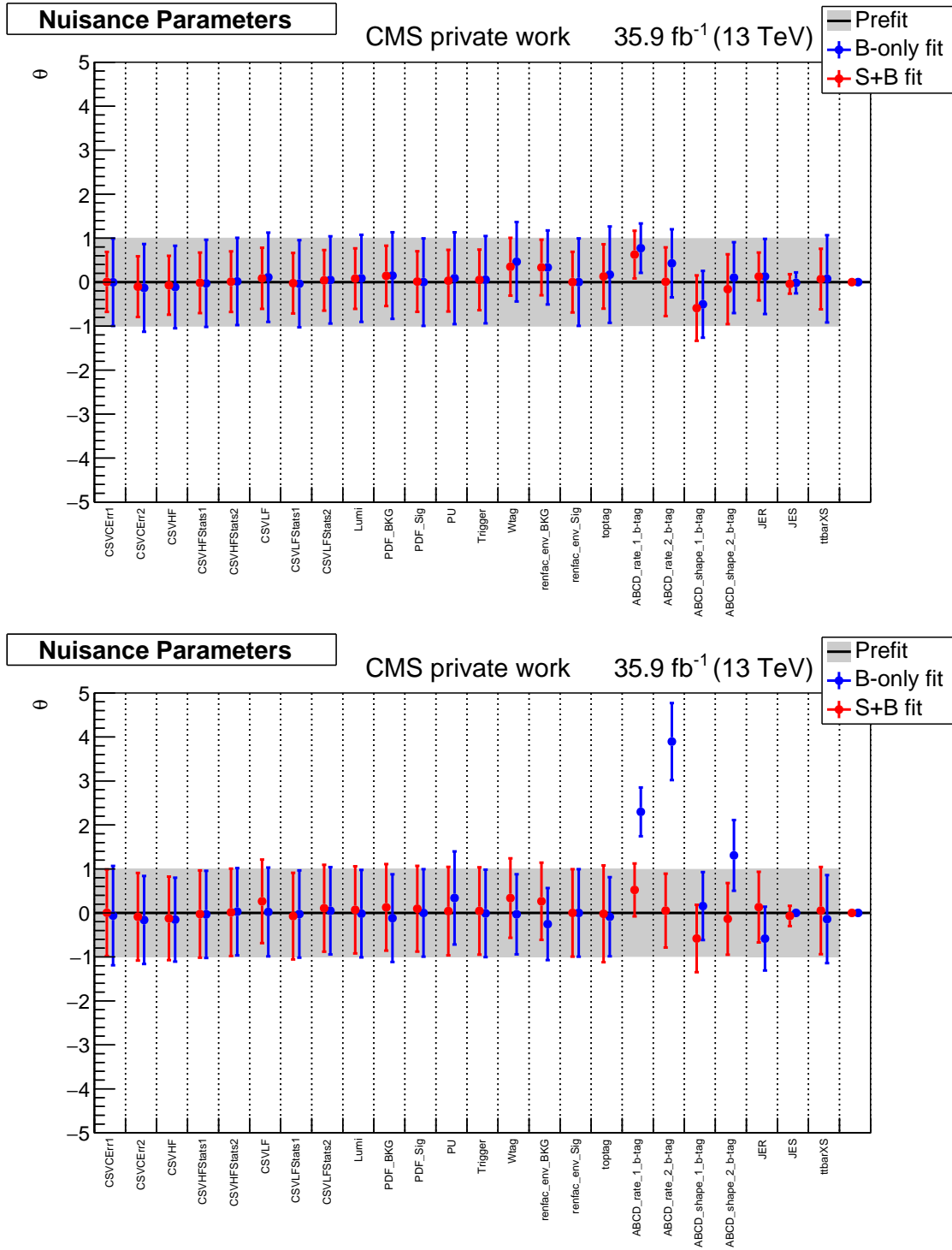
Figure 5.20: Nuisance parameter pulls of simulated background data. Difference between pre-fit and post-fit nuisance parameter values and their uncertainties relative to the pre-fit value for the maximum likelihood estimation of a signal hypothesis of $m_{Z'} = 2000\,\mathrm{GeV}$, $m_T = 1200\,\mathrm{GeV}$, $\mathrm{BR}(T \to \mathrm{Wb}/\mathrm{Zt}/\mathrm{Ht}) = 50\,\%/25\,\%/25\,\%$. Top: simulated data derived from simulated backgrounds only, bottom: signal injected into simulated data with a cross-section of $1.0\,\mathrm{pb}$.

Z′-mass of the signal hypothesis, a pull on the nuisance parameters assigned to the shape uncertainties of the bin-by-bin ABCD method can result in a similar effect. A pull on the nuisance parameter corresponding to the W-tag uncertainty, on the other hand, does not directly affect the QCD-multijet background. But since the uncertainties are considered anti-correlated between two of the four regions respectively, and since ABCD variables cannot be considered uncorrelated to the signal process or the Top background, a pull on the W-tag nuisance parameter has an indirect impact on the QCD-multijet background. This way, a pull on the W-tag nuisance parameter can give space to fit a signal as well.

The way these nuisance parameters impact the fit result can also be studied in the form of an *impact plot*: A single nuisance parameter is set to $\pm 1\,\sigma$ and the MLE is re-performed with the single nuisance parameter fixed. By comparing the new fit result of the MLE with the nominal MLE fit result, the relative impact of a single nuisance parameter on the final fit result can be estimated. Figure 5.21 shows two example impact plots derived from Asimov data with and without injected signal ($m_{Z'} = 2000\,\text{GeV}$, $m_T = 1200\,\text{GeV}$, $\text{BR}(\text{T} \to \text{Wb/Zt/Ht}) = 50\,\%/25\,\%/25\,\%$). The figure shows that the uncertainties on the ABCD method have the largest impact on the fit result, if no signal is present. When injecting a signal, the impact of the systematic uncertainties on the ABCD method on the fit result remain roughly the same. On the other hand, the impact of other systematic uncertainties, like for example the W-tagging uncertainty, drastically increases since they are strongly correlated with the signal which defines the signal region.

The post-fit $m(Z')$ distributions for MLEs performed on Asimov data with an injected signal ($m_{Z'} = 2000\,\text{GeV}$, $m_T = 1200\,\text{GeV}$, $\text{BR}(\text{T} \to \text{Wb/Zt/Ht}) = 50\,\%/25\,\%/25\,\%$) are shown exemplary in Figures 5.22 and 5.23. In order to get a realistic idea about the signal distributions in the four regions, a relative signal strength of $\mu = 0.34$ was assumed. The assumed signal strength corresponds to the latest limit on the production cross-section of such a signal hypothesis derived in [Usa17].

Since all signal and sideband regions are fitted simultaneously and are connected via the bin-by-bin ABCD method, the presence of a signal is not only visible in the signal region but also in the sideband regions. The minor residual deviations in the signal+background fit are caused by numerical fluctuations in the fit.

5.7.2 Analysis sensitivity

Although the final expected limits are calculated using real data (see Section 5.7.3), the limit predictions from Asimov data can be used to estimate the analysis sensitivity and to identify the major uncertainties limiting the analysis sensitivity. Table 5.8 illustrates the dependency of the median expected limit on the signal hypothesis. For the sake of clarity, only a selection of signal hypotheses is shown here.

Although designed for the $\text{T} \to \text{Wb}$ decay channel, the analysis is still sensitive to the $\text{T} \to \text{Zt}$ and the $\text{T} \to \text{Ht}$ decay channels. Two major trends are visible for the different kinematics. With increasing $m(Z')$, the analysis sensitivity increases, since the background production cross-sections rapidly drop. At the same time, an increased T-quark mass relative to the Z′ mass reduces the analysis sensitivity, since the top quark in the $\text{Z}' \to \text{Tt}$ decay is less boosted and therefore its decay products cannot be clustered into a single t-jet. This results in a strongly reduced signal event selection efficiency and analysis sensitivity. This behavior most present in the $\text{T} \to \text{Wb}$ decay channel (see A.1), since only a single top quakr is created in the decay. For the $\text{T} \to \text{Zt/Ht}$ decay channels, the second top-quark created in the decay of the T quark can be boosted enough to be considered as a signal
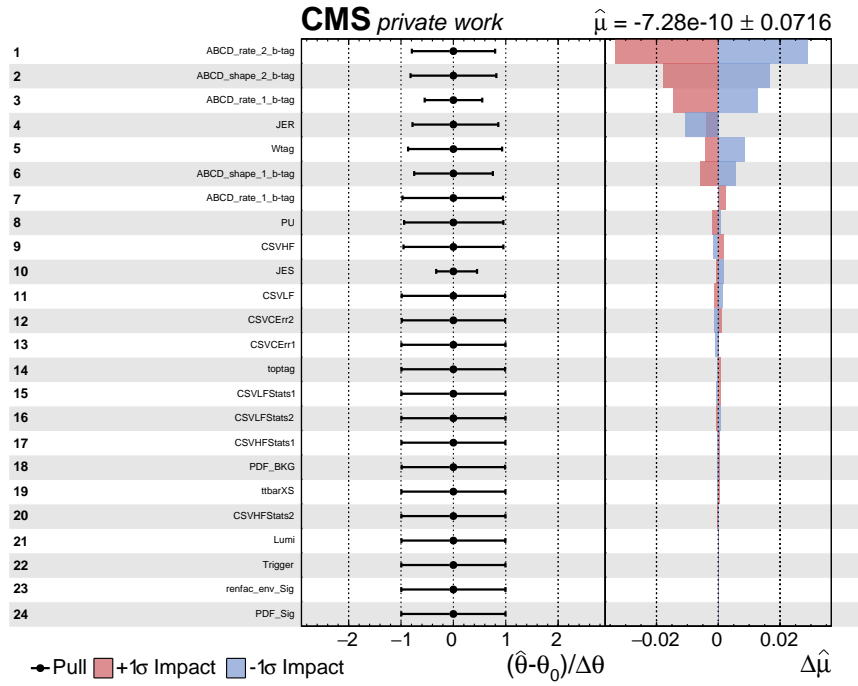
(a) no signal injected
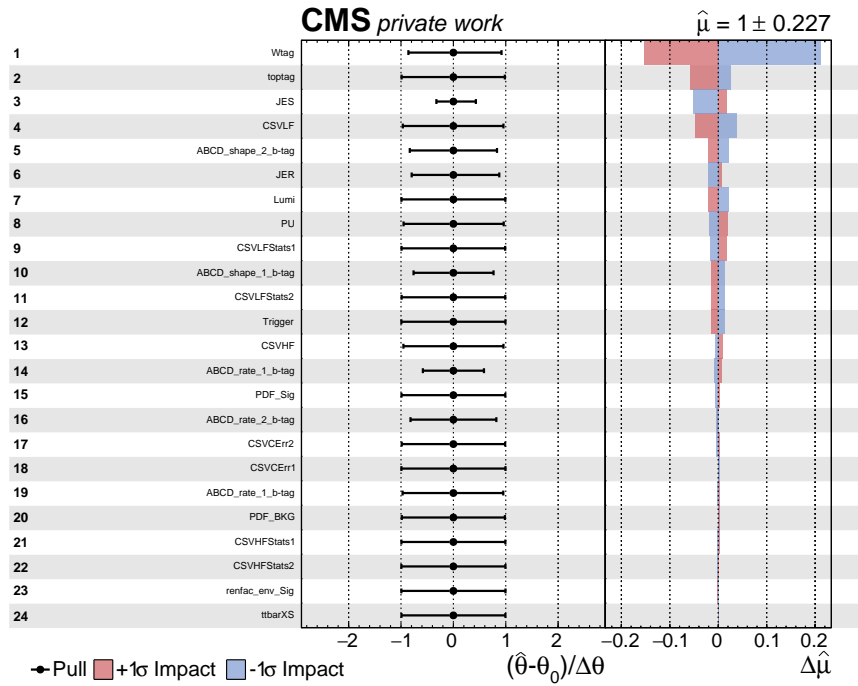
(b) signal injected with $\mu = 1$

Figure 5.21: Impact of nuisance parameters on the fit result. Post-fit nuisance parameter pulls and their impact on the fitted signal strength $\hat{\mu}$. The nuisance parameter pulls are shown relative to the pre-fit values θ_0 and uncertainties $\Delta\theta$. The impact $\Delta\hat{\mu}$ is computed as the difference to the nominal best fit value $\hat{\mu}$ obtained when fixing the nuisance parameter under study to its best-fit value $\hat{\theta}$ plus/minus its post-fit uncertainty. Top: impact of nuisance parameters on the fit result using Asimov data without a signal injected, Bottom: impact of nuisance parameters on the fit result using Asimov data with a signal injected ($m_{Z'} = 2000\,\text{GeV}$, $m_{T} = 1200\,\text{GeV}$, BR($T \rightarrow \text{Wb/Zt/Ht}$) = 50 %/25 %/25 %, $\mu = 1$).
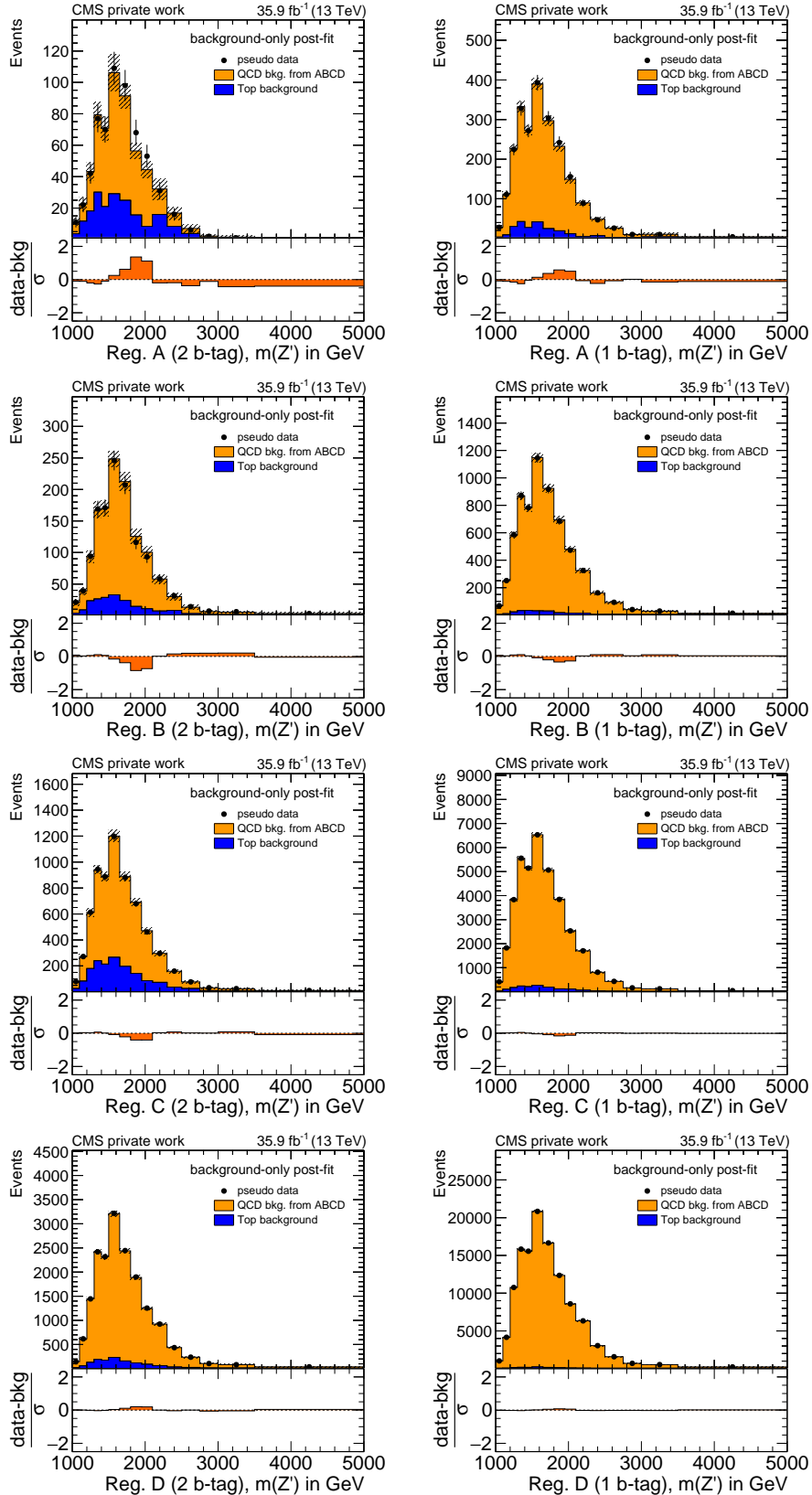
Figure 5.22: Background-only post-fit m(Z') distributions for Asimov data. Asimov data with signal presence after a background-only fit (signal hypothesis of $Z' \to Tt$ with $BR(T \to Wb/Zt/Ht) = 50\,\%/25\,\%/25\,\%$ and $m_{Z'} = 2000\,GeV$, $m_T = 1200\,GeV$, $\sigma_{Sig.} = 0.34\,pb$). Left column: 2 b-tag category, right column: 1 b-tag category. From top to bottom: Region A, B, C, D.
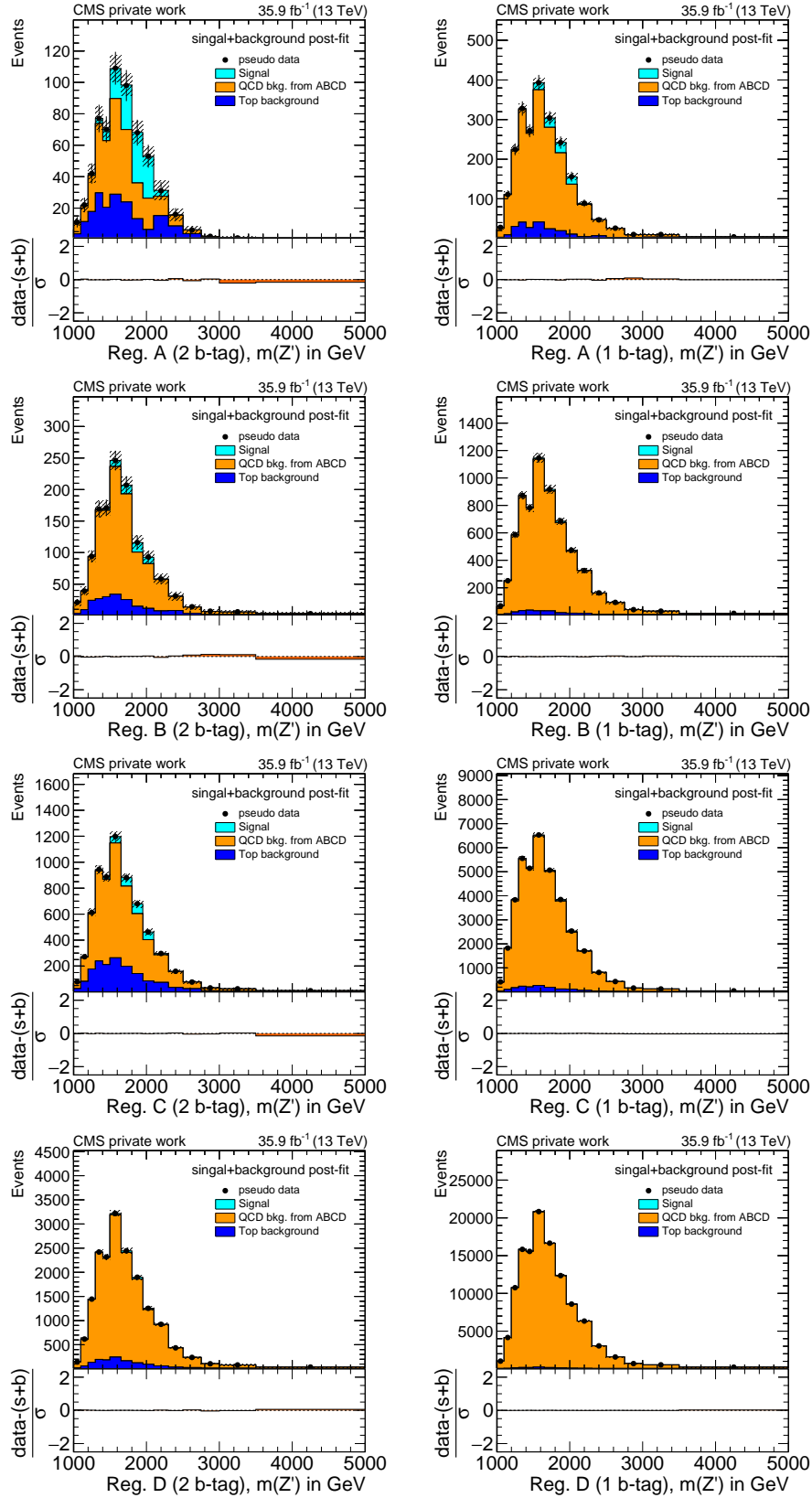
Figure 5.23: Signal and background post-fit m(Z') distributions for Asimov data. Asimov data with signal presence after a signal and background fit (signal hypothesis of $Z' \to Tt$ with $BR(T \to Wb/Zt/Ht) = 50\%/25\%/25\%$ and $m_{Z'} = 2000\,\mathrm{GeV}$, $m_T = 1200\,\mathrm{GeV}$, $\sigma_{\mathrm{Sig.}} = 0.34\,\mathrm{pb}$). Left column: 2 b-tag category, right column: 1 b-tag category. From top to bottom: Region A, B, C, D.

Table 5.8: Expected analysis sensitivity using Asimov data. Median of the expected limit as a function of the signal hypothesis. The estimation is based on Asimov data derived from MC simulations. A 95 % confidence level is assumed.

		median of the expected limit in pb		
$m_{Z'}$ in TeV	m_T in TeV	$T \to Wb$	$T \to Zt$	$T \to Ht$
1.5	0.7	0.18	0.38	0.58
1.5	0.9	0.35	0.31	0.53
1.5	1.2	4.6	0.74	2.2
2.0	0.9	0.084	0.17	0.39
2.0	1.2	0.10	0.13	0.37
2.0	1.5	0.57	0.13	0.44
2.5	1.2	0.070	0.096	0.26
2.5	1.5	0.078	0.078	0.25

event. As a result, the sensitivity drop due at large T-quark mass relative to the Z' mass is not as strong for the $T \to Zt/Ht$ decay channels as for the $T \to Wb$ decay channel.

When comparing the sensitivity of the analysis to different T-quark decay channels, an anti-correlation between the masses of the bosonic decay products (boosted W, Z or Higgs boson) and the analysis sensitivity is visible. This can be explained by the W-tagging mass criterion that is fulfilled to lesser extent, at higher masses of the heavy bosonic decay products ($\epsilon_{\text{W-tagging}}(\text{W-jet}) > \epsilon_{\text{W-tagging}}(\text{Z-jet}) > \epsilon_{\text{W-tagging}}(\text{H-jet})$).

Furthermore, the impact of a group of uncertainties on the analysis sensitivity can be estimated by performing the limit expectation with a single group of uncertainties removed. The impact on the total analysis sensitivity can then be estimated as:

$$\frac{\Delta_{\text{syst.}}\sigma_{\text{limit}}}{\sigma_{\text{limit, all syst.}}} = \frac{\sqrt{\sigma^2_{\text{limit, all syst.}} - \sigma^2_{\text{limit, N-1 syst.}}}}{\sigma_{\text{limit, all syst.}}} \tag{5.15}$$

where $\sigma_{\text{limit, all syst.}}$ corresponds to the total analysis sensitivity for a certain signal hypothesis and $\sigma_{\text{limit, N-1 syst.}}$ corresponds to the analysis sensitivity estimated without the considered uncertainty. The impact of the statistical uncertainty can be estimated by freezing all systematic uncertainties:

$$\frac{\Delta_{\text{stat.}}\sigma_{\text{limit}}}{\sigma_{\text{limit, all syst.}}} = \frac{\sigma_{\text{limit, no syst.}}}{\sigma_{\text{limit, all syst.}}}. \tag{5.16}$$

In general, the impact of an uncertainty on the analysis sensitivity depends on the signal hypothesis. A representative overview assuming a $\text{BR}(T \to Wb/Zt/Ht) = 50\,\%/25\,\%/25\,\%$ signal hypothesis with $m_T = 1200\,\text{GeV}$ is given in Table 5.9. As expected, the analysis sensitivity is dominantly limited by the statistical precision, followed by the systematic uncertainties arising on the W-tagging and the systematic uncertainties arising from the bin-by-bin ABCD method itself. The impact of systematic uncertainties arising from

Table 5.9: Relative change of the expected limit with systematic uncertainties. Relative change of the expected analysis limit in dependence of groups of uncertainties for a BR(T → Wb/Zt/Ht) = 50 % / 25 % / 25 % signal hypothesis with $m_T = 1200\,\text{GeV}$. Shown is the limit improvement, if a group of uncertainties were not applied. The numerical precision is limited and can only be used as a rough estimation. Groups: bin-by-bin ABCD method (rate uncertainties and shape uncertainties), b-tagging (eight uncertainties from data/MC scale factors), t-tagging (top-tag data/MC scale factor), W-tagging (W-tag data/MC scale factors for high & low purity), JEC (Jet Energy Scaling, Jet Energy Resolution), theory (factorization & renormalization, PDF, $t\bar{t}$-cross-section), experimental (pileup, Luminosity, Trigger).

group of uncertainties	$m_{Z'} = 1.5\,\text{TeV}$	$m_{Z'} = 2.0\,\text{TeV}$	$m_{Z'} = 2.5\,\text{TeV}$
statistical prec.	65 %	79 %	66 %
ABCD method	39 %	35 %	39 %
t-tagging	below res.	12 %	below res.
W-tagging	51 %	42 %	44 %
b-tagging	12 %	12 %	below res.
JEC	below res.	12 %	14 %
other experimental	below res.	below res.	below res.
theory	below res.	below res.	below res.

theoretical calculations and other experimental techniques is kept small since they typically affect the events of the Top background similarly in all signal and sideband regions.

The analysis sensitivity is also limited by potential signal presence in the sidebands. Assuming the analysis would have been designed without considering the potential signal presence in the sideband regions, the signal presence in the sidebands would cause an overestimation of the background in the signal region. Consequently the fitted signal strength would be underestimated $\mu^{\text{fit}} < \mu^{\text{real}}$. This behavior has been verified by performing the MLE without considering the signal presence using simulated background data (signal hypothesis: $m_{Z'} = 2000\,\text{GeV}$, $m_T = 1200\,\text{GeV}$, BR(T → Wb/Zt/Ht) = 50 % / 25 % / 25 %). The fitted signal strength was 25 % smaller than the injected signal strength. Since, the calculation of cross-section limits is based on MLEs, also the estimated and observed limits would be impacted. In particular, without considering the presence of a potential signal presence, the analysis sensitivity would be overestimated by the same factor the fitted signal strength would have been underestimated.

However, in order to estimate the impact of the signal on the data-driven background estimation, the limit was determined with the MC signal contamination explicitly removed from the sidebands. The limits were re-determined and the impact was calculated as:

$$\frac{\Delta_{\text{sig. cont.}}\sigma_{\text{limit}}}{\sigma_{\text{limit}}} = \frac{\sigma_{\text{limit}} - \sigma_{\text{limit, no signal cont.}}}{\sigma_{\text{limit, all syst.}}}, \tag{5.17}$$

with $\sigma_{\text{limit, no signal cont.}}$ corresponding to the limit expectation without a signal presence in the sideband regions. The impact of the signal contamination has a very small dependence

on the signal kinematics. However, the signal contamination impact shows a dependence on the T-quark decay channel. For a T-quark decay $T \to Wb$, the presence of signal in the sideband regions reduces the analysis sensitivity by approximately 20 %. For a $T \to Ht$ T-quark decay, the signal presence in a sideband region reduces the analysis sensitivity by approximately 30 %. This dependency can be explained by the reduced discrimination power the N-subjettiness τ_{21} has for a Higgs boson jet, since the hadronic decay products of the boosted Higgs boson are not fully clustered into a single AK8 fat-jet.

These observations vindicate the integration of the bin-by-bin ABCD method into the final fit in order to correctly consider the impact of signal presence in the sidebands. Without these considerations, the estimated sensitivity would have been overestimated by up to 30 %.

5.7.3 Results and interpretation

After successfully commissioning the background estimation technique as well as the behavior of the final fit for different signal hypotheses, the $35.9\,\mathrm{fb}^{-1}$ of data recorded during the LHC Run II in 2016 were analyzed. MLEs were performed as described in Section 5.7.1. No significant excess in data above the SM background hypothesis is observed. Post-fit distributions for an exemplary signal hypothesis ($m_{Z'} = 2000\,\mathrm{GeV}$, $m_T = 1200\,\mathrm{GeV}$, $\mathrm{BR}(T \to Wb/Zt/Ht) = 50\,\%/25\,\%/25\,\%$) and a background-only hypothesis as well as a signal+background hypothesis are shown in Figure 5.24 and Figure 5.25. The corresponding pull plot is given in Figure 5.26. For the corresponding correlation matrices, the reader is referred to Figure A.25.

No excess that is not compatible with a background-only hypothesis is visible in any of the Z'-mass bins. However, there is a minor trend visible that causes a reduced number of observed events in the high $m(Z')$ range of the 2 b-tag category signal region and an increased number of observed events in the high $m(Z')$ range of the 1 b-tag category. The trend is also visualized by the nuisance parameter pulls shown in Figure 5.26. Such a trend can be explained by a residual correlation between the CSV_v2 output of the b-jet candidate and the N-subjettiness of the W-jet candidate, that was not correctly considered in the QCD-multijet MC simulations. With such a residual correlation present in data, the MLE favors a signal strength that would cause such residual correlation. The trend further results in a smaller fitted signal strength for signal hypotheses with a large Z'-mass ($m_{Z'} > 2000\,\mathrm{GeV}$), and a larger fitted signal strength for signal hypotheses with a small Z'-mass ($m_{Z'} < 2000\,\mathrm{GeV}$). However, such trends are covered by the shape uncertainties that are assigned to the ABCD method. Therefore, no signal is claimed.

Furthermore, no unexpected correlations between the nuisance parameters of the fit occur (see Figure A.25). The most dominant correlation is observed between the uncertainties on W-tagging, the ABCD rate uncertainties and the signal strength, as expected from the fit studies performed on Asimov data before.

In absence of a signal, limits were derived on the cross-section times branching ratio of all signal hypothesis. In order to calculate the expected limits, Asimov data were constructed similar to Section 5.7.1, but using the real data in the sideband regions B, C, D instead of MC predictions. This allows a more realistic estimation of the analysis sensitivity based on the data. The observed limits were then calculated based on the data in all signal and sideband regions. No major deviations between the expected and observed limit were found for any of the signal hypotheses. A detailed listing of the observed limits is given in Appendix A.5 of this thesis. Figure 5.27 and Figure 5.28 give a graphical representation of the observed limit as a function of $m_{Z'}$ and m_T.
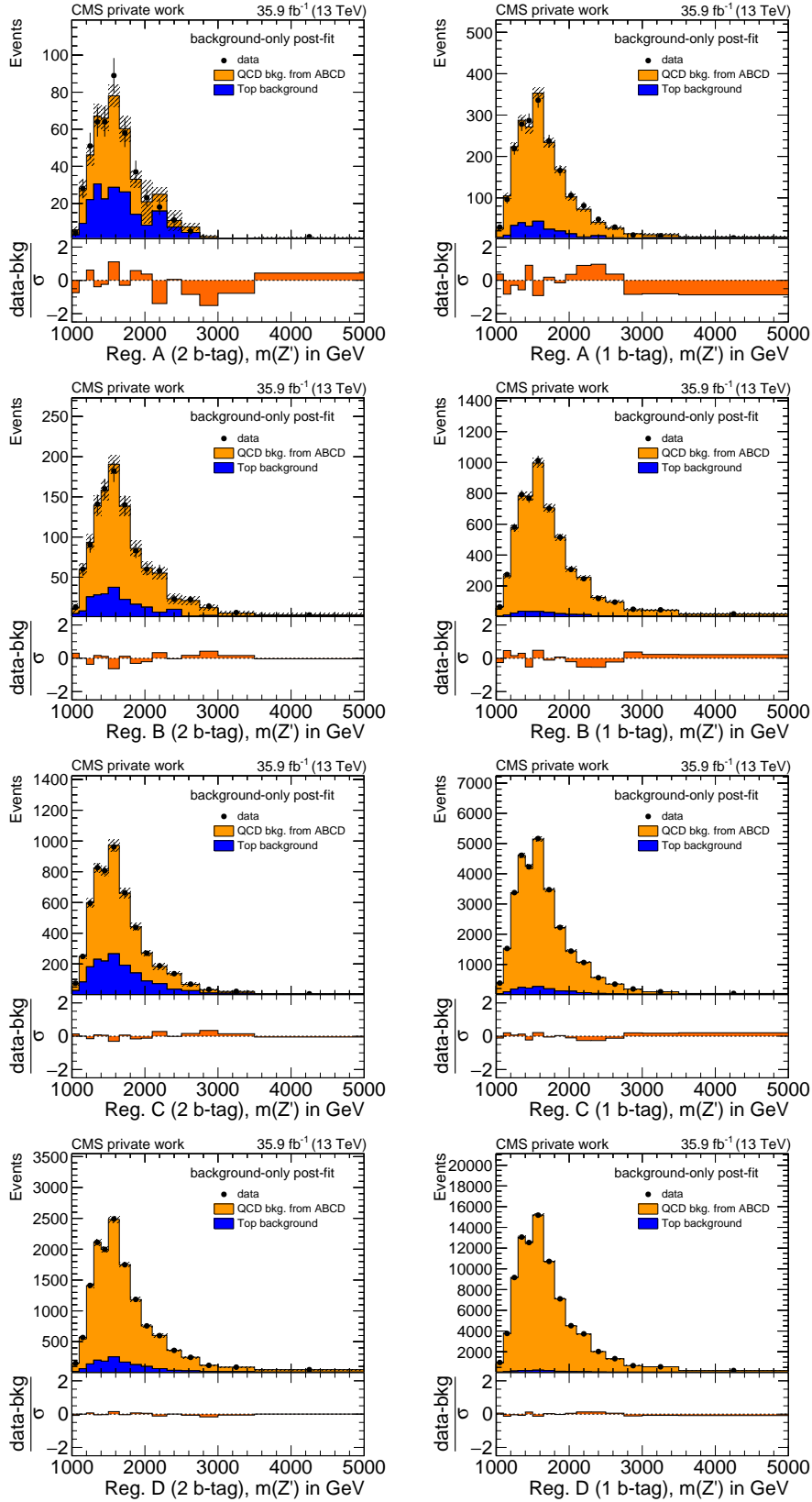
Figure 5.24: Background-only post-fit m(Z') of data. Data after a signal+background fit (signal hypothesis of $Z' \rightarrow Tt$ with $BR(T \rightarrow Wb/Zt/Ht) = 50\%/25\%/25\%$ and $m_{Z'} = 2000\,\text{GeV}$, $m_T = 1200\,\text{GeV}$). Left column: 2 b-tag category, right column: 1 b-tag category. From top to bottom: Region A, B, C, D.
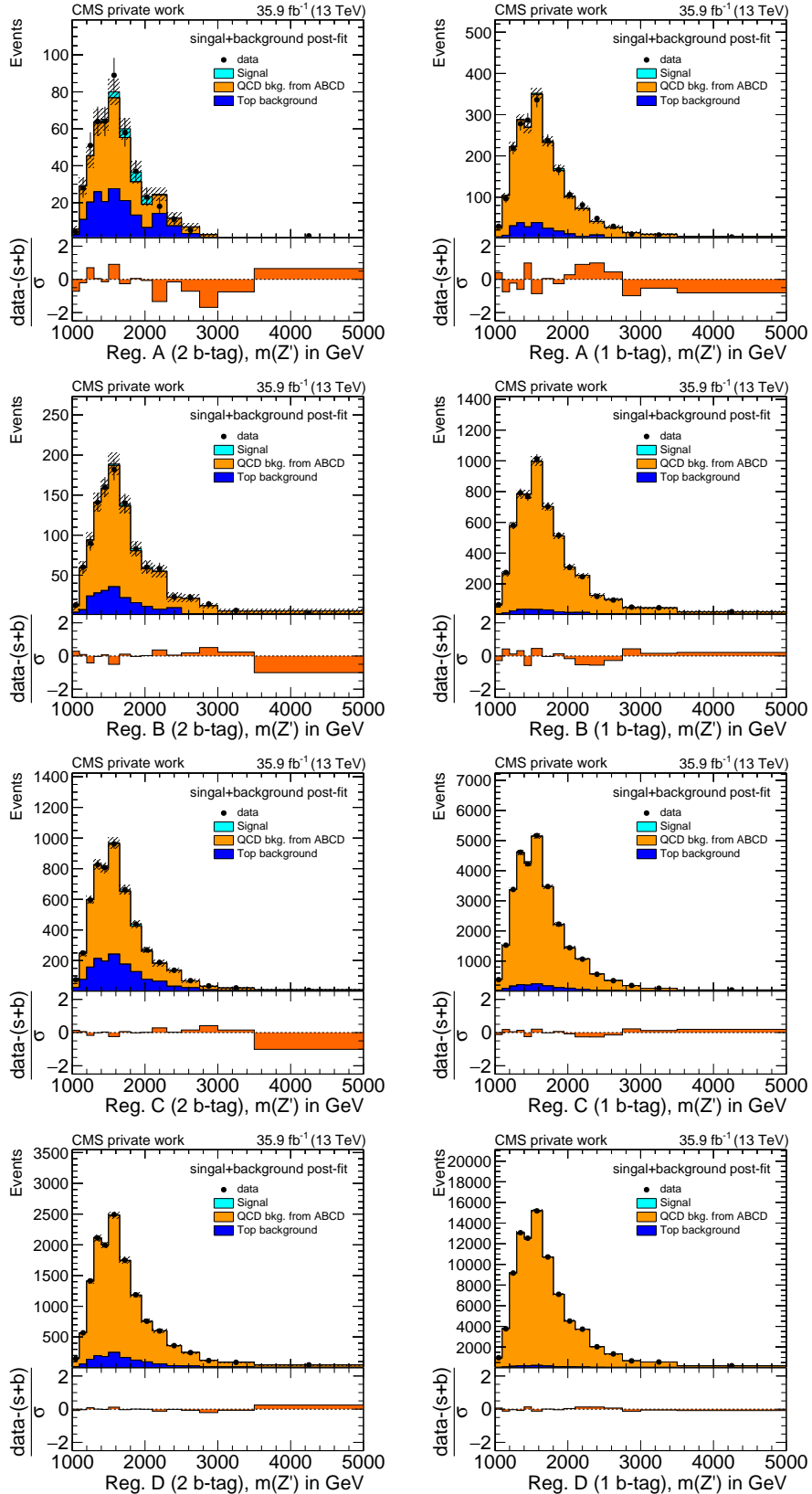
Figure 5.25: Signal+background post-fit m(Z') of data. Data after a signal+background fit (signal hypothesis of Z' → Tt with BR(T → Wb/Zt/Ht) = 50 %/25 %/25 % and $m_{Z'} = 2000$ GeV, $m_T = 1200$ GeV). Left column: 2 b-tag category, right column: 1 b-tag category. From top to bottom: Region A, B, C, D.
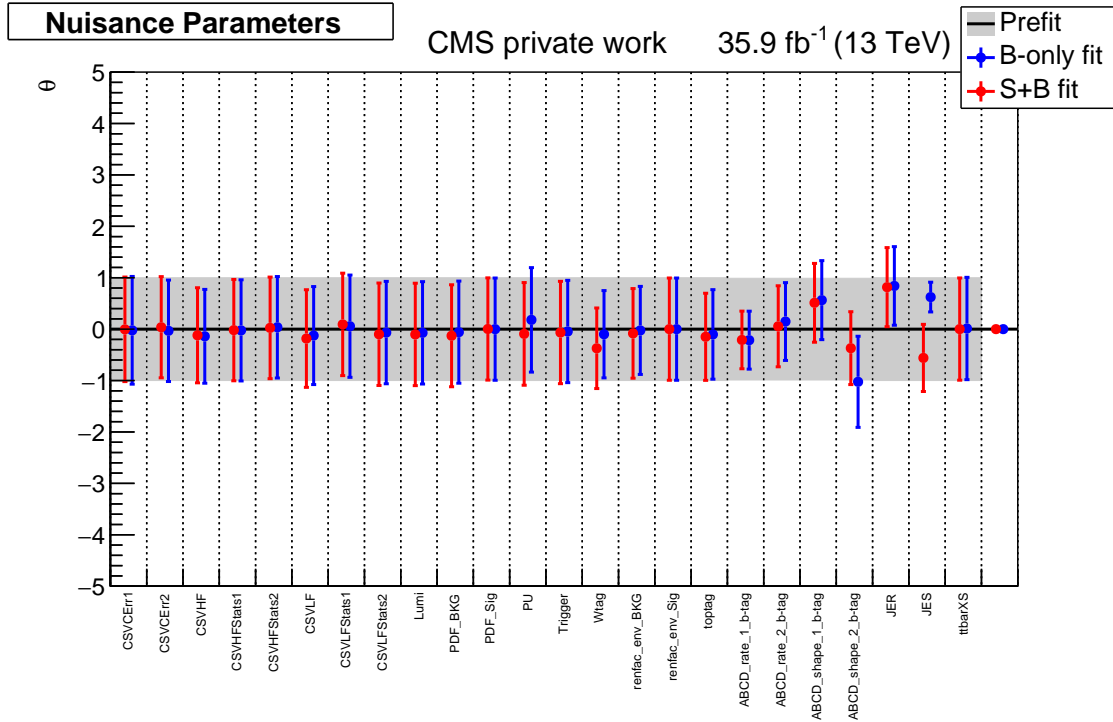
Figure 5.26: Nuisance parameter pulls of data. Difference between pre-fit and post-fit nuisance parameter values and their uncertainties relative to the pre-fit value for the maximum likelihood estimation of a signal hypothesis of $m_{Z'} = 2000\,\mathrm{GeV}$, $m_T = 1200\,\mathrm{GeV}$, $\mathrm{BR}(T \to Wb/Zt/Ht) = 50\,\%/25\,\%/25\,\%$.

Although no major deviations between the median expected and the observed limit were found, a trend can be observed when comparing the observed and the expected limit (see Appendix A.5). With increasing $m(Z')$, the observed limit decreases below the expected limit. This behavior can be assigned to the trend that was already observed in the MLEs and can be explained by residual correlations in QCD-multijet background contribution on data. However, the correlation is well within the uncertainties assigned to the ABCD method.

The analysis presented as part of this thesis is designed as a model independent search for HBRs decaying via VLQs. However, the results can be compared with and interpreted within a theoretical model. For example, the T-quark mass can be fixed to to a certain mass in order to derive one-dimensional cross-section times branching ratio limits as a function of $m(Z')$. Here, these cross-section limits are interpreted in two models: the little-Higgs model described in Section 2.2.3 for which a T-quark mass of $m_T = 1.2\,\mathrm{TeV}$ and a decay branching ratio of $\mathrm{BR}(T \to Wb/Zt/Ht) = 0/0.5/0.5$ is assumed, and the warped extra dimension model described in Section 2.2.4 for which a T-quark mass of $m_T = 1.3\,\mathrm{TeV}$ and a decay branching ratio of $\mathrm{BR}(T \to Wb/Zt/Ht) = 50\,\%/25\,\%/25\,\%$ [BCV12]. Since individual samples for both of these signal hypotheses are available, theory predictions on the cross-section are directly compared with the corresponding signal samples. Figure 5.29 shows the derived upper limits in comparison with theoretical predictions for those two models. The cross-section predictions are taken from [Usa17] and adapted to the assumed T-quark masses [BCV12].
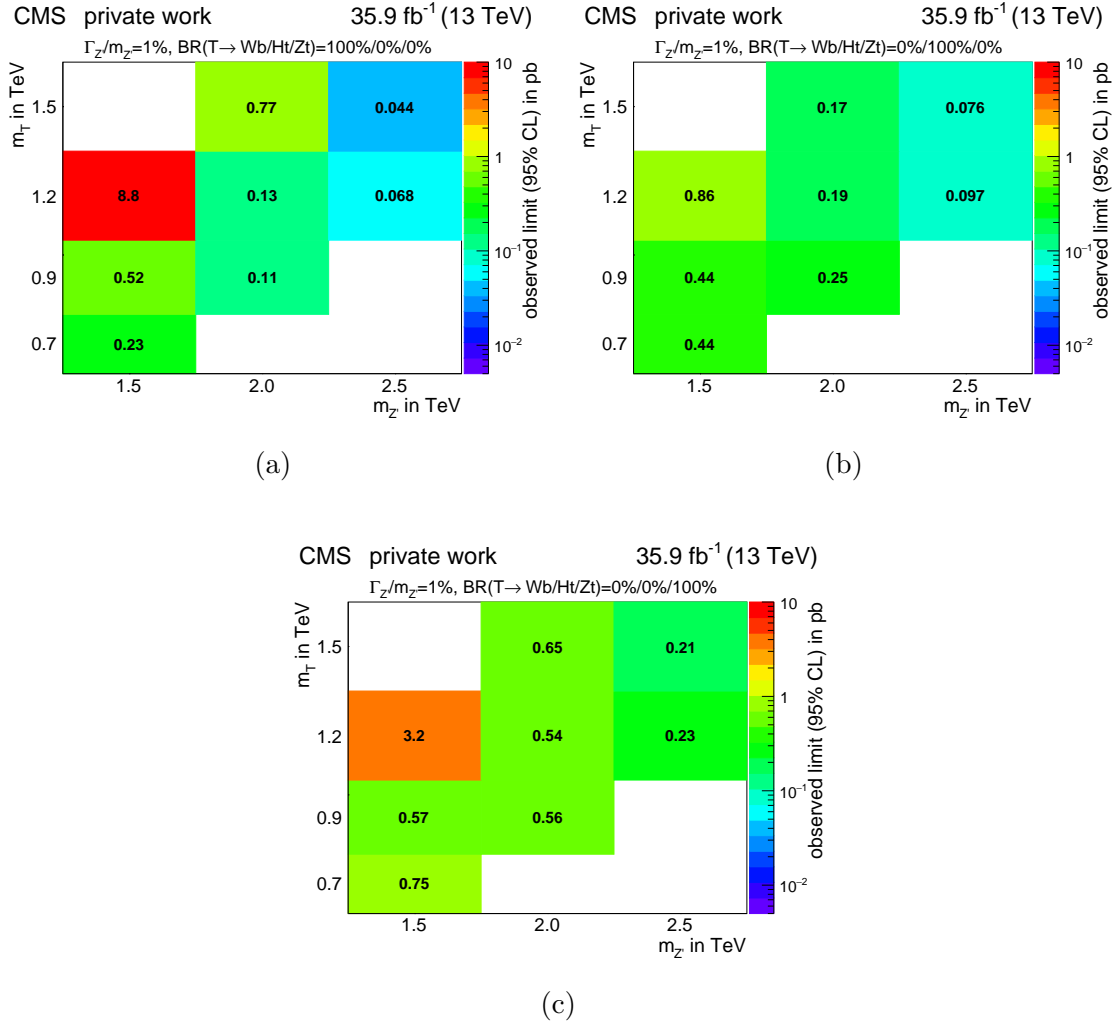
Figure 5.27: Observed limits on cross-section (little-Higgs model). Observed limits on the production cross-section times branching ratio at a 95 % CL as a function of the Z′-mass $m_{Z'}$ and the T-quark mass m_T. The limits are calculated using the signal events based on the little-Higgs model. (a): BR(T → Wb/Zt/Ht) = 100 %/0 %/0 %, (b): BR(T → Wb/Zt/Ht) = 0 %/100 %/0 %, (c): BR(T → Wb/Zt/Ht) = 0 %/0 %/100 %.
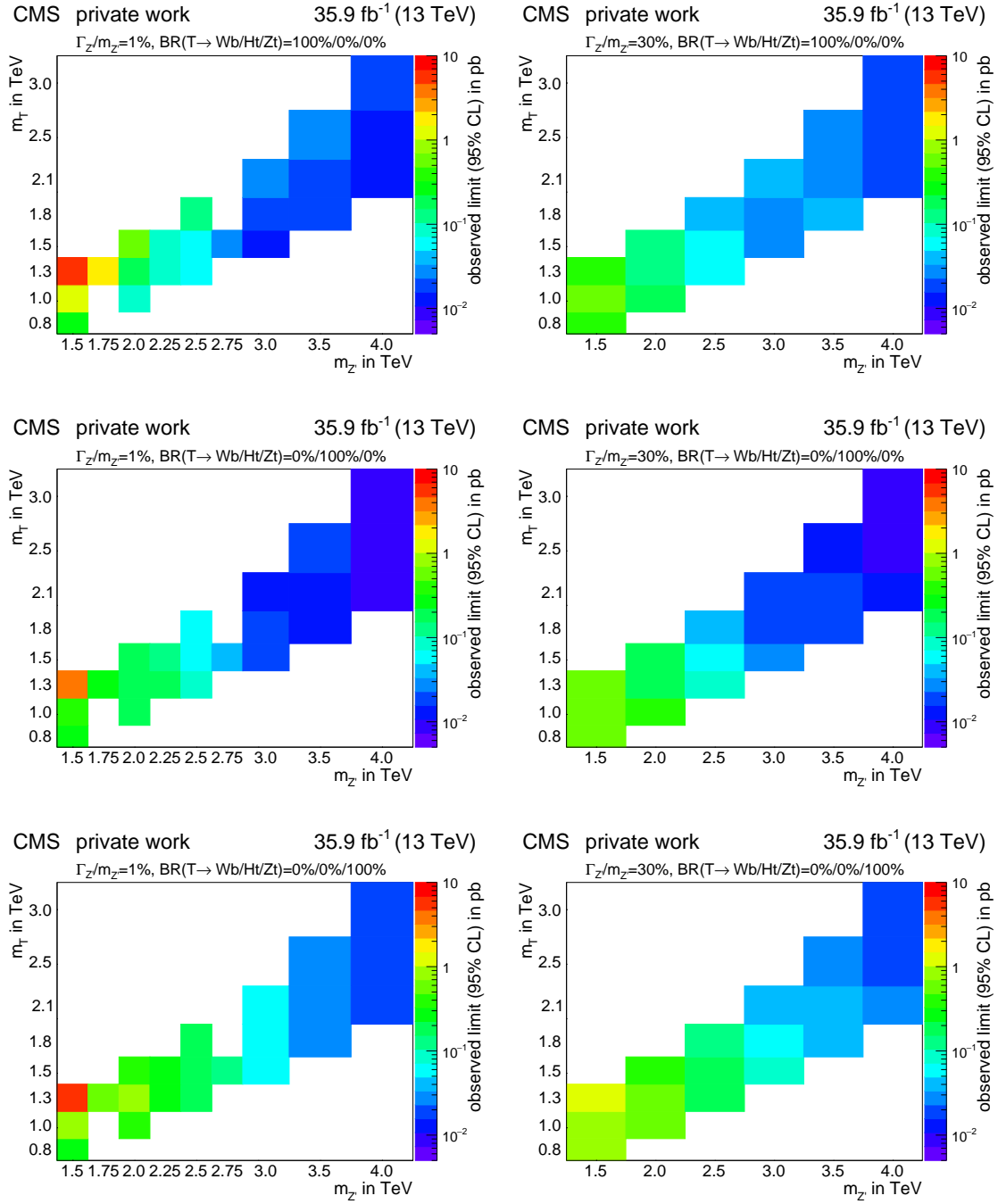
Figure 5.28: Observed limits on cross-section (warped extra-dimensions model). Observed limits on the production cross-section times branching ratio at a 95 % CL as a function of the Z'-mass $m_{Z'}$ and the T-quark mass m_T. The limits are calculated using the signal events based on the warped extra-dimensions model. Left: resonances of narrow width $\Gamma_{Z'}/m_{Z'} = 1\%$, Right: resonances of wide width $\Gamma_{Z'}/m_{Z'} = 30\%$ Top: BR(T $\rightarrow$ Wb/Zt/Ht) = 100 %/0 %/0 %, Center: BR(T $\rightarrow$ Wb/Zt/Ht) = 0 %/100 %/0 %, Bottom: BR(T $\rightarrow$ Wb/Zt/Ht) = 0 %/0 %/100 %.
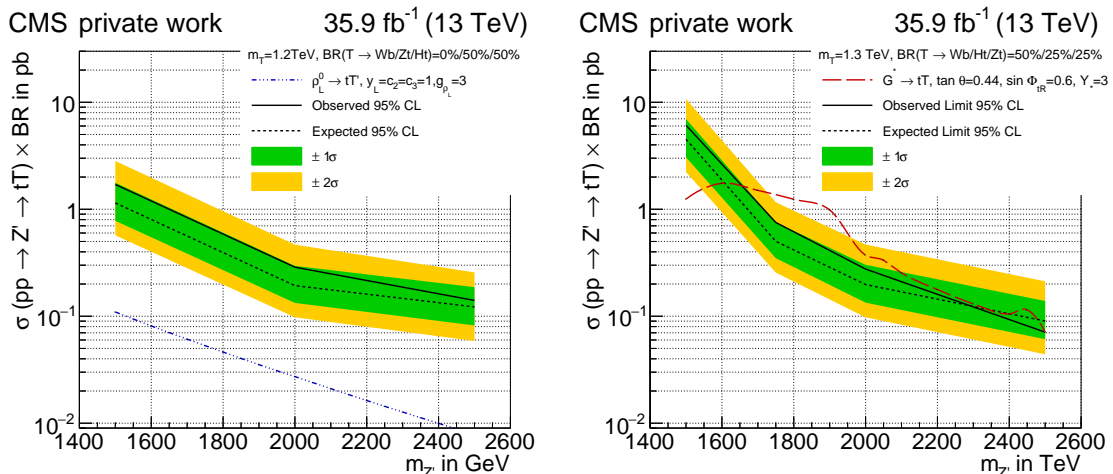
Figure 5.29: Limits in comparison with theory predictions. Expected and observed cross-section times branching ratio limits at a 95 % CL in comparison with theory predictions as a function of the Z'-mass. The T-quark mass and the T-quark decay branching ratio is fixed to benchmark values. Left: $m_T = 1200\,\text{GeV}$, BR(T $\rightarrow$ Wb/Zt/Ht) $= 0\,\%/50\,\%/50\,\%$. Right: $m_T = 1300\,\text{GeV}$, BR(T $\rightarrow$ Wb/Zt/Ht) $= 50\,\%/25\,\%/25\,\%$. The limits are compared with the cross-section prediction of a little-Higgs model $\rho_L^0 \rightarrow$ Tt (left) and a warped extra-dimension model $G^* \rightarrow$ Tt (right).

Three changes in the slope of the production cross-section predicted by the warped extra-dimensions model are visible. The first, located around a Z'-mass of approximately 1.5 TeV, can be explained by the Z' $\rightarrow$ Tt decay channel, investigated in this thesis, becoming kinematically possible. The second change is located around a Z'-mass of approximately 1.9 TeV and is caused by the opening of the decay into a $T_{5/3}\overline{T}_{5/3}$ pair. For resonance masses larger than $m_{Z'} = 1.9\,\text{TeV}$, the additional decay channel also results in an increased resonance width up to 30 %. The third change in the slope is located at around 2.5 TeV, where the decay channel into $T\overline{T}$ pairs starts to become available. In order to correctly consider the increased resonance width, the displayed cross-section limits above $m_{Z'} = 1.9\,\text{TeV}$ are calculated using the wide resonance width samples $\Gamma_{Z'}/m_{Z'} = 30\,\%$ and the cross-section limits below $m_{Z'} = 1.9\,\text{TeV}$ are calculated using the narrow resonance width samples $\Gamma_{Z'}/m_{Z'} = 1\,\%$. Based on the observed and estimated limits, the warped extra-dimension benchmark model with a T-quark mass of $m_T = 1.3\,\text{TeV}$ can be excluded in a parameter range of $m_{Z'} \approx 1650\,\text{GeV} - 2500\,\text{GeV}$.

The little-Higgs model, used as the second benchmark model of this analysis, is still beyond the sensitivity of the analysis by approximately one order of magnitude.

In comparison with the fully-hadronic analysis performed using the LHC run II data set of 2015, the average expected analysis sensitivity was improved by a factor of approximated 2.8 [Usa17]. In addition to the improvement in the analysis sensitivity, the robustness of background estimation has been improved by minimizing the dependence on MC-simulated QCD-multijet events. Furthermore, the analysis presented as part of this thesis is sensitive to resonances with a narrow and resonances with a wide decay width. Additional signal samples, based on a different benchmark model, allow probing an extended mass range with resonances masses up to 4 TeV.

The semi-leptonic analysis, performed using the LHC run II data set of 2016, shows an average expected sensitivity approximately ten times better than the average expected sensitivity of this analysis. This large difference in sensitivity can be explained by the almost QCD-multijet-free final state investigated by the semi-leptonic analysis. Without QCD-multijet background, no data-driven background estimation method is required, thus removing the impact of any uncertainties in the sideband regions on the final analysis sensitivity. However, when considering signals with $\mathrm{BR(T \to Wb/Zt/Ht)} = 100\,\%/0\,\%/0\,\%$ and signal hypotheses that result in a boosted top quark, the sensitivity of this analysis is better than the sensitivity of the semi-leptonic analysis by a factor of approximately 2.6. This way, the two analyses are complementary to each other and allow a wide probing of the parameter range predicted by models beyond the SM.

5.8 Summary and outlook

A model independent search for an HBR decaying via a top quark and a vector-like T quark in the all-hadronic final state has been presented. The analysis exploits the expected high transverse momenta of SM decay products created by such HBRs in order to reduce the background arising from QCD-multijet processes. Jet substructure techniques were used to identify jets created by hadronically decaying boosted heavy objects like top quarks or W bosons. Two categories of backgrounds contribute: processes producing top quarks, and QCD-multijet events. In order to correctly estimate the QCD-multijet background as independently of MC simulations as possible, a dedicated background estimation method was developed. The method was validated using simulated events as well as data control regions similar to the signal region. By implementing the background estimation method into the final statistical analysis, the impact of systematic uncertainties and the presence of a potential signal in the sideband regions is correctly propagated into the signal region.

No excess of the data above the SM background-only hypothesis was observed. Model independent upper limits on the production cross-sections times branching ratio were set as a function of the resonance mass, the mass of the vector-like T quark and its decay branching ratios. By comparing the observed upper limits with the cross-section predictions of different theoretical models, the analysis limits the parameter range of warped extra-dimension models. HBRs predicted by composite-Higgs models still lie beyond the achieved sensitivity.

Although the event selection of this analysis was optimized to provide a robust analysis sensitivity for a large variety of signal hypotheses, there is still room for improvement.

The data-driven QCD-multijet background estimation method was performed independently for the two analysis categories (2 b-tag and 1 b-tag). This approach was conservatively selected since the correlation between the QCD-multijet background within the two analysis categories is not trivial and difficult to study in MC simulations, because the it is unclear whether the correlations are correctly modeled. However, it appears promising to dedicate a study to the investigation of these connections in order to combine the data driven background estimations in the two analysis categories. This way, the good statistical precision in the 1 b-tag category could be used to constrain the uncertainties on the QCD-multijet background in the 2 b-tag category.

Furthermore, the analysis is designed to be orthogonal to another analysis that focuses on the same HBRs with a semi-leptonic final state [Ben18]. The analyses were designed to be complementary to each other, and are optimized to a different T-quark decay and final state. By combining the two analyses, not only the total signal efficiency could be increased, but also several of the systematic uncertainties could be constrained by the semi-leptonic

analysis. All in all, an increase in sensitivity in all signal hypotheses is expected by a combined analysis of the data.

So far, both analyses are mainly limited by the amount of data and the resulting statistical precision. However, with the expected increase in integrated luminosity provided by the LHC, as described in Section 3.4, the amount of data is expected to be increased by a factor of approximately ten until the end of 2022. This would drastically improve the statistical precision of the analysis. Assuming all other uncertainties would remain the same, the analysis sensitivity is expected to be improved by more than a factor of two based on the increased amount of data of an expected integrated luminosity of $300\,\mathrm{fb}^{-1}$.

In addition, the Phase I Upgrade of the CMS detector described in Section 3.4 and in Part II of this thesis, improves jet identification techniques such as b tagging, W tagging or t tagging. Furthermore, the usage of more elaborate jet identification algorithms is expected to increase the jet tagging performance. At this time, it is difficult to quantify the impact the Phase I Upgrade will have on analyses like this one. Qualitatively, any improvements of the jet identification techniques are not only expected to improve the signal efficiency but also to reduce the QCD-multijet background faking heavy boosted objects in the signal region. Additionally, the systematic uncertainties on jet identification techniques are expected to be reduced as well as the impact of signal presence in the sideband regions on the background estimation.

In summary, many of the uncertainties considered in this analysis are expected to be reduced within the upcoming years of data taking as well as by a combined statistical analysis. It is therefore expected that analyses like the one presented in this thesis will become sensitive to possible physics beyond the SM, or will be able to further constrain larger parts of the parameters space of physics beyond the SM.

The following second part of this thesis focuses on the Phase I Upgrade of the CMS pixel detector and the production of semiconductor pixel detector modules for the barrel region that form the backbone of a high data quality for the next years of data taking at the LHC.
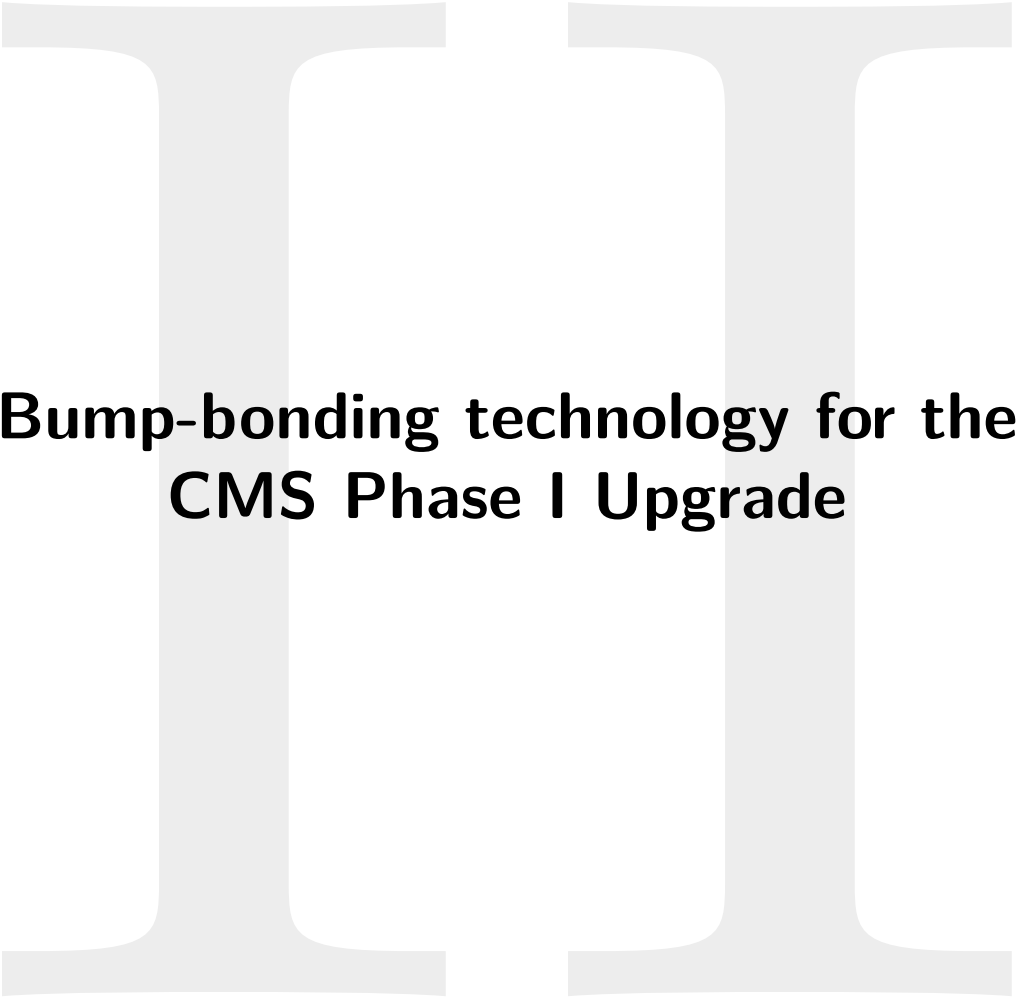
Bump-bonding technology for the CMS Phase I Upgrade

Outline

The CMS Phase I Upgrade, as mentioned in Section 3.4 of this thesis, is a big international enterprise carried out by many different institutions around the globe. The second part of this thesis is dedicated to the upgrade of the innermost detector component of the CMS experiment, the CMS pixel detector. After an introduction into the basics of semiconductors and their usage in particle physics. the bump bonding interconnection technology – a specific high density packaging technology – required for the production of detector modules at Karlsruhe Institute of Technology is described in more detail. Then, a more overview of the CMS Phase I Upgrade of the vertex detector is given. Finally, the production line at KIT to produce the new CMS pixel detector modules is described with a special focus on the so-called bare-module production and the bump bonding process developed and used at the Institute for Data Processing and Electronics.

6

Semiconductor pixel detectors for high-energy physics

This chapter is dedicated to the basics of semiconductor pixel detectors used in high-energy physics. The variety of designs for semiconductor pixel detectors exceeds the number of possible applications. Nevertheless, the intention is to give an idea about the commonalities in order to allow a better understanding of the CMS-specific designs tackled in chapter 7.

6.1 Basics of semiconductors

Semiconducting materials are known since the discovery of the rectifier effect observed in 1874. Major interest in these materials and their widespread use did not start until the invention of the transistor in 1947 by Bardeen and Brattain [BB48]. Nowadays, semiconductors are widely used and can be found in almost every electrical device. In most cases, they are used as basic logic devices and sensors but also as much more complex integrated circuits like Central Processing Units (CPUs), Graphics Processing Units (GPUs) and Field-Programmable Gate Arrays (FPGAs). A somehow special application of semiconductors is their usage as sensitive materials for the detection of ionizing particles. Macroscopically, semiconductors distinguish themselves from ordinary conductors by a lower electrical conductivity with a stronger temperature dependence than expected from the Drude model[1].

The most common semiconductor representative, due to its large availability and usage in micro-electronics, is silicon, wich is described in more details in the following sections.

6.1.1 Semiconductors in the energy-band model

A microscopic description of semiconductors is given by the energy band model. In this model, the periodicity of a solid state lattice is exploited to describe the possible energy states available to electrons in a periodic cell as continuous bands. The exact size and shape of the bands of possible electron energy eigenstates depends on material specific characteristics like the lattice structure and the internal structure of the atoms within a periodic cell. This allows a quantum mechanical description of the macroscopic structure

---

[1]The Drude model is a semi-classical model to describe the electrical conductivity of materials and its temperature-dependence based on the concept of quasi-free charge carriers frequently scattering on atoms in a periodic lattice [Dru00].

as a collection of available energy states without solving over $\mathcal{O}(N_{\mathrm{Avogadro}}) = \mathcal{O}(10^{23})$ differential equations. All energy bands have in common that, due to the periodic structure of the lattice, electrons have to fulfill the Bloch theorem. This prohibits certain energy states and causes the formation of gaps in between the energy bands. Since electrons are fermions, the energy eigenstates of the bands are filled from low energies to high energies following the Fermi-Dirac distribution [Dir26; Fer26; Kit04]

$$f(E) = \frac{1}{\exp\left(\frac{E-\mu}{\mathrm{k_B}T}\right) + 1}. \tag{6.1}$$

The distribution depends only on the temperature T and the material-specific chemical potential μ. At $T = 0$, the chemical potential μ equals the Fermi level E_{F}. The Fermi level is defined at $T = 0\,\mathrm{K}$ as the energy up to which all electron energy eigenstates are occupied. The Boltzmann constant is given by $\mathrm{k_B}$ and the particle energy is given by E. At temperatures $T > 0\,\mathrm{K}$ the occupation density is smeared around the chemical potential. The highest energy band occupied by electrons at $T = 0\,\mathrm{K}$ is called the valence band while the lowest empty energy band is called conduction band. In the energy-band model, the conductivity of a material is determined by the availability of unoccupied electron eigenstates and the energy needed to occupy these states. Since, in a solid state body, the absence of an electron within a crystal lattice can be considered as a hole – a charge carrier with equal charge but of opposite sing – all following considerations can be similarly applied to holes.

In case of conductors, the valence band and conduction band overlap and the Fermi level is situated within an energy band. This provides many possible unoccupied energy eigenstates to electrons and holes, even without any thermal excitation. This fits the macroscopic observation of good conductivity, even at low temperatures.

For insulators, the Fermi level is situated within a large band gap between the valence band and the conduction band ($E_{\mathrm{gap}} > 3\,\mathrm{eV}$ [GM12]), allowing no charge carriers to contribute to the electrical conductivity without a large external excitation.

Semiconductors on the other hand are somehow similar to insulators. The Fermi level is also situated within the energy gap in between conduction and valence band, but the energy gap of semiconductors ($0.1\,\mathrm{eV} < E_{\mathrm{gap}} < 3\,\mathrm{eV}$) is not as far as in insulators [Kit04]. While no energy states are available at low temperature, every increase in the temperature drastically increases the number of available energy eigenstates according to the Fermi-Dirac distribution (see Equation (6.1)). An illustration of the different energy bands in case of conductors, insulators and semiconductors is given in Figure 6.1. In general, any kind of excitation of an electron from the valence into the conduction band has to conserve energy as well as momentum. For this reason, the excitation energy does not only depend on the size of the energy gap but also on the shape of the valence and conduction band. This allows further categorization into direct and indirect semiconductors as shown in Figure 6.1. For direct semiconductors, the excitation does not change the momentum of the electron/hole, ergo a maximum of the valence band and a minimum of the conduction band can be found at the same wave number k. For indirect semiconductors, the maximum of the valence band and the minimum of the conduction band show different wave numbers. This means, to excite an electron from the valence band to the conduction band, either an excitation energy larger than the energy gap has to be raised, or momentum has to be added or removed from the excitation (e.g. by a phonon), making the excitation process much less probable at low temperatures. These excitations are possible for direct semiconductors, though less probable. Silicon is a typical representative of indirect semiconductors with
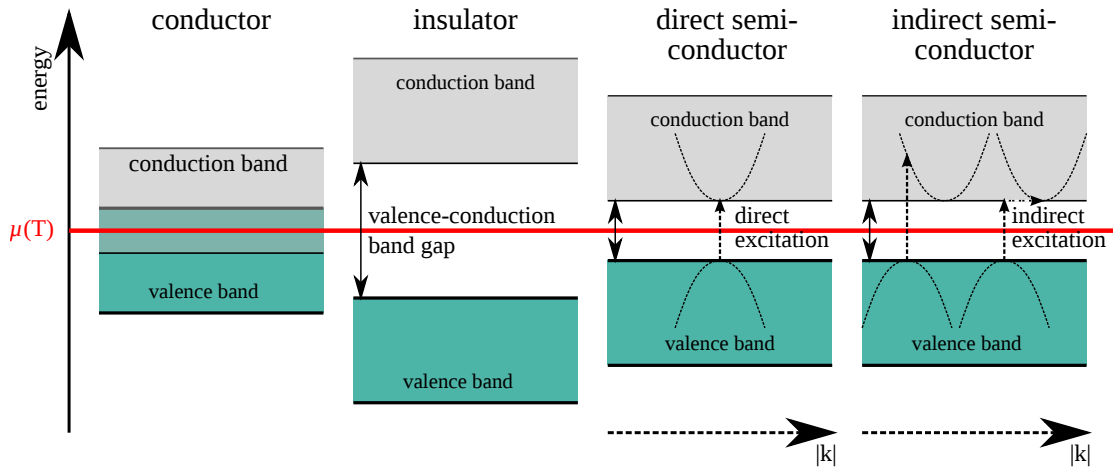
Figure 6.1: Energy bands for different types of material. The different energy bands and Fermi energies are shown for conductors (left), insulators (center left), direct semiconductors (center right) and indirect semiconductors (right). The size of the valence-conduction band gap and the relative position of the valence and conduction bands in reciprocal space defines the conductivity of the material.

an effective excitation energy of $\Delta E_{\text{excite}} = 3.67\,\text{eV}$ [Par12] and an energy gap of only $\Delta E_{\text{gap}} = 1.12\,\text{eV}$ [Lut07]. So far, the illustrations of the energy band structure were strongly simplified. Figure 6.2 shows a more realistic representation of the silicon energy band structure.

It should be mentioned here that also a large number of semiconductors with more than one atom within the unit cell exist. For simplicity reasons and with the focus of this thesis set on silicon pixel detectors, the following sections are limited to silicon.

6.1.2 Doping of semiconductors and pn-junction

In the context of semiconductors, doping typically describes the intentional contamination of a semiconducting material with the purpose of modifying its electrical properties. This process changes semiconductors from intrinsic to extrinsic. In case of silicon (member of the forth main group of elements), inserting atoms of the third main group (acceptors) into its bulk removes electrons from the lattice structure. In the energy band model, this creates additional free energy states above the valence band of silicon (acceptor states). The Fermi level is reduced by the unoccupied acceptor states to a value between the valence band and the acceptor states. Electrons from the valence band can be easily excited into the acceptor states and contribute to the electrical conductivity, even at room temperature. Semiconductors that are doped in such a way are called n-doped semiconductors.

Analogously, the insertion of atoms from the fifth main group (donors) into a semiconducting bulk from the forth main group, adds electrons to the lattice. In the energy band model, this creates additional occupied electron states below the conduction band (donor states). The Fermi level is increased to a value between the conduction band and the donor states. The electrons occupying the donor states can be thermally excited into the conduction band at room temperature already. Semiconductors doped in such a way are called p-doped semiconductors. Figure 6.3 illustrates this behavior. By the concentration of impurities inside the bulk, the size of these effects can be tuned.
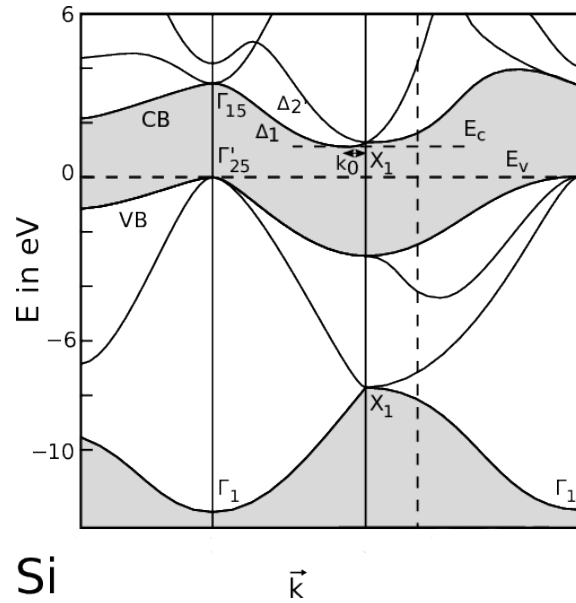
Figure 6.2: Reduced zone scheme of silicon. The shape of electron energy eigenstate as a function of the electron momentum (for quasi-free particle $\vec{k} = \vec{p}/\hbar$). Energy bands are depicted in white, and energy gaps are depicted in grey. Since silicon is an indirect semiconductor, the maximum in the valence band (E_V) and the minimum in the conduction band (E_C) can be found at different electron momenta. This results in an effective excitation energy (3.6 eV) distinctively larger than the energy band gap (1.12 eV). Alternatively, additional momentum can be added to the excitation process by a phonon, resulting in a much less likely "diagonal" transition (modified from [CC74]).
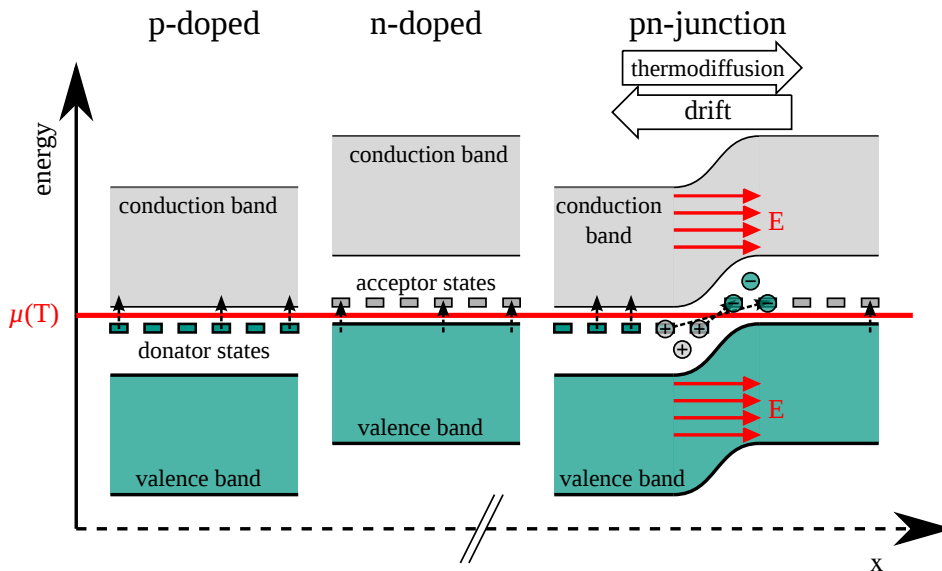
Figure 6.3: Extrinisic semiconductors and the pn-junction. Insertion of additional energy states into the band gap by doping for n-doped (left) and p-doped (center) extrinsic semiconductors. Also, a pn-junction with its depletion region without any external voltage is shown (right). The electric field inside a pn-junction is illustrated in red. The x-axis corresponds to the spatial separation of the p-doped and n-doped parts of a pn-junction.

The combination of p-doped and n-doped semiconductors allows the creation of many basic electrical components as diodes or transistors, which again can be combined into more complex structures like CPUs, etc. In this section, a short look at the two most basic component, from which more complex devices can be created, is taken.

When contacting p-doped and n-doped semiconductors, important boundary effects become relevant and a pn-junction is created. Electrons from the donor states of the n-doped region thermally diffuse into the p-doped region and occupy the free acceptor states. The chemical potentials of the p-doped and n-doped regions equalize, which causes a deformation of the energy bands. At the boundary between the p-doped and n-doped material, a region without free charge carriers forms. This region is typically called depletion zone. The growth of the depletion zone is limited by the formation of an electric field created by the ionized immovable atoms nuclei which are still fixed by the lattice structure and cannot diffuse the same way as their electrons. Figure 6.3 illustrates the thermal diffusion and the formation of the depleted zone within a pn-junction.

When applying an external voltage to the pn-junction it shows a characteristic behavior depending on the voltage polarity.

- Reverse bias: If the positive node is connected to the n-doped side and the negative node is connected to the p-doped side, the external voltage causes an additional charge separation, increasing the depletion zone as well as the electric field. Since the depletion zone is increased, no free charge carriers are available and current flow is suppressed. Only a small current flow is observed when operating the pn-junction in reverse bias. However, at high reverse bias voltages, a breakthrough occurs, the depletion zone vanishes and the pn-junction becomes conductive.

- Forward bias: On the other hand, if the negative node is connected to the n-doped side and the positive node is connected to the p-doped side, the voltage reduces the energy levels of the energy bands. This causes electrons from the donor states to drift into the p-doped region reducing and finally removing the depletion zone. Without the depletion zone, current can flow through the pn-junction.

The behavior of a pn-junction with reverse bias and forward bias applied is illustrated in Figure 6.4. By exploiting boundary effects like the pn-junction, many different basic components can be created. The most basic one is the diode, which consists of a single pn-junction. The central part of a diode is the depletion zone within the pn-junction. Its thickness ($d_{\text{depl.}}$) depends on material specific parameters as well as the donor and acceptor concentrations and the voltage applied. It can be estimated as

$$d_{\text{depl.}} = \sqrt{\frac{2\epsilon_0 \epsilon_r}{e} \cdot \left(\frac{1}{N_D} + \frac{1}{N_A} \right) \cdot |V_{\text{eq}} - V_{\text{bias}}|} \tag{6.2}$$

where N_A and N_D are the doping concentration of donors and acceptors in the n-doped and p-doped regions. The applied voltage is given as V_{bias} and the voltage due to thermal diffusion of the electrons is given as V_{eq}. ϵ_r is the relative permittivity of the material, ϵ_0 is the vacuum permittivity and e is the electron charge [Lut07].

6.2 Pixelated semiconductors as vertex detectors

Semiconductor particle detectors are widely used in many different fields of physics. Depending on the particle type that needs to be detected, the needed energy range, readout frequency, precision, etc., the detector designs vary strongly. In the context of this thesis,
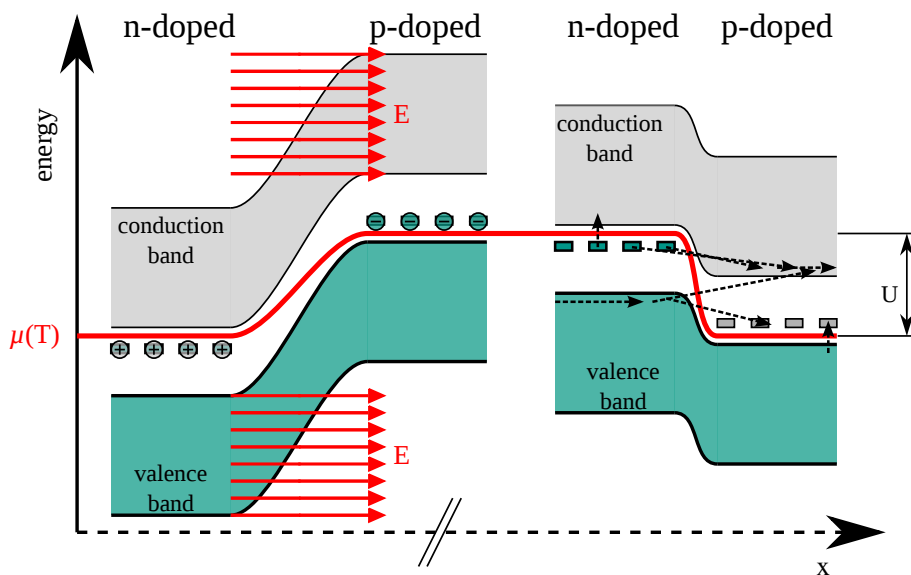
(a)
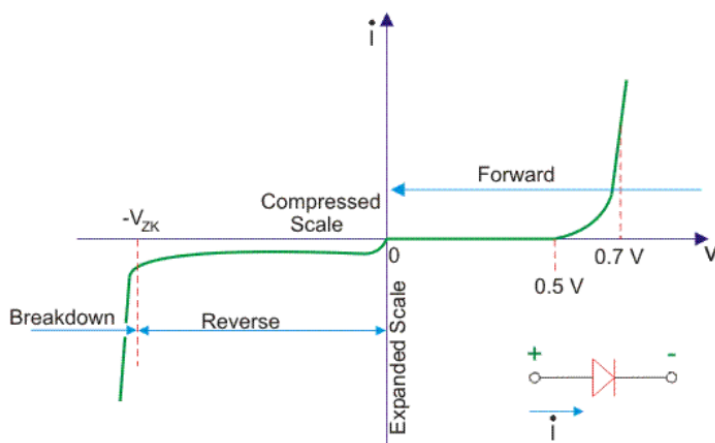
(b)

Figure 6.4: Behavior of a pn-junction with an external voltage applied. Depending on the polarity of applied voltage, the depletion zone is increased (a left, reverse bias) or reduced and removed (a right, forward bias). The electric field inside a pn-junction is illustrated in red. Furthermore the IV-behavior of a pn-junction is illustrated (b) [Ele18].

focus is set on semiconductor particle detectors for tracking ionizing particles in high energy physics experiments. Special focus is set on pixelated vertex detectors.

Semiconductor particle detectors have been used since the 1970s [Lut07] and have almost replaced gaseous particle detectors as tracking detectors in today's hadron collider experiments. Compared to gaseous tracking detectors, their main advantages are a higher density of states and lower excitation energies ($E_{\text{ionization}}(\text{Ne}) \approx 36\,\text{eV}$, $E_{\text{excitation}}(\text{Si}) \approx 3.67\,\text{eV}$ [Sha98; Par12]) resulting in a better signal-to-noise Ratio (SNR) at the front-end electronics, and a faster charge collection, allowing higher readout frequencies ($40\,\text{MHz}$ at the LHC). Furthermore, a strong industrial sector provides frequent technology improvements and allows close co-operations with industry. Of course semiconductors also come with challenges that need to be tackled, such as: radiation damage on the lattice structure that reduce the charge collection efficiency, large power consumption due to leakage current that requires cooling, which results in an increased material budget.

6.2.1 Interaction of ionizing charged particles with matter

A very basic impression of the way the different particles created at the LHC interact with the different parts of the detector has been given in Section 3.3. Particles can interact with matter in many different ways, creating particle showers as well as just some light ionization of the material. However, tracking sub-detector systems are typically designed as lightweight structures suppressing the formation of particle showers. In the context of this thesis, it is therefore sufficient to focus on electro-magnetic interactions of charged high-energy particles with the semiconducting sensitive layers of the inner tracker.

Swift heavy charged particles lose energy via different processes. At low particle momenta, energy loss is dominated by ionization. At high particle momenta, radiative energy loss processes such as Bremsstrahlung emission become dominant. The energy loss by ionization can be quantitatively described by the Bethe equation. It depends on the particle's mass, energy and charge as well as the material [Par12].

$$-\frac{dE}{dx}_{\text{ion}} = \underbrace{4\pi N_A r_e c^2}_{\text{constants}} \cdot \frac{Z}{A} \cdot \frac{z^2}{\beta^2} \cdot \left[\frac{1}{2} \cdot \ln\left(2m_e c^2 \cdot \frac{\beta^2 \gamma^2 T_{\text{max}}}{I^2} \right) - \beta^2 - \frac{\delta(\beta\gamma)}{2} - \frac{C}{Z}(\beta\gamma) \right]. \quad (6.3)$$

N_A is the Avogadro number, r_e the classical electron radius, m_e the electron mass and c the speed of light. The maximum momentum transferred to an electron is given by T_{max}. The relative velocity and Lorentz factor of the particle are described by $\beta = \frac{v}{c}$ and $\gamma = \left(1 - \beta^2 \right)^{-\frac{1}{2}}$, while its charge is given by z in units of the elementary charge. The target material is characterized by its atomic number Z, its atomic mass A and the mean excitation energy I. At low particle energies, additional material specific corrections due to the atomic structure of the target atoms $\frac{C}{Z}(\beta\gamma)$ need to be taken into account. At high energies, additional corrections due to polarization effects and density corrections $\delta(\beta\gamma)$ have to be considered. The energy loss by radiation is dominated by Bremsstrahlung emission and can be roughly estimated as proportional to the particle energy

$$-\frac{dE}{dx}_{\text{rad}} \propto \frac{r_e^2 Z^2 N_A}{A} E. \quad (6.4)$$

Again, N_A is the Avogadro number, r_e the classical electron radius, Z the atomic number and A the atomic mass of the target material. Figure 6.5 shows the stopping power/energy loss of a heavy charged particle as a function of the particle momentum, at the example of an anti-muon in copper. For a momentum range of $\beta\gamma = 10^0 - 10^1$, heavy charged particles can be considered minimum ionizing particles (MIPs).
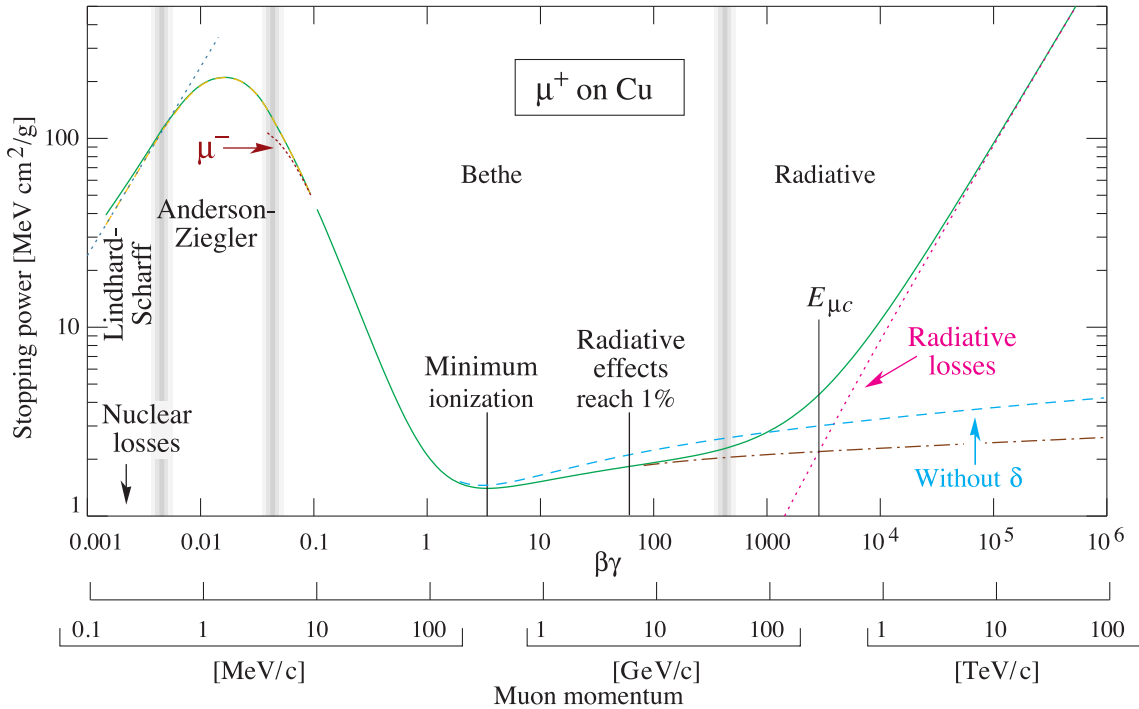
Figure 6.5: Energy loss of heavy charged particles in material. Shown is the stopping power of material on a heavy charged particle at the example of an anti-muon in copper, as well as the dominant energy loss processes. At $\beta\gamma = 1 - 10$ a particle can be considered as minimum ionizing [Par12].

Light charged particles like electrons and positrons on the other hand, cannot be described by the Bethe equation. Since they are much lighter, radiation losses are more prominent at lower energies. Also, they are indistinguishable from the electrons in the material, allowing additional scattering and annihilation processes. The energy range in which they can be considered as minimal ionizing as well as their energy deposition inside a target material strongly depends on the target material. Figure 6.6 shows the energy loss of light particles as a function of the particle energy with the example of lead as target material.

In the application of semiconductor tracking detectors, the sensitive detector material is typically arranged in thin layers of several hundred micrometers. In such thin layers of silicon, the energy loss of charged particles is characterized by statistical fluctuations of the ionization process. The energy loss can be approximately described by an asymmetric distribution called Landau distribution. According to the Landau distribution, ionizing particles have an increased probability compared to a Gaussian distribution to deposit lots of energy. This asymmetric behavior can be explained by the creation of secondary electrons. Secondary electrons are created by hard scattering process of a charged particle and deposit energy in addition to the charged particle itself [Lan44]. Figure 6.7 shows the Landau distributed energy loss of 500 MeV pions for silicon targets of different thickness.

Since the approach of high energy physics experiments is to fully reconstruct all particles created in the event, a tracking detector system has to be capable of detecting all particles generated in this event. The energy deposit by a MIP is 390 eV/μm. Within a silicon semiconductor a MIP is expected to generate on average 108 electron-hole pairs/μm but most probably only creates 73 electron-hole pairs/μm.
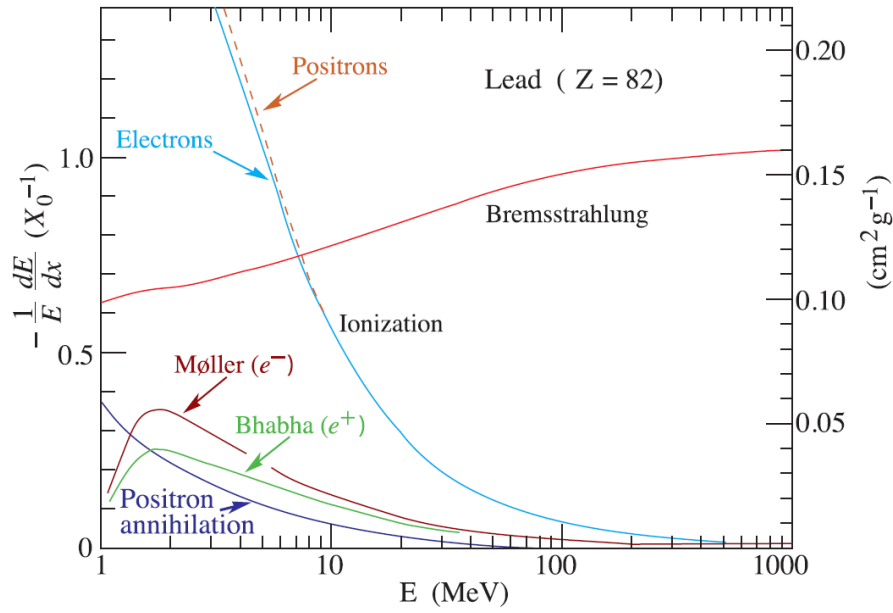
Figure 6.6: Energy loss of light charged particles in material. Shown is the the energy loss of light particles (electrons and positrons) per radiation length as a function of particle energy. Lead is chosen as the target material. It is visible that energy losses due to bremsstrahlung become dominant at medium particle energies of tens of MeV already [Par12].
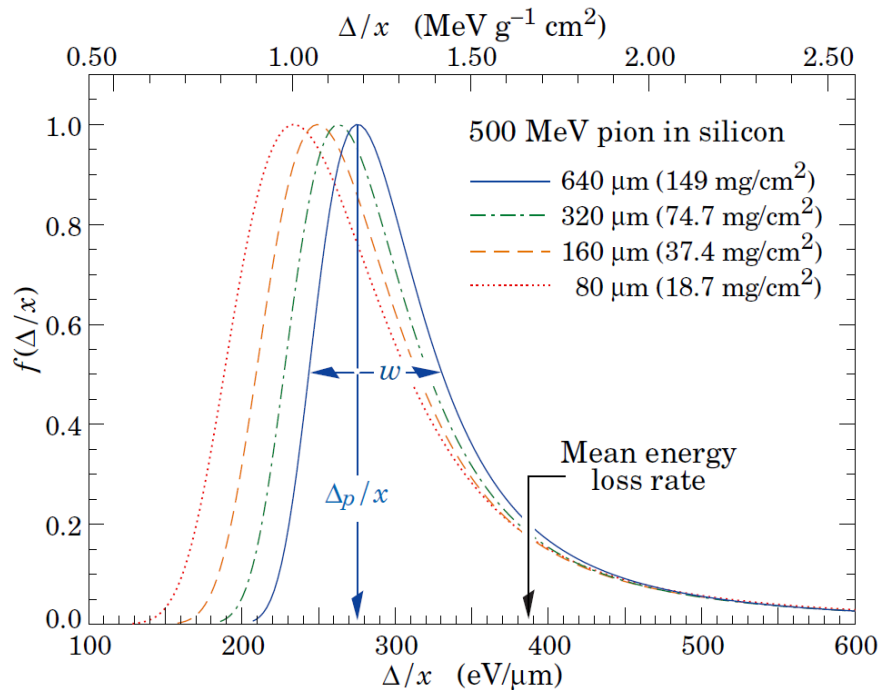
Figure 6.7: Energy loss distribution in thin silicon layers. Normalized energy loss distribution of 500 MeV pions traversing silicon layers of different thickness. The most probable value is situated at approximately two-thirds of the mean energy loss [Par12].

6.2.2 Semiconductors as detectors for ionizing particles

To achieve maximum SNR, the ideal material for particle tracking detectors should provide:

- small excitation energies and a high density of excitable states in order to provide maximum signal output;

- minimal density of free charge carriers to reduce the noise arising from leakage current;

- fast charge collection and electrical readout to allow the construction of very fast detector systems;

- sufficient radiation hardness to withstand the high particle flux in a high energy physics experiment;

- availability in large numbers;

- easy segmentation of the material.

Many of these requirements can be fulfilled by silicon. Still, the number of free charge carriers at room temperature ($\approx 10^9$) is several times higher than the number of electron-hole pairs generated by an ionizing particle ($\approx 10^4$), making it impossible to distinguish signal from noise [Har17]. A possible approach to tackle this issue is to cool the semiconducting material to cryogenic temperatures. Thereby, thermal excitations get reduced, allowing a better SNR. Though suited for some cryogenic astro-particle physics applications, this approach cannot be used in the environment of a high energy physics detector. Another approach is the usage of a pn-junction as sensitive detector material, drastically reducing the number of free charge carriers at room temperature. As mentioned in Section 6.1.2, a pn-junction generates a depletion zone without charge carriers. Operating the pn-junction in reverse bias mode increases the depletion zone to a region with a high density of non-free charge carriers that can be excited and read out, while reducing the noise from thermal excitation.

When an ionizing particle traverses the depletion zone, electrons from the valence band get excited into the conduction band all along the particle track. The strong electric field within the depletion zone separates electrons and holes from each other. The drift of electrons or holes within the electric field can be read out as a signal current.

In silicon, depending on the material resistivity, a typical depletion zone without any bias voltage applied has a thickness up to a few micro meters, which would result in only a few electron-hole pairs. To increase the thickness of the depletion zone, a thick layer of slightly doped semiconducting material is inserted in-between the highly doped p-type and the n-type regions. This way, Equation (6.2) is modified to:

$$d_{\text{depl.}} = \sqrt{\frac{2\epsilon_0\epsilon_r}{e} \cdot \left(\frac{1}{N_{\text{D,eff}}} + \frac{1}{N_{\text{A,eff}}}\right) \cdot |V_{\text{eq}} - V_{\text{bias}}|}, \tag{6.5}$$

with $N_{\text{D,eff}}$ and $N_{\text{A,eff}}$ as effective donor and acceptor doping concentrations. The effective donor and acceptor concentrations are calculated as a combination of all donor and acceptor doping concentrations in the p-doped, n-doped, and slightly doped or intrinsic intermediate region. As a result, the depletion zone quickly grows within the intrinsic or slightly doped intermediate region, event at low bias voltages applied. The increase of the depletion zone by the insertion of a slightly doped region and the generation of electron-hole pairs within
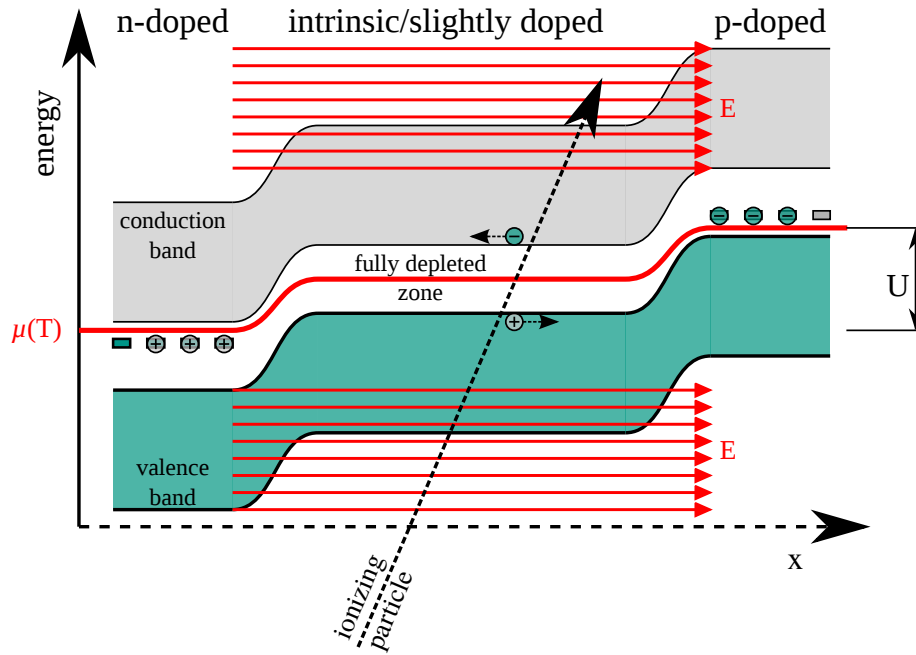
Figure 6.8: pin-junctions in particle detectors. Sensitive area of a semiconductor particle detector illustrated in the energy band model. Electron-hole pairs generated within the depleted pn-junction can be read out as signal current. The electric field inside a pn-junction is illustrated in red.

the depletion region is illustrated in Figure 6.8. In high energy physics, typical sensor thicknesses are between $200\,\mu m - 500\,\mu m$. Typical bias voltages to work under depletion of the while sensor bulk material are in the range of $100\,V - 1000\,V$. The charge deposited by MIPs in such silicon sensors ranges from 16000 to 40000 electrons [Tin11].

Thanks to a large industry, the implementation of several pn-junctions into a single bulk of silicon is easily possible. This way, a large variety of implementations of different segmentations is allowed to gain information about the position at which an ionizing particle traversed the sensor structure. In this thesis, the focus shall be set on the implementation of pixelated structures that allow optimal spatial resolution in two dimensions. Figure 6.9 shows the working principle of a position sensitive silicon particle detector.

A key parameter to a good spatial resolution is the distance between two readout electrodes, also called pitch. For pixelated detectors, the pitch is determined by the pixel size. A basic geometric estimation of the resolution, assuming a binary pixel readout, is given by

$$\sigma = \frac{\text{pitch}}{\sqrt{12}}. \tag{6.6}$$

According to the Shockley-Ramo theorem, when an ionizing particle generates charge carriers along its trajectory within a detector, the charge carriers are spread over an area larger than the typical pitch [Sho38; Ram39]. In addition, when operated within a magnetic field, charge carriers experience an additional drift orthogonal to the electric field insiede the sensor. The angle between the electric field and the drift direction is called Lorentz angle. More information on the Lorentz angle can be found in [Nür14]. Although the spread of charge carriers reduces the SNR in every readout channel, it also allows the calculation
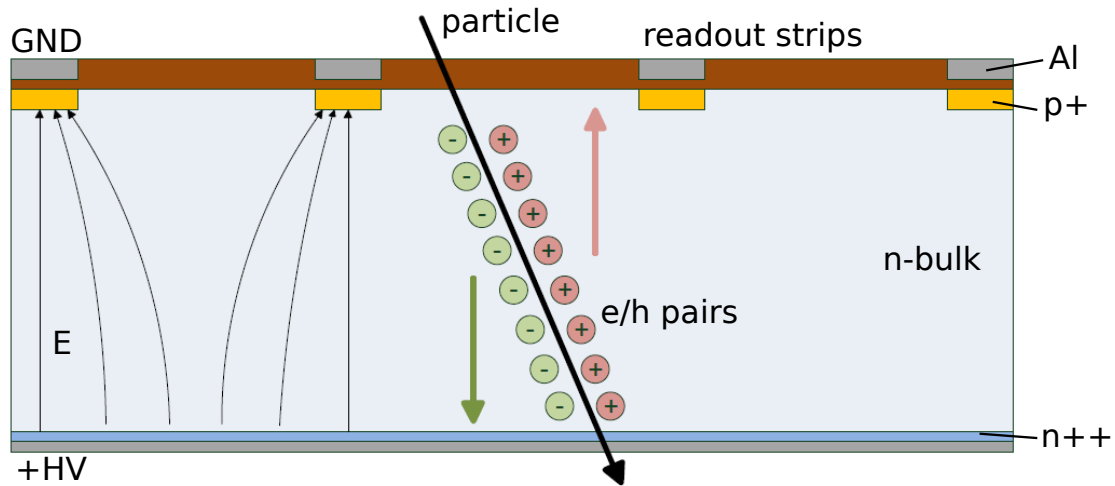
Figure 6.9: Silicon sensor structure for particle tracking. The figure shows a basic design of a position-sensitive particle detector. Several pn-junctions are implemented in a single bulk between the p-doped implants (yellow) and the n-doped bulk silicon (light blue). By applying a high voltage from the backplane, the bulk material is depleted from free charge-carriers. Ionizing particles generate electron-hole pairs that are separated by the electric field inside the bulk and read out by the electronics (modified from [Ebe13]).

of the particle position via the center-of-gravity method. The detector resolution then follows

$$\sigma \propto \frac{\text{pitch}}{\text{SNR}}. \tag{6.7}$$

In case of the CMS pixel detector, the usage of this method improved the detector resolution approximately by a factor of 2.5 [CMS12a].

6.2.3 Readout electronics for semiconductor particle detectors

In order to give a basic impression on the requirements of the readout electronics for silicon detectors, this section is dedicated to give a short introduction to the basic concepts. Furthermore, some specific requirements for the operation of CMS are considered.

In general, typical detector readout electronics need to provide four basic process stages: signal amplification, signal shaping, signal digitization, and storing and transmitting the signal [Spi05]. A basic process flow is illustrated in Figure 6.10 and typically looks as follows:

1. A pre-amplification stage is used to increase the input amplitude and convert the charge into voltage for further processing. The characteristics of the pre-amplification stage need to be carefully designed in order to match the sensor characteristics.

2. To improve the SNR, a shaper stage is used. The basic concept here is to exploit as much information about the expected signal shape as possible in order to suppress background from stochastic noise. Though design and complexity of the shaper stage strongly depend on the application and its requirements, a commonality is the usage of charge integrator stages in combination with frequency band filters, such as
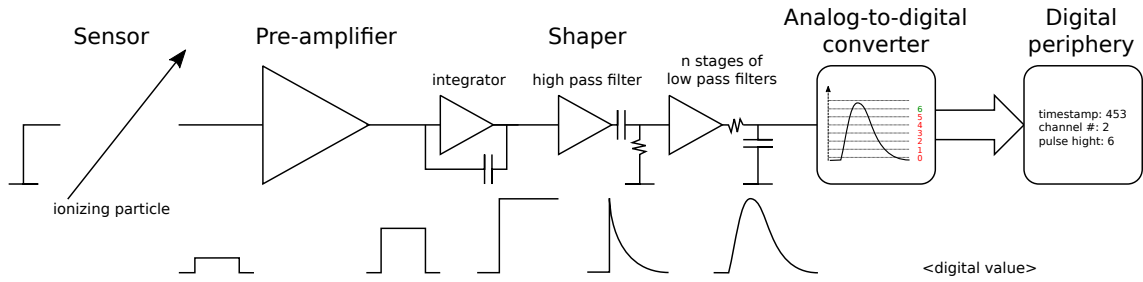
Figure 6.10: Signal process flow of front-end electronics. Shown are the first stages of signal processing for a typical semiconductor particle detector. Below the process stages, the expected signal shape is shown. A charge signal induced by an ionizing particle is amplified by the preamplifier first. Before digitization of the signal, several steps of shaping are performed to improve the SNR. Finally the pulse-height of the signal is digitized and forwarded to the periphery for further processing (adapted from [Spi05]).

semi-gaussian filters with a single differential stage and several orders of integrator stages.

3. The signal is digitized by an Analog-Digital Converter (ADC). ADCs are common in almost every industrial process. For the application of semiconductor particle detectors, flash ADCs are typically used, since they can provide sufficient speed to provide the required readout rate. Again, the characteristics of the ADC are typically designed to fit the expected signal shape and readout rate.

4. The signal is transmitted to some digital periphery for further processing or stored for later use. At this stage, additional information like the channel number or a time stamp is added.

Nowadays, all these stages can be realized by a fast combination of ADCs and FPGAs. This allows to first digitize the signal and perform all shaping processes on the digitized data using FPGAs. Although such a work-flow provides high flexibility in laboratory setups, it is not feasible for high-energy physics applications in large detectors, where all the functions need to be implement in a minimum space. For such applications, the signal processing needs to be implemented into custom front-end ASICs in order to reduce the bandwidth required by the analog signals [Cos18; Spi05].

In high energy physics, signal sensitive pn-junction and front-end electronics are typically implemented in a hybrid solution with a passive silicon sensor die and an active readout chip. This kind of implementation has the advantage of allowing independent developments of the sensor material and the readout electronics while considering the different requirements for the semiconductor material independent from each other. On the downside, hybrid implementation require more material as well as cost intensive interconnection technologies to connect every sensitive channel of the sensor to the corresponding front-end electronics of the readout chip. Pixelated semiconductor particle detectors require the bump bonding interconnection technology that is at the center of this part of this thesis. An introduction to the bump bonding interconnection technology is given in Section 6.3. Figure 6.11 illustrates the implementation of a pixelated semiconductor particle detector in a hybrid solution for a single pixel cell connected via a bump bond to the corresponding front-end electronics. More detailed insight into the bump bonding
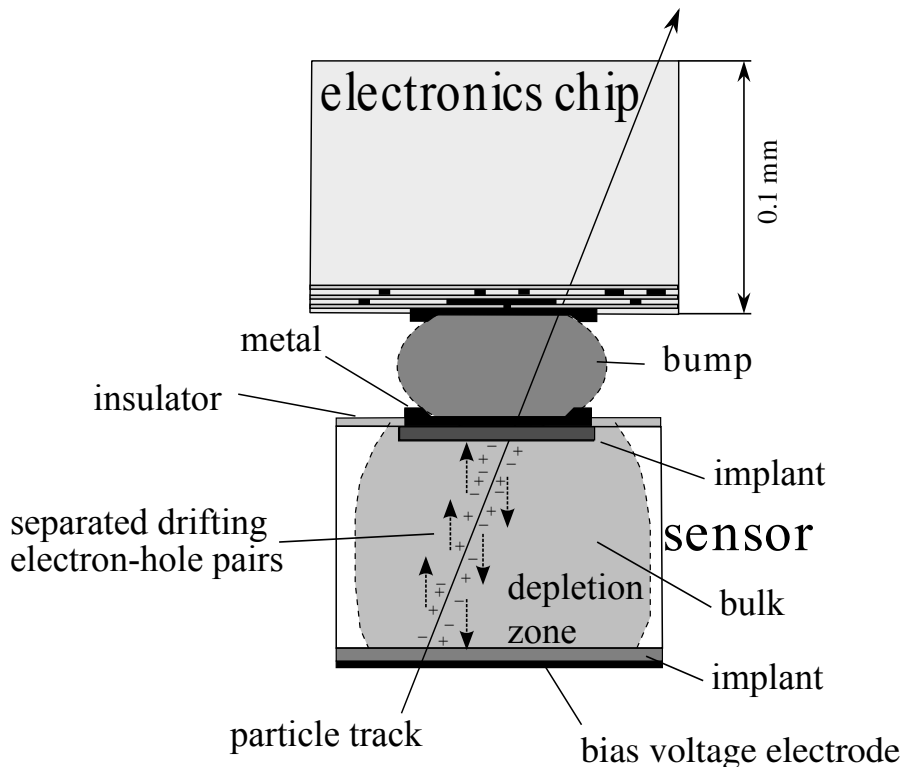
Figure 6.11: Hybrid solution of pixelated semiconductor particle detector. A possible hybrid solution for the integration of a pixelated semiconductor particle detector and the frontend electronics is shown. Every single pixel cell is connected to its corresponding readout electronics via a bump bond interconnection (modified from [Ros+06]).

interconnection technology used for the CMS Phase I Upgrade is given in Section 8. It should be mentioned here that a lot of effort is currently put into the development of monolithic implementations of sensitive silicon and readout electronics into a single silicon die (for more information see e.g. [Per+15]). Still, hybrid solutions are standard so far.

6.3 Bump bonding interconnection technology

Rapid developments in micro-electronics towards smaller structures and more interconnection lines, increasingly demand the usage of high density interconnect technologies to connect micro electronic devices like FPGAs or ASICs. Also in high energy physics, pixelated silicon vertex detectors require a high interconnection density, while keeping the length of the connection as low as possible in order to keep the inductance and capacitance of the interconnection as low as possible and to minimize noise and crosstalk. These requirements favor the use of the bump bonding interconnection technology over the standard wire bonding interconnection technology. This section will give an overview of the bump bonding technology and its possible implementations.

Although the focus of this part of the thesis lies on the pixel module production for the CMS Phase I Upgrade, KIT is very active in the design and qualification of new semiconductor particle detectors. The research and development of these future semicon-

1) Prepare first chip
2) Place bumps
3) Flip chip
4) Align to second chip
5) Precision placement
6) Bonding by thermocompression
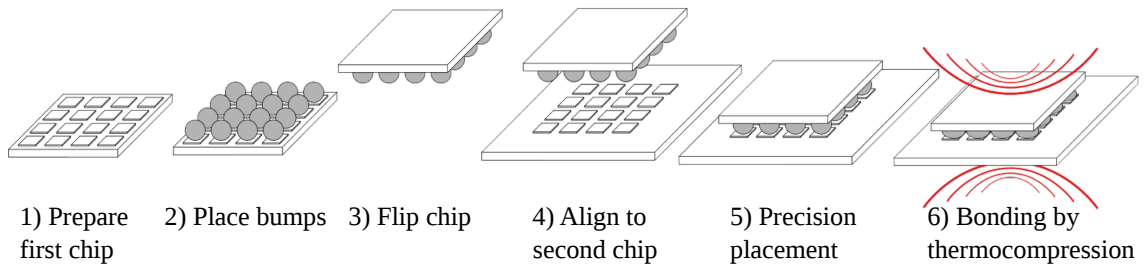
Figure 6.12: Working principle of the bump bonding interconnection technology. A schematic of basic working principle of the bump bonding interconnection technology is shown. After the bump deposition on the chip surface, it is flipped, and aligned to the contact areas of a second chip. By thermo-compression, a mechanical and electrical connection between the corresponding contact areas is established (modified from [Uni14]).

ductor particle detectors requires dedicated bump bonding interconnection technologies, tailored to the requirements of the individual development processes. As part of this thesis, several bump bonding interconnection technologies have been developed, including a bump bonding technology that can be performed at relatively low process temperatures $< 80\,^\circ\mathrm{C}$. Since a detailed description of these bump bonding interconnection technologies would go beyond the constraints of this thesis, the reader is referred to [Fre17; Sch15], where this technology was used.

6.3.1 Basic working principle

The basic concept of the bump bonding interconnection technology is to establish many short vertical solder joints in between two chips providing a both mechanical and electrical connection[2]. The process is typically performed in several steps that are illustrated in Figure 6.12. These steps can be categorized into two main subprocesses:

1. **bump deposition** (also called bumping, pictured in step 1 and step 2 of Figure 6.12): The chip is prepared for processing and the bump material is deposited on the contact areas. Depending on the bumping technology, this process can also include pre-processing of the contact areas or post-processing of the bumps to provide a wettable contact area and a good bump shape. A short overview over some of the most common bump deposition technologies will be given in Section 6.3.2.

2. **flip-chip bonding** (steps 3-6 in Figure 6.12): One of the chips is flipped and positioned above the sensor or another chip. After precise x-, y-alignment of the chips the bumps are brought in contact with the corresponding contact area. The connection is typically established by thermo-compression causing a metal diffusion between the bump material and the metals of the contact area. Depending on the technology, an ultrasonic movement can be added to cause addition frictional heat at the contact area. This kind of bonding is called thermo-ultrasonic bonding.

After establishing a mechanical and electrical connection, further improvement of the inter-metallic connection can be achieved by heating the assembly above the solder melting temperature. Such a process is called *reflow*. In addition, an under-fill material can be used to provide further mechanical stability to the assembly.

---

[2]The connections are typically established orthogonally to the surface of the silicon dice, though current developments show an increasing interest in die-to-edge bonding, allowing easy 3D integrations.

6.3.2 Bump deposition technologies

There are many different bump bonding interconnection technologies currently available to the high-energy physics community. Sharing the basic concept, most of them mainly differ in the bump material and the process used to deposit the bump material. Common bump materials are: indium solder (In), tin-lead solder (SnPb), tin-silver copper solder (SnAgCu), gold (Au) or copper (Cu). This section will shortly introduce a small selection of the most common bumping technologies. A more detailed and more complete description can be found at [Kud14; Hei12; BCL07; Bla+15; Cas+16].

Most bumping technologies are designed and implemented as large industrial photo-lithographic processes with complex setups, allowing cheap simultaneous processing of many wafers. All processes with a lithographic bump deposition have in common that the standard top metal layers (typically Al) do not provide a wettable surface for solders. To provide a wettable seed surface and to ensure a good inter-metallic connection, additional metal layer stacks need to deposited before the bump material. These layers are called Under Bump Metallization (UBM) [LTF01]. Depending on the bumping material, UBM materials and layer thicknesses need to be adapted.

However, the development of new devices often requires more flexible bump bonding interconnection technologies, providing short setup-times and the possibility to process single dies.

Bump deposition by metal evaporation   The standard bump deposition process is the Controlled Collapse Chip Connection (C4) process, developed by International Business Machines Corporation (IBM) almost 50 years ago [Mil69]. It can be used to deposit large diameter bumps ($> 100\,\mu$m) and is primarily used for Ball Grid Array (BGA) applications with large distances between the bumps (pitch $> 250\,\mu$m). For the C4-process, a molybdenum mask is created to cover the complete wafer surface, except the area to be bumped. All metallic layers of the UBM are deposited onto the wafer through the holes of the molybdenum by metal evaporation. After the UBM deposition, the bump material is evaporated through the mask. In the following reflow, the material is heated above the melting temperature of the bump material increasing the quality of the inter-metallic connection between UBM and bump material. Furthermore, the surface tension of the liquefied bumps creates a more spherical bump shape. A typical bump material for the C4-process is SnPb ($5\,\%/95\,\%$) with a phase transition temperature of $340\,°$C, but also other materials are common [Ros+06].

An improvement of the C4 process was achieved by the Paul Scherrer Institute (PSI), by using indium as a bump material and UV patterned photo-resist masks instead of molybdenum masks. This allows the bumping of structures with much smaller pitch ($< 100\,\mu$m). Similar to the C4 process, UBM and bump material are evaporated through the holes in the mask and a reflow reshapes the bumps into spheres ($T_{\text{melting}}) \approx 160\,°$C). Also the original CMS pixel detector has been built using the indium bumping process. Due to its softness, indium provides interconnections with a mechanical strength of only $\approx 2\,$mN/bump [Bro+06]. Within the last years, a lot of effort has been put into developing alternative bumping technologies that can provide similar minimal pitches but larger mechanical strength.

Plating bump deposition   Bump deposition by plating can be performed electro-less as well as electro-chemical. The electroplating bumping process relies on bump deposition by an electro-chemical separation within a solvent. The electro-chemical deposition on the substrate surface is induced by a voltage applied to the chip, requiring a conductive
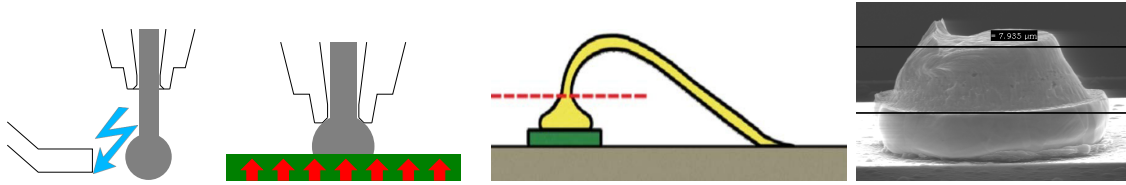
Figure 6.13: Stud bumping process. The basic concept of a stud bumping process is shown. After creating a metal ball at the end of a bonding wire (left), a capillary brings it into contact with the substrate. After establishing a connection via thermo-ultrasonic bonding (left center), the capillary shears the bonding wire right above the stud bump (right center) (adapted from [Jor03; Jun14; Kud14]).

substrate. The material deposition can be limited to specific contact areas by the usage of lithographic masks [Huf+03]. Electroless plating bump deposition, on the other hand, does not require any conductive substrates, since the material deposition is based on chemical red-ox reactions inside a solvent. The reactions cause a plating on all uncovered metal surfaces [BCL07]. In general, electroplating allows fast and well controllable material depositions but requires more complex setups. Electro-less plating is mainly used for the deposition of micro-bumps and UBMs since the material deposition is very slow and hard to control. Both processes have been used for the KIT production line of the Phase I Upgrade of the CMS pixel detector and are discussed in more details in Section 8.

Stud bumping The stud bumping technology shall be mentioned here as common representative of non-lithographic bumping technologies. This technology had been developed from the ball wire bonding process and sequentially places bumps on a substrate, chip or wafer. To do so, a small ball is created at the end of a thin metal wire by an electric discharge. By thermo-ultrasonic bonding, an inter-metallic connection to the substrate surface is created and the wire is sheared of right above the bump. The stud bump can be placed on top of aluminum pads as well as on top of a pre-existing suitable UBM. Figure 6.13 shows the basic working principle of the stud bumping process. Typical bump materials are gold and copper, resulting in typical bump diameters of approximately 60 μm [Tri+10]. To make this bumping technology suitable for high energy physics applications, KIT has improved the bumping process during the last years, resulting in minimum bump diameters of 30 μm. A detailed description of the process development can be found in [Kud14]. The stud bumping technology is most advantageous for R & D and low-quantity productions, since it does not require any lithographic process or UBM, resulting in low costs and short setup time. Furthermore, it allows the processing of many different substrates on chip as well as wafer level, providing high flexibility. Since gold or copper are used as bump material, the interconnection provides high mechanical strength, as well as excellent conductivity, while being resistant to most chemicals. However, with a bump deposition rate of approximately 20 bumps per second, the stud bumping process is not suitable for productions that require the deposition of several million bumps.

7

Phase I Upgrade of the CMS pixel detector

In experimental particle physics, the sensitivity of an analysis does not only depend on the experimental analysis methods and the amount of data but also on the tracking resolution ensured by a high performance of the experimental setup. By continuous improvements, the instantaneous luminosity of the LHC is expected to increase to $2 \cdot 10^{34} \text{cm}^{-2}\text{s}^{-1}$, twice its design luminosity. These upgrades are expected to greatly increase the sensitivity of measurements limited by the statistical precision due to the limited amount of the data – like the analysis presented in part I of this thesis. However, these upgrades also impose high requirements on the detector systems. To retain a good data quality, the pixel detector was upgraded as part of the CMS Phase I Upgrade in the EYETS in early 2017.

This section is dedicated to the detector upgrades that were performed on the CMS pixel detector as part of the CMS Phase I Upgrade. First, an overview on the performance and performance limitations of the original CMS pixel detector is given, motivating the upgrade (Section 7.1). Next the upgrades and changes in the detector design are explained (Section 7.2). Special focus is set on the design and functionality of barrel pixel modules, since their construction is a central part of this thesis (Section 7.3).

7.1 Performance limitation of the CMS pixel detector

During its operation from 2010 to 2016, the original CMS pixel detector has performed very well, collecting over $70 \, \text{fb}^{-1}$ of data [CMS17i]. During this period, on average more than 95% of the readout channels of the pixel detector have been active and have been used for high-level trigger decisions as well as vertex reconstruction, b-tagging, τ-tagging, electron/photon-discrimination and muon reconstruction. Measurements showed an average single hit efficiency $> 99\%$ of working channels during the whole period of data taking. The impact parameter resolution was measured to be $10 \, \mu\text{m} - 250 \, \mu\text{m}$ depending on particle type, transverse momentum and pseudorapidity [CMS14b].

Nevertheless, the measurements also show a decrease in the hit efficiency with increasing particle rates due to an increased number of proton-proton interactions in single bunch crossing (pileup) as shown in Figure 7.1. Especially for events with more than 40 primary vertices, the single hit efficiency further decreases, especially in the innermost detector layer. The observed inefficiencies were caused by dynamic inefficiencies due to the limited internal buffer size of the readout chip that stores hit data until the trigger decision, as well as by temporary losses of modules. sect An additional decrease in the tracking efficiency was observed for $|\eta| > 1.2$ in comparison with the central detector region [CMS17j; CMS14b]. This behavior can be explained by the additional amount of material, also referred to as *material budget*, arising from the service structures (mounting structures, cooling system,
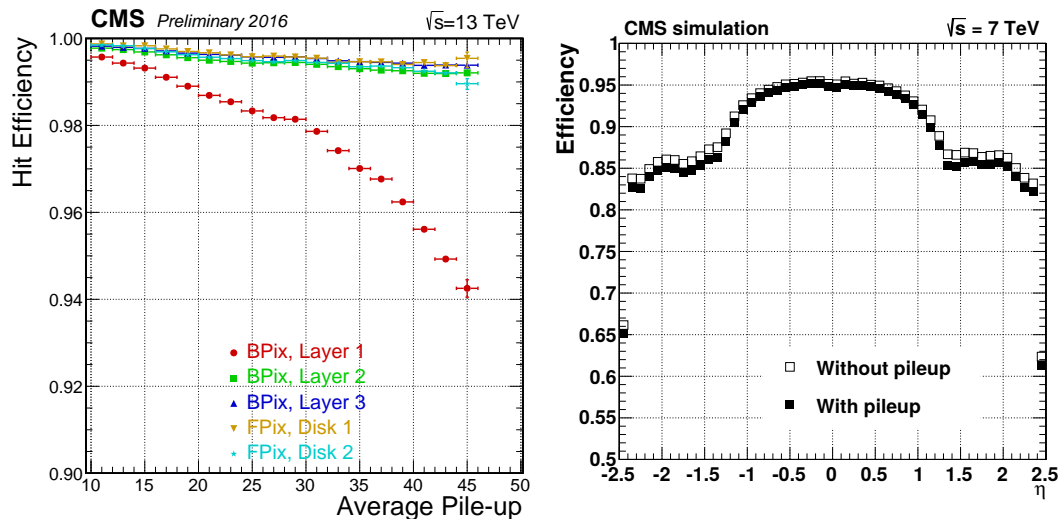
Figure 7.1: Hit efficiency of original CMS pixel detector. The average single hit efficiency is shown for the different layers and disks of the original pixel detector in dependence of event pileup (left) [CMS17j]. The tracking efficiency for charged particles in simulated $t\bar{t}$-events is shown as a function of η (right) [CMS14b].

powering and readout cables) of the pixel detector located in this region. In general, the presence of insensitive material is undesired within a tracker, since it causes scattering and absorption of the collision products, resulting in a reduced tracking resolution.

In addition to this behavior, the CMS pixel detector had been operated longer than it was designed for, resulting in increasing radiation damage due to the harsh environment close to the interaction point, and a reduced tracking resolution [Erd+10]. With the planned LHC upgrades, an increase in the instantaneous luminosities far beyond the design value is expected, causing a further increase of the dynamic inefficiency up to 16 % (see Table 7.1).

To mitigate all these issues, the CMS Collaboration has decided to replace the pixel detector with a new and upgraded version as part of the CMS Phase I Upgrade in the EYETS in early 2017 [CMS12a]. The upgraded version is designed to meet the following three objectives:

- reduced data loss in events with high pileup by an increased size of data buffers on the readout chip and an improved readout chain [Käs13];

- increase of tracking efficiency and tracking resolution by adding a fourth layer and moving the innermost layer closer to the interaction point;

- increase of CMS detector performance by reducing the material budget, which results in less multiple scattering and radiation losses.

With the Phase I Upgrade of the CMS pixel detector, the vertex resolution and tracking efficiency required for jet-identification techniques (e.g. b-tagging, τ-tagging, boosted object identification) are expected to be not only retained at higher pileup but to be improved. For a description of typical jet identification techniques like b-tagging or boosted object jet identification, see Sections 4.4 and 4.5. The tracking fake rate is expected to be reduced by a factor of three, thanks to the tracking input of the additional layer. Furthermore, the impact parameter resolution is expected to be improved by 30 %, thanks to an improved

Table 7.1: Simulated hit loss for original and new Phase I pixel detector. The expected average data loss in the original pixel detector and the Phase I pixel detector is listed for the design instantaneous luminosity ($1 \times 10^{34} \mathrm{cm}^{-2}\mathrm{s}^{-1}$) as well as the instantaneous luminosity of $2 \times 10^{34} \mathrm{cm}^{-2}\mathrm{s}^{-1}$). The barrel region of the pixel detector is typically called BPIX and was extended by an additional detector layer in the Phase I Upgrade. The forward region of the pixel detector – called FPIX – was extended by an additional disk [CMS12a; Fre17].

detector	radius	hit loss in % for	
	(mm)	$1 \times 10^{34}\,\mathrm{cm}^{-2}\mathrm{s}^{-1}$	$2 \times 10^{34}\,\mathrm{cm}^{-2}\mathrm{s}^{-1}$
original pixel detector			
BPIX 1	44	4.0	16.0
BPIX 2	73	1.5	5.8
BPIX 3	102	0.7	3.0
FPIX 1 and 2	-	0.7	3.0
Phase I pixel detector			
BPIX 1	30	1.19	2.38
BPIX 2	68	0.23	0.46
BPIX 3	102	0.09	0.18
BPIX 4	160	0.04	0.08
FPIX 1 to 3	-	0.09	0.18

spatial resolution. Exemplary, the expected improvements in b-tagging efficiency, tracking efficiency and tracking resolution are illustrated in Figures 7.2 and 7.3. Depending on the b-tagging algorithm used[1], the working point selected, the quark flavors to be discriminated against and the pileup, the b-tagging efficiency is expected to improve by 30 % or the misidentification rate is expected to be reduced by a factor of five [CMS12a].

Especially physics analyses that heavily rely on jet-identification techniques – like the analysis performed as part of this thesis – are expected to benefit from the Phase I Upgrade of the pixel detector, since the background originating from misidentified jets is expected to be reduced. By decoupling the pixel upgrade from the long shutdown periods and upgrading the pixel detector before the LHC upgrades, CMS is able to fully exploit the increased luminosity until Long Shutdown 2 (LS2) while ensuring high data quality.

In the following, an overview of the technical implementation of the CMS Phase I Upgrade of the pixel detector is given. Special focus lies on the pixel detector modules for the barrel region. For a more detailed and complete description of the CMS Phase I Upgrade, see [CMS12a].

---

[1]Further improvements in b-tagging are expected from a more intense use of deep neural networks for b-jet identification [CMS17d].
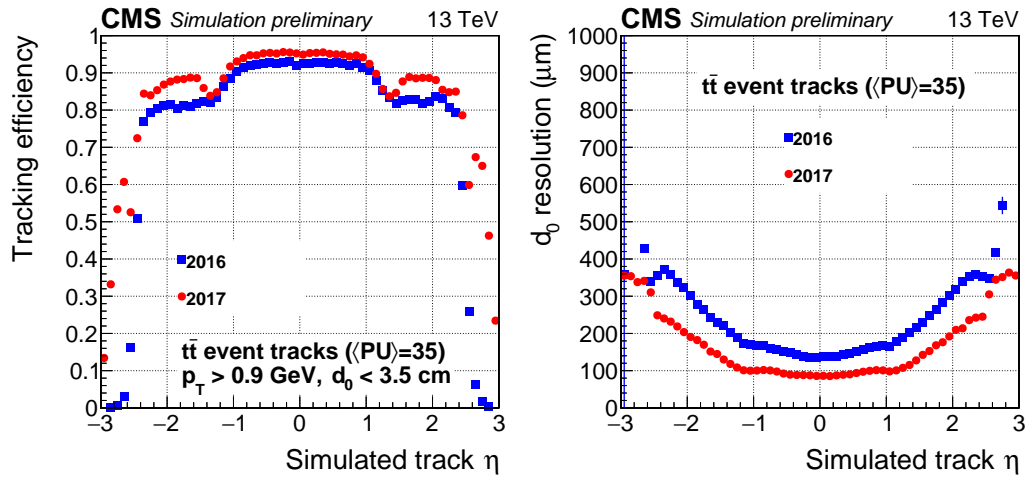
Figure 7.2: Expected improvement in tracking efficiency and tracking resolution. The expected charged particle tracking efficiency (left), and the impact parameter resolution in $r - \varphi$ are shown as a function of η (right), for the original detector – operated until 2016 – and the upgraded pixel detector – in operation since 2017. For this estimation, simulated tracks with $p_T > 0.9\,\text{GeV}$ originating from $t\bar{t}$-events at an average pileup of 35 have been considered [CMS17b].
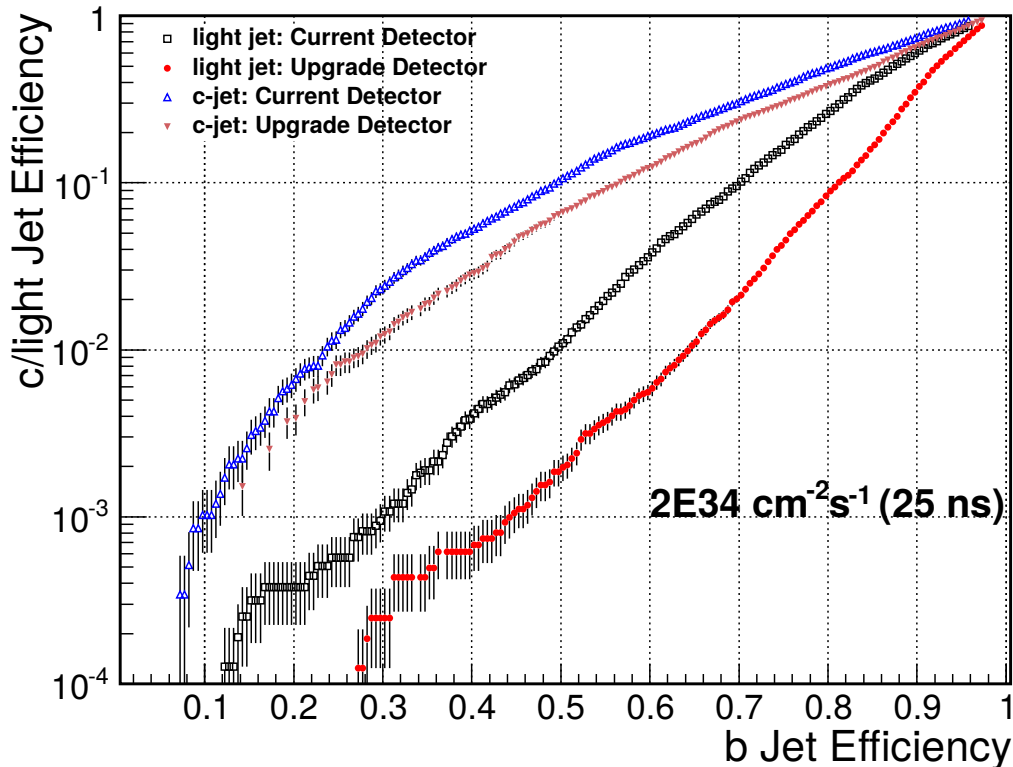
Figure 7.3: Improvement in b-tagging. Expected improvement in b-tagging efficiency of b-jets versus the expected c/light-jet tagging efficiency at an average pileup of 50 using the Combined Secondary Vertex b-tagging algorithm [CMS12a].
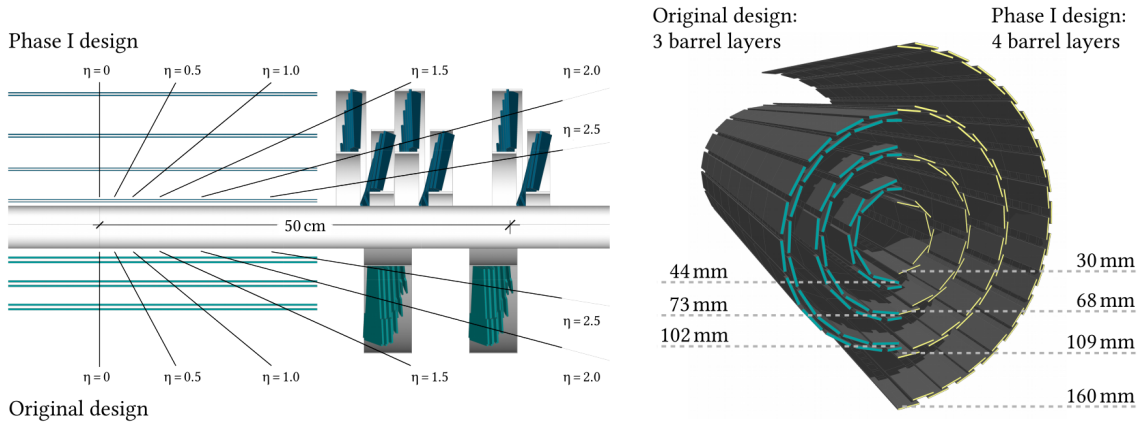
Figure 7.4: Changes in the pixel detector layout. Comparison between the geometric layouts of the original and the upgraded CMS pixel detector. On the left, a cross section through both pixel detector layouts along the beam pipe is shown. An additional layer in the barrel layer and an additional disk in the end-cap region provide four point coverage for tracks with pseudorapidity $|\eta| < 2.5$. On the right, the changes in the barrel region are illustrated together with the radii at witch the layers are mounted (modified from [CMS12a]).

7.2 Phase I pixel detector geometry and support structures

Compared with the original pixel detector, the design of the Phase I pixel detector underwent significant changes. Similar to the original pixel detector, a barrel and end-cap design was selected. Below, the barrel region is called BPIX and the forward/end-cap region is called FPIX. While the original pixel detector was equipped with three detector layers in the BPIX region and two disks in each FPIX region, the upgraded pixel detector is equipped with an additional barrel layer and an one additional disk in each end-cap. The geometric changes of the upgrade are illustrated in Figure 7.4. In 2013/2014 the beam pipe was replaced with a new version of smaller outer diameter ($r_{\mathrm{original}} = 30\,\mathrm{mm} \rightarrow r_{\mathrm{upgrade}} = 22.5\,\mathrm{mm}$). By moving the innermost layer closer to the interaction point, the extrapolation distance to the vertex is reduced by approximately 30 %. At the same time, the additional fourth layer in the formerly un-instrumented space between the pixel detector and the silicon strip tracker, provides an addition 3D tracking point. Together with the additional end-cap disks, the CMS pixel detector provides four space-point coverage up to $|\eta| = 2.5$, allowing an improved track distinction in events with a large number of particle tracks.

The additional detector layers come at the cost of an increased material budget due to the additional sensitive material and the required support and service structures. Therefore, the cooling system and the support structures were upgraded. In the FPIX region, the former half disk support structures, made of beryllium, were replaced by turbine like support structures made of Thermal Pyrolytic Graphite (TPG), which shows superior thermal conductivity of $> 1500\,\mathrm{W/mK}$, and encapsulated by Carbon-Fiber Reinforced Plastic (CFRP). The blades of the support structure are titled at an angle 12° to the disk plane to ensure charge sharing among the pixel cells of the detector modules (see Section 6.2.2) [CMS12a]. In the BPIX region, the former support structures, made out of aluminum and carbon fiber, were exchanged by a light-weight support structure of 200 µm thick carbon fiber facets and end-flanges made from a sandwich structure of Airex® foam

(a)

(b)

(c)
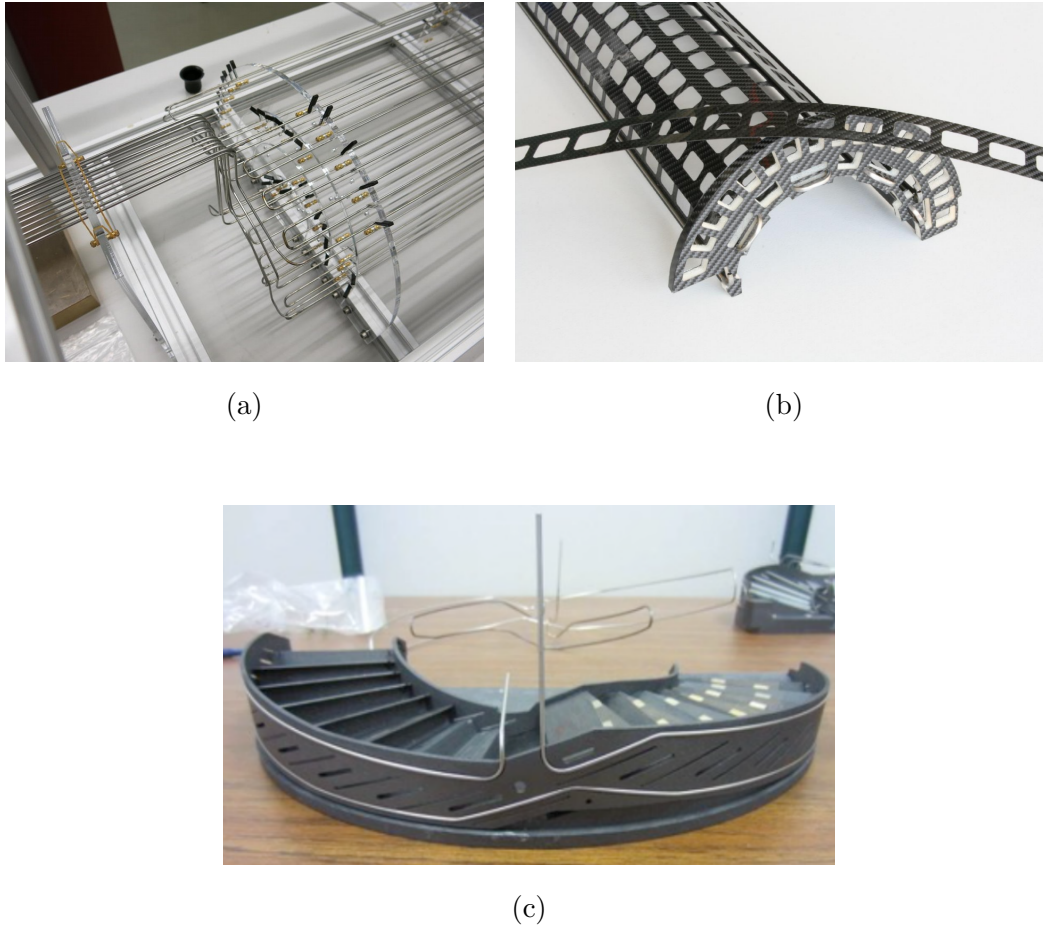
Figure 7.5: Cooling and support structures of the CMS pixel detector. Prototype of the cooling structure of the BPIX region of the CMS Phase I pixel detector (a) [Erd15]. Support structure prototype for the BPIX region (b) [CMS12a]. Support structure for the FPIX region (c) [Aly17].

and carbon fiber [Air18]. To minimize the weight, material not needed to mount pixel modules was milled away.

The cooling system, on the other hand, was integrated into the support structures by countersinking and gluing the cooling tubes into grooves in the support structures. This way, not only the surface between cooling tube and support structure was maximized providing maximum thermal conductivity, also the cooling tubes themselves contribute to the mechanical stability of the support structure. Figure 7.5 shows prototypes of the new support structures as well as prototypes of the cooling tubes. The cooling tubes are made of stainless steel and have a diameter of $2.0\,$mm with a wall thickness of $0.1\,$mm. Inside the cooling tubes, a bi-phase cooling system based on CO_2 is operated to dissipate the heat arising from the operation of the pixel detector caused by leakage currents and power consumption of the readout electronics. An increase in the cooling capacity was achieved by using a bi-phase approach instead of the original tetradecaflourohexane (C_6F_{14})-based cooling. While the C_6F_{14}-based cooling system was limited by the heat conductivity of C_6F_{14} ($1.1\,$J/g K) [3M00], the bi-phase system is based on the large heat of vaporization of CO_2 (e.g. $304\,$J/g at $-30\,$°C), requiring less coolant and therefore smaller cooling tubes [DF00]. In the end, the use of a bi-phase cooling system results in more homoge-
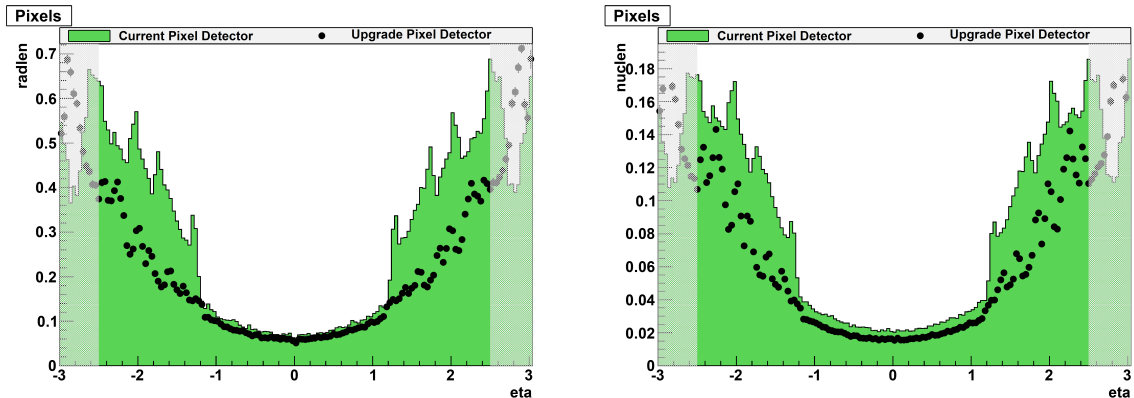
Figure 7.6: Amount of material of original and upgraded pixel detector. Shown is a comparison between the expected material budget of the new CMS pixel detector and the material budget of the original CMS pixel detector as a function of the pseudorapidity (eta). On the left, the material budget is given in units of radiation lengths (radlen). On the right, the material budget is given in units of nuclear interaction lengths (nuclen). In both cases, the material budget of the original pixel detector is shown in green and the material budget of the upgraded version is visualized as black dots. The pale bands illustrate the new location of the electronics boards outside the tracker [CMS12a].

neous cooling along the structure at higher heat load while simultaneously reducing the contribution of the cooling system to the total material budget in the detector. For more information on bi-phase CO_2 cooling systems see [Fel+11; Dag+15; Che+08; Woe+02; Agu+15].

Both the BPIX region as well as the FPIX region of the upgraded CMS pixel detector are cooled by independent cooling loops connected to independent cooling plants, allowing individual operation temperatures. Still, each of the cooling systems has been designed and tested to provide for both sub-detector systems in case of a failure in one of the systems. For further information, see [Ren17].

By using new twisted-pair cables distributing power and data and differential signal transmissions, larger distances between detector modules and support electronics are possible while minimizing the amount of material. This allowed moving the electronic boards providing high voltage and readout to the detector modules outside the sensitive tracker volume, further reducing the material budget within the tracker. This way, the decrease in tracking resolution observed for $|\eta| > 1.2$ in the current detector due to overlap of electronics and sensitive layers (see Figure 7.2) is expected to be mitigated.

Overall, although an additional sensitive detector layer was installed, the total material budget in the tracker volume was reduced, as shown in Figure 7.6. Main drivers of this improvement are the improved bi-phase cooling system and the relocation of the service modules outside the tracker volume. The latter results in a drastic reduction of the material budget in the $1.2 < |\eta| < 2.5$ region, while adding material budget in the very forward region (indicated by the pale bands at $|\eta > 2.5|$).

Table 7.2: Summary of geometric parameters of upgraded CMS pixel detector [Kud14].

name	radius/z-pos. (mm)	faces/ blades	modules	chips	pixels (10^6)	sensitive area (m^2)
BPIX Layer 1	30/-	12/-	96	1536	6.4	0.10
BPIX Layer 2	68/-	28/-	224	3584	14.9	0.24
BPIX Layer 3	109/-	44/-	352	5632	23.4	0.37
BPIX Layer 4	160/-	64/-	512	8192	34.1	0.54
FPIX Disk ± 1	$45 - 161/\pm 291$	$-/2 \times 24$	2×112	2×1792	2×7.5	2×0.11
FPIX Disk ± 2	$45 - 161/\pm 396$	$-/2 \times 24$	2×112	2×1792	2×7.5	2×0.11
FPIX Disk ± 3	$45 - 161/\pm 516$	$-/2 \times 24$	2×112	2×1792	2×7.5	2×0.11
total	$30 - 161/\pm 516$	148/144	1856	29696	123.8	1.9

7.3 Phase I barrel pixel modules

By adding a fourth barrel layer and an additional disk the area that needed t be instrumented was increased by approximately $80\,\%$. All this area of $1.9\,\mathrm{m}^2$ had to be equipped with pixel detector modules – the smallest subunit of the CMS pixel detector, housing both the sensitive silicon sensor and the front-end electronics. In total, 1856 detector modules had to be produced to fully equip the upgraded detector, not including spare modules. Table 7.2 summarizes the geometric parameters, sensitive area and number of pixels for the upgraded CMS pixel detector.

The design of the new pixel modules is based on the original pixel detector modules. In the original detector, modules of different sizes and geometries existed. With the Phase I Upgrade, the module designs were unified into two BPIX designs[2] and a single FPIX design. This allows more flexibility in the selection of modules for detector integration. The BPIX and FPIX designs are conceptionally similar and only differ in the sensor design and the interconnection to the CMS periphery.

In the following, the internal structure of a CMS BPIX detector modules of layer $2 - 4$ is discussed, since they represent the majority of pixel detector modules and since their production has been done as part of this thesis. For information about the design and production of FPIX pixel modules and layer 1 BPIX modules, see [Kle17; CMS12a; SBM17].

A layer $2 - 4$ BPIX pixel module houses $66\,650$ pixels and has a size of $66\,\mathrm{mm} \times 22\,\mathrm{mm}$ and a total thickness of approximately $1\,\mathrm{mm}$. An exploded view of a layer $2 - 4$ CMS BPIX detector module is shown in Figure 7.7. The central part of the pixel module is the silicon sensor that works as the sensitive material where ionizing particles create electron-hole pairs. The signal created in the silicon sensor is read out and processed by one of 16 readout chips (ROCs) arranged in a 2×8 pattern and connected to the silicon sensor via the bump-bonding interconnection technology (detailed in Sections 6.3 & 8.5). The assembly of

---

[2]The pixel detector modules of the innermost layer are equipped with a more radiation-hard and faster readout chip [SBM17].

combined signal
and power cable

Token Bit Manager (TBM)

High Density
Interconnect (HDI)

silicon sensor

16 readout
chips (ROCs)

silicon nitrite
base strips
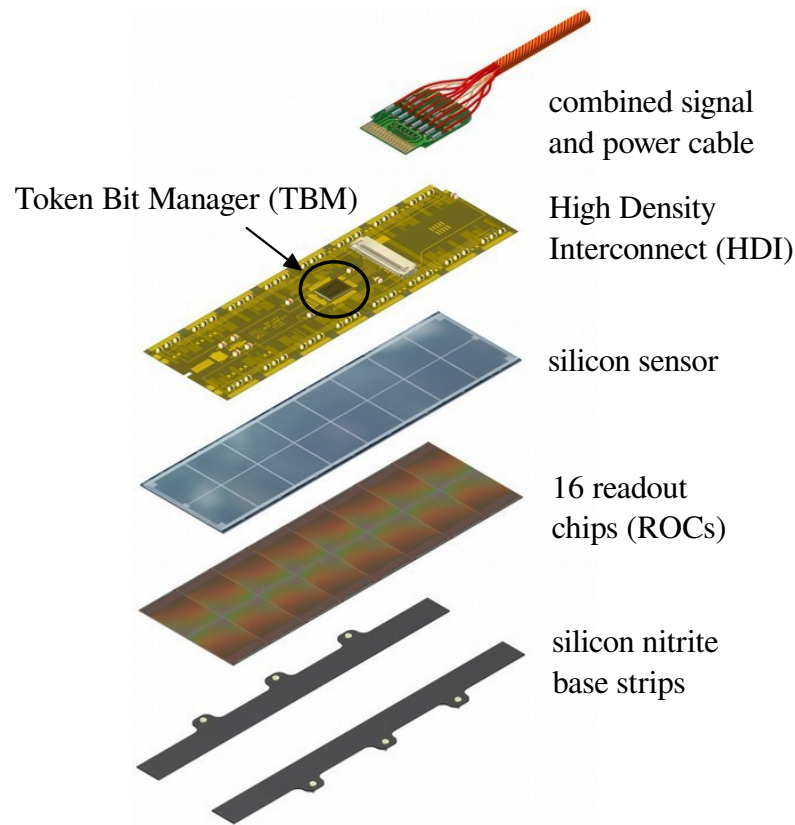
Figure 7.7: Exploded view of layer two to four CMS BPIX detector module. The silicon
sensor, where ionizing particles create electron-hole pairs, is at the center of the pixel
module. Sixteen readout chips are connected from below via the bump bonding
interconnection technology allowing the readout and processing of the signal. A thin
flexible printed circuit board called High Density Interconnect (HDI) is glued on top
of the sensor and provides the connection between all components. The Token Bit
Manager is glued to the HDI and manages the communication via a combined power
and data cable. Electrical connections are established via wire-bonds. At the bottom
base strips are glued to the readout chip (ROC) backsides and can be used to mount
the module (modified from [Erd15]).

silicon sensor and ROCs is called a *bare module*. On top of the sensor, a flex-print structure called High Density Interconnect (HDI) is glued and electrically connected to the ROCs via wire-bonds. The HDI distributes voltage, power, clock and trigger to the ROCs and provides the interconnection between ROCs, Token Bit Manager (TBM) chip and CMS periphery. The TBM manages the communication between ROCs and CMS periphery and is glued and wire-bonded on top of the HDI. The powering and data communication between the module and the CMS periphery is provided by a twisted pair cable, connected to a fine-pitch connector soldered to the HDI. On the bottom side of the module, two silicon nitride structures called *base strips* are glued to the backside of the ROCs. The base strips provide mechanical stability to the module. Furthermore, they dissipate the heat created by the readout chip (ROC)s, which create the main heat load of the module. The base strips are also used to mount the module on the support structures.

The focus of this thesis lies on the bump bonding interconnection technology used to connect every single pixel cell of the silicon sensor with the corresponding front-end electronics of the ROC via a small solder joint. Therefore, the silicon sensor and the ROC are described in more detail.

7.3.1 BPIX silicon sensor

The design of the Phase I silicon sensor is based on the design used in the original CMS pixel detector, which has shown sufficient performance and radiation-hardness for the requirements of the Phase I Upgrade. The silicon sensor has a size of $64.8\,\mathrm{mm} \times 16.2\,\mathrm{mm}$ and a thickness of $285\,\mu\mathrm{m}$. It is segmented into 8×2 sub-matrices each housing 52×80 pixel cells with a size of $150\,\mu\mathrm{m} \times 100\,\mu\mathrm{m}$.

The pixel pitch in $r\varphi$-direction is optimized to the magnetic field provided by the CMS solenoid. With a resulting Lorentz angle of $25°$ and a sensor thickness of $285\,\mu\mathrm{m}$, the charge created by a transversing ionizing particle is spread among two pixel cells, resulting in an optimum hit resolution in $r\varphi$-direction. The $150\,\mu\mathrm{m}$ pitch in z-direction is determined by the minimum area required by the micro electronic read out structures on the ROC [Erd+10]. Since the ROCs are cut out of a wafer at some point of processing, an inactive area around the active electronics is required to ensure no damage to the electronics during the cutting process. For this reason, the edge/corner pixels of every sub-matrix are doubled/quadrupled in size resulting in pixel sizes of $150\,\mu\mathrm{m} \times 200\,\mu\mathrm{m}$, $300\,\mu\mathrm{m} \times 100\,\mu\mathrm{m}$ and $300\,\mu\mathrm{m} \times 200\,\mu\mathrm{m}$ to provide the additional space required by the ROC.

The silicon sensor is based on an $\mathrm{n^+}$-in-$\mathrm{n^-}$ design. The separation into pixel cells is formed by $\mathrm{n^+}$-implants into the $\mathrm{n^-}$-bulk. The backplane is formed by a homogeneous $\mathrm{p^+}$ layer. The pixel cells are insulated from each other by a uniformly applied p-doped layer (p-spray). Each pixel cell of the silicon sensor houses a bump bonding contact pad allowing the front-end electronics to readout the signal. Additional punch through structures and an aluminum bias grid enable the application of a bias voltage to all pixel implants, even without a ROC providing the ground potential needed for depletion. This allows testing the silicon sensor for its characteristic electrical behavior without a ROC connected. Figure 7.8 shows a cluster of 2×2 pixel cells together with the implant and the bias grid structures and a schematic cross-section through a sensor cell. The sensor surface is protected by a passivation layer, providing openings in all areas required for electrical contact.

The sensor is produced in a two-sided process, allowing the implementation of another bias grid structure on the backside of the sensor to ensure homogeneous bias voltage distribution. Furthermore, this design allows the implementation of a guard ring structure
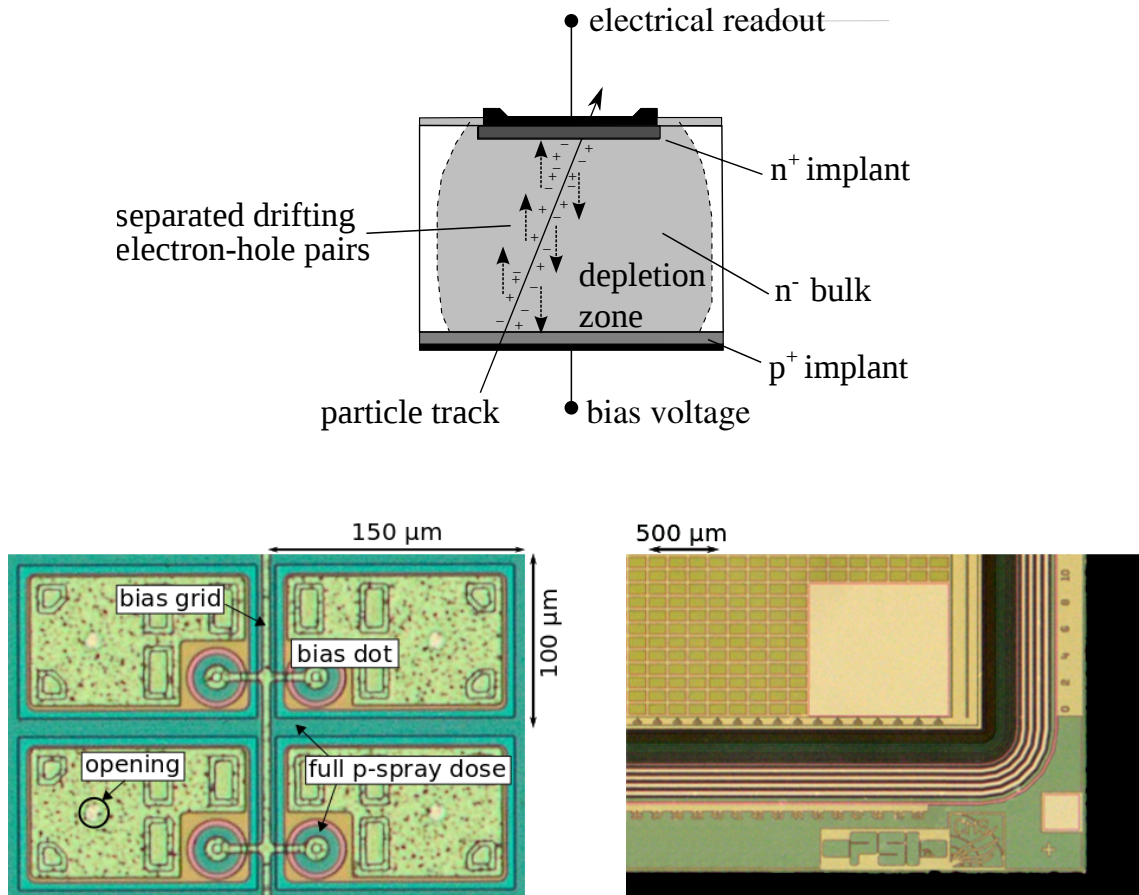
Figure 7.8: Pixel cell structure of BPIX silicon sensor. Schematic cross section through a sensor cell illustrating the charge separation in the depletion zone. Also shown is the front side of a cluster of four pixel cells in a BPIX silicon sensor (left). Features like the opening in the passivation layer, the front side bias grid and the p-spray insulation are visible. Part of the sensor backside with the bias grid and the guard ring structure is shown (right, modified from [Ros+06],[Col16]).

on the sensor backside shielding the sensor edges from high voltage. This reduces the risk of an electric discharge via the air gap between the sensor edge and the ROCs.

The usage of n^+-in-n^- technology has the benefit of using electrons as charge carriers to be read out. Electrons show larger mobility in silicon than holes and therefore allow faster charge collection while providing a larger Lorentz angle and increased charge sharing.

In this application, a technology based on an n^--doped bulk shows superior radiation-hardness over a technology relying on a p^--doped bulk, since lattice defects generated by radiation dominantly cause the creation of acceptor energy states. This means that radiation damages slowly transform the n^--doped bulk material into p^--doped like bulk material. This process is also known as type inversion. Up to the point of type inversion, the effective doping concentration in the bulk is reduced, resulting in a delay of the potential moment the sensor cannot be fully depleted any more due to radiation damages.

Another benefit of an n^+-in-n^- technology compared to a p^+-in-n^- technology is the way the depletion zone grows around the pn-junction. Before type inversion, the depletion zone is established from the pn-junction between the p^+-doped backplane and the n^--doped

bulk. In order to read out a signal from the implant side, the sensor needs to be fully depleted, which seems like a disadvantage at first. After type inversion, however, the depletion zone is established from the pn-junction between the n^+-doped implants and the now p^--doped bulk, allowing the readout of a charge signal from the depletion zone, even if the sensor is not fully depleted. This behavior can be of great benefit if the voltage required to fully deplete the sensor cannot be provided, e.g. due to strong radiation damage in the silicon bulk. In such a scenario, the sensor can still be operated with a partially depleted sensor, since the electrons created in the depletion zone can still be read out via the n^+-doped implants. Further information on the behavior of the sensor material after large radiation damage, see [Fre17; Roh+11].

7.3.2 Readout chip

The ROCs of the BPIX detector module fulfill several purposes. Every 25 ns, they read out the charge signal from the sensor, amplify it, discriminate it from noise and store the hit information until a L1-trigger decision is made. If the L1-trigger decision is positive, the ROCs digitize the hit information and forward it to the CMS periphery via the TBM.

The readout chips have undergone the biggest changes of all components in the BPIX detector module. The original *PSI46V2* version was replaced by the Phase I version *PSI46digV2.1-respin* [Käs+06; Käs13]. In this section, the working principle of the ROCs is explained while simultaneously pointing out the improvements that were performed as part of the CMS Phase I Upgrade [HS15]. Several issues were tackled by dedicated changes in the ROC design:

- cross-talk between analog electronics of neighboring pixels

- noisy pixels requiring high comparator threshold;

- dynamic hit data loss due to limited data buffers;

- limited speed of analog readout of module.

The PSI46digV2.1-respin has a size of $7.9\,\text{mm} \times 10.2\,\text{mm}$, which is $0.5\,\text{mm}$ longer than the original PSI46V2 due to an enlarged periphery. It is thinned to a material thickness of $175\,\mu\text{m}$. Both, the original and the upgraded version of the ROC were fabricated with a commercial 250 nm Complementary Metal-Oxide-Semiconductor (CMOS) technology, that proved to be reliable and sufficiently radiation-hard. While the original ROC housed five metal layers, the upgraded version comes with an additional metal layer to reduce the effects of cross-talk between neighboring pixels.

The layout as well as the hit data process flow can be separated into three basic parts. An overview of the ROC layout is given in Figure 7.9. The first and largest part is the matrix of $52\,\text{rows} \times 80\,\text{columns}$ Pixel Unit Cells (PUC)s each reading out and processing the charge signal from the corresponding pixel cell of the silicon sensor. The second part is the ROC Double Column (DCol) periphery and data buffers, collecting hit information from the PUCs, and storing it until the L1-trigger decision. The third part is formed by the control and interface block housing an 8-bit ADC to digitize the hit information. Furthermore, it contains the logic to control and operate the readout chip as well as to communicate with the TBM. The ROC has two power supplies, one providing power required for the analog processing steps and one providing power for the digital processing. The routing schemes of these two power lines are designed to minimize cross-talk in order to keep the noise contributions well under control.
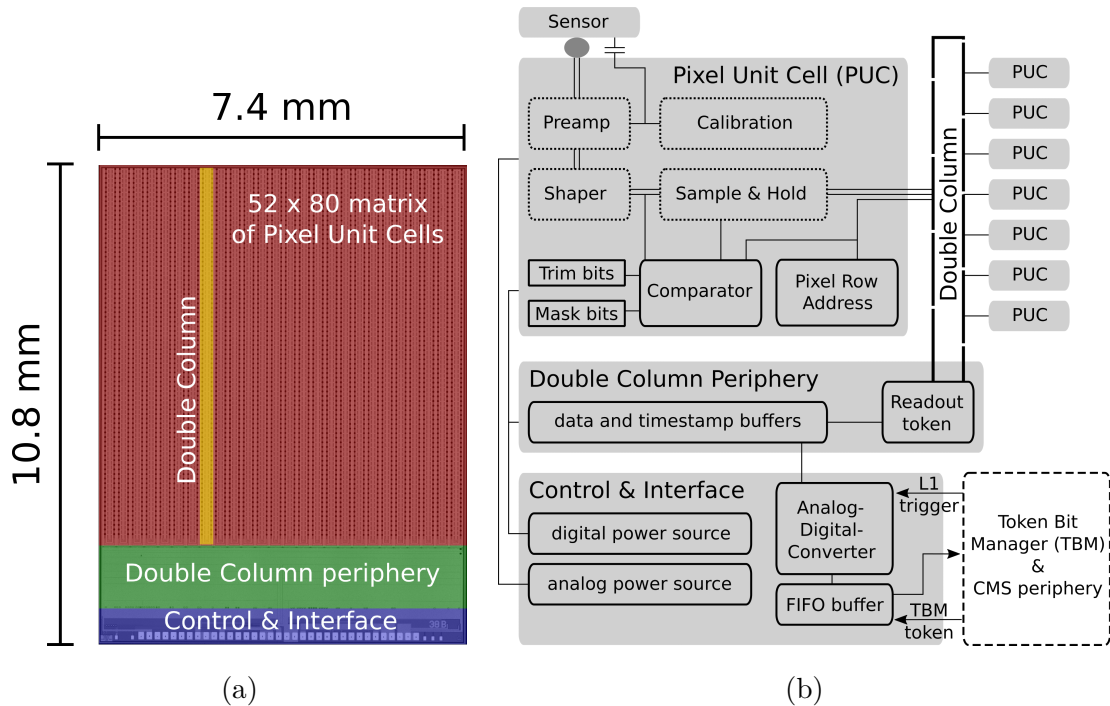
Figure 7.9: Overview of CMS Phase I pixel ROC. Illustration of the geometry (a) and basic layout (b) of the CMS Phase I pixel ROC. The separation into the different logic parts of the ROC is shown, as well as the double column structure and the wire bond pads allowing the connection to the High Density Interconnect.

Every PUC contains the electronics needed to read out and process the charge signal. Due to the electric field inside the sensor, a charge signal created in the sensor drifts towards the n^+-implants where it is collected and read out by the PUC connected via a bump-bond. The signal is further processed by the preamplifier and shapers, amplifying the signal while suppressing electrical noise. After passing a comparator threshold, the analog signal is locally stored in a sample-and-hold capacitance while the PUC notifies the Double Column Periphery and waits to be read out.

Due to variations in the production process, variations in the gain of the preamplifier and the threshold of the comparator are common. To accommodate these variations, so called *trim bits* can be used to modify the local threshold of the analog signal processing stage of the PUC in a global calibration procedure. Alternatively, bad or noisy pixels can be completely muted using so called *mask bits*. These calibration procedures have been systematically performed for all pixel modules produced, as described in Section 8.7.2. For internal calibration purposes, the PUC houses a calibration block that allows the internal injection of a well-defined charge signal into the PUC. This test signal can be injected directly into the preamplifier or into the sensor material via an air gap and then be read out again by the PUC.

Compared to the original PSI46V2 ROC design, the PSI46digV2.1-respin ROC has a reduced comparator threshold of about 1 800 electrons instead of 3 500 in the original design, while providing increased flexibility in the trimming and muting of single PUCs.

The readout of the PUCs is organized in so called Double Columns (DCols) grouping two columns of PUCs into a single readout unit. The DCol periphery houses the logic to collect

data from hit PUCs and buffers to store these data and timestamps during the L1 trigger latency. 80 data and 24 timestamp buffers are assigned to every single DCol. When a PUC initiates the so called "double column drain", the DCol periphery stores the bunch-crossing timestamp into a timestamp buffer cell. Furthermore, it sends out a token along the DCol, subsequently triggering the PUCs to send the hit information out to the DCol periphery for storage.

Compared with the original PSI46V2 ROC design, the PSI46digV2.1-respin ROC has an increased buffer size to avoid dynamic inefficiencies due to high pileup. In this way, the data loss due to buffer overflow can be reduced to $< 0.5\,\%$ at a hit rate of $600\,\mathrm{MPix\,s^{-1}\,cm^{-2}}$, compared to an expected data loss of $16\,\%$ in the original design. To provide the space required for these buffers, the PSI46digV2.1-respin has been enlarged by $0.5\,\mathrm{mm}$ compared to the PSI46V2.

If the L1-trigger decides to read out the tracker, the DCol buffers are read out by the control and interface block. The content of the data buffers is digitally encoded using an $80\,\mathrm{MHz}$ 8-bit ADC. Before forwarding the data to the TBM the data is temporarily stored in a First In First Out (FIFO) buffer, waiting for an external readout token from the TBM. This temporary storage allows the refilling of the buffers while the ROC is waiting for the readout token from the TBM. This reduces the dead time of the module to less than $1\,\%$. By using an ADC to digitize the data already on the ROC, the module can be read out at an increased speed of $160\,\mathrm{Mbit/s}$ compared to of the original $40\,\mathrm{MHz}$ analog readout.

The improvements of the new ROC compared to the original ROC design can be summarized as follows: reduced cross-talk due to an additional metal layer, educed comparator threshold and more trimming flexibility, less data loss thanks to enlarged buffers, digital readout increases data readout speed.

7.4 Pixel module production

Similar to the original detector, the FPIX modules for the upgraded version were produced by a US consortium of Purdue University, the University of Nebraska, and Fermilab. In total, about 800 FPIX modules (including $20\,\%$ spares) needed to be produced to equip the disks of the Phase I pixel detector.

For the BPIX modules however, the CMS collaboration decided to split the production of the upgraded CMS pixel detector among five independent production lines, operated by universities and institutes across Europe. This way about 1400 BPIX modules (including about $20\,\%$ spares), were produced within a total production time of 18 months, by parallelizing the assembly process. Also, the availability of several production lines provided redundancy to cope with a potential downtime in one of the production lines.

The Swiss consortium composed of the Paul Scherrer Institute (PSI), the Eidgenössische Technische Hochschule Zürich (ETH), and the University of Zürich was in charge of producing the pixel modules required for layer 1 & 2. The layer 3 modules were produced in two production lines, operated by universities in Italy as well as CERN, Finland, and Taiwan. The BPIX modules required for layer 4 were produced in two production lines by a German consortium of the Deutsches Elektronen-Synchrotron (DESY), the University of Hamburg (UHH), the Rheinisch-Westfälische Technische Hochschule Aachen (RWTH), and Karlsruhe Institute of Technology (KIT). Half of the modules needed to equip the fourth layer were produced and tested DESY and UHH, while the other half was produced at KIT and tested at RWTH [CMS12a].

8

Production of CMS Phase I barrel pixel modules

The pixel module production for the CMS Phase I Upgrade of the CMS pixel detector was a major project carried out by a large collaboration of different institutes around the globe. This chapter shall be dedicated to the production of BPIX detector modules at KIT. After a first overview of the production process, the grading scheme that was used for the production is introduced. Focus is set on the bump bonding interconnection technology and the quality assurance tests developed, implemented and performed to ensure a good bump bonding quality. Therefore, the pre-processing and material selection are discussed in more detail. After a detailed description of the bump bonding process, the further processing steps of the KIT production line are described. Finally, the module production yields and quality are presented. For a more general overview, including also other production lines, see [Kle17].

The production of a BPIX detector module is a complex and delicate process. To ensure a good and homogeneous production quality among all five production lines, the CMS collaboration decided to introduce several quality checks in-between the different assembly steps. The philosophy of frequent quality checks allowed CMS to identify and tackle quality issues as early as possible and assured a high overall yield by using only high quality material for the subsequent production steps. Furthermore, it allowed the exchange of knowledge and experience on certain issues among the different production lines in frequent collaborative meetings. At the same time, all data concerning the production of module, its status, quality, and the components used to assemble it were stored in a centralized database. The centralized database also allowed early identification of component shortages at any production line.

The German consortium of DESY, UHH, RWTH and KIT, charged with the production of BPIX detector modules for layer 4, operated two production lines, one at DESY together with UHH, and one at KIT. The final quality grading of KIT modules was performed at RWTH Aachen. Both production lines showed a strong and close cooperation by matching some of their sub-processes and technologies to provide maximum compatibility.

8.1 Overview of the KIT production line and grading scheme

In this first section, the reader shall be given a rough overview of the KIT production line and the different assembly steps. In doing so, the KIT production can be considered as
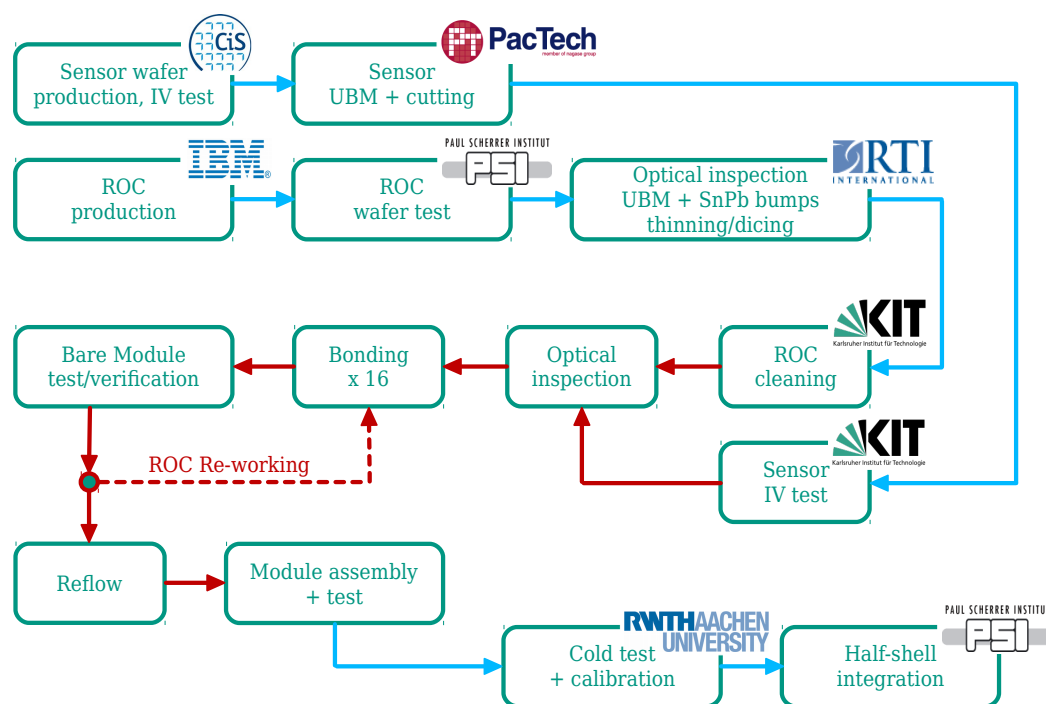
Figure 8.1: Overview of KIT production work flow. The KIT workflow for producing and assembling BPIX detector modules is shown. The labels of the institutes or external vendors are attached to the corresponding sub-processes. Red lines illustrate the process steps performed at KIT [Fre17].

representative production line for all BPIX production lines. Other production centers mainly differ in the bump bonding interconnection technology selected or the vendor providing this technology. Nevertheless, the general sequence of assembly steps is similar.

The KIT production line was operated by the Institute of Experimental Particle Physics (ETP) and the Institute for Data Processing and Electronics (IPE). In total, KIT was responsible for producing at least 256 good modules plus additional 20 % spares. KIT decided to further deepen the BPIX philosophy of frequent quality checks, by assigning quality criteria to every single process step. In order to still be able to produce the required number of modules within the production time of 18 months while assuring a good production quality at moderate cost, complex and delicate process steps were performed in-house while simpler process steps were distributed to external industrial vendors.

KIT aimed for an average production capacity of 16 full modules per week. An overview of the work flow for the BPIX modules production at KIT is given in Figure 8.1. At KIT, IPE was responsible for the production of bare modules by bump bonding the ROCs to the silicon sensors while ETP was responsible for the assembly of the full module and the quality assurance tests. A more detailed description of the full module assembly is given in section 8.7.

For the bump bonding technology, KIT decided to use a process, where the ROCs are equipped with SnPb solder bumps and the sensor side with a UBM structure. The bump bonding process step was divided into UBM deposition, bump deposition and cutting

performed by external vendors. By performing the complex flip chip bonding process at IPE, KIT had full control over the process while keeping the processing cost as low as possible. Furthermore, the possibility to also perform the quality checks in house provided short turn-around times and allowed a quick response to possible quality issues.

PacTech© was selected as external vendor for the UBM deposition on the silicon sensor and the dicing of the sensor dices. PacTech© also provided the UBM deposition for the DESY production line, allowing the exchange of sensor material between KIT and DESY. Research Triangle Institute (RTI)^{TM} was selected as external vendor to provide the bump deposition on the ROC-side, as well as dicing and thinning of the ROCs. RTI had already proven to be a reliable vendor in the FPIX production of the original CMS pixel detector and had been assigned the task of bump bonding for the FPIX detector modules of the upgraded CMS pixel detector.

Based on the results of the final qualification tests, a grade was assigned to every module. The CMS collaboration agreed on a tripartite quality grading scheme (more on the final grading in section 8.7.2).

- grade A: module suitable for installation in final detector

- grade B: module with minor defects, but still usable for final detector if necessary

- grade C: module not suitable for detector operation

This grading scheme had been adapted to qualify intermediate process steps and to select material for further processing. The grades on intermediate process components have been assigned according to the final module grade they are expected to create.

Since the final yield of the full BPIX production was unknown a priori, the general KIT policy was to only create modules from grade A components. The remaining components of lower quality were combined in such a way that the number of defects in a single grade B module were minimized.

8.2 Silicon sensor pre-processing

All BPIX silicon sensors were produced in a two-sided four inch wafer process by CiS Forschungsinstitut für Mikrosensorik GmbH (CIS) in Erfurt, Germany. CIS already produced the BPIX silicon sensors for the original pixel detector and proved to be a reliable manufacturer. Also, the selection of CIS as manufacturer allowed reusing the process masks and reinstalling the production process of the original pixel detector, ensuring a high sensor quality at low cost. After processing, an electrical test to perform the electrical behavior of each sensor had been performed by CIS, before delivering the wafers to PacTech© – Packaging Technologies GmbH in Nauen, Germany.

8.2.1 UBM deposition and dicing

At PacTech©, the UBM, which is required to create a wettable seed surface for SnPb bump bonding, was deposed. The UBM deposition was performed in a mask-less electroless plating process called ENEPIG. Electroless nickel electroless palladium immersion gold (ENEPIG) coatings are very common and treated as "universal surface finish" since they are suitable for soldering, solder based bump bonding as well as gold and aluminum wire bonding. This universality is essential for further processing, since it provides a single coating suitable for

(a) Electroless plating

(b) Electroless immersion coating

(c) ENEPIG structure

(d) ENEPIG UBM surface
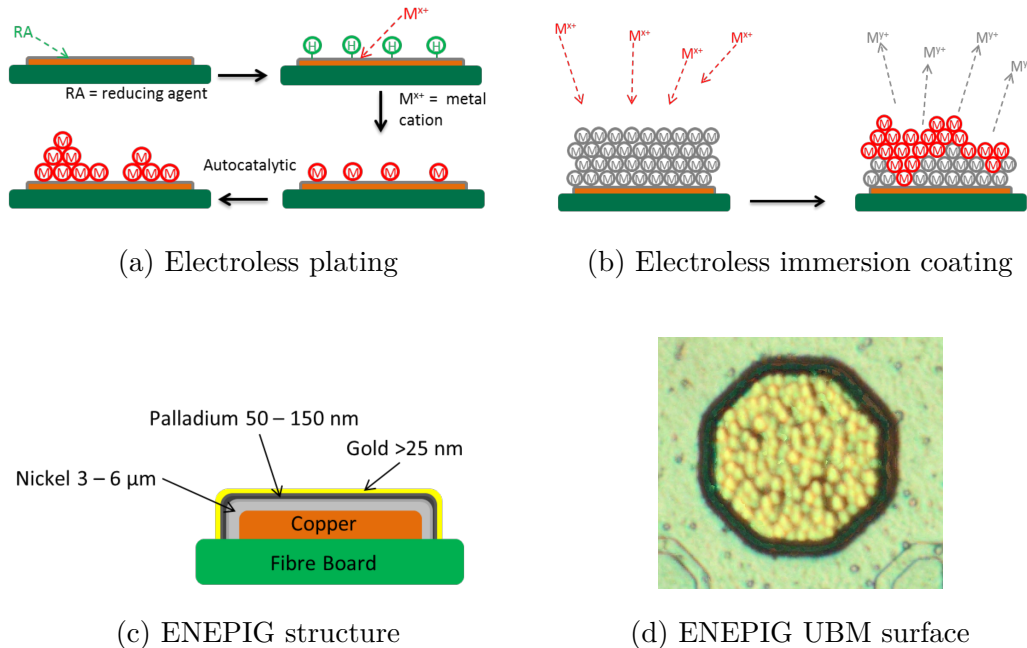
Figure 8.2: Electroless plating of ENEPIG structure. The working principles of an electroless plating process (a) and an electroless immersion coating (b) are shown. By combining these two processes an electroless nickel electroless palladium immersion gold (ENEPIG) structure can be created (c). A top view onto an Under Bump Metallization created by an ENEPIG process is shown on the bottom right (d) [BJR18].

connecting the ROC to the silicon sensor but also for establishing a wire bond connection between the HDI and the silicon sensor, all in a single mask-less process.

In electroless plating, the substrate is dipped into a solvent bath of strong reducing agents and a salt of the metal that needs to be deposited. The curing agents, typically based on solvents containing phosphorus or palladium, are adsorbed onto all uncovered metal surfaces and activate the surface. In a redox process, the metal cations then react with reducing agents and are adsorbed onto the substrate surface. From this point on, the process continues auto-catalytically and further layers of metal cations are adsorbed and reduced in redox reactions. The process continues until it is somehow quenched or the substrate is removed from the bath. In this way, several metal layers can be deposited at the metal surface, each requiring a unique and customized solvent bath.

A variation of the electroless plating is the electroless immersion coating. In this process, no reducing agents are required. Instead the plated surface itself acts as a reducing agent. In a solvent bath with metal salt, the top layer of the plated surface is oxidized and replaced by a more electronegative metal which forms a thin coating above the substrate. Figure 8.2 illustrates the concept of electroless plating and electroless immersion coating as well as the typical structure of an ENEPIG layer.

The ENEPIG coating consists of three metal layers as shown in Figure 8.2. The wettable base of the coating is provided by a thick 5 µm Ni-layer that is deposited first in an electroless plating process. Although nickel is a well wettable seed surface, it can be easily oxidized, losing this feature. For this reason, a second layer of palladium is deposited on top, providing a diffusion barrier for the Ni-atoms as well as residual phosphorus atoms from the bath contaminating the nickel. The third and last gold layer provides a chemically resistant finishing, protecting the nickel from oxidation, that is deposited in an electroless

immersion coating process. To avoid gold embedding into the actual solder material, the thickness of the gold layer is kept as low as possible. A typical thickness for the palladium diffusion barrier is 200 nm, while the gold layer has a typical thickness of 50 nm. While the nickel and palladium layers are typically deposited by electroless plating, the gold layer is typically deposited in a electroless immersion process [IPC12].

Since the ENEPIG coating is a mask-less process, all metal surfaces uncovered by a passivation layer are coated. This ensures good electrical conductivity when contacting the high voltage contact areas for electrical characterization of the sensor.

Besides three large BPIX sensors used to produce modules, the sensor wafer also contains several test structures as well as smaller versions of the silicon sensor. These smaller sensor versions and the test structures were to initially develop the flip chip bonding process, as well as to validate the process quality during the production. Furthermore, they provided test material for the development of other bump bonding technologies. For more information on the sensor wafer design, see [Hei16].

After the deposition of the ENEPIG UBM, the wafers were cut to obtain the the single sensors and sent to KIT.

8.2.2 Electrical characterization and optical inspection of sensors

At KIT, all delivered sensors were tested for eventual damages caused by UBM deposition, dicing, transport or handling. This was done by an optical inspection as well as an electrical characterization. Since a similar electrical characterization was performed on wafer level by CIS, this allowed a direct feedback on the processing quality to PacTech as well as CIS itself.

The electrical characterization is achieved by performing an I-V measurement. Therefore, the sensor is depleted using the biasing structures on the sensor described in section 7.3.1 to apply a bias voltage in reverse bias. The leakage current is measured as a function of the bias voltage applied. The leakage current had to fulfill two criteria [CMS12a]:

- **Leakage current:** For the typical operation voltage of 150 V, the leakage current of the silicon sensor had to be below 2 µA. This operation voltage corresponds to approximately two times the full depletion voltage.

$$I_{\text{leak}}(150\,\text{V}) \leq 2\,\mu\text{A} \tag{8.1}$$

  During operation in the detector, the depletion voltage is expected to rise to values $> 100\,\text{V}$ due to radiation damage in the bulk material [Fre17].

- **Slow breakdown:** To avoid large leakage currents in case the bias voltage has to be increased due to radiation damage, the sensors have to show a slow breakdown behavior. The criterion to ensure this was defined to be that the leakage current at 100 V is less than half as large as the leakage current at 150 V bias voltage.

$$\frac{I_{\text{leak}}(150\,\text{V})}{I_{\text{leak}}(100\,\text{V})} \leq 2 \tag{8.2}$$

Figure 8.3 illustrates the sensor selection based on the I-V measurement. The I-V measurements were performed in a dedicated probe station at ETP. For this qualification the grading scheme had been reduced to only two categories, grade A and grade C. Only grade A silicon sensors were further used to produce bare modules.
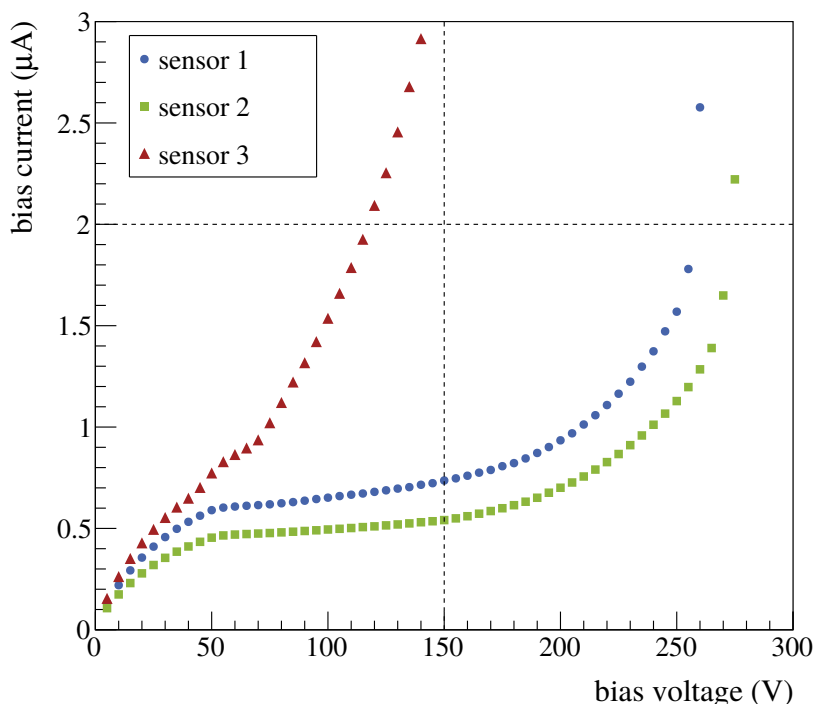
Figure 8.3: IV-curves of silicon sensors. Exemplary IV-curves measured in the sensor qualification of the BPIX module production at KIT are shown. Sensors 1 and 2 pass selection criteria and are turned into bare modules. Sensor 3 fulfills does not pass the selection criteria and therefore is removed from the production queue (modified from [Hei16]).

In total, over 500 IV-curve measurements were performed at KIT, with 80.5 % being graded as grade A. Only 5.6 % of the sensors initially graded good at CIS were graded C at KIT, hence confirming the good sensor and processing quality. Due to time constraints, the systematic IV-curve measurement was skipped for the last part of the production ($\approx 20 \%$ of all available silicon sensors). This was tolerable since the sensors had proven to be of high quality and since a systematic optical inspection as well as the introduction of an additional IV-curve testing at bare module level already provided a good screening. For more information on the sensor testing at ETP, see [Hei16].

Before entering the bare module production sequence, the sensor underwent another final optical screening using a Keyence$^{\mathrm{TM}}$VHX 5000 digital optical microscope [KEY18]. This optical inspection was dedicated to the detection of those failures in the silicon sensor production, UBM deposition or dicing processes that cannot be detected by an I-V measurement. Such failures are for example:

- cratering or scratches in the silicon due to bad dicing or due to bad handling during or after the IV-curve measurements;

- failures in the lithographic processing influencing the performance of a single sensor pixel cell or a cluster of pixel cells;

- missing, damaged, or oxidized UBM structures. Such failures can be caused by contaminated or overused solvent baths, resulting in an imperfect coating. Nickel

that has not been perfectly covered oxidizes over time and can be distinguished by a grayish or black color;

- any kind of pollution or contamination of the surface structure.

Figure 8.4 shows a selection of typical failures on the BPIX silicon sensors. All issues detected during the optical inspection were documented to allow cross-checking with later electrical and mechanical test results. Contaminations and pollutions were removed in an individual cleaning procedure based on isopropyl alcohol, if possible.

Since, at this stage, a variety of quality issues with an even larger variety of combinations is possible, the sensors had to be selected individually. The general philosophy for the selection was based on an estimation of the number of pixel cells affected by the quality issue. For example, a missing UBM in a single pixel cell was expected to only affect that one single pixel cell. On the other hand, a scratch through the guard-ring structure on the back-side of the sensor was expected to affect all pixel cells. By summarizing the numbers of expected defective pixels, a sensor selection was performed. Only sensors with maximum of four defective pixel cells for each of the 8×2 sub-matrices were accepted.

In total, 444 silicon sensor were inspected in this way. Problematic silicon sensors were retained until the end of the production to ensure that only the highest quality sensors are turned into bare modules. In the end, only 7 silicon sensors (1.6 %) have been removed from the production queue due to failures not detected in the IV-measurement. Nevertheless, the optical inspection was necessary to provide valuable feed-back to the flip-chip bonding process and to ensure that no ROCs are wasted on bad sensors.

8.3 Readout chip pre-processing

The ROCs were all produced centrally by IBM in an eight-inch wafer process, housing 244 ROCs per wafer. Each wafer was sent to PSI in Villingen, Switzerland where the wafer was probed and the functionality of every PUC was tested and documented. After testing the wafers were distributed among the production centers. In total, 37 wafers with over 9000 ROCs were designated for KIT and were directly sent to RTI in North Carolina, US, for bump deposition, thinning and dicing.

8.3.1 Bump deposition, dicing and thinning

At RTI, the ROCs were equipped with solder bumps made from an eutectic tin lead mixture (mixing ratio Sn/Pb = 63/37)[1]. The bump deposition was performed in a lithographic electroplating bumping process providing a bump diameter of 30 µm, while ensuring a high wafer uniformity. The process had been developed and used in the context of the original FPIX detector [Huf+03]. The RTI bumping process is performed in seven process steps, as illustrated in Figure 8.5:

1. Removing the original passivation layer from the wafer and deposition of a new passivation layer made from Benzocyclobutene (BCB, CYCLOTENE™). BCB is a photosensitive polymer that protects the surface during further processing. Furthermore, it provides a uniform and planar base and acts as a stress buffer

---

[1]According to the thermodynamics of mixed phases, the temperature required to liquefy a mixture depends on its relative composition. In the eutectic composition, the two elements liquefy simultaneously into a single phase. The melting temperature required for the phase transition is lower than the melting temperature of either of the single components [AD09]. For an eutectic tin lead mixture of 63 % tin and 37 % lead, this phase transition occurs at a temperature of 183 °C.

(a)

(b)

(c)

(d)

(e)

(f)
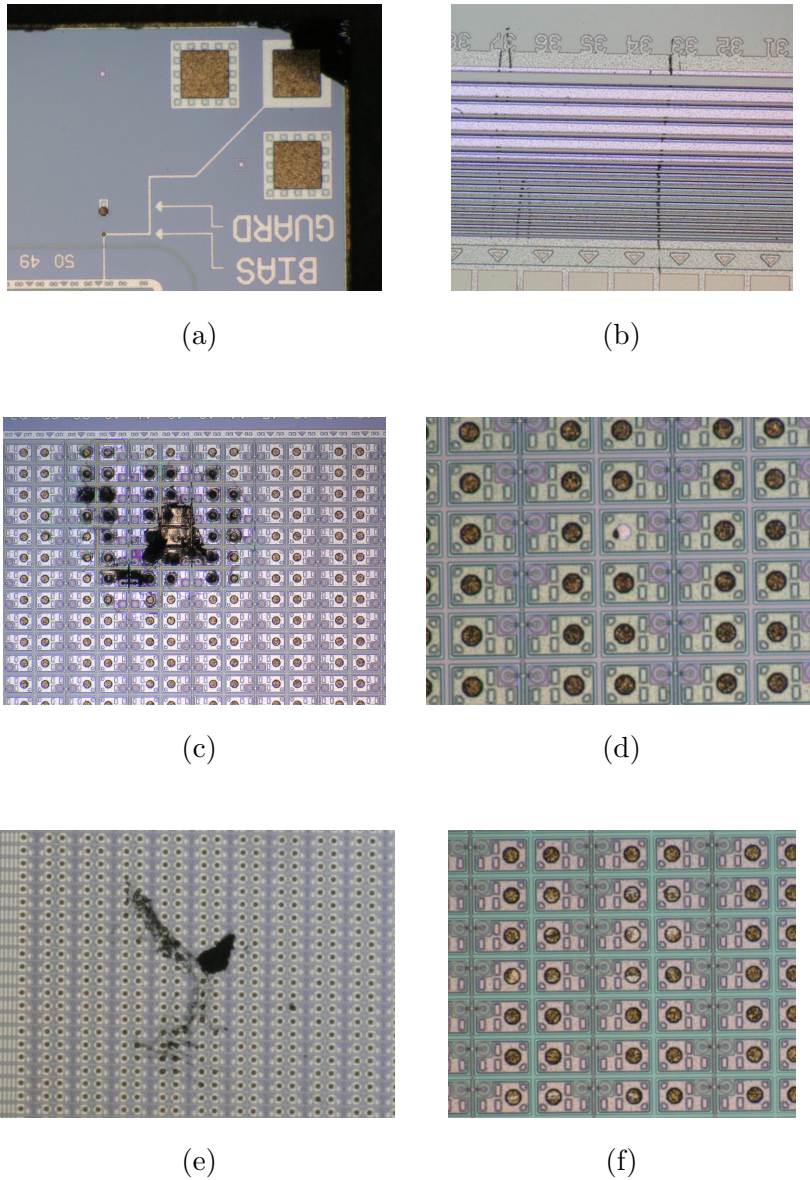
Figure 8.4: Sensor failures detected in optical inspection. A collection of typical quality failures detected in the optical inspection during production is shown: (a) broken corner, (b) scratch through guard ring structure, (c) micro-electronic damages, (d) missing UBM structure, (e) pollution on UBM structure, (f) potentially damaged UBM structure with uncovered nickel layer.
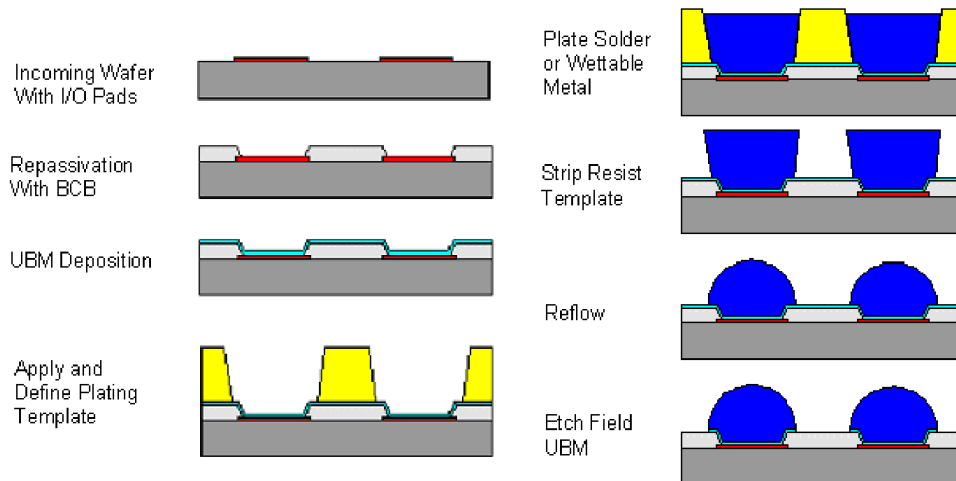
Figure 8.5: SnPb bump deposition process. The basic steps of the lithographic SnPb bump deposition process developed by RTI are shown. The process is based on electroplating using lithographic masks. For every process step, a cross-section view is given [Huf+03].

between the silicon wafer and the SnPb bumps increasing the thermo-mechanical reliability of the system [Bur+90; The18]. To access the I/O metal pads for bumping, the BCB is removed at the bump positions by a lithographic process.

2. Next, a suitable UBM layer is deposited onto the whole wafer surface in a electroless plating process. It consists of several thin metal layers. The exact thickness and composition of the UBM metal layers is not disclosed by RTI. Nevertheless, a typical UBM composition looks as follows (from metal pad side to bump side): a thin layer of titanium or tungsten acting as a diffusion barrier, a nickel layer of few micrometer thickness acting as wettable seed layer, covered by a thin gold layer protecting the UBM structure from oxidation.

3. In a photo-lithographic process, a thick photo-resist layer is deposited leaving openings for bump deposition at the corresponding bumping positions. The usage of a photo-lithographic process allows very fine structures while providing good uniformity across the wafer.

4. Next, the bump material is deposited in a electroplating process. By tuning the electroplating current, the rate at which the material is deposited on the UBM as well as the total amount of bump material can be controlled well.

5. Chemical removal of the photo-resist template.

6. To re-shape the solder pillars into spheres, the wafer is heated above the phase transition temperature of the solder. The surface tension of the liquefied solder as well as the adhesion to the UBM structure cause the creation of spherical bumps. In addition, the inter-metallic connection between the UBM and the bump material is ensured by the high temperature.

7. In an etching procedure, the UBM not covered by the bump sphere is removed. Access to the wire bonding pads is enabled by removing the BCB above the wire bond pads in a final photo-lithographic dry etching process.

After the bump deposition, a thick photo-resist layer was spin-coated on top of the wafers to protect the bumps from oxidation, contamination, and mechanical damage during further processing, transport, storage and handling. The photo-resist layer also eases the handling and manipulation of single chips at KIT.

To reduce the material budget originating from the ROC silicon bulk, dead material was removed from the backside. The ROCs were thinned from a thickness of approximately $700\,\mu m$ to a thickness of approximately $175\,\mu m$ in a wafer back grinding process. Afterwards, the ROCs were diced into rectangles of $7.9 \times 10.3\,mm$ and placed into Gel-Pak® Vacuum Release Trays (VRTs). The VRT is designed to handle and transport sensitive micro-electronics in a electrostatic discharge (ESD)-safe way. By applying a vacuum from the backside, the adhesion of the device to the Vacuum Release Tray (VRT) is reduced, allowing the operator to remove it.

Before sending the ROCs to KIT, a final optical inspection was performed at RTI, screening major defects caused by the bumping, thinning and dicing procedures.

8.3.2 Readout chip cleaning

In general, the processing of microelectronic devices is very sensitive to any kind of pollution or contamination. Depending on the kind of contamination, devices can be mechanically damaged during processing or surfaces can become inactive to the process. The contaminations can originate from many different sources, like impure process baths, transportation, handling tools or the operators themselves. Event though the amount of contaminations can be reduced by working in a clean room environment, it can never be fully avoided.

To get rid of pollutions and contaminations, dedicated cleaning procedures can be introduced. Dust particles adsorbed from the air are typically removed by flushing the surface with compressed air. Inorganic contaminations, such as ionic compounds or salts are typically removed by flushing water or water baths, since the strong polarity of water allows dissolving polar components. Non-polar components, such as organic compounds on the other hand are typically removed by acetone. A compromise that allows removing both organic as well as inorganic contaminations is isopropyl alcohol, due to its polar OH-group and its non-polar CH_3-group. Additionally mechanical power can be added by using ultrasonic baths. In an ultrasonic bath, a generator creates compression waves with a frequency of $20\,kHz - 400\,kHz$, applying a small force on contaminations on the surface. This can be used to remove very strong and chemically resistive contaminations (e.g. metal).

In the KIT production line, the bump structure of the ROCs was shielded from contamination by a thick layer of photo-resist. To further process the ROCs, this photo-resist layer had to be removed in a chemical cleaning process. The basics of the cleaning process have been established in [Kud14]. It has later been further developed in [Col16] as well as in this thesis.

The cleaning process was based on sequential wet baths of acetone, isopropyl alcohol and water to remove inorganic contaminations. Organic pollutions as well as the photo-resist layer itself were removed in a bath of pure acetone ($> 99\,\%$). Next, the removal of inorganic pollutions in a pure bath of water would have been intuitive. But since non-polar acetone does not mix with polar water, an intermediate bath of pure isopropyl alcohol ($> 99\,\%$) was introduced to remove the acetone. Using water as a final bath has the advantage that water can typically be provided at much higher purity than chemical solvents like acetone or isopropyl alcohol, keeping impurities originating from the baths themselves at

minimum. To speed up the evaporation of the remaining water, the cleaning tray (CT) was placed into a a vacuum chamber and heated to approximately $50 - 70\,°C$ until all water was evaporated.

To handle the ROCs during the cleaning procedure, a customized tray structure has been designed and produced. The CT is made of a thermoplastic material called Polyoxymethylen (POM) that is doped with small conductive particles embedded into the polymer structure[2]. These conductive particles make the POM slightly conductive and ESD-safe [KHP14]. POM has been selected as the ideal compromise of several requirements. It is:

- chemically resistant to the solvents used in the cleaning procedure;

- safe against ESD;

- soft enough not to scratch the ROCs;

- well mill-able with standard industrial Computerized Numerical Control (CNC) machines to allow precise mechanical processing;

- temperature stable up to $70\,°C$.

The CT houses a matrix of 7×5 cavities to keep the ROCs in position during the cleaning baths. Each cavity has a depth of $300\,\mu m$ and its geometric dimensions fit those of the ROC including $150\,\mu m$ at each side of the ROC ($7.9\,mm + 0.3\,mm \times 10.3\,mm + 0.3\,mm$). Each cavity is equipped with a small hole, allowing the application of a vacuum to the ROC backside to keep the ROCs in position. The vacuum itself is created by a Venturi tube. The fixation via a vacuum on the backside could be used to remove dust particles with compressed air. During the chemical baths, however, the usage of a Venturi tube vacuum system would have been dangerous for the operators[3]. To keep the ROCs from floating during the cleaning process, a Polytetrafluoroethylene (PTFE) grid fixed to an aluminum frame is mounted on top of the CT. Figure 8.6 shows the CT structure as well as the PTFE grid.

During the time of production, the cleaning procedure was continuously improved, in order to improve the quality, while minimizing the time and the amount of chemicals required. The final cleaning procedure looked as follows:

1. pick electrically good ROCs from VRT and place them into cavities of CT using vacuum tweezers and mount PTFE grid. Since the ROCs are still protected by the thick photo-resist layer, the usage of vacuum tweezer is much more indulgent than using standard tweezers.

2. place CT into first acetone bath for $2\,min$ to remove photo-resist

3. move CT from first into second acetone bath for $2\,min$ to remove residual photo-resist and other organic pollutions. The second acetone bath would become the first acetone bath of the next cleaning procedure

4. move CT into intermediate isopropyl alcohol bath for $2\,min$ to remove residual acetone

---

[2]Such a conductive Polyoxymethylen material is commercially known as POM-ESL.

[3]Acetone has a low evaporation pressure of approximately $0.3\,mbar$ at room temperature [AST74]. Any acetone leaking into the Venturi tube would evaporate immediately and irritate all operators in the room [Uni18]. Furthermore, it is highly flammable.
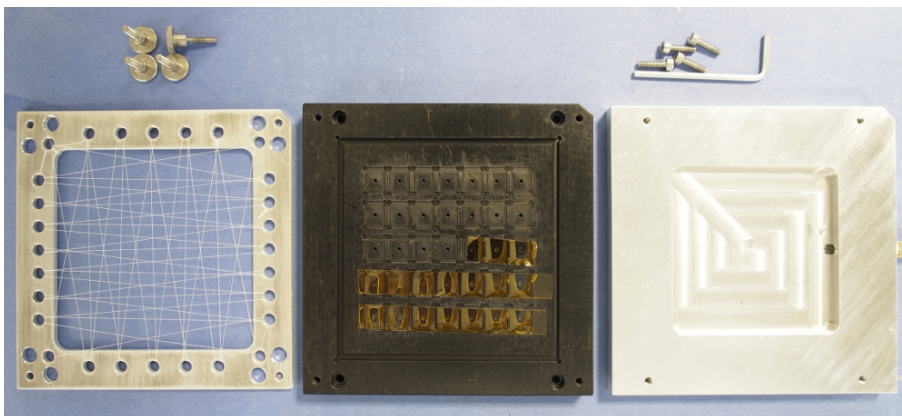
Figure 8.6: Cleaning tray structures used for cleaning procedure. The cleaning tray used to house the readout chips (ROCs) during the cleaning procedure is shown. On the left, the Polytetrafluoroethylene grid used to keep the ROCs from floating is shown. The vacuum system used to apply vacuum at the backside of the ROCs is shown at the right [Kud14].

5. move CT into first water bath for 2 min to remove inorganic pollutions and contaminations as well as remaining residuals of isopropyl alcohol

6. move CT from first into second water bath to ensure highly pure final cleaning bath

7. remove CT from second water bath, remove PTFE grid and place CT in vacuum chamber

8. apply vacuum and heat and wait for water to evaporate.

In total, the cleaning of a single CT housing 35 ROCs took about 30 min. About half of that time was required to evaporate the remaining water within the vacuum chamber, allowing the operator to start a second cleaning sequence in parallel.

The CT was designed in such a way that the backside vacuum could be used to keep all 35 ROCs in position while flipping the CT on top of a VRT. Alignment structures in the CT cause the ROCs to be released onto the VRT bumped area facing down and arranged in a regular 7×5 matrix once the backside vacuum was released. Before flipping the ROCs onto the VRT, a detailed optical inspection was performed. The optical inspection and its results are presented in the following section.

8.3.3 Optical inspection and selection of readout chips

To ensure good bump bonding quality and to give direct feedback to the cleaning sequence, a detailed systematic optical inspection was performed on all ROCs. For complex components like ROCs that have undergone many different processing steps a large variety of failures can occur. A selection of typical failures are listed here:

- organic or inorganic residuals from cleaning process potentially influencing the intermetallic connection between bump and sensor UBM

- dust particles adsorbed from clean room air potentially causing a misplanarity of the flip-chip bonding or damages to the microelectronic structures

- cratering at the ROC edges or silicon pieces originating from dicing, causing damages to the microelectronic structures

- missing or miniaturized bumps due to failures in the bump deposition, resulting in a missing bump bond connection

- misshaped or enlarged bumps due to failures in the bump deposition, resulting in shorts between pixels

- oxidized or contaminated wire bonding pads, potentially making wire bonding to the HDI impossible

- missing BCB passivation potentially having caused damages to the microelectronics structure during the bump deposition process

Figure 8.7 shows exemplary failure modes observed during the production.

To systematically check for so many different failure modes on over 8000 electrically good ROCs with over 30 million bumps, a dedicated optical inspection process was established. Since the optical occurrence of failures could vary on a case-by-case basis, the presence of an experienced operator in the assessment of potential failures and the selection of good material was indispensable. At the same time, the enormous number of bumps that had to be inspected required some kind of pre-selection.

A compromise between the different requirements was found by developing a basic pattern recognition software program that directly points the experienced operator to potential defects on the ROC. The operator then inspected the potential defects and decided whether the ROC is suitable for production. The optical inspection procedure was separated into three major steps:

1. A gray scale high resolution picture of every ROC in a CT is taken and stored for inspection and later reference using a semi-automatic digital microscope.

2. A basic pattern recognition software program analyzes the pictures and searches for potential failures.

3. An experienced operator analyzes the potential failures and decides whether the ROC is suitable for bonding, has to return to the cleaning process, or has to be removed from the production queue.

The pattern recognition software was developed (although not documented) as part of [Hit15]. It is based on National Instruments^{TM} LabWindows^{TM} and uses pattern recognition packages provided by National Instruments^{TM} Vision [Nat17a; Nat17b].

First, microelectronic structures on the chip are used to align the picture and extract the bumped matrix of PUCs. The gray scale picture is transferred into a binary image with darker pixels considered black and brighter pixels considered white. The threshold for this transformation has been determined empirically at the beginning of the production. For further analysis of the picture, clusters/structures of black pixels have been considered. To suppress statistical noise, small structures with fewer than 10 pixels have been ignored. To identify objects and to distinguish them from well-shaped bumps, the area as well as the circumference of pixel structures have been measured. If a structure shows significant deviations from the expected bump area and circumference it is shown to the operator, who decides whether it is a real failure or not. In addition, the ROC edges as well as the wire bonding pads are shown to the operator. Figure 8.8 shows the graphical user

(a)

(b)

(c)

(d)

(e)

(f)

(g)
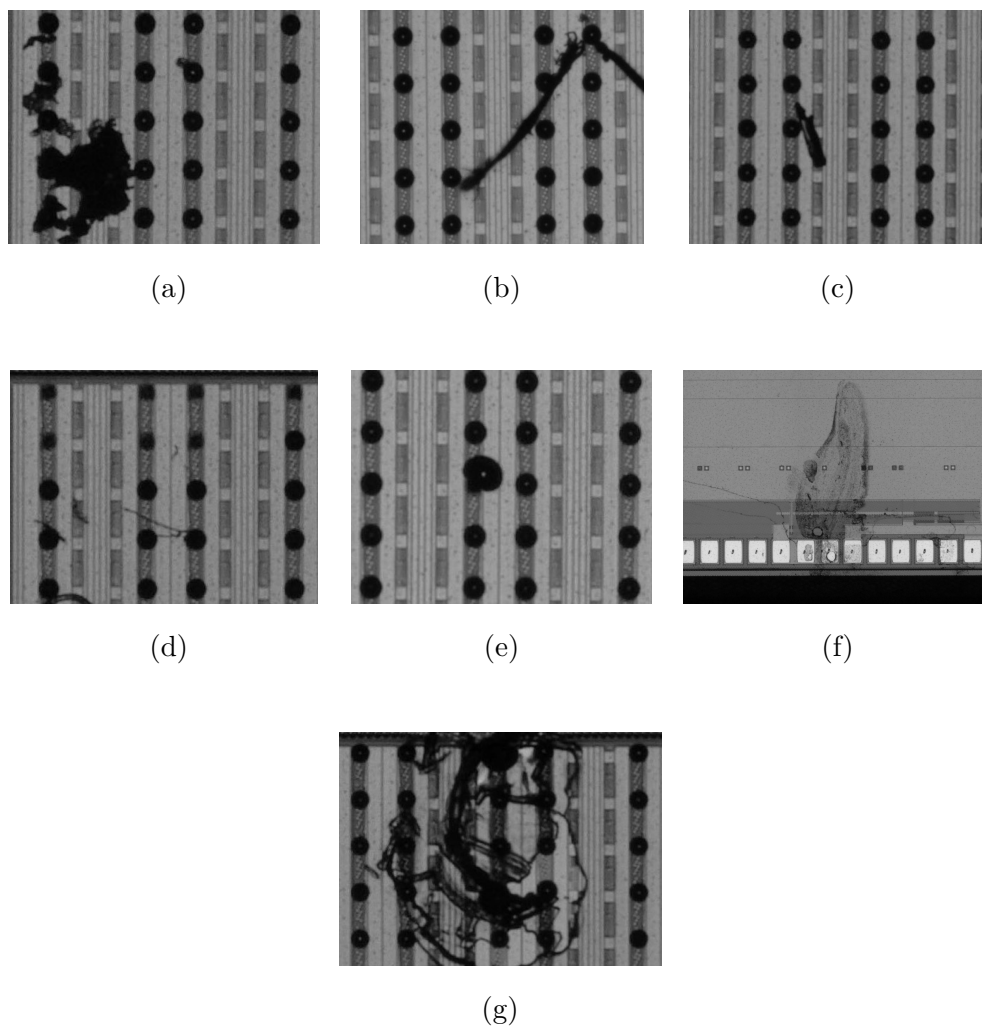
Figure 8.7: Typical failures detected in optical inspection of readout chips. A selection of typical issues on the ROCs detected by the optical inspection during the production: a) organic contamination, b) dust particle from clean-room environment, c) silicon splinter, d) missing bumps, e) enlarged/misshaped bump, f) contaminated wire bonding pad, g) failure in Benzocyclobutene passivation.
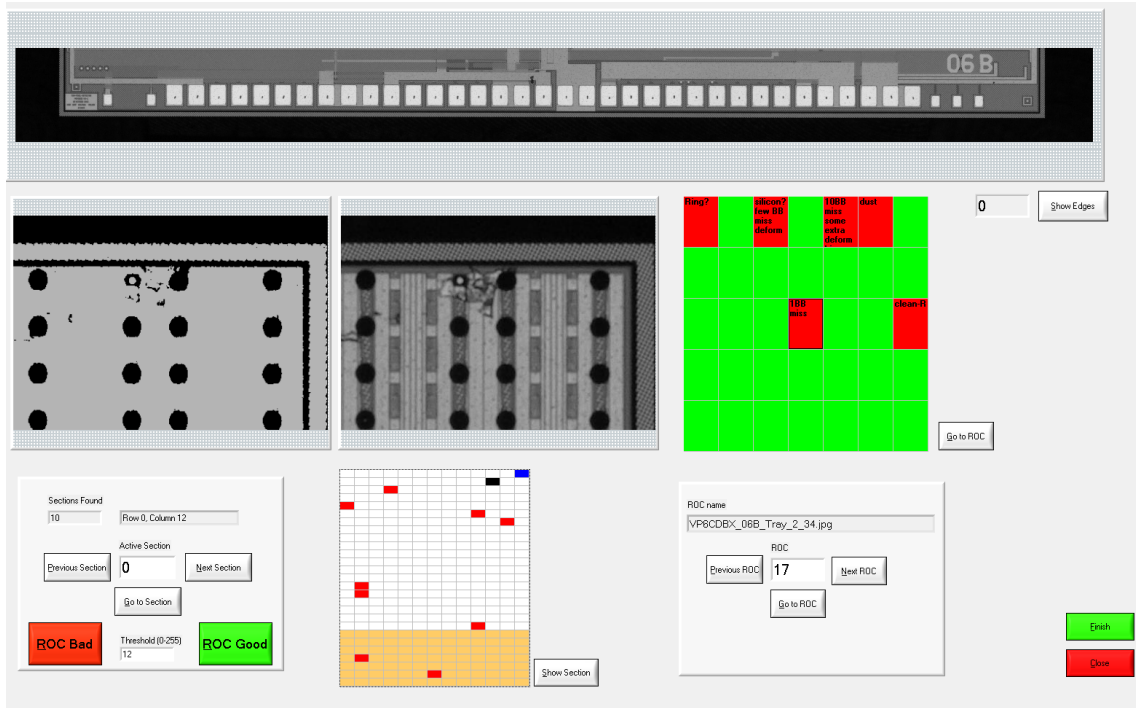
Figure 8.8: Semiautomatic optical inspection software. The GUI of the custom optical inspection software is shown. On the top, the wire bonding pad area and ROC edges can be displayed. On the right, an overview of the optical inspection results of a cleaning tray is displayed. ROCs at green positions are accepted for production, red ROCs show issues to be resolved. The center left shows a region with a bumping failure in the binary picture as well as the gray scale picture. An overview of the regions with potential failures is shown below.

interface (GUI) of the optical inspection software and gives an idea about the pattern recognition principle.

By operating the optical inspection software on a server equipped with sufficient Random Access Memory (RAM) to process the large pictures, the optical inspection was decoupled from the rest of the bump bonding operations, preventing any interference in the work flow.

Based on the failures detected during the optical inspection, the ROCs were selected. To do so, criteria similar to the optical inspection of the silicon sensor were defined, by estimating the number of readout channels potentially affected by the failures. For example, a missing bump was expected to only cause a single missing readout channel, while a oxidized wire bonding pad was expected to make the whole ROC unreadable. Only ROCs with not more than four defective readout channels were used for the production of bare modules. If a ROC showed issues connected to the cleaning process, the ROC was returned into the cleaning procedure. Pollutions like dust particles from the clean room environment could be removed by flushing with compressed nitrogen.

For the majority of the production period, KIT decided not to use ROCs processed on different wafers within a single bare module. This way, no risk of processing variations between different wafers influencing the module quality was taken. Furthermore, any undetected processing issues in the production of a ROC wafer would not be spread over many

Table 8.1: Results of optical inspection of readout chips. The table shows the most relevant failure modes detected during the production at KIT. The failure modes are listed as percentages of all inspected ROCs, and as percentages of the fraction of ROCs that were the accepted/rejected for the production.

Failure mode	all ROCs	accepted/rejected ROCs
92 % accepted for production (grade A)		
no failures	65 %	71 %
minor bump deformations	16 %	17 %
removable pollutions	8 %	9 %
< 5 missing bumps	2 %	2.2 %
contaminations on < 5 bumps	1 %	1.1 %
8 % rejected in optical selection (grade C)		
irremovable contaminations	6 %	75 %
≥ 5 missing bumps	1 %	12.5 %
others (bad dicing, oxidized wire bond pads, missing BCB, enlarged bumps)	1 %	12.5 %

detector modules but be limited to only those modules produced from the corresponding wafer. Only at the very end of the production period, the remaining ROCs were combined into bare modules built from two different ROC wafers each. By doing so, KIT made sure that a maximum efficiency of material usage was achieved while keeping the number of mixed bare modules as low as possible.

On average, the optical inspection and ROC selection of a CT housing 35 ROCs took about 60 min. In total, about 90 % of the 9000 ROCs produced for KIT were initially tested as electrically good by PSI. From these ROCs approximately 8 % where rejected in the optical inspection and removed from the production queue. The majority of those rejected ROCs ($\approx 75\%$) were rejected due to contaminations that could not be removed in additional cleaning sequences. The origins of these contaminations could partially be tracked back to the bumping process at RTI. After reporting to RTI, the contamination issue was fixed. Only 3 % of the inspected ROCs showed missing bumps and only 1 % were rejected due to missing bumps. Table 8.1 illustrates the distribution of the most frequent failure modes.

The majority ($\approx 71\%$) of the accepted ROCs did not show any issues, proving the high quality of the bumping, dicing, thinning and cleaning processes. For 17 % of the accepted ROCs, especially in the first batch of ROCs, minor bump deformations had been detected. The influence of the bump deformation on the bump bonding quality has been tested to be negligible. By giving feedback to RTI, the issue could be fixed for the subsequent batches.

The optical inspection and selection of ROCs embodied a central role within the quality assurance at the KIT production line, by giving frequent feedback to the bumping and cleaning processes. At the same time, the ROC selection got frequent feedback from the bare module and full module qualification described in section 8.4.2 and 8.7.2. However, the process was associated with a large human effort. It is therefore strongly recommended to intensify the use of more automated pattern recognition techniques. Furthermore, it is recommended to consider the use of advanced machine learning technologies to achieve a basic material categorization and reduce the human effort [Nie18; GBC16].

8.4 Quality assurance tests of bare modules

To develop and implement an in-house flip-chip bonding process at KIT, several quality assurance tests had been introduced. This follows the BPIX philosophy of frequent checks and feedback to ensure a high production quality. The development of the quality-assurance test was performed in close cooperation with other production lines providing comparability among the quality of the different production lines.

The quality-assurance tests introduced at KIT to monitor the bump bonding interconnection quality can be separated into two categories that are described here, mechanical tests and electrical tests.

8.4.1 Mechanical quality-assurance tests

By destructive and non-destructive mechanical tests, the flip-chip bonding alignment as well as the inter-metallic connection and the resulting mechanical strength can be tested before and after a reflow[4]. Five different types of test methods were available for developing and the monitoring the production. An illustration of the mechanical quality-assurance test is given in Figure 8.9.

1. By applying an increasing controlled force perpendicular to the bump bonding plane of an assembly, the connection can be strained until it breaks. This quality test is also known as *pull test*[5]. The force at which the breaking point is reached, is a good indicator for the mechanical strength of the assembly. Furthermore, the breaking mechanism indicates the quality of the inter-metallic connection. A good mechanical strength is required since it typically is accompanied by a good electrical connection.

   In a single sided bump bonding process with bumps only applied to one silicon die, the ideal breaking mechanism is either a break within the bump leaving both UBMs covered in solder or a lift-off of the whole aluminum contact pad. Both breaking mechanisms show that the mechanical strength of the bump bonding process is only limited by the mechanical strength of the solder or the silicon die itself. The numerical value of the force required to separate the dies depends on the process quality, the number of interconnections, the bump diameter and the bump material. Typical pull forces for bump bonding processes with bumps of $30\,\mu m$ diameter are $2 - 20\,mN/bump$ [Kud14; Bro+06].

2. Another mechanical quality check can be performed by applying an increasing controlled force parallel to the bump bonding plane until the bump bonding connection breaks. This test, also known as *shear test* can be performed on bump bonding

---

[4]The most common standard for such quality assurance tests is the so-called MIL-STD-883 developed by the Department of Defense of the United States of America [US 91].

[5]Corresponding to test-procedure 2031.1 of the MIL-STD-883.

assemblies to test the quality of the interconnection as well as on single bumps to test the quality of the bumping process itself. Besides the numerical value of the force required to break the assembly, the breaking mechanism indicates the quality of the inter-metallic connection.

Similar to the pull test, a break within the bump material is desired, since it indicates a good inter-metallic connection between the UBM and the bump material. Depending on the bump material and diameter, shear forces of $20\,\mathrm{mN/bump} - 100\,\mathrm{mN/bump}$ are expected for bump diameters of $30\,\mathrm{\mu m}$. During the production of BPIX detector modules at KIT, the shear test has been used on a random basis to check the quality of the RTI bumping process by shearing single bumps. During the whole production period, the expected shear force of $> 4.5\,\mathrm{mN/bump}$ could be confirmed [Huf+03].

All pull tests and shear tests were performed using a DAGE 4000 bond tester manufactured by Nordson. A cartridge able to apply forces up to $\approx 100\,\mathrm{N}$ was used for the pull tests and a cartridge able to apply forces up to $\approx 2\,\mathrm{N}$ was used for the shear tests [Nor18]. For a more detailed description of the pull test and the shear tests procedure, see [Kud14].

3. The alignment, planarity and the inner structure of a bump bonding interconnection, can be checked in a cross-section. Here, a bump bonding assembly is ingrained into an epoxy resin protecting structures on micrometer level. In well controlled and precise grinding processes, material is removed from the assembly until the region of interest is reached. Further polishing of the surface using diamond polishes with grain sizes down to $1\,\mathrm{\mu m}$ gives vision to a planar cross-section through the assembly [Str18]. The cross-section then can be inspected with an optical microscope, an SEM or energy-dispersive X-ray (EDX), allowing a detailed inspection of the metal composition within a single bump but also measurements on the assemblies' planarity and alignment.

4. Another, non-destructive, way to inspect the planarity of a bump bonding assembly are precise laser metrology measurements. Here, a laser measurement device measures the distance between the backside of the ROC and the surface of the silicon sensor die with sub-micrometer precision. Assuming a homogeneous thickness of the ROC, the distance between ROC and sensor can be estimated. Furthermore, the measurement can be used to estimate the bending of ROCs and sensor before and after the reflow.

5. X-ray scans of the assembly give an additional way to non-destructively inspect the alignment of an assembly. If the resolution is good enough, they further allow the measurement of metal density distributions within a bump and can be used to check for possible mechanical or structural anomalies. Unfortunately, this measurement was not available in-house and therefore was only rarely used.

   All X-ray scans have been performed at RJL Micro & Analytic in Karlsdorf-Neuthard, Germany using Bruker SkyScan 1172 and SkyScan 1272 computer tomography machines [Bru18].

During the development of the flip-chip bonding process at KIT, mainly destructive mechanical tests (1-3) have been performed, since they allow more insight into the process parameters and the physics at microscopic level. During the production of bare modules, destructive mechanical tests have been performed on a sample basis using test structures, since they are very time consuming and since the test material was limited. Instead non-destructive measurements (4 and 5) were more and more used to ensure a consistent bump bonding process.
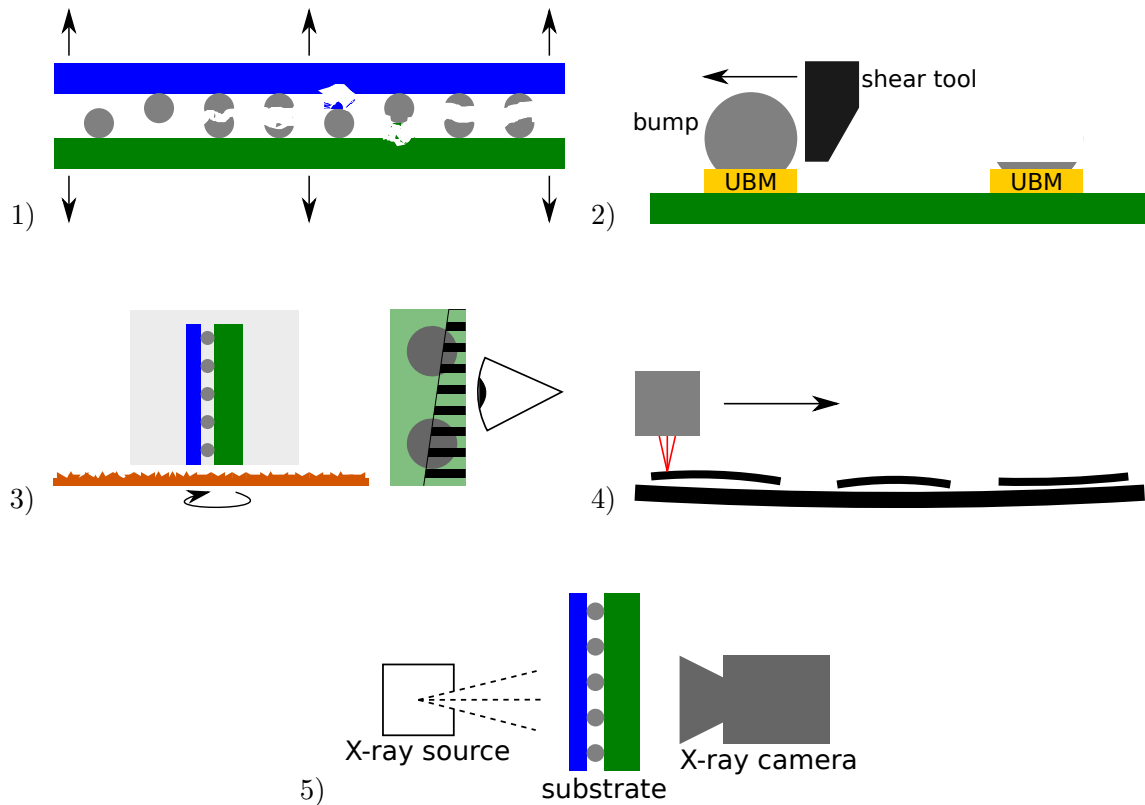
Figure 8.9: Illustation of mechanical quality assurance test. The working principles for the quality checks available to develop the flip-chip bonding process and to produce bare modules at KIT are illustrated: 1) pull-test, 2) shear-test, 3) cross-section, 4) laser metrology, 5) X-ray scan.

8.4.2 Electrical bare module test

By electrical tests, the conductivity of every bump bonding interconnection can be tested as well as the influence of the flip-chip bonding process on the noise condition and the readout efficiency. Electrical tests on the quality of the bump bonding process have been performed on every bare module during the production allowing a systematic monitoring of the bump-bonding quality. To perform such a large number of test in a clean environment and to allow a quick feedback to the flip-chip bonding process as well as the material selection, a dedicated bare module probe station was installed within the class 1000 clean room next to the flip-chip bonder[6]. The bare module probe station was designed and built at KIT. Further dedicated test routines and a semi-automatic test software was designed, developed and implemented at KIT. Since the electrical bare module test was a central quality assurance instrument, an overview of the setup and the test sequence shall be given. For a more detailed description, see [Hit15; Fre17]

The basic idea of the KIT bare module probe station is to temporarily contact a bare module allowing the depletion of the silicon sensor and the operation of a single ROC.

---

[6]Clean rooms are typically classified by the number of particles allowed in a certain volume of air. A class 1000 clean room, according to the US FED-STD-209E standard has a maximum of 1000 particles with a size larger than $0.5\,\mu$m in cubic foot of air. This roughly corresponds to a class ISO 6 clean room according to the more recent ISO 14644-1 standard.
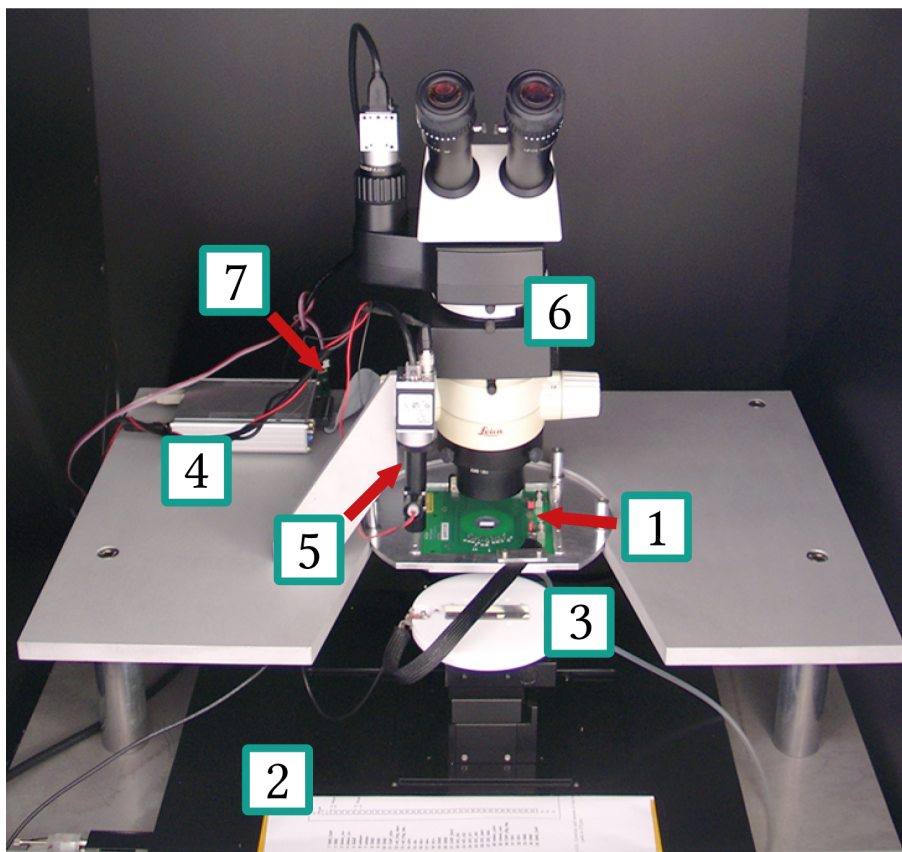
Figure 8.10: KIT bare module probe station. The inside of the KIT bare module probe station is depicted. Labeled are the central components of the bare module probe station: 1) needle card, 2) motorized stages, 3) PTFE chuck with bare module loaded, 4) Digital Test Board, 5) alignment camera, 6) stereo microscope, 7) temperature and humidity sensors. In the background, the metal housing is visible [Fre17].

Figure 8.10 shows the inside of the KIT bare module probe station. The central part of the bare module probe station is a motorized positioning stage that allow precise x-, y- ,z- and φ-movements. A PTFE chuck is mounted on top of the positioning stage to fix a bare module by vacuum while shielding it from the static noise of the motorized stages. Alignment pins on the PTFE chuck are used for a rough alignment of the bare module. The bare module is placed with the sensor side up and its backside is contacted via a needle allowing an external Keithley 2410 high voltage power supply to apply a bias voltage [Kei17]. The ROCs can be contacted by a needle probe card, which is equipped with 35 fine needles arranged in a pattern corresponding to the wire bonding pads of the ROCs. The probe card is permanently fixated to the probe station's structure. Using the motorized stages, the ROCs can be brought into contact with the needles of the probe card allowing the operation of a ROC. The ROC is operated and read out by a Digital Test Board (DTB), a custom FPGA-based board designed for laboratory tests during the production [SMP15]. The KIT bare module probe station is equipped with two optical systems. The first one is a fixated high magnification camera used for automated alignment of the bare module. The second one is an optical stereo microscope that can be used to verify the alignment and the contacting of the ROCs. To ensure a safe, controlled, dark, dry and noise-free environment for the bare module testing, the test setup is surrounded

by a metal housing continuously flushed by dry air. The whole probe station is placed on top of an anti-vibrational table, decoupling the station from external vibrations potentially causing a crash of the needles into the wire bonding pads.

A custom GUI-based software controls all movements and operations of the probe stations. It is written with National Instruments LabWindows/CVI and the National Instruments Vision Development Module [Nat17a; Nat17b]. The software automatically performs all pattern recognition, and alignment processes, test sequences and movements, supervised by an operator. Implemented within the GUI-based software, a custom test software called pixel Xpert analysis & readout (pXar) performs the actual electrical test of the ROC [SMP15]. After the automated test sequences, the test results are displayed to the operator as well as stored into the central database.

Using the KIT bare module probe station, the following three tests have been systematically performed on all bare modules produced at KIT:

- **Electrical characterization of the silicon sensor:** Based on an I-V measurement, the silicon sensor is tested for possible damages in the sensor structure caused by the flip-chip bonding sequence.

  Although similar to the test sequence already described in Section 8.2.2, the I-V measurement on bare module significantly differs in the way the current flow through the sensor is measured. Different to the I-V measurement on sensor level, the ground for the I-V measurement is not provided by the bias grid on the sensor front side but by the ground of the connected ROC. While the depletion via the bias grid relies on a good connection between front and back-side using the sensor edges and the punchthrough structure, the grounding via the ROC depletes the sensor in the way it is intended to be depleted. This enables a more reliable detection of defects in the sensor bulk material.

  During the production period, a significant number of silicon sensors (≈ 8) showed worse I-V characteristics when using the connected ROC as ground potential than the standard I-V measurement using the bias grid on the sensor front side. This behavior has been interpreted as silicon bulk defects, not detectable by the sensor selection described in Section 8.2.2. To screen such bulk defects and minimize the amount of ROCs wasted on such undetected bad sensors, the flip chip bonding sequence was interrupted for an additional I-V measurement within the bare module probe station. This I-V measurement was performed with only two of the 16 ROCs connected, allowing an automated alignment and a sensor characterization while keeping the amount of potentially lost ROCs at minimum. If the sensor passed the selection, the flip-chip bonding of the remaining 14 ROCs was performed.

- **Test of electrical functionality and programmability of ROCs:** This test performs several functionality checks on the readout structures of the ROC as well as every single PUC. To do so, the internal calibration block of the PUC (described in Section 7.3.2) is exploited. Figure 8.11 illustrates the internal calibration mechanism. By injecting a built-in calibration signal into the preamplifier of the PUC, the full readout chain can be tested. 10 calibration pulses injected into every PUC are used to determine the noise level, possible cross-talk among pixels, and as well as dead pixels.

- **Custom bump bonding quality test** To test the bump bonding quality, a dedicated bump bonding test has been introduced. In this test, the built-in calibration
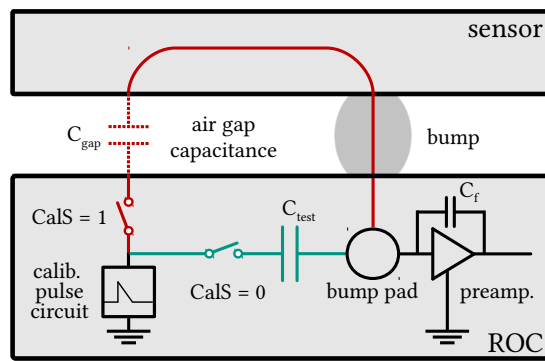
Figure 8.11: Internal calibration mechanism of readout chip. By creating internal calibration pulses, the front-end electronics as well as the bump bond interconnection can be tested. The CalS register controls whether the calibration pulse is directly injected into the preamplifier (turquoise) or into the sensor (red). Only if the calibration pulse can be read out either way, the pixel is considered good (modified from [Fre17]).

signal is not injected directly into the preamplifier of the PUC, but into the depleted sensor via the small air-gap between silicon sensor and ROC. The charge induced into the signal can then be readout by the ROC, if a reliable bump bonding interconnection exists. The concept of this test is illustrated in Figure 8.11. For the bump bonding test performed at KIT, 100 calibration pulses were injected into the sensor. If more than 50 % of the calibration pulses could be read out, the bump bonding interconnection was considered to be reliable.

In general the parameters and efficiencies of this test strongly depend on the noise conditions as well as the air gap distance between ROC and sensor. This air gap distance is defined by the bump bonding process and parameters used. In order to find a reliable parameter set, a dedicated study has been performed. The selected parameter set has been tested on a test module which had single solder bumps intentionally removed before flip-chip bonding. Figure 8.12 shows the results of this verification test. Additional validation was provided by efficiency tests using characteristic X-rays and electrons from a ^{90}Sr source to generate charge carriers within the silicon sensor. For a more detailed description on the studies around the KIT bump bonding test, see [Hit15; Fre17].

The complete test sequence required approximately 60 min with the dominant time ($\approx$ 40 min) dedicated to the electrical tests of the ROCs. The remaining time is required for motor movements and alignment ($\approx$ 10 min), I-V measurement ($\approx$ 5 min) and the loading and unloading of the bare module ($\approx$ 5 min). Since the KIT bare module probe station was located within the same room as the flip-chip bonding machine, the electrical test provided essential feedback with a turn-around time of only one hour.

Based on the results of the electrical tests, the bare modules were categorized into grades corresponding to the expected grade the full module would have. The categorization was performed as follows:

- **Grade A.** Bare modules with low leakage current ($I_{\text{leak}}(150\,\text{V}) \leq 2\,\mu\text{A}$) at room temperature and a slow breakdown ($I_{\text{leak}}(150\,\text{V})/I_{\text{leak}}(100\,\text{V}) \leq 2$) as well as a low digital current consumption on all ROCs ($I_{\text{dig}} < 65\,\text{mA}$). Furthermore, the
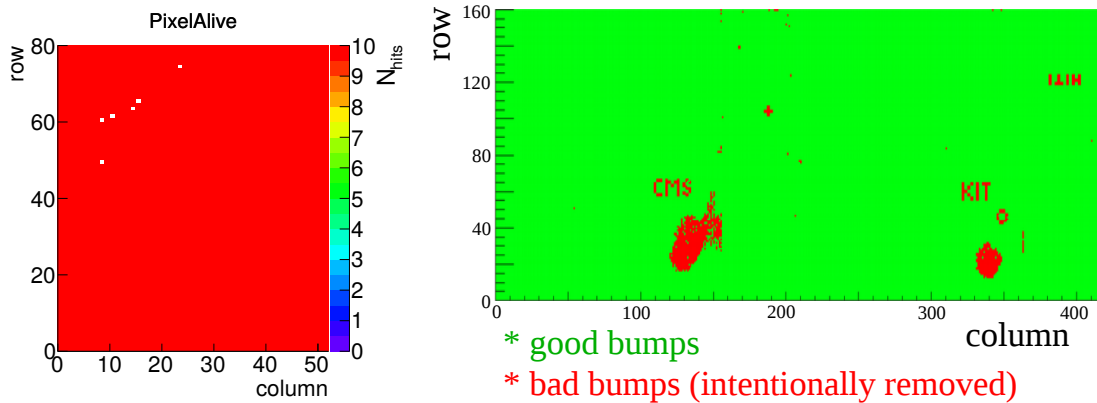
Figure 8.12: Electrical bare module test results. Exemplary results of the pixel alive test (left) and the KIT bump bonding test (right) are shown. In the pixel alive test, pixels that did not detect any injected calibration pulses are considered dead and are marked white. The bump bonding test was performed on a customized bare module that was used to tune the parameters of the bump bonding test. It is visible that the locations of intentionally removed bumps are detected by the bump bonding test procedure [Hit15; Kud17].

number of defective readout channels of every ROC is required to be < 42 (1%). Defective readout channels can be caused by defective PUCs, broken bump bond interconnections or defects in the DCol.

- **Grade B.** Minor defects in the performance of the bare module compared to the grade A bare modules, such as an increased leakage current at room temperature ($2\,\mu A < I_{\mathrm{leak}}(150\,\mathrm{V}) \leq 10\,\mu A$) or an increased number of defective readout channels ($42 \leq \mathrm{number\,of\,defective\ pixels} < 167$, $1\% - 4\%$).

- **Grade C.** Major defects in the performance, such as a high leakage current at room temperature ($I_{\mathrm{leak}}(150\,\mathrm{V}) > 10\,\mu A$) or a fast breakdown ($I_{\mathrm{leak}}(150\,\mathrm{V})/I_{\mathrm{leak}}(100\,\mathrm{V}) > 2$). Also bare modules with an increased digital current consumption ($I_{\mathrm{dig}} \geq 65\,\mathrm{mA}$) or a large number of defective readout channels ($167 > \mathrm{defective\ pixels}$, $> 4\%$) on any of its 16 ROCs are considered as grade C.

For the sake of clarity it should be mentioned here that KIT decided to perform the electrical bare module test before the reflow. This allowed the replacement of single defective ROCs, which would not have been possible after a reflow had been performed on the bare modules. A more detailed description of the so-called reworking procedure is given in Section 8.5.4. Depending on the grading, the bare module was either prepared for the reflow, underwent the reworking, or was rejected from further processing.

8.5 Flip-chip bonding

While a basic overview of the flip-chip bonding process has already been given in Section 6.3, this section is dedicated to a more detailed understanding of the process as well as the technical requirements and challenges of this process. First, the machinery used during the production is described before the optimization processes of the flip-chip bonding process is discussed.

The flip-chip bonding process at KIT can be divided into two subprocesses that were performed on different machineries. The first subprocess is the precision placement of the ROCs onto the silicon sensor and the establishment of an interconnection by thermocompression – also called tacking. The second subprocess is the reflow of the bonded assembly.

8.5.1 Infrastructure at IPE

The tacking subprocess was performed using a full-automatic FINEPLACER®femto flip-chip bonder machine manufactured by Finetech GmbH in Berlin, Germany. Since the FINEPLACER®femto was selected by both, KIT as well as DESY, a frequent exchange of experience and ideas among the production centers was possible and technical issues were tackled in close cooperation with the manufacturer[7]. Figure 8.13 shows the FINEPLACER® femto flip-chip bonder machine as well as a detailed view on the bonding area of the machine.

The central part of the flip-chip bonder machine is formed by a movable *bonding table*. Linear motors allow fast and precise movements in x-, y- and φ-direction. An additional high resolution drive in combination with a sensitive force sensor allow precise z-movements and the placement of sensitive material. Two *presentation plates* are mounted on the left and right side of the bonding table and can be used as input and output areas for components used in the process. At the center of the bonding table where the actual bonding takes places, a highly planar $100\,\text{mm} \times 100\,\text{mm}$ *bonding area* is situated. The temperature of the bonding area can be controlled thanks to an external heating module and a custom-designed cooling system based on compressed air. Vacuum structures within the bonding area as well as within the presentation places allow a reliable fixation of bonding components as well as VRTs. The vacuum itself is provided by a Venturi tube system.

Above the bonding table, a *placement arm* is located. It is mounted perpendicular to the surface of the bonding area and has a single rotational degree of freedom around the x-axis. Driven by a direct current motor, the placement arm can be rotated by $90\,°$ down onto the bonding surface and apply a user-defined force onto the bonding area to tag a die onto a substrate. An inclination sensor monitors the arm position and a dedicated force sensor measures the force applied by the placement arm. At the far end of the placement arm, the *bond head* is mounted. It consists of a gimballed *pickup tool* and a dedicated vacuum and heating system. The pickup tool is equipped with a vacuum structure connected to the Venturi tube vacuum system to hold components. The gimbal suspension allows the pickup tool to adapt to any surface underneath and maintain the acquired orientation during the bonding process. The pickup tool is designed to fit the geometric dimensions of the ROC. It is mounted in such a way, that the pivot point of the gimbal joint is centered above the center-of-gravity of the ROC bumping matrix, ensuring a homogeneous force distribution among all solder bumps of the ROC.

In general, the bonding area can be closed by a motorized lid, creating a *process chamber* and allowing the usage of process gases during the bonding and even enabling the possibility of performing a reflow on the flip-chip bonder machine itself. This way a well controlled environment can be ensured during the bonding process. At the center of the metallic lid, a circular hole allows the placement arm to reach the bonding area through the lid. The

---

[7]Much of the experience collected during this production went into the design of the next generation of finetech flip-chip bonder machines [Fin17].
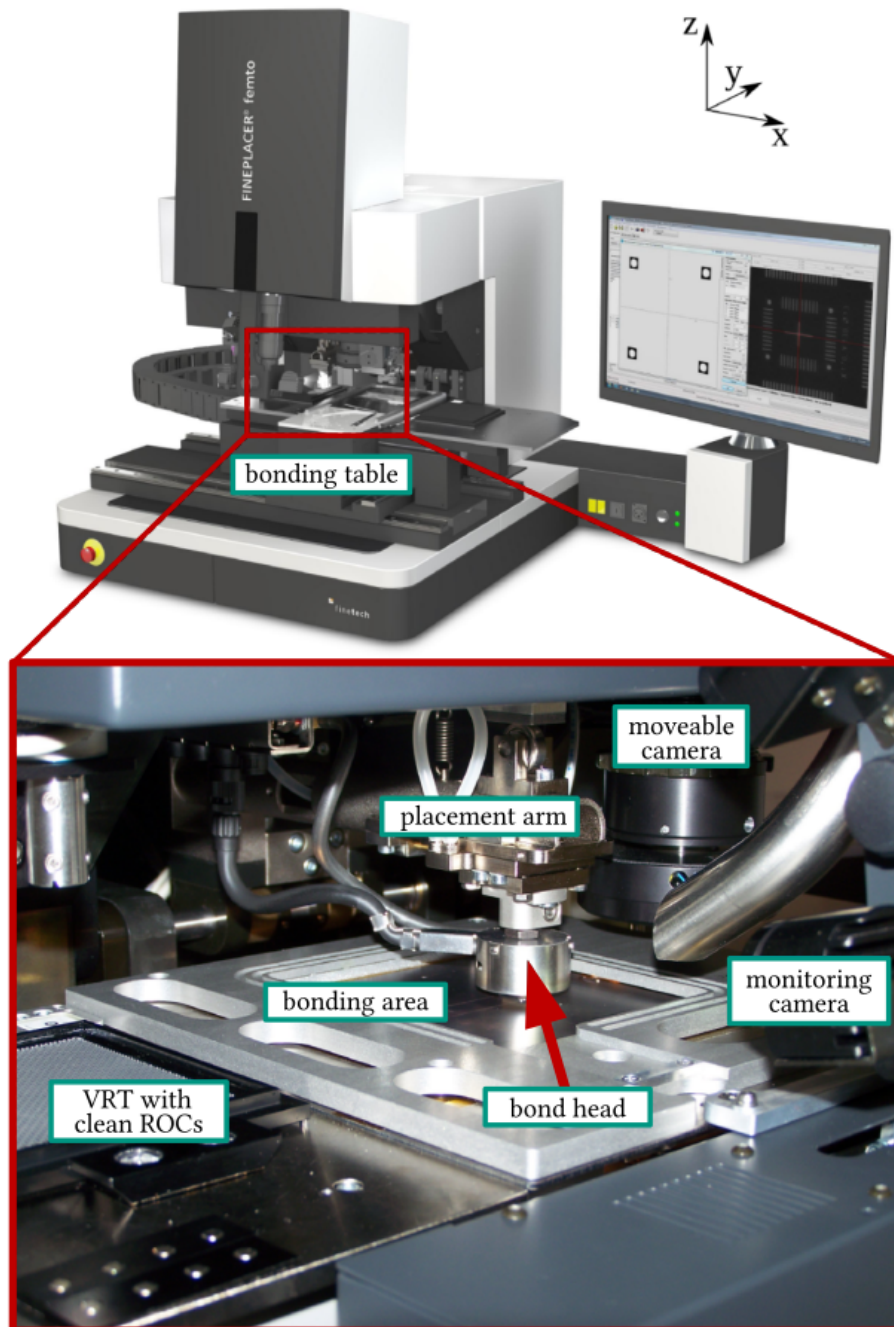
Figure 8.13: Flip-chip bonding machine. An overview of FINEPLACER®flip-chip bonder machine at the Institute for Data Processing and Electronics is shown (top) as well as a more detailed view of the bonding area and its surroundings (bottom). The machine is shown with the placement arm in "touch-down position" lowered onto the bonding area (modified from [Kud14]).

size of the hole corresponds to the diameter of the bond head resulting in the bond head closing the process chamber once the placement arm is lowered onto the bonding area.

The FINEPLACER® femto flip-chip bonder machine is equipped with two optical camera systems. Above the bonding table, a high resolution camera is mounted movable along the x-axis. A 60 mm long beam splitter is mounted below the camera, allowing a single camera to simultaneously visualize a component picked up by the placement arm and a substrate placed on the bonding area via two independent optical focusing systems. The usage of a beam splitter is common for such precision placement applications since it enables a much more precise alignment of the components than using two independent camera systems. Since the FINEPLACER® femto is a fully automatic flip-chip bonder, the alignment of components is provided by sophisticated pattern recognition software. A second camera is mounted in front of the bonding area and can be used to monitor the bonding process.

The whole bonder machine is placed on an anti-vibrational table to decouple the machine from external vibrations and tremors. The control of the machine is provided by an external computer running custom software provided by the manufacturer.

With the FINEPLACER® femto flip-chip bonder machine, it is possible to place components with a placement accuracy of approximately $0.5\,\mu m$ and a planarity resolution $< 4\,\mu rad$. For the thermo-compression bonding, forces of $0.5\,N - 500\,N$ can be applied and the pickup tool as well as the bonding area can be individually heated to temperatures of $50\,°C - 400\,°C$[8].

To reflow tacked and successfully tested bare module assemblies, two reflow systems were available. During the development of the bump bonding process at KIT, the possibility to perform the reflow within the process chamber of the FINEPLACER® femto flip-chip bonder was heavily exploited to derive and investigate the basic process parameters. The FINEPLACER® femto machine is designed to handle nitrogen (N_2) and formic acid (H_3COOH) as well as mixtures of these two as process gases at temperatures up to $400\,°C$. These process gases can be tuned to the bump bonding process to prevent or remove oxidation of the metals during the process and to improve the bump shape.

Later on, the SRO-700 vacuum reflow oven manufactured by ATV Technologie GmbH in Vaterstetten, Germany was made available. Figure 8.14 shows the SRO-700 reflow oven installed during the production period. The SRO-700 has the advantage of a better control over the reflow parameters and environment conditions during the reflow thanks to its hermetically closed vacuum chamber. Furthermore, its approximately $23\,cm \times 22\,cm$ large vacuum reflow chamber allows to reflow several bare modules assemblies simultaneously, greatly increasing the possible throughput of the reflow subprocess. The SRO-700 vacuum reflow oven is able to handle a large variety of process gases (N_2, H_3COOH, H_2, etc.), but also is able to perform reflow processes under vacuum thanks to a dedicated vacuum pump reducing the pressure within the process chamber below $5\,mbar$ [ATV18]. An array of eight high-power infra-red Quartz glass tubes provides process temperatures of up to $450\,°C$ and temperature ramp-up rates of up to $3.5\,K/s$. By flushing the process chamber with N_2 at the maximum available flux, a cool-down rate of $2\,K/s$ can be achieved.

Both machines were located within the Institute for Data Processing and Electronics (IPE) class 1000 clean room. Only the vacuum pump of the SRO-700 vacuum reflow oven was moved outside the clean room to avoid pollutions originating from its oil based lube.

---

[8]The FINEPLACER® femto flip-chip bonder machine is operated at a base operation temperature of $50\,°C$, limiting the minimum bonding temperature.
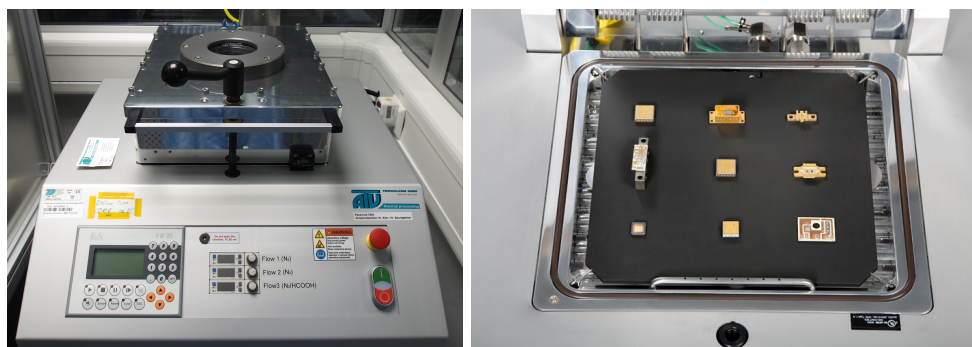
Figure 8.14: SRO-700 vacuum reflow oven. The industrial vacuum reflow oven that was used to perform the reflow of bare module assemblies during the bare module production (left) is shown as well as its large reflow chamber equipped with some electronics components (right) [ATV18].

8.5.2 Optimization of tacking subprocess

In order to provide a reliable bump bonding process, a well controlled and optimized tacking process is essential. Since the tacking process is defined by a large variety of parameters, KIT decided to iteratively optimize the tacking process for alignment, planarity, mechanical strength, reliability and speed.

To do so, a basic process sequence that seemed feasible was selected as a starting point and was continuously adapted and improved during the optimization. The basic process sequence looked as follows, and can be considered as a general basic process sequence:

1. A pattern recognition identified a ROC in a VRT placed on the left presentation plate as well as a silicon sensor die placed on the bonding area.

2. By lowering the placement arm onto the ROC and applying a vacuum to the vacuum structure of the pickup tool, the ROC was picked up from the VRT.

3. Another pattern recognition identified the bumping structure on the ROC and the UBM structure on the silicon sensor.

4. After aligning the bump and UBM structures, the placement arm was lowered into its touch-down position above the sensor and by raising the bonding table, ROC and silicon sensor were brought into contact.

5. For about $60\,\mathrm{s}$, the placement arm applied a defined bonding force of $100\,\mathrm{N}$ perpendicular to the sensor surface while the temperature of both, the pickup tool and the bonding area, was increased to $150\,^{\circ}\mathrm{C}$.

6. The vacuum on the pickup-tool was released and the placement arm was raised leaving the ROC bonded to the silicon sensor.

In the first iteration, the placement accuracy and planarity were optimized. Although the FINEPLACER® femto machine possesses internal procedures to calibrate the precision placement, the final placement accuracy strongly depends on the application, the component geometry as well as the bonding parameters. To optimize the placement for this specific application, a series of assemblies has been created using the basic process sequence. After separating the components in a pull-test (see Section 8.4.1), an optical inspection was performed on the bumps on the ROC-side. The footprint of the UBM structure released

(a) not aligned   (b) aligned
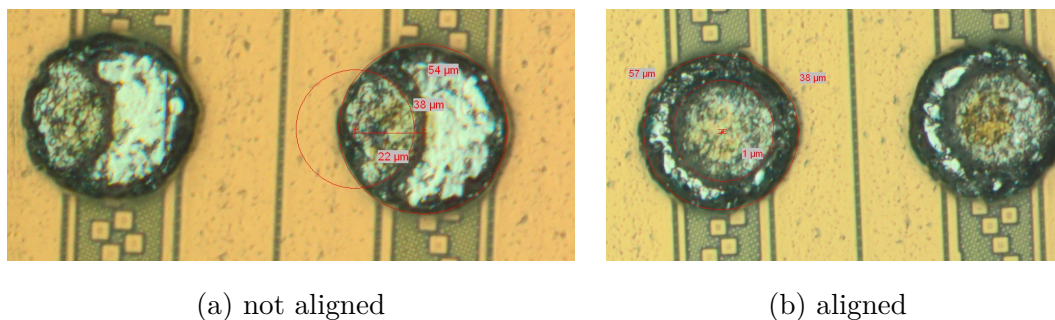
Figure 8.15: Optimization of the placement accuracy. The footprints released by the sensor UBM structure onto the solder bumps after a pull-test are shown. The deviation of the center of the footprint from the center of the solder bump was used to estimated the residual misalignment and to optimize the placement accuracy. a: UBM footprint before placement optimization, b: UBM footprint after placement optimization.

onto the soft solder bumps was used to measure the placement precision. To do so, the deviation of the center of the UBM footprint from the center of the solder bump was measured at different positions of the bump bonding matrix. By comparing the deviations at different locations, systematic shifts could be distinguished from rotations. This way the precision placement was re-calibrated to ensure that the bumps are well aligned to the UBM structure for all bump bond positions. Figure 8.15 shows the footprint released by the UBM structure on the solder bumps before and after the re-calibration of the precision placement.

During the beginning of the production period, a large variance of the placement accuracy was observed driven by single assemblies with displacements much larger than the average typical precision. The origin of these outliers could be tracked down to variations in the bumping process, resulting in an insufficient precision in the pattern recognition, since only two of the bumps were used to align the components. To be independent of these variations, the pattern recognition was performed on micro-electronic structures on the ROC and the silicon sensors for the further production. To further ensure that the thermal conditions during the bonding sequence were uniform for all ROCs bonded to silicon sensor, the temperature of the silicon sensor was kept at a constant value during the whole tacking sequence. This way, any residual influence of thermal dilatations could be minimized.

The planarity of the flip-chip bonded assembly was ensured by several different parameters. In order to exploit the ability of the gimballed pickup tool to adapt to the sensor surface, the bonding force profile of the thermo-compression bonding was modified. By adding a low-force bonding step with only $30\,\mathrm{N}$ applied before the actual thermo-compression bonding, the gimbal suspension could adapt to the sensor surface without deforming the solder bumps too much. Figure 8.16 shows the working principle of the gimbal mechanism.

The gimbal mechanism showed to be able to compensate a major mis-planarity. However, it was not able to provide a reliable planarity $< 1\,\mathrm{mrad}$. The reason for this behavior was found in the way the vacuum system of the pickup tool was designed. By applying a vacuum to the pickup tool, an additional friction within the gimbal suspension is introduced, resulting in the inability of the gimbal mechanism to compensate mis-planarities at small scales. Furthermore, the performance of the gimbal mechanism depends on the precision of the initial pickup, since the pivot point of the gimbal suspension is required to be centered
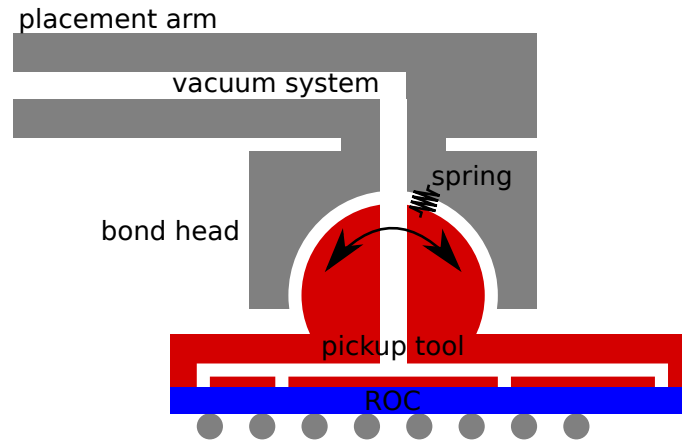
Figure 8.16: Gimbal machanism for adaptive planarity. The working principle of the adaptive gimbal mechanism, designed to provide a good planarity, is illustrated. Mounted movable in its orientation relative to the sensor surface and above the center-of-gravity of the bump matrix, the gimbal mechanism ensures a homogeneous force distribution among all bumps. By applying vacuum to the system, the readout chip is fixed to the pickup tool.

above the center-of-gravity of the bump position matrix. Both these effects make the performance of the gimbal mechanism strongly dependent of the ROC pickup from the VRT. Since the surface of the VRT cannot be guaranteed to be parallel to the bonding area and since the pattern recognition of the ROC edges on the VRT showed to be not reliable, an additional intermediate process step was implemented.

Before placing the ROC on the sensor surface, it is lowered onto a flat ceramic surface located at the right presentation table of the flip-chip bonder machine. Since the ROC could be well distinguished from the ceramic surface independently of the ROC dicing quality, the precision and reliability of the pattern recognition could be improved. By lowering the placement arm into touch-down position and applying an extra force of 4 N to the ROC without any vacuum applied, the gimbal mechanism could fully adapt to the ceramic surface before picking up the ROC. A good parallelism between the ceramic surface and the bonding area was achieved by an iterative optimization procedure of alternating planarity adjustments on the ceramic surface and planarity checks based on cross-sections through the flip-chip bonded assemblies (see Section 8.4.1).

As a next step, the parameters of the thermo-compression bonding were optimized in order to provide a strong and reliable mechanical connection based on inter-metallic diffusion. Providing a good alignment and planarity, the thermo-compression bonding is defined by the force applied during the bonding, temperatures of the materials and the duration of the thermo-compression bonding. In general, the bonding temperature is required to be as low as possible to avoid electro-migration processes, but high enough to provide sufficient inter-metallic diffusion. Likewise, the bonding force is required to be large enough to provide a suitable bump deformation and a full coverage of the UBM surface with solder, but small enough to ensure no damage to the components nor any short circuits among the solder bumps. The influence of the bonding duration on the mechanical strength is minor as long as it is long enough to ensure stable conditions during the thermo-compression bonding.

(a) not optimized   (b) optimized
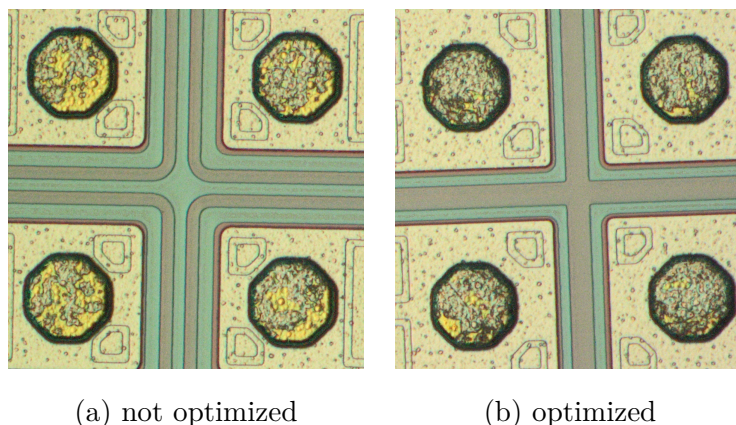
Figure 8.17: Thermal diffusion of solder onto sensor UBM. Sensor UBM structures for an un-optimized (a) and an optimized (b) tacking process after the pull-test are depicted. The percentile area of the UBM (gold) covered in SnPb (gray) from the solder bumps was used as an indicator for a homogeneous metal diffusion.

Using internal force and temperature sensors of the FINEPLACER® femto flip-chip bonder machine, conditions like the applied force and the temperature were monitored during the process and a total bonding duration of approximately 85 s was selected. In a series of test assemblies, the bonding temperature and bonding force were optimized. The assemblies were separated in pull-tests (see Section 8.4.1) and the mechanical strength as well as the breaking mechanisms were used to identify a suitable parameter combination. In addition, the percentage of UBM surface covered by SnPb solder after the pull-test was considered. Figure 8.17 shows exemplary test results of this optimization process. A parameter combination was considered to provide a suitable and homogeneous metal diffusion of bump material into the UBM structure if more than 80 % of every UBM structure was covered by residuals of SnPb solder.

Since the alignment of the precision placement also depends on the bonding force and temperature the alignment optimization procedures were repeated, providing an optimum precision placement as well as a suitable thermo-compression.

The following tacking process sequence and parameters were developed and later used to produce all bare modules:

1. Placement of the silicon sensor die on the bonding area with the UBM side facing up. Alignment pins can be used to ensure a flawless pattern recognition sequence later on. The silicon sensor is fixed by the built-in vacuum system.

2. Using the movable high resolution camera system, a pattern-recognition algorithm identifies the position the two lower corners of the silicon sensor. These are used to calculate the position and orientation of the sensor die relative to the internal reference system of the machine.

3. A VRT containing a pre-aligned 7×5 matrix structure of cleaned and selected ROCs (see Section 8.3.2) is placed on the left presentation table and vacuum is applied to the VRT backside.

4. After moving the presentation table below the movable camera system, the corners of the ROC are identified by a pattern recognition algorithm. The movable camera

moves aside and the placement arm is lowered onto the ROC. By applying a vacuum to the pickup tool, the ROC is picked up from the VRT and the placement arm is raised.

5. The right presentation table, housing the flat ceramic surface, is moved below the placement arm. The placement arm is slowly lowered onto the ceramic surface ensuring no damage to the bump structure, and the ROC is released on the ceramic surface.

6. In an additional pattern recognition sequence, the corners of the ROC are identified with high precision. The placement arm carefully picks up the ROC, applying a force of 4 N and allowing the gimbal suspension to adapt to the chip surface before raising back into its vertical home position.

7. In the meantime, the temperature of the bonding area has been increased to 140 °C. Using the beam-splitter, the machine simultaneously illuminates the ROC and the silicon sensor. Another pattern recognition procedure identifies unique micro-electronic structures on the ROC as well as on the selected bonding position of the silicon sensor. The position and orientation of the bonding table is iteratively adapted until a user-defined alignment precision is reached.

8. By lowering the placement arm the bumps of the ROC are brought into contact with the UBM structures on the sensor side, initiating the actual thermo-compression bonding process. While the placement arm lowers, the temperature of the ROC and the pickup tool is matched to the temperature of the bonding area. Figure 8.18 shows the force and temperature profile used for the thermo-compression bonding as a function of time. While the bonding temperature is kept at a constant value of 140 °C during the whole bonding process, the force profile shows "step-like" behavior. This step-like structure with a first step of 30 N has been selected to ensure a good, stable and planar contact before applying the actual bonding force of 100 N ($\approx$ 24 mN/bump) over a period of 50 s.

9. The vacuum on the pickup tool is released, the placement arm returns to its home position, and the temperature of the pickup tool is reduced to 65 °.

10. Steps $4-8$ were repeated until all the eight bond positions of the lower row of the sensor were equipped with ROCs. The partially bonded bare module was manually rotated by 180 °C in order to perform the bonding of the remaining eight bond positions requiring a re-alignment of the silicon sensor. During the KIT bare module production however, this process was interrupted by an additional I-V measurement on the KIT bare module probe station (see Section 8.4.2) to screen bad silicon sensors.

During the whole tacking process, the process chamber of the flip-chip bonder machine was flushed with N_2 at a continuous rate of 5 l/s.

An overall placement accuracy of 1.8 µm $\pm$ 0.16 µm[9] and a placement precision of 1.9 µm was achieved for the tacking process as well as a planarity of $\leq$ 1 mrad $\pm$ 0.16 mrad. However it should be mentioned here that the reflow process described in Section 8.5.3 further improved all of these quantities. In total, the flip-chip bonding of a full bare module, not including the time required for the intermediate I-V measurement, was performed within

---

[9]The uncertainties are derived as the expected statistical uncertainty on the average value derived from the measured distribution of the test samples. The limited sample size has been considered according to the Student's t-distribution assuming a 95 % confidence level [Gos08].
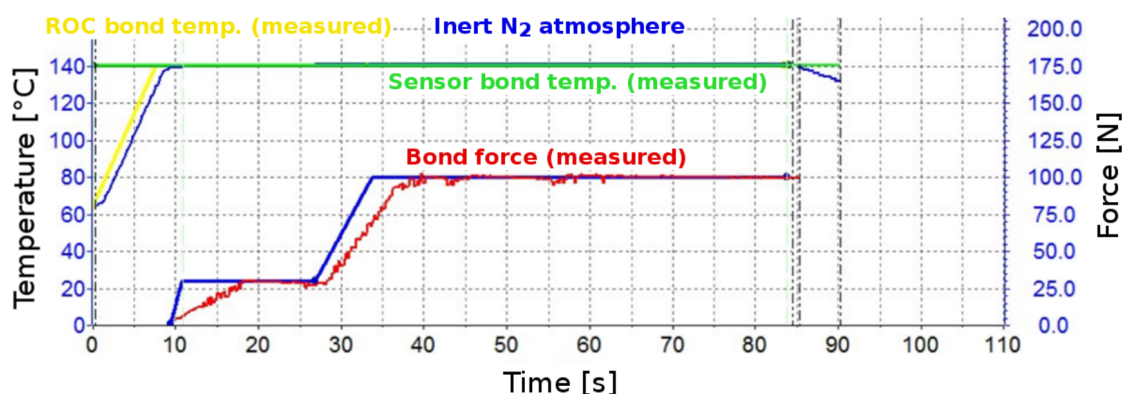
Figure 8.18: Force and temperature profiles of the KIT flip-chip bonding process. In the lower part, the force applied during the thermo-compression is shown (blue: set force, red: measured force). In the upper part, the temperature profile is shown (blue: set temperature of pickup tool, yellow: measured temperature of pickup tool, dark green: set temperature of bonding area, light green: measured temperature of bonding area). Since the temperature of the bonding area is set as constant during the whole process, the set and measured temperature profiles overlap [Col16].

approximately 60 min. Together with the time required for the electrical test of the bare module, this resulted in a typical turn-around time of 120 min, allowing a quick response to eventual quality issues.

8.5.3 Reflow subprocess

If a bare module had been successfully tested and was graded as production quality, it was ready to enter the reflow subprocess, designed to improve and fix the bump bonding interconnection. This was achieved by heating the assembly above the melting temperature of the eutectic SnPb solder (183 °C) in a controlled environment [Tu07]. The high temperatures increase the inter-metallic diffusion improving the mechanical strength of the assembly. At the same time, adhesive and cohesive forces within the liquefied solder ensure a homogeneous wetting of the UBM structure while reshaping the bump into a more spherical shape. In addition, the surface tension of the liquefied solder bump is minimized resulting in a self-alignment of the ROCs with respect to the silicon sensor.

The performance of the reflow process depends on many parameters (temperature profile, process gas composition) as well as the chemical processes happening at sub-micrometer level. Since the chemical processes are difficult to control on such small structures and since the chemical analysis of these processes requires expensive and time consuming analysis techniques, the optimization of the reflow process was a complex task mainly carried out as part of [Col16]. Nevertheless, a short summary of the investigations performed on the reflow process and the issues observed shall be given here.

In the early stages of the process development, the possibility to perform a reflow within the process chamber of the FINEPLACER® femto flip-chip bonder machine was exploited to develop a basic reflow process as starting point for further optimizations. In this basic process, the components were heated to a temperature of 235 °C for 100 s while continuously flushing the process chamber with a mixture of nitrogen and formic acid. The formic acid

(a)   (b)
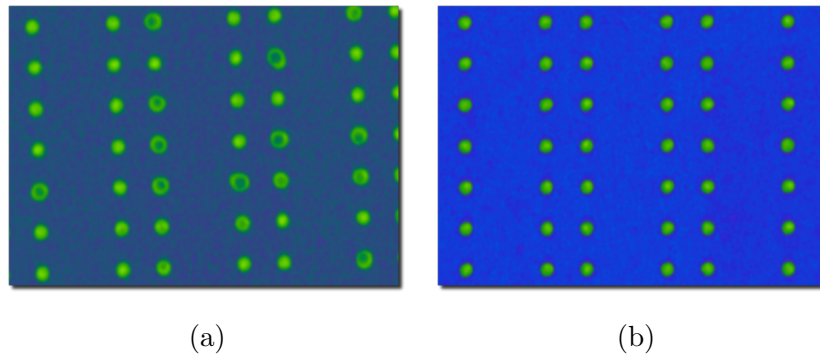
Figure 8.19: Micrometric voids within solder bumps. Shown are two X-ray scans of reflow test assemblies. The material density is shown as a color scheme with green corresponding to an area of high material density and blue corresponding to low material density. On the assembly shown on the left (a), a non-optimized reflow with a long dwell time ($\approx 225\,\mathrm{s}$) was performed. On the right (b), the result of a reflow with a dwell time $< 100\,\mathrm{s}$ is shown [Col16].

was added to reduce possible oxidations and to improve the surface tension of the bump. Detailed investigations of these early reflow tests in scanning electron microscopy (SEM) and EDX measurements as well as optical inspections and X-ray scans showed two issues.

The solder bumps showed a highly irregular and not spherical shape, and a lot of oxygen present on the bump surface. These observations were interpreted as a consequence of insufficient metal-oxide reduction due to the long time at high temperatures above the melting temperature of SnPb, if a hermetic process environment cannot be fully provided. Since especially the tin component of the eutectic SnPb solder is oxidized, the solder becomes non-eutectic resulting in a multi-phase condition. Similar behavior had been observed in other applications of larger geometric scales [NB82]. By introducing a two-step temperature profile with a first plateau at $150\,^\circ\mathrm{C}$ and a second rise to the peak temperature of $235\,^\circ\mathrm{C}$, the dwell-time was reduced, resulting in less metal-oxidation as well as a better temperature control during the process.

In addition, the formation of *micrometric voids* ($\varnothing \approx 5\,\upmu\mathrm{m} - 30\,\upmu\mathrm{m}$) within the solder bumps was observed in X-ray scans as well as in optical inspections of cross-sections and pull-tests (see Section 8.4.1). Although they do not directly affect the mechanical strength of the assembly, the concern with the micrometric voids was that they might reduce the long-term stability of the assembly during the operation within CMS. The formation of these micrometric voids was observed to be correlated to the length of the dwell-time, and was interpreted as a coalescence of smaller gas bubbles trapped inside the liquid solder bumps during the liquid phase [GA96]. The process gas used during the reflow process was identified as the origin of the gas bubbles, and by reducing the dwell-time the presence of micrometric voids was reduced. Figure 8.19 shows two X-ray scans of reflow test assemblies that were processed with an optimized and a non-optimized process.

Using the SRO-700 vacuum reflow oven allowed to address both of the observed quality issues. Since the SRO-700 provided a hermetically closed vacuum chamber, a oxygen-free environment could be provided by evacuating and flushing the process chamber with nitrogen multiple times. Furthermore, the possibility to perform the reflow under vacuum allowed to minimize the presence of process gases that could be dissolved within the liquid solder of the bumps. In addition, the SRO-700 vacuum reflow oven provided a more powerful cooling system than the FINEPLACER® femto flip-chip bonder machine
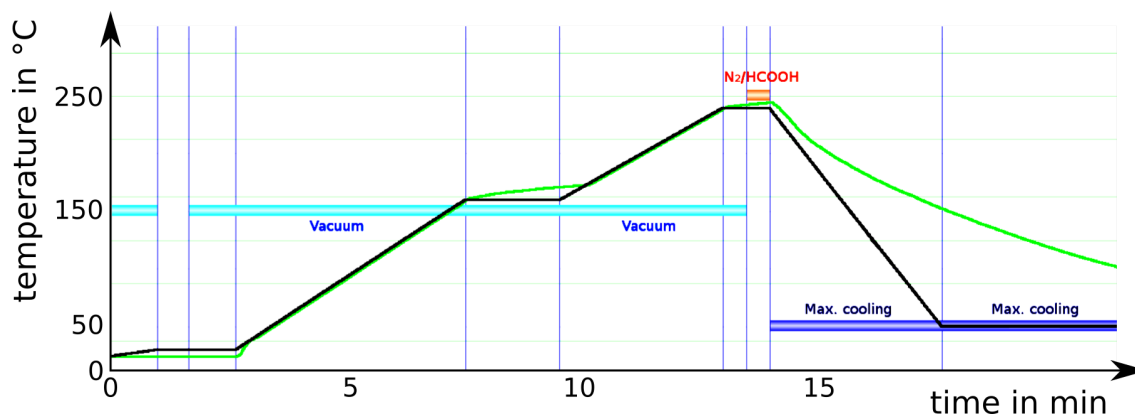
Figure 8.20: Temperature profile of reflow process used at KIT. The black line shows the set temperature of the profile, while the green line illustrates the measured temperature in the process chamber. During the vacuum reflow, a pressure of 3 mbar was reached. Only for a short time at the peak temperature (240 °C) a N_2/HCOOH mixture was injected into the process chamber. The final cooling at maximum speed (Max. cooling) was achieved by flushing the chamber with nitrogen (modified from [Col16]).

reducing the risk of an excessive formation of *inter-metallic layers* that could potentially create brittle solder bumps and reduce the overall mechanical strength [Pan+06].

The final reflow was performed using the SRO-700 vacuum reflow oven. The temperature profile of the final reflow process used during the bare module production at KIT is shown in Figure 8.20. Before entering the reflow process, all bare modules underwent another optical inspection to ensure no kind of contamination or pollution was present. This screening was necessary since residual pollutions or contaminations could become irremovable or even damage the assembly due to the high temperatures present during the reflow. After evacuating the air from the process chamber, it is flushed with nitrogen which is again evacuated ensuring a oxygen free process. The majority of the reflow was performed under vacuum. Only for a short period of time, the N_2/HCOOH gas mixture was released into the process chamber to improve the bump shape and to remove eventual metal-oxides originating from the pre-processing, tacking or testing. To cool down the process chamber as fast as possible, it was flushed with nitrogen at the maximum capacity available. Since the reflow was the last process of the bare module production sequence at IPE, a final optical inspection ensured that no potentially damaged material entered the full-module assembly at ETP. A special focus was put onto the wire bonding pads in order to screen potential oxidations on the pads caused by the reflow process.

In total, a full reflow process was performed within approximately 30 min, not including the time required for the final optical inspection. But since several bare module assemblies could be reflowed simultaneously, this was acceptable and the reflow process did not create any kind of bottleneck within the production workflow.

8.5.4 Bare module reworking

In a process as complex as a full bump bonding process, failures in the material selection and the processing are inevitable. To avoid that a single failure on a ROC compromises the quality and functionality of a whole bare module, the bare module reworking procedure

has been developed, allowing the replacement of a single ROC. The bare module reworking procedure was not only used to increase the overall production yield, but also to provide additional feedback to the tacking subprocess as well as the material selection.

If a ROC was selected to be replaced based on the electrical bare module test, the mechanical connection of this ROC to the silicon sensor had to be destroyed and a status similar to the one before the bonding of the ROC had to be established at its position. To avoid the risk of damaging neighboring ROCs, the bare module reworking procedure was performed before the reflow, while the bump bonding interconnection was still weak enough to ensure a controlled removal of the selected ROC.

To remove a single ROC, the whole bare module was placed on the bonding area of the FINEPLACER® femto flip-chip bonder machine, fixed by vacuum and heated to 130 °C. The problematic ROC was then removed by hand using tweezers to pull the part of the ROC housing the Double Column periphery and the wire bonding pads upwards. This way the bump bond interconnections were destroyed subsequently in a "domino-like" way, allowing a controlled and safe removal of the ROC[10]. The removed ROC was used to monitor the alignment and thermo-compression quality of the tacking process by optically investigating the footprint of the UBM structure released on the the SnPb bumps connected to the ROC as well as the amount of SnPb connected to the UBM structure. Furthermore, an optical inspection was performed with the aim of identifying the source of the failure of the ROC. The results of this optical inspection were cross-checked with the optical inspection performed after the cleaning.

Since the tacking process was optimized for high mechanical strength and since the passivation opening on the ROC-side was more than four times smaller than the passivation opening on the sensor side, about $0.5\% - 5\%$ of the bump bond interconnections were destroyed during ROC removal in a UBM lift-off on the ROC-side, leaving the solder bumps connected to the UBM on the sensor side. These bump remnants are potentially dangerous to a new ROC placed at this position since they might cause misalignments, reduce the planarity and create short circuits among several pixels.

To remove these bump remnants, a dedicated bump removal procedure has been established. In this procedure, the silicon sensor was fixed to a PTFE coated jig and fixed by vacuum. The bump remnants were individually sheared using the Nordson DAGE 4000 bondtester analog to the bump shear test described in Section 8.4.1. A series of shear tests showed that a shear-height of 7 μm was sufficient to prevent any damage to the UBM structure dealt by the shear tool. Figure 8.21 illustrates the reworking and the bump removal procedure.

If the bump remnants had been successfully removed, the bare module returned into the tacking sequence, a new ROC was tacked similar to the original ROC. To ensure that no damage has been dealt to the bare module by the bare modules reworking procedure, the new ROC and all adjacent ROCs were retested as well as an additional I-V measurement was performed, before performing a reflow. KIT limited the number of reworking procedures performed per bare module to one in order to limit the amount of oxidation and pollution on bare modules entering the full-module assembly.

Depending on the number of bump remnants connected to the sensor side, the bare module reworking procedure typically required 15 min to 45 min.

---

[10] A "domino-like" breaking mechanism is typically not desired in a classic pull-test (see Section 8.4.1), but in this context it has the benefit of a minimum risk for adjacent structures.
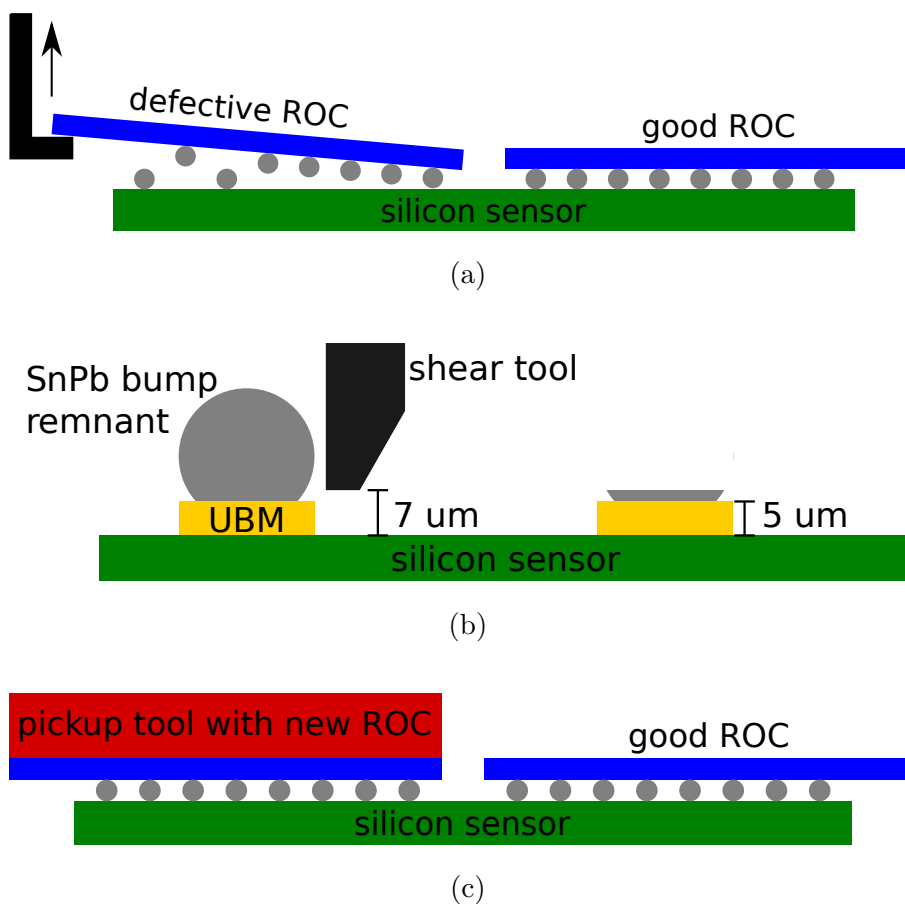
Figure 8.21: Bare module reworking procedure. The working principle of the reworking procedure developed at KIT are illustrated. After removing the selected ROC from the bare modules (a), the bump remnants on the sensor side were removed in a shearing process (b). At the same time the ROC-side was inspected to identify the origin of the defect. After the removal of the bump remnants, a new ROC was placed (c).

(a) (b)
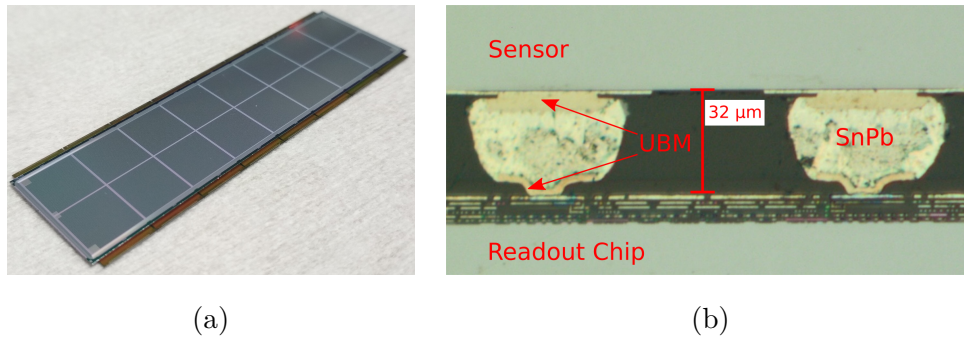
Figure 8.22: Bare module flip-chip bonded at KIT. On the left, a BPIX bare module assembled at KIT for the CMS Phase I Upgrade is shown. The silicon sensor and the 16 ROCs connected are visible. The right picture shows a cross section through a test assembly produced at KIT to verify the flip-chip bonding process. The picture shows that the UBM on both the ROC and the sensor side is well covered and that the solder bump is free of voids.

8.6 Bare module production results

During the whole production period at KIT, the production of bare modules was at the center of the process sequence. Designed to ensure a high bump bonding interconnection quality, the KIT bare module production process also had to provide a suitable production rate while using material efficiently and staying within the financial scope of the project.

During a period of approximately one year (May 2015 - May 2016), more than 8000 ROCs and 444 silicon sensors were cleaned, inspected and turned into bare modules. In total, 437 bare modules had been produced and electrically tested at KIT. This section is dedicated to summarizing the production yields, the mechanical and electrical quality-assurance test results as well as limitations in production rate.

Mechanical strength, placement accuracy and planarity After the reflow, the flip-chip bonding process developed at KIT showed a placement accuracy of $< 1\,\mu$m and a misplanarity of less than $0.3\,$mrad. The air-gap between the silicon sensor and the readout chip was measured to be approximately $32\,\mu$m wide and the diameter of the solder bumps was measured to be typically around $45\,\mu$m $- 65\,\mu$m. Figure 8.22 shows a bare module produced at KIT as well as a cross-section through a test assembly.

Mechanical tests performed on a sample basis showed excellent mechanical properties for the flip-chip bonding process. The strength of the mechanical connection was found to be typically larger than $10\,$kg/ROC ($23\,$mN/bump) but never less than $8\,$kg/ROC ($19\,$mN/bump). Optical inspections after the pull-tests showed UBM lift-offs from the ROC as the most common breaking mechanism indicating a reliable inter-metallic connection between the sensor UBM and the solder. The lift-off from the ROC-side is expected in these assemblies, since the un-passivated area connecting the UBM with the silicon structure on the ROC-side is more than four times smaller than the corresponding area on the silicon sensor side. The shear force value of $45\,$mN/bump quoted by RTI could be confirmed.

Bare module reworking yield Designed to enable the recovery of single bare modules that nearly missed the quality criteria, the bare module reworking procedure showed to be of such high quality that it soon became a backbone of the bare module production. Although

185

Table 8.2: Yield of the bare module reworking procedure. A reworking was performed if a ROC showed a cluster of more than ≈ 20 dead channels. The minus sign after the grade is used to distinguish between reworked an non-reworked bare modules. Overall, the rework improved the bare module quality in $90\,\%$ of the cases. Only for one bare module, the reworking procedure decreased the quality. On the other hand, 65 bare modules were recovered that would otherwise have been rejected (modified from [Fre17]).

grade	before rework		
after rework	A	B	C
A-	7	6	63
B-	0	2	2
C-	0	1	6

the original intention was to only rework grade C bare modules, the high reworking yield gave confidence to also perform reworks on selected grade A and grade B bare modules with a clusters of more than ≈ 20 defective pixels.

In total, 87 bare modules ($20\,\%$ of all produced bare modules) underwent the reworking procedure. In a majority of cases ($84\,\%$ of reworks) only a single ROC was replaced. Table 8.2 summarizes the yields of the reworking procedure based on the bare module grades before and after the reworking. For $90\,\%$ of the bare modules, the reworking procedure resulted in an improvement of the bare module grading. Only in a single case, the grading of a bare module was reduced from grade B to grade C, due to an early break down of the silicon sensor after the reworking. Overall, the reworking procedure resulted in a surplus of 64 bare modules that would otherwise have been rejected, which corresponds to one eighth of the modules required to equip layer 4 of the new CMS pixel detector. The quality of two grade B bare modules could not be improved. The optical inspection during the reworking procedure revealed scratches across the UBM structure which cannot be recovered by the placement of a new ROC. Six of the grade C bare modules could not be recovered, due to early breakdowns of the silicon sensors after the rework, mechanically damaged or electrically dead replacement ROCs, or due to large scale discolorations in the sensor UBM structures. It is unclear whether the damaged replacement ROCs and silicon sensors with UBM damages were missed by the optical and electrical inspections or whether they were damaged during handling.

The most common failure modes triggering the reworking procedure were electrically dead ROCs, problematic PUCs and DCol structures as well as missing bump bonding interconnection due to broken bump bonds or misalignments in the tacking process. For a more detailed analysis of the observed failure modes triggering the reworking, see [Fre17].

Electrical quality test results As already mentioned in Section 8.4.2, a significant percentage of silicon sensors showed an unexpected leakage current behavior not detected in any electrical characterization performed at CIS and ETP. By implementing an intermediate I-V measurement on silicon sensors connected to just two ROCs, such problematic sensors were screened. Over the period of the production, 422 of these so-called pre-test bare modules were produced and tested. A majority of 389 pre-test bare modules were graded A in the I-V measurements, while 13 were graded B and 20 were graded C. Unfortunately,
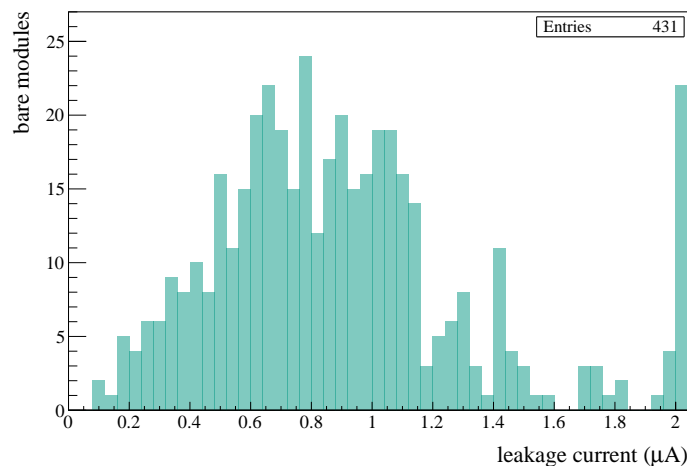
Figure 8.23: Leakage current distribution of bare modules. The distribution of measured leakage current at $V_{\text{bias}} = 150\,\text{V}$ for the 431 bare modules that could be depleted are shown. For the majority of bare modules, a leakage current distinctively smaller than the grading limit of $I_{\text{leak}}(150\,\text{V}) = 2\,\mu\text{A}$ was measured. The overflow bin contains all bare modules with larger leakage currents. Six bare modules produced at KIT could not be depleted due to an early break down and therefore are not included [Fre17].

a more detailed investigation of the I-V behavior of the silicon sensors was not possible, since the original wafer ID assignment was lost at PacTech$^{©}$. Since the yield of the other production processes was unknown at the beginning of the production, KIT decided to only turn grade A pre-test bare modules into full bare modules. Only two grade B pre-test bare modules were turned in to full bare modules at the end of the production period, maximizing the bare module output. By introducing the additional IV-measurement on pre-test bare modules, not only the number of ROCs but also the working time lost to defective silicon sensors were minimized. Overall, 29 additional bare modules could be produced within almost the same time, thanks to the additional pre-test bare module I-V measurement.

Based on the leakage current behavior of their sensors and the number of defective pixels detected, all bare modules produced during the production period were electrically qualified as described in Section 8.4.2.

Of the 437 bare modules assembled at KIT, 409 (94 %) showed a leakage current of $I_{\text{leak}}(150\,\text{V}) \leq 2\,\mu\text{A}$. For 22 bare modules (5 %), a leakage current of $I_{\text{leak}}(150\,\text{V}) > 2\,\mu\text{A}$ was measured. Six of the 437 bare modules produced (1.4 %) could not be depleted and therefore not be tested due to an early break down of the silicon sensor. In the following, only the test results of the 431 testable bare modules are shown. The measured leakage current distribution of the testable silicon sensors after the flip-chip bonding is shown in Figure 8.23. On average a leakage current of $I_{\text{leak}}(150\,\text{V}) = 0.9\,\mu\text{A} \pm 0.36\,\mu\text{A}$ (stat) was measured.

The number of defective readout channels per module, especially clusters of defective pixels, sets a strong limit on the tracking efficiency of the CMS pixel detector since the four tracking point coverage cannot be fully provided any more. For this reason, the number of defective readout channels (defective PUCs and defective bump-bond interconnections) is a common quantity to quantify the quality of a bare module. The number of defective pixels
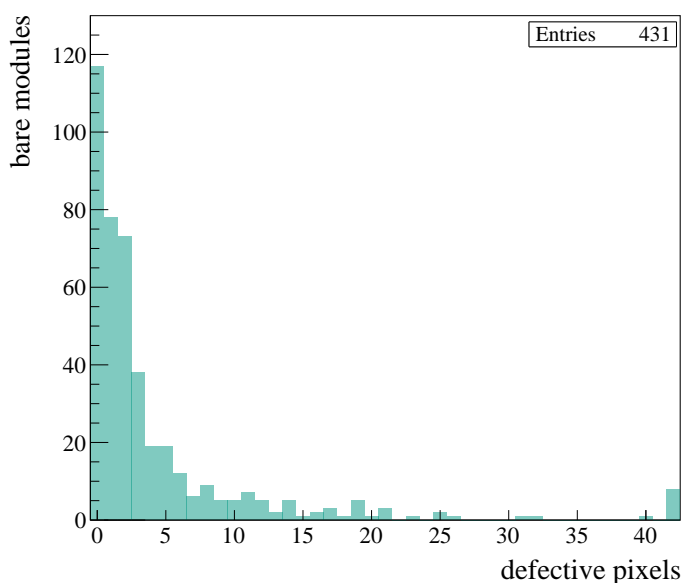
Figure 8.24: Distribution of defective pixels per bare module. The number of defective pixels was determined from the electrical qualification test. The overflow bin contains all bare modules with more than 41 defective pixels. Six of the 437 bare modules could not be tested due to an early voltage breakdown [Fre17].

is derived from the electrical functionality test and the custom bump bonding quality test. The distribution of the number of defective pixels per bare module is shown in Figure 8.24. The majority of bare modules (27 %) show zero defective pixels and 80 % of the bare modules have only five or fewer defective pixels. Only eight of the 431 tested bare modules have more than 40 defective pixels from which four are still grade A and the remaining four are grade C. Overall, 427 of the tested bare modules ($> 99\,\%$) fulfill the grade A criterion of fewer than 42 defective pixels per ROC. Two of the four remaining bare modules still fulfilled the grade B criterion of fewer than 167 defective pixels.

Bare module production yields Designed with the capacity to produce up to 16 bare modules per week[11], the bare module production line at KIT was operated for approximately one year, producing 437 bare modules. Figure 8.25 illustrates the production rate achieved at KIT by the number of bare modules produced and tested per week. It is clearly visible that the actual number of bare modules produced and tested per week reveals strong fluctuations. This is caused by the availability of components that were distributed among the production centers in several batches. During the summer of 2015, delays in the ROC production at IBM, and the ROC processing at RTI resulted in long interruption on the production. Additional interruptions were caused by the Christmas break 2015/2016 and by a temporary delay at RTI due to missing packaging material and due to a shortage of silicon sensors at the end of the production (Spring 2016). Since the silicon sensors and ROCs had to undergo several time consuming stages of pre-processing before being used to produce bare modules, stockpiling of components was not possible. So every lack of components resulted in an production stop and required a re-ramping of the production.

---

[11]The throughput was optimized to fit the maximum production capacity achievable by the full module assembly described in Section 8.7.
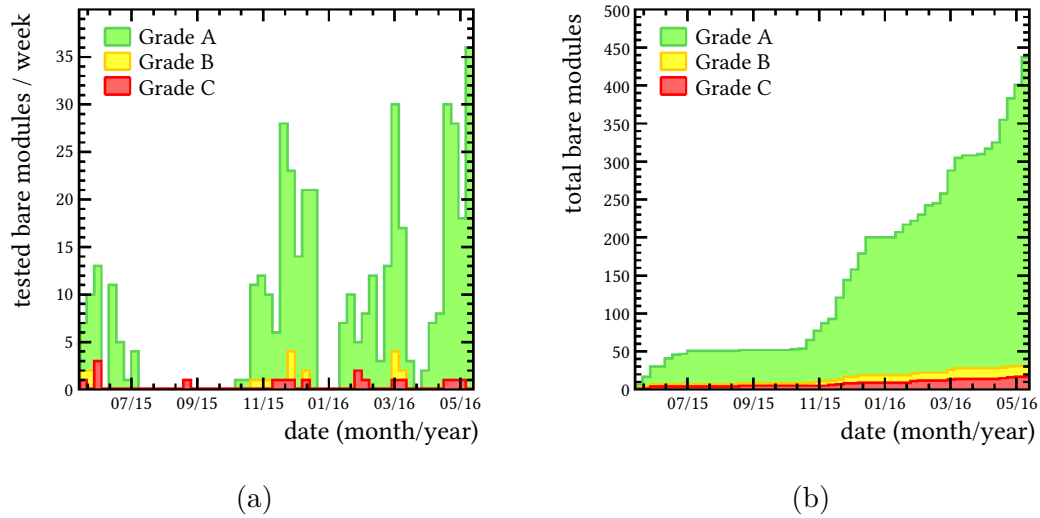
Figure 8.25: KIT bare module production rate. Number of bare modules qualified per week as a function of time (a) and cumulative number of bare modules produced and tested over time (b). The shortage of components is clearly visible. The large percentage of grade A bare modules in combination with high peak production rates confirm the high performance of the KIT bare module production line (modified from [Col16]).

At KIT, the production down times were used to optimize the production processes and quality checks. In this way, the production throughput was increased to up to 36 bare modules produced and tested per week at the end of the production period.

Figure 8.25 also illustrates the excellent bare module production yield achieved by KIT. By introducing the additional I-V measurement on pre-test bare modules and the reworking procedure, the percentage of grade A bare modules was continuously improved. In total, 406 of the 437 produced bare modules (93 %) fulfilled the grade A requirements, 14 (3 %) were graded B and 17 (4 %) failed the requirements and were graded C. Since grade A as well as grade B are suitable for detector integration 96 % of the bare modules produced are qualified for the full module assembly. A summary of the final bare module yield is given in Table 8.3.

In the end, production of further bare modules was limited by the number of suitable ROCs available. Overall, 7300 ROCs passed the optical inspection and were selected for the bare module production. The majority ($> 98 \%$) were used to produce bare modules and to perform the reworking. Roughly 200 of the ROCs were assigned to quality tests and process development. The few remaining silicon sensors were delivered to the production line at DESY and UHH which had a small surplus of ROCs and was able to use the remaining components, since the bump bonding technologies were compatible.

All the results of the bare module production presented in this section confirm the excellent quality of the KIT bump bonding process. By committing to the BPIX philosophy of frequent quality assurance tests and a detailed understanding of the process, KIT achieved an outstanding performance among all production lines in terms of quality, production rate and efficiency, while staying within the project's budget.

Table 8.3: Bare module production yield. By combining the results of the I-V measurement, the electrical functionality tests and the bump bonding test, the bare modules are graded. All grade A and grade B modules were used to assemble full modules. Six of the bare modules could not be depleted and therefore their ROCs could not be tested for their electrical functionality.

Grade	I-V measurement	Pixel alive & bump bond	Combined
A	409	427	406
B	14	0	14
C	14	4	17
Sum	437	431	437
Yield(A+B)	97 %	> 99 %	96 %

8.7 Full module assembly

Although the focus of this theses lies on the bare module production, the full modules assembly shall be shortly introduced to give the full perspective view on the KIT production line. For a more complete and detailed description of the full module assembly at ETP, see [Hei16].

8.7.1 Module assembly line

While the bare modules were produced at IPE, the other components required for a full BPIX detector module were tested and prepared at ETP.

The Token Bit Manager (TBM) chips, produced and diced by IBM, were electrically tested by the US consortium producing the FPIX detector modules, and were distributed among all production centers. The High Density Interconnect (HDI) polyimide flex-prints were produced by Hightech MC AG in Lenzburg, Switzerland. The HDIs are equipped with components soldered to the HDI in a surface mount device (SMD) soldering process. After a short initial test and a quick optical inspection, the HDIs were distributed among the BPIX production centers. At KIT, the HDIs underwent an additional more detailed optical inspection, screening HDIs with broken solder connection, un-precise cutting, kinks, scratches or contaminations. 54 of the 486 ($\approx 11\,\%$) HDIs delivered to KIT were rejected based on this optical inspection.

HDIs passing the optical inspection were equipped with a single TBM-chip using two-component glue (Araldite$^{\circledR}$ 2011). The glue application was performed in a custom-designed gluing station. With the TBM gluing station, up to eight HDIs could be processed simultaneously. The actual TBM placement was performed by hand using a vacuum pipette and an optical stereo microscope. A placement accuracy of $\leq 0.5\,\mathrm{mm}$ was required to ensure access to the wire bonding pads. After a 24 h cure-out of the glue, the electrical connection between HDI and TBM was established in an ultrasonic wedge-to-wedge aluminum wire bonding process. The wire bonding process was performed in a Hesse & Knipps Bondjet 710 wire bonding machine using an aluminum-silicon alloy wire (Al/Si=99/1) with a diameter

of 25 μm. A detailed parameter optimization was performed resulting in a mechanical strength of more than 10 g for every wire bond[12].

To test the TBM-HDI assembly for its functionality, a dedicated electrical test system was designed. In the electrical test, the HDI was fixed by a vacuum system and a custom-designed needle card was used to contact the HDI. The functionality of the TBM was validated by measuring its analog and digital current consumption as well as multiple signal types sent by the TBM [BM14]. Furthermore, an electrical qualification of the high voltage circuits on the HDI was performed by measuring the electrical resistances of the circuits. 420 of the 432 tested HDIs ($\approx 97\,\%$) passed the electrical qualification. Half of the HDIs failing the electrical qualification were rejected due to missing signals from the TBM. The other half of the rejected HDIs showed issues in the high voltage distribution.

The silicon nitride (Si_3N_4) base strips required to handle and mount the BPIX detector module, were produced by the KYOCERA Corporation, Japan. They were cut out of the wafers in a laser-cutting process by a company in Switzerland before being distributed among the production centers. Si_3N_4 had been selected since its thermal expansion coefficient is compatible with the one of silicon, minimizing thermal stress inside the bare module during operation. The base strips are produced with a nominal thickness of 200 μm, but due to variations in the production process deviations of this nominal value were common as well as bent base strips. Furthermore, the laser-cutting process creates burrs at the base strip edges. Since the base strips are required to provide a good thermal contact to the light-weight support structures, a suitable flatness is essential to maximize the contact area between the base strips and the support structures. Furthermore, the layer of glue showed a typical thickness of 10 μm, requiring flat base strips to ensure a homogeneous gluing to the ROC backsides. To provide a suitable flatness, all base strips were deburred by hand, optically inspected and sorted by their thickness. Only pairs of flat, successfully deburred base strips of similar thickness (± 5 μm) were used to produce full modules [Hei16]. Approximately 25 % of the 1150 base strips delivered to KIT were rejected since they did not fulfill the flatness requirements or no matching base-strip could be found.

Components passing all selection criteria were used to turn the bare modules into full-modules. As a first step, a pair of suitable base strips was glued to the backside of the ROCs using Araldite® 2011 two-component glue. To guarantee reliable alignment and planarity, the glue application as well as the placement of components was performed using custom-designed gluing stages. All components were fixed by vacuum structures during the gluing as well as during the 24 h cure-out. After the base strip gluing, an HDI equipped with a TBM, that had passed the optical inspection as well as the electrical test was glued to the backside of the silicon sensor of the bare module. Similar to the gluing of the base strip, custom-designed gluing stages and Araldite® 2011 two-component glue was used. All components were fixed by vacuum structures and for the full 24 h curing time. For further information on the gluing procedure and the gluing stages, see [Str11]. Four identical assembly lines were set up to provide the required production throughput. All assembly lines were set up in a clean room environment and monitored using a high-resolution stereo microscope. Additional validation of the alignment of components was provided by a Zeiss coordinate measuring machine.

As a final production step at KIT, the electrical connection between the HDI, ROCs and the silicon sensor were established by a wire bonding process similar to the one used to electrically connect the HDI and the TBM. The wire bonding process parameters were

---

[12]Corresponding to test number 2011.7 of the MIL-STD-833 standard [US 91]
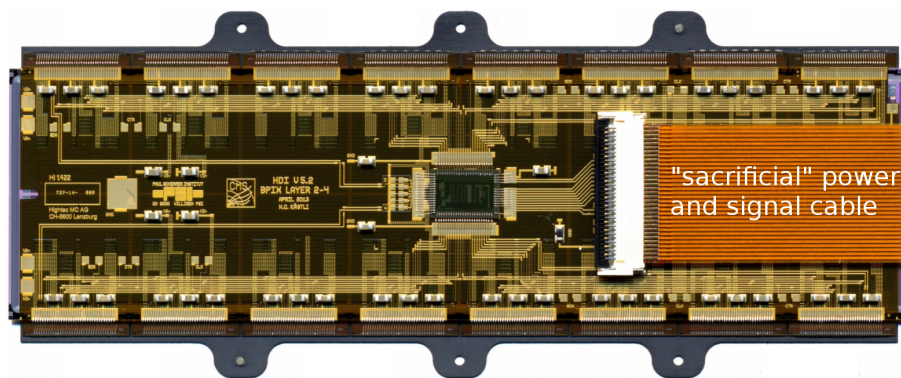
Figure 8.26: BPIX layer 3 and 4 detector module assembled at KIT. A top view of a BPIX layer 3 and 4 detector module with its over 560 wire bond connections is shown. The wire bonds connecting the HDI and the readout chips are visible along the long side of the module. Furthermore, the wire bonds connecting the Token Bit Manager chip with the HDI (center) and the wire bonds connecting distributing high voltage to the silicon sensor (right edge) are visible. A "sacrificial" power and signal cable is connected for test purposes.

optimized in a dedicated parameter study resulting in a mechanical strength of approximately 100 mN for each wire bond connection. In total, about 30 min were needed to establish the approximately 560 wire bond connections. A "sacrificial" power and readout cable was connected for further test and qualification. This cable has been replaced by a final power and readout cable before the detector integration. A BPIX layer 3 and 4 detector module assembled at KIT is shown in Figure 8.26.

After several full module quality checks the module is shipped to RWTH Aachen for final module qualification and the final grading. The full module qualification tests are shortly described in the upcoming section. The final assembly process is performed at Eidgenössische Technische Hochschule Zürich, by equipping the modules with a polyimide protection cap. The protection cap is glued to the surface-mounted capacitors of the module using a UV curing glue and protects the wire bonding interconnections during the detector integration and the operation within CMS. A final reception test at PSI ensures that the modules were not damaged during the protection cap gluing or transportation, before being mounted onto the carbon fiber support structure.

8.7.2 Testing and final qualification

The final grading of BPIX detector modules produced at KIT was performed at RWTH Aachen. However, a subset of the final module tests were also performed at KIT to provide a quick feedback and to screen damage caused by the transportation. In this section, a short overview of the final quality grade tests performed at every module is given. For a more excessive description, see [Kud17; Moy16; Fre17; Fre15].

A series of electrical tests was performed on the modules, to validate a good electrical communication with the module and verify no excessive power consumption of any component, which would indicate failures in the sensor structure or the microelectronics components of the module. Furthermore, the readout chain and the bump bonding quality of every ROC was tested using the calibration pulse block in the PUCs analog to the

electrical tests performed in Section 8.4.2. After determining the electrical noise of the pixels, the comparator thresholds of the individual pixels were adjusted in order to provide an ideal SNR. To make the pixel outputs comparable to each other and to allow the calculation of the charge's center of gravity from the charge distribution among several pixels, a gain calibration is performed on all pixel cells. The final electrical characterization of the silicon sensor was based on I-V measurements similar to the I-V measurements performed on bare modules (see Section 8.4.2).

All electrical tests were performed at two different operation temperatures of 17 °C and −20 °C in a temperature and humidity controlled cold box. The modules were required to show similar test results independent of the operation temperature. Furthermore, the leakage current of the silicon sensors was expected to follow

$$I_{\text{leak}}(T) \propto T^2 \exp\left(\frac{-1.21\,\text{eV}}{2\text{k}_{\text{B}}T}\right), \tag{8.3}$$

since the majority of leakage current was expected to be thermally induced into the sensor bulk material [Chi13]. To further test whether the module can stand the thermally induced mechanical stress during the detector operation within CMS, a mechanical stress test by thermal cycling was performed. Therefore, 10 thermal cycles between +17 °C and −25 °C were performed with an average temperature gradient of 4.5 K/min and followed by a final electrical test at 17 °C.

So far, only electrical calibration pulses of the ROC were used to qualify the module performance, not considering the charge collection process within the silicon sensor. A more realistic test of the module performance can be achieved by irradiating the silicon sensor with high energy photons or electrons. Although electrons emitted from a ^{90}Sr source create the most realistic charge signal within the silicon sensor, the limited particle rates of typical ^{90}Sr sources only allow tests on a sample basis and no systematic quality checks. A more suitable compromise is using X-ray photons created in a powerful X-ray tube. Though the energy deposition of photons within the silicon sensor is less realistic than the one of electrons emitted from a ^{90}Sr source, an X-ray tube can provide much larger particle rates enabling systematic quality checks on all pixels of a module as well as dedicated rate capability checks. Furthermore, characteristic X-ray photons can be used to calibrate the electric response of the module.

Exploiting the direct illumination of the detector module in combination with a random readout trigger, all pixel cells can be tested simultaneously for their hit efficiency. Figure 8.27 shows the results of a hit efficiency test performed on a BPIX detector produced at KIT. By increasing the tube current of the X-ray tube, the photon particle rate can be increased and the rate capability of the detector module can be verified in the so-called high rate test. An increased particle hit rate causes an overflow of the data buffers on the ROCs resulting in a dynamic inefficiency. The dependence of the detection efficiency from the particle hit rate is shown in Figure 8.27. A calibration of the detector module response is performed by indirect illumination with characteristic X-ray photons. Therefore, different target materials are illuminated with a continuous X-ray beam causing an excitation of the target material and the emission of characteristic X-ray photons (typically photons produced in the K_α transition). Depending on the target material the characteristic X-ray photons deposit a different energy within the silicon sensor. For BPIX detector modules, four target materials (zinc, zirconium, molybdenum and silver) were used to calibrate the detector response of every detector module and to verify the linearity of the electrical response. Figure 8.27 shows the calibration fit result of a BPIX detector module produced at KIT.

(a)

(b)

(c)
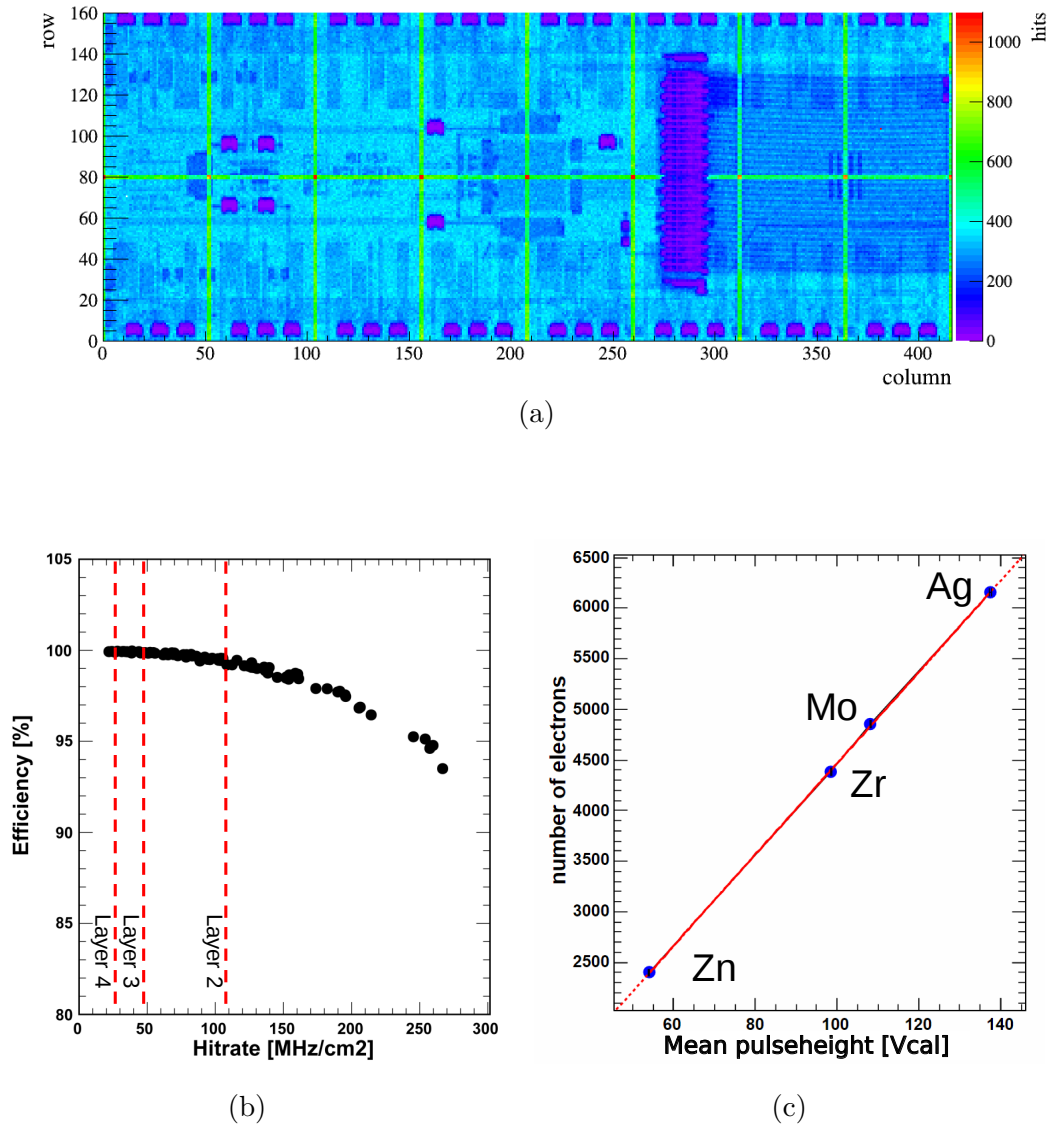
Figure 8.27: X-ray module qualification results. Three results derived from the X-ray module qualification performed on a BPIX detector module produced at KIT are shown. (a): X-ray hit efficiency map of the full module. Defective pixels or missing bump bond connections would be visible as white spots. The number of hits detected below the surface mount device (SMD) components is reduced due to the additional material of the SMD components shielding the X-ray radiation. The edge pixels covering the space between adjacent ROCs are hit more often due to their larger size. Bottom left: ROC hit efficiency as a function of the hit rate showing a dynamic rate inefficiency. For further illustration, the hit rates expected at the different detector layers during the LHC operation are added. (c): Energy calibration fit. Linear fit performed on the expected number of electrons created by characteristic X-ray photons of the four elements as a function of the mean of the pulseheight distribution (modified from [Kud17]).

Table 8.4: KIT BPIX module production results. The production yields are derived from the qualification and classification tests performed at RWTH Aachen as well as the reception test performed at ETH Zürich. The full production yield is derived as a combination of all derived yields [Hei16].

Grade	Electrical Test	X-ray Test	Reception Test	Combined
A	153	339	344	140
B	225	9	33	203
A+B	378	348	377	343
C	13	43	3	48
Non-graded (defective)	18	18	18	18
Sum	409	409	398	409
Yield	92 %	85 %	95 %	84 %

All test results were uploaded to a centralized database. Based on the results from the electrical and the X-ray tests, the modules were graded A, B or C. In the final module selection for detector integration, not only the module grade was considered but also the full qualification results. This way, the most suitable modules for the corresponding position in the detector could be selected.

8.8 Full module production results

The KIT module production of BPIX detector modules for the CMS Phase I Upgrade lasted approximately twelve months and was finished in June 2016. Overall, 409 BPIX detector modules were assembled at KIT, tested at RWTH Aachen and delivered to ETH Zürich for the reception test.

140 of the 409 detector modules produced were graded A and 203 were graded B resulting in 343 detector modules (grade A or grade B) qualified for detector implementation. KIT not only surpassed the initial requirement of $256 + 51$ good detector modules (50 % of the modules required to equip layer 4 and 20 % contingency) by 12 %, its production line also showed a high production yield of 84 %. The KIT-RWTH Aachen production line did not only provide the most detector modules suitable for detector implementation among all five BPIX production centers, it also showed the highest overall module production yield. A more detailed summary of the production yield and the grading based on the different qualification tests is given in Table 8.4.

A closer look at the test results shows a large number of modules graded as grade B that have been graded A in the bare module test. The reason for this down-grading is the leakage current of the silicon sensors not following the expected temperature dependence. According to Equation (8.7.2), a scaling factor of approximately 40 is expected between the leakage current measurements at $+17\,°C$ and $-20\,°C$. However, most downgraded

modules show a leakage current larger than the expected value in the I-V measurement at $-20\,°C$. Since the I-V measurement in the electrical bare module qualification test was only performed at room-temperature, this effect could not be observed on bare module level (see Section 8.4.2). This behavior of the silicon sensor was observed across all production centers and therefore was interpreted as an intrinsic feature of the silicon sensor not caused by any of the processes within the KIT production line. A possible explanation for such a leakage current behavior could be given by an increased amount of surface currents or other non-thermally induced currents, which do not scale according to Equation (8.7.2).

However, this behavior is not considered a long term problem for the operation within CMS. If the increased leakage current is not thermally induced, it is also not expected to create the risk for a potential thermal run-away behavior of the detector module but only a slightly increased overall power consumption. Furthermore, the leakage current increase due to radiation damage in the sensor bulk material is expected to be dominant within a few weeks of operation inside CMS. As soon as the leakage current is dominated by bulk defects, its temperature dependence is expected to be correctly described by Equation (8.7.2), and as a consequence will not exceed the power supply limitations.

Most of the modules failing the qualification tests were graded C due to HDI quality issues that could not be detected in the electrical HDI test. Common failure modes were oxidized or contaminated wire bonding pads that could not be wire bonded as well as broken solder connections at the connector that could not be re-soldered due to the low thickness of the HDI polyimide flex-print. These quality issues were not known at the beginning of the production period and should not have passed the quality control at Hightec MC AG. By giving feedback to Hightec MC AG and by putting a special focus on these failure modes in the optical inspection, the number of lost modules due to defective HDIs was minimized. Defective detector modules due to mechanical damage, defective ROCs or missing bump bond connections were rare, verifying the high production quality.

Regarding the reworking procedure, neither any major differences between full detector modules assembled from reworked bare modules and full modules assembled from non-reworked bare modules nor any correlations between the reworking process and any failure modes was observed. This gives confidence that the reworking process does not have any influence on the performance of the detector modules.

Similar to the results of the electrical bare module test, a very low number of defective readout channels was detected in the electrical test and X-ray tests on full module level. Requiring at least five hits for a pixel to be considered active an average number of 8.7 defective pixels per module (66560 pixels per module) were found. This corresponds to a yield of active pixels larger than 99.98 %. The majority of modules showed zero defective pixels and approximately two thirds of the modules showed less than five defective pixels. These results verify the good material selection and high bump bonding quality achieved by KIT considering that mathematically a module with up to 2656 dead pixels would have still been acceptable for CMS.

For a majority ($\approx 95\,\%$) of the modules, a good agreement between the defective pixels detected in the electrical bare module test and X-ray test was observed. On the remaining modules, larger deviations between the bare module and the full module test results were observed. The majority of deviations could be ascribed to mechanical damages during handling and DCol readout structures failing during the X-ray test. Only two modules showed areas of defective pixels that could be ascribed to failures in the UBM structure, which were either missed in the optical inspect or were optically un-detectable. For more details on the test results of the X-ray test, see [Fre17].

Overall, the BPIX detector module production for the CMS Phase I Upgrade was a great success. In the final detector integration, 323 detector modules produced at KIT were mounted, proving the superior production quality provided by KIT. The majority of detector modules produced at KIT was mounted on barrel layer 3 (193 modules). The remaining 130 detector modules were mounted on barrel layer 4.

8.9 Detector installation and commissioning

The final installation and commissioning of the CMS pixel detector was performed at CERN in March and April 2017. A low signal threshold of 1800 electrons was achieved for the modules mounted in the layers $2-4$ of the BPIX region, as well as for the FPIX modules. The detector threshold of the innermost first layer of the BPIX region had to be increased to 2500 electrons due to crosstalk [Ves17]. As a result, all layers and disks show the expected hit resolution, with the exception of layer 1, whose hit resolution suffers from the increased threshold. By mid-August 2017, over 95 % of the approximately 124 M detector readout channels were active. Figure 8.28 shows an overview of the occupancy of the installed detector modules based on the data derived in August 2017. Due to a loose power supply line, one of the 32 sectors in the second and third layer of the BPIX region, does not provide any data. Furthermore, a defective portcard results in a defective region in the forward part of the detector. Another sector in the forth layer has been disabled since it cannot be operated above a certain temperature and would result in an increased thermal load. In addition, single event upsets (SEUs), caused by ionizing particles, can result in the TBM not sending out any tokens (visible as single inactive modules in Figure 8.28). This requires frequent powercycles of one or more detector modules by disabling and re-enabling the DC/DC converters. For more information on the installation, commissioning and operation in 2017, see [Son17].

In the end of 2017, the whole CMS pixel detector had to be removed from the CMS detector to investigate reoccurring failures in the DC/DC converters. Since the high voltage distribution among the modules is designed with another granularity than the low voltage distribution, these failures in the DC/DC converters resulted in the application of a high-voltage to detector modules while not powering the modules. Such a voltage configuration resulted in damages to several detector modules [Bal18]. After removing the pixel detector, all DC/DC converters and as many of the accessible defective pixel modules as possible were replaced, and most of the inactive channels were repaired. After the re-installation in February 2018, 97 % of all readout channels were active [But18]. Since April 2018, the CMS pixel detector is taking data during collisions provided by the LHC.

With the new pixel detector, CMS was able to enter a new era of high-quality data acquisition providing the basis for physics analyses at the highest energies. Furthermore, all production lines collected lots of experience relevant for the development and production of future silicon detector systems. At KIT, the availability of an in-house flip-chip bonding process allows a more efficient and more flexible development of future semi-conducting particle detectors, and the experience gathered during the production period already enters other non-high energy physics detector projects.
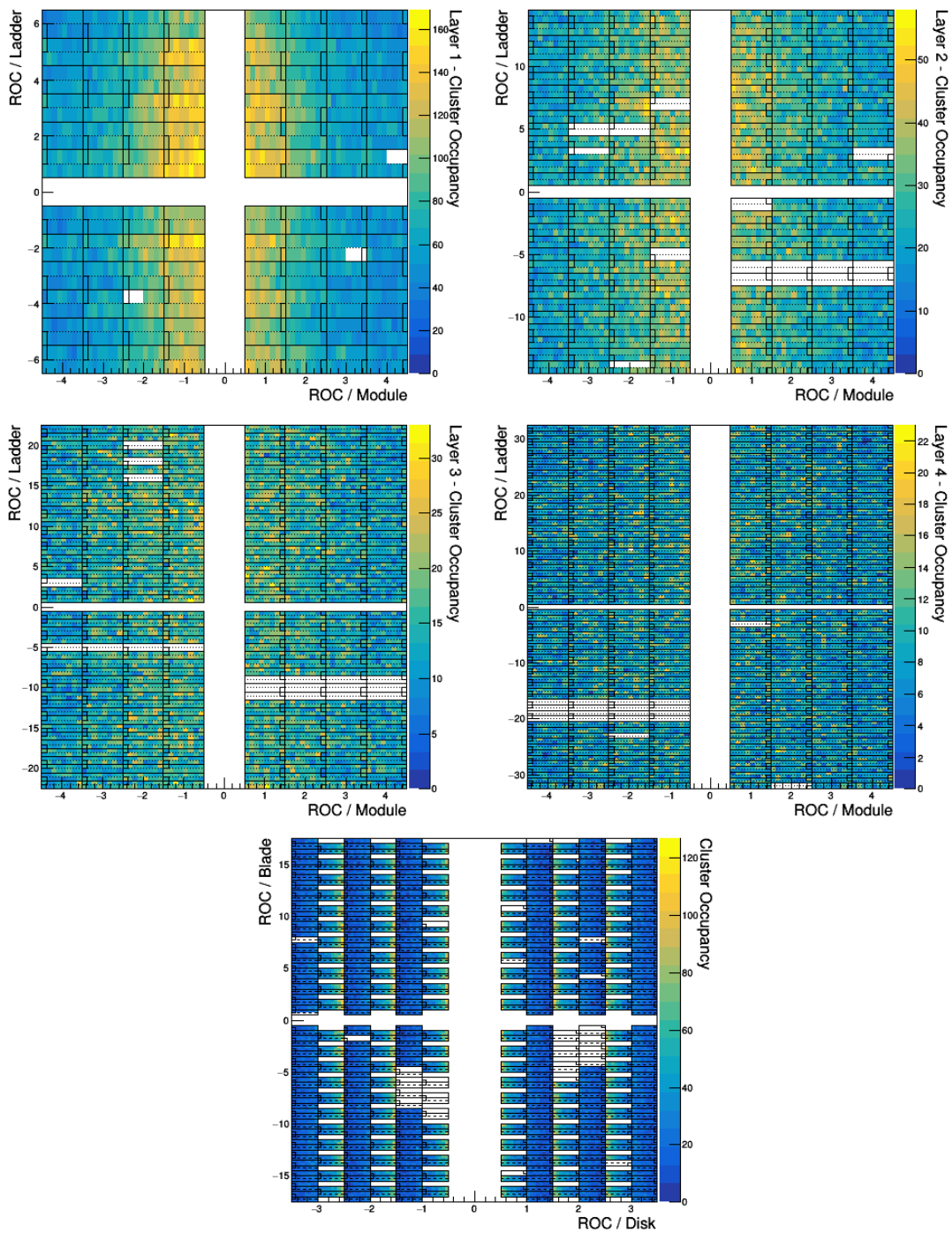
Figure 8.28: Occupancy map of installed pixel detector. The module occupancy is illustrated as a function of the relative module position within a disk/ladder in the FPIX/BPIX region. The single white spots are examples of non-responding Token Bit Managers after a single event upset [CMS18o].

This is the end, beautiful friend,
this is the end, my only friend, the end...

        Jim Morrison (The Doors)

9

Summary and conclusions

Over the last decades, high-energy physics (HEP) experiments like the CMS experiment at the LHC at CERN allowed a detailed probing of the Standard Model of Particle Physics (SM) at the highest energies and provided a more detailed understanding of the nature of our universe. However, observations in cosmology and HEP experiments indicate the existence of physics beyond the SM. Within the CMS experiment, a wide variety of analyses are dedicated to the search for such new physics in the high-energy proton-proton collision provided by the LHC.

In the first part of this thesis, a model-independent search for physics beyond the SM was presented. The search focused on heavy bosonic resonances (HBRs) decaying via so called vector-like quarks (VLQs). The existence of such HBRs and VLQs is predicted by many theoretical models beyond the SM. Depending on the masses of the HBR and the VLQ, the decay of the HBR into a top quark and the vector-like top quark partner is dominant. The vector-like top quark partner T, on the other hand, can decay into a W boson and a bottom quark, a Z boson and a top quark or a Higgs boson and a top quark.

    The search analyzed the fully-hadronic final state by exploiting boosted jet identification techniques in order to reduce background arising from QCD-multijet background. The event selection was optimized for the T-quark decay $T \to Wb$. Two sets of signal samples, based on two different theoretical benchmark models, were produced and allowed the interpretation of the analysis results in two different classes of physics beyond the SM. Since the dominant QCD-multijet background is difficult to simulate, a data-driven background estimation method was developed. Other background processes were estimated using Monte Carlo simulations. The data-driven background estimation was validated in a control region similar to the signal region that was also used to derive systematic uncertainties. By implementing the data-driven background estimation method into the final fit, the impact of the statistical and systematic uncertainties on signal and background processes in the sideband regions were propagated into the signal regions.

    No excess of the data above the SM prediction was found in the $35.9\,\mathrm{fb}^{-1}$ of data collected in 2016. Upper production cross-section limits on the production were derived and interpreted in two theoretical models. The analysis constrains the parameter range of theoretical models based on warped extra dimensions. Models predicting the existence of a composite-Higgs boson are still beyond the analysis sensitivity. So far, the analysis sensitivity is limited by its statistical precision and the systematic uncertainties on the jet identification techniques. Both of these uncertainties are expected to be reduced within

the upcoming years, due to an increased amount of data, continuous developments in the jet identification techniques as well as detector upgrades to improve the performance.

The second part of this thesis was dedicated to the Phase I Upgrade of the CMS pixel detector. Although the original CMS pixel detector was performing very well over the last years, it was not designed for the increase in the instantaneous luminosity of up to $2 \cdot 10^{34} \mathrm{cm}^{-2} \mathrm{s}^{-1}$ expected to be provided by the LHC within the upcoming years. The increase in instantaneous luminosity would have resulted in an intolerable decrease in the performance of the original pixel detector. Therefore, the original pixel detector was replaced with an upgraded version in spring 2017 that included an additional detector layer, enhanced readout electronics and a reduced material budget. In total, the number of readout channels was increased from 66 million to 124 million. The production of semiconductor pixel detector modules and installation of the new pixel detector was carried out by a consortium of several universities and research institutions around the globe. As part of this consortium, the Institute of Experimental Particle Physics (ETP) and the Institute for Data Processing and Electronics (IPE) at the Karlsruhe Institute of Technology (KIT), in cooperation with Rheinisch-Westfälische Technische Hochschule Aachen (RWTH), produced and qualified 409 detector modules for the barrel region of the upgrade CMS pixel detector between May 2015 and June 2016.

The thesis reviewed the entire production and assembly of barrel region detector modules performed at KIT. Special focus was set on the bump bonding process used at KIT to establish a high density interconnection between the silicon sensor and its 16 readout chips (ROCs) in order to create so-called bare modules. By separating the bump bonding process into a bumping process, performed by an external vendor, and the flip-chip bonding process, performed at IPE, turn-around times were minimized. This allowed frequent and quick feedback to other production processes as well as to other production centers, and helped to increase the overall production quality. Great effort was put on an optimal material selection to avoid material losses caused by the use of damaged components. A dedicated cleaning procedure and an optical inspection process were developed to provide a detailed material screening. By optimizing the flip-chip bonding and reflow sub-processes, a die-to-die placement accuracy of $< 1\,\mu\mathrm{m}$ was achieved. The strength of the mechanical connection between the silicon sensors and the ROCs was measured to be more than $19\,\mathrm{mN/bump}$, indicating a strong and reliable interconnection. Several optical, mechanical and electrical quality assurance tests were introduced in order to optimize and monitor the production quality during the production period, as well as to give quick feedback to the flip-chip bonding process. To further increase the bare module production yield, a reworking procedure had been developed and introduced. If a ROC had been identified as defective, this reworking procedure was used to replace the defective ROC with a new one. All these measures resulted in a bare module production yield of $96\,\%$ and 420 bare modules that were fulfilling the bare module criteria for the integration into the CMS pixel detector.

At ETP, the bare modules were turned into fully functional detector modules and their functionality was systematically qualified in an electrical as well as in an X-ray test, before sending the modules to RWTH for the final module qualification. Approximately $84\,\%$ of all detector modules produced at KIT were graded as suitable for detector integration. In the final detector, 323 detector modules produced at KIT were mounted (the target was 256 mounted modules), proving the good module production quality achieved by KIT and RWTH.

With the new pixel detector, in operation since spring 2017, the CMS experiment is suited for a new period of high-energy physics data taking at an increased instantaneous luminosity of $2 \cdot 10^{34} \text{cm}^{-2}\text{s}^{-1}$, while maintaining a high tracking precision and data quality. The data collected during this period will allow a more detailed probing of the SM as well as a more sensitive search for physics beyond the SM. Especially analyses that are limited by their statistical precision or heavily rely on jet-identification techniques – like the analysis presented in the first part of this thesis – are expected to benefit from the new pixel detector and the increased amount of high quality data.

A
Appendix

A.1 Signal efficiencies

Table A.1: Signal efficiency for little-Higgs model samples. The table lists the signal efficiencies, including the statistical uncertainties, for both signal regions in case of the little-Higgs model.

	Signal sample			efficiency in %	
$m_{Z'}$ in GeV	$\Gamma_{Z'}/m_{Z'}$ in %	m_T in GeV	decay channel	2 b-tag	1 b-tag
1500	1	700	T→Wb	0.92 ± 0.05	0.71 ± 0.05
1500	1	900	T→Wb	0.49 ± 0.04	0.39 ± 0.03
1500	1	1200	T→Wb	0.06 ± 0.01	0.06 ± 0.012
2000	1	900	T→Wb	1.18 ± 0.06	1.09 ± 0.06
2000	1	1200	T→Wb	0.97 ± 0.05	0.78 ± 0.05
2000	1	1500	T→Wb	0.23 ± 0.03	0.24 ± 0.03
2500	1	1200	T→Wb	1.03 ± 0.06	1.05 ± 0.06
2500	1	1500	T→Wb	0.94 ± 0.05	0.85 ± 0.05
1500	1	700	T→Zt	0.43 ± 0.04	0.35 ± 0.03
1500	1	900	T→Zt	0.49 ± 0.04	0.39 ± 0.03
1500	1	200	T→Zt	0.25 ± 0.03	0.24 ± 0.03
2000	1	900	T→Zt	1.05 ± 0.06	0.91 ± 0.05
2000	1	1200	T→Zt	1.37 ± 0.06	1.08 ± 0.06
2000	1	1500	T→Zt	1.01 ± 0.06	0.91 ± 0.05
2500	1	1200	T→Zt	1.39 ± 0.06	1.32 ± 0.06
2500	1	1500	T→Zt	1.61 ± 0.07	1.51 ± 0.07

Signal sample				efficiency in %	
$m_{Z'}$ in GeV	$\Gamma_{Z'}/m_{Z'}$ in %	m_{T} in GeV	decay channel	2 b-tag	1 b-tag
1500	1	700	T→Ht	0.33 ± 0.03	0.26 ± 0.03
1500	1	900	T→Ht	0.32 ± 0.03	0.23 ± 0.03
1500	1	1200	T→Ht	0.11 ± 0.02	0.09 ± 0.016
2000	1	900	T→Ht	0.64 ± 0.04	0.54 ± 0.04
2000	1	1200	T→Ht	0.66 ± 0.04	0.62 ± 0.04
2000	1	1500	T→Ht	0.5 ± 0.04	0.45 ± 0.03
2500	1	1200	T→Ht	0.72 ± 0.05	0.67 ± 0.04
2500	1	1500	T→Ht	0.76 ± 0.05	0.69 ± 0.04

Table A.2: Signal efficiency for warped extra dimensions samples. The table lists the signal efficiencies for both signal regions in case of the little-Higgs model.

Signal sample				efficiency in %	
$m_{Z'}$ in GeV	$\Gamma_{Z'}/m_{Z'}$ in %	m_{T} in GeV	decay channel	2 b-tag	1 b-tag
1500	1	800	T→Wb	0.91 ± 0.05	0.7 ± 0.05
1500	1	1000	T→Wb	0.2 ± 0.02	0.22 ± 0.03
1500	1	1300	T→Wb	0.04 ± 0.01	0.05 ± 0.012
1750	1	1300	T→Wb	0.17 ± 0.02	0.2 ± 0.02
2000	1	1000	T→Wb	1.37 ± 0.06	1.11 ± 0.06
2000	1	1300	T→Wb	0.82 ± 0.05	0.67 ± 0.04
2000	1	1500	T→Wb	0.28 ± 0.03	0.28 ± 0.03
2250	1	1300	T→Wb	1.14 ± 0.06	0.92 ± 0.05
2250	1	1500	T→Wb	0.84 ± 0.05	0.67 ± 0.04
2500	1	1300	T→Wb	1.2 ± 0.06	1.12 ± 0.06
2500	1	1500	T→Wb	1.03 ± 0.06	0.9 ± 0.05
2500	1	1800	T→Wb	0.6 ± 0.04	0.56 ± 0.04
2750	1	1800	T→Wb	1.08 ± 0.06	1.01 ± 0.05
3000	1	1500	T→Wb	1.06 ± 0.06	1.06 ± 0.06
3000	1	1800	T→Wb	0.9 ± 0.05	0.82 ± 0.05
3000	1	2100	T→Wb	0.64 ± 0.04	0.59 ± 0.04
3500	1	1800	T→Wb	0.9 ± 0.05	0.95 ± 0.05

Signal sample				efficiency in %	
$m_{Z'}$ in GeV	$\Gamma_{Z'}/m_{Z'}$ in %	m_{T} in GeV	decay channel	2 b-tag	1 b-tag
3500	1	2100	T→Wb	0.79 ± 0.05	0.85 ± 0.05
3500	1	2500	T→Wb	0.54 ± 0.04	0.56 ± 0.04
4000	1	2100	T→Wb	0.73 ± 0.05	0.88 ± 0.05
4000	1	2500	T→Wb	0.6 ± 0.04	0.72 ± 0.05
4000	1	3000	T→Wb	0.43 ± 0.04	0.49 ± 0.04
1500	1	800	T→Zt	0.53 ± 0.04	0.42 ± 0.04
1500	1	1000	T→Zt	0.46 ± 0.04	0.38 ± 0.03
1500	1	1300	T→Zt	0.13 ± 0.02	0.11 ± 0.018
1750	1	1300	T→Zt	0.78 ± 0.05	0.71 ± 0.05
2000	1	1000	T→Zt	1.16 ± 0.06	0.92 ± 0.05
2000	1	1300	T→Zt	1.36 ± 0.06	1.12 ± 0.06
2000	1	1500	T→Zt	1.0 ± 0.05	0.9 ± 0.05
2250	1	1300	T→Zt	1.5 ± 0.07	1.21 ± 0.06
2250	1	1500	T→Zt	1.53 ± 0.07	1.26 ± 0.06
2500	1	1300	T→Zt	1.45 ± 0.07	1.29 ± 0.06
2500	1	1500	T→Zt	1.61 ± 0.07	1.4 ± 0.06
2500	1	1800	T→Zt	1.5 ± 0.07	1.33 ± 0.06
2750	1	1800	T→Zt	1.6 ± 0.07	1.45 ± 0.07
3000	1	1500	T→Zt	1.48 ± 0.07	1.46 ± 0.07
3000	1	1800	T→Zt	1.68 ± 0.07	1.62 ± 0.07
3000	1	2100	T→Zt	1.68 ± 0.07	1.58 ± 0.07
3500	1	1800	T→Zt	1.48 ± 0.07	1.56 ± 0.07
3500	1	2100	T→Zt	1.64 ± 0.07	1.69 ± 0.07
3500	1	2500	T→Zt	1.54 ± 0.07	1.66 ± 0.07
4000	1	2100	T→Zt	1.49 ± 0.07	1.68 ± 0.07
4000	1	2500	T→Zt	1.59 ± 0.07	1.77 ± 0.07
4000	1	3000	T→Zt	1.4 ± 0.07	1.67 ± 0.07
1500	1	800	T→Ht	0.41 ± 0.03	0.29 ± 0.03
1500	1	1000	T→Ht	0.28 ± 0.03	0.2 ± 0.02
1500	1	1300	T→Ht	0.07 ± 0.01	0.06 ± 0.013

	Signal sample			efficiency in %	
$m_{Z'}$ in GeV	$\Gamma_{Z'}/m_{Z'}$ in %	m_T in GeV	decay channel	2 b-tag	1 b-tag
1750	1	1300	T→Ht	0.5 ± 0.04	0.4 ± 0.03
2000	1	1000	T→Ht	0.76 ± 0.05	0.61 ± 0.04
2000	1	1300	T→Ht	0.82 ± 0.07	0.63 ± 0.06
2000	1	1500	T→Ht	0.68 ± 0.04	0.51 ± 0.04
2250	1	1300	T→Ht	0.9 ± 0.05	0.69 ± 0.05
2250	1	1500	T→Ht	0.89 ± 0.05	0.72 ± 0.05
2500	1	1300	T→Ht	0.87 ± 0.05	0.76 ± 0.05
2500	1	1500	T→Ht	0.94 ± 0.05	0.76 ± 0.05
2500	1	1800	T→Ht	0.86 ± 0.05	0.72 ± 0.05
2750	1	1800	T→Ht	0.89 ± 0.05	0.8 ± 0.05
3000	1	1500	T→Ht	0.89 ± 0.05	0.88 ± 0.05
3000	1	1800	T→Ht	0.91 ± 0.05	0.85 ± 0.05
3000	1	2100	T→Ht	0.89 ± 0.05	0.83 ± 0.05
3500	1	1800	T→Ht	0.88 ± 0.05	0.89 ± 0.05
3500	1	2100	T→Ht	0.87 ± 0.05	0.88 ± 0.05
3500	1	2500	T→Ht	0.87 ± 0.05	0.88 ± 0.05
4000	1	2100	T→Ht	0.86 ± 0.05	0.91 ± 0.05
4000	1	2500	T→Ht	0.83 ± 0.05	0.91 ± 0.05
4000	1	3000	T→Ht	0.78 ± 0.05	0.87 ± 0.05
1500	30	800	T→Wb	0.88 ± 0.05	0.7 ± 0.05
1500	30	1000	T→Wb	0.57 ± 0.04	0.48 ± 0.04
1500	30	1300	T→Wb	0.39 ± 0.03	0.32 ± 0.03
2000	30	1000	T→Wb	1.19 ± 0.06	0.97 ± 0.05
2000	30	1300	T→Wb	0.84 ± 0.05	0.7 ± 0.05
2000	30	1500	T→Wb	0.57 ± 0.04	0.52 ± 0.04
2500	30	1300	T→Wb	1.11 ± 0.06	1.01 ± 0.05
2500	30	1500	T→Wb	0.88 ± 0.05	0.84 ± 0.05
2500	30	1800	T→Wb	0.64 ± 0.04	0.61 ± 0.04
3000	30	1500	T→Wb	0.97 ± 0.05	0.96 ± 0.05
3000	30	1800	T→Wb	0.83 ± 0.05	0.77 ± 0.05

Signal sample				efficiency in %	
$m_{Z'}$ in GeV	$\Gamma_{Z'}/m_{Z'}$ in %	m_{T} in GeV	decay channel	2 b-tag	1 b-tag
3000	30	2100	T→Wb	0.6 ± 0.04	0.62 ± 0.04
3500	30	1800	T→Wb	0.82 ± 0.05	0.88 ± 0.05
3500	30	2100	T→Wb	0.68 ± 0.04	0.72 ± 0.05
3500	30	2500	T→Wb	0.52 ± 0.04	0.57 ± 0.04
4000	30	2100	T→Wb	0.71 ± 0.05	0.77 ± 0.05
4000	30	2500	T→Wb	0.56 ± 0.04	0.63 ± 0.04
4000	30	3000	T→Wb	0.43 ± 0.04	0.52 ± 0.04
1500	30	800	T→Zt	0.54 ± 0.04	0.42 ± 0.04
1500	30	1000	T→Zt	0.66 ± 0.04	0.52 ± 0.04
1500	30	1300	T→Zt	0.8 ± 0.05	0.71 ± 0.05
2000	30	1000	T→Zt	1.06 ± 0.06	0.9 ± 0.05
2000	30	1300	T→Zt	1.27 ± 0.06	1.05 ± 0.06
2000	30	1500	T→Zt	1.27 ± 0.06	1.1 ± 0.06
2500	30	1300	T→Zt	1.37 ± 0.06	1.23 ± 0.06
2500	30	1500	T→Zt	1.54 ± 0.07	1.32 ± 0.06
2500	30	1800	T→Zt	1.47 ± 0.07	1.36 ± 0.06
3000	30	1500	T→Zt	1.49 ± 0.07	1.38 ± 0.06
3000	30	1800	T→Zt	1.64 ± 0.07	1.51 ± 0.07
3000	30	2100	T→Zt	1.56 ± 0.07	1.55 ± 0.07
3500	30	1800	T→Zt	1.56 ± 0.07	1.53 ± 0.07
3500	30	2100	T→Zt	1.59 ± 0.07	1.63 ± 0.07
3500	30	2500	T→Zt	1.49 ± 0.07	1.59 ± 0.07
4000	30	2100	T→Zt	1.56 ± 0.07	1.69 ± 0.07
4000	30	2500	T→Zt	1.56 ± 0.07	1.73 ± 0.07
4000	30	3000	T→Zt	1.29 ± 0.06	1.62 ± 0.06
1500	30	800	T→Ht	0.36 ± 0.03	0.3 ± 0.03
1500	30	1000	T→Ht	0.41 ± 0.03	0.32 ± 0.03
1500	30	1300	T→Ht	0.51 ± 0.04	0.39 ± 0.03
2000	30	1000	T→Ht	0.7 ± 0.05	0.53 ± 0.04
2000	30	1300	T→Ht	0.79 ± 0.05	0.6 ± 0.04

Signal sample				efficiency in %	
$m_{Z'}$ in GeV	$\Gamma_{Z'}/m_{Z'}$ in %	m_T in GeV	decay channel	2 b-tag	1 b-tag
2000	30	1500	T→Ht	0.74 ± 0.05	0.62 ± 0.04
2500	30	1300	T→Ht	0.86 ± 0.05	0.76 ± 0.05
2500	30	1500	T→Ht	0.88 ± 0.05	0.8 ± 0.05
2500	30	1800	T→Ht	0.85 ± 0.05	0.74 ± 0.05
3000	30	1500	T→Ht	0.91 ± 0.05	0.79 ± 0.05
3000	30	1800	T→Ht	0.89 ± 0.05	0.86 ± 0.05
3000	30	2100	T→Ht	0.87 ± 0.05	0.8 ± 0.05
3500	30	1800	T→Ht	0.89 ± 0.05	0.89 ± 0.05
3500	30	2100	T→Ht	0.9 ± 0.05	0.92 ± 0.05
3500	30	2500	T→Ht	0.84 ± 0.05	0.86 ± 0.05
4000	30	2100	T→Ht	0.88 ± 0.05	0.91 ± 0.05
4000	30	2500	T→Ht	0.84 ± 0.05	0.93 ± 0.05
4000	30	3000	T→Ht	0.76 ± 0.04	0.88 ± 0.05

A.2 Robustness of data-driven background estimation
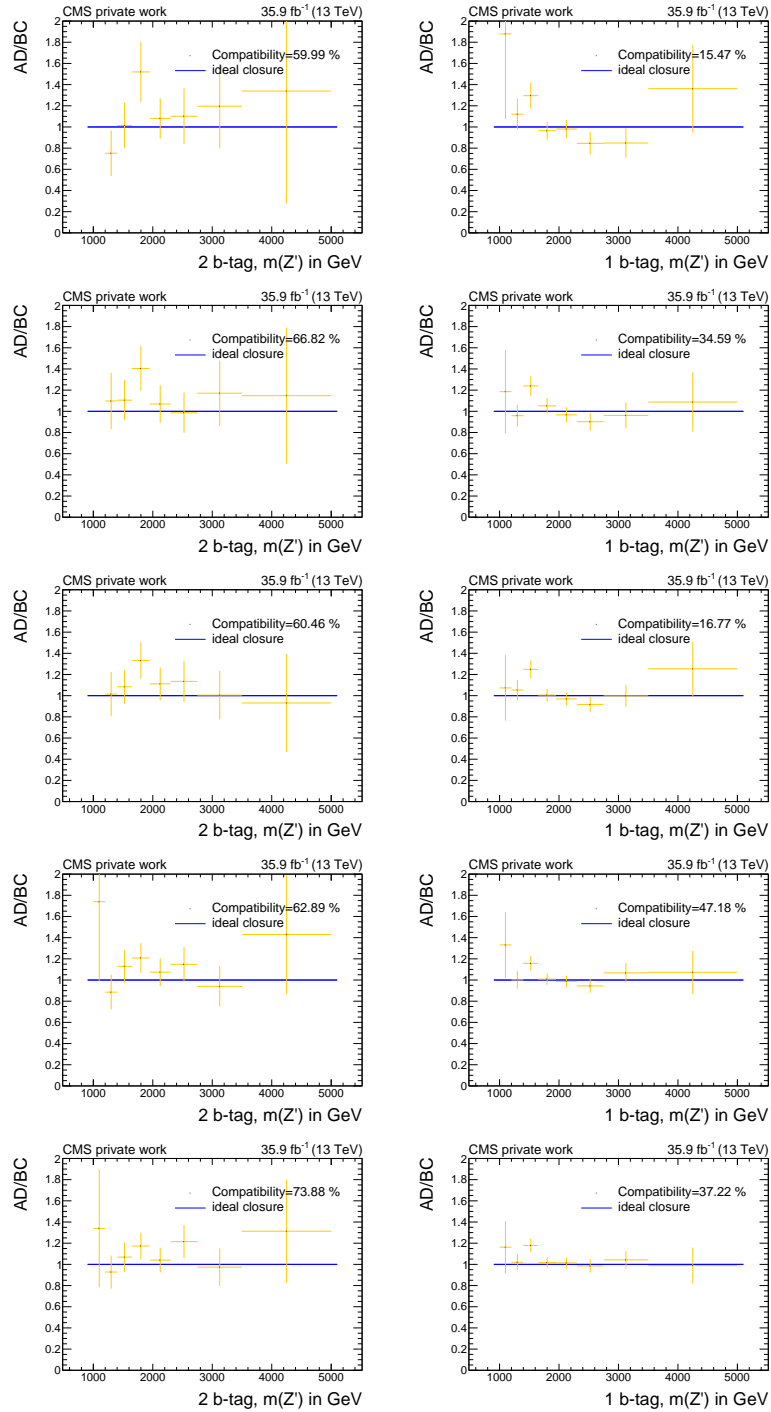
Figure A.1: Compatibility of CSV-varied closure tests with ideal closure. Left: 2 b-tag category, Right: 1 b-tag category. First row: CSV_v2 10 % tighter, second row: CSV_v2 5 % tighter, third row: nominal, forth row: CSV_v2 5 % looser, fifth row: CSV_v2 10 % looser
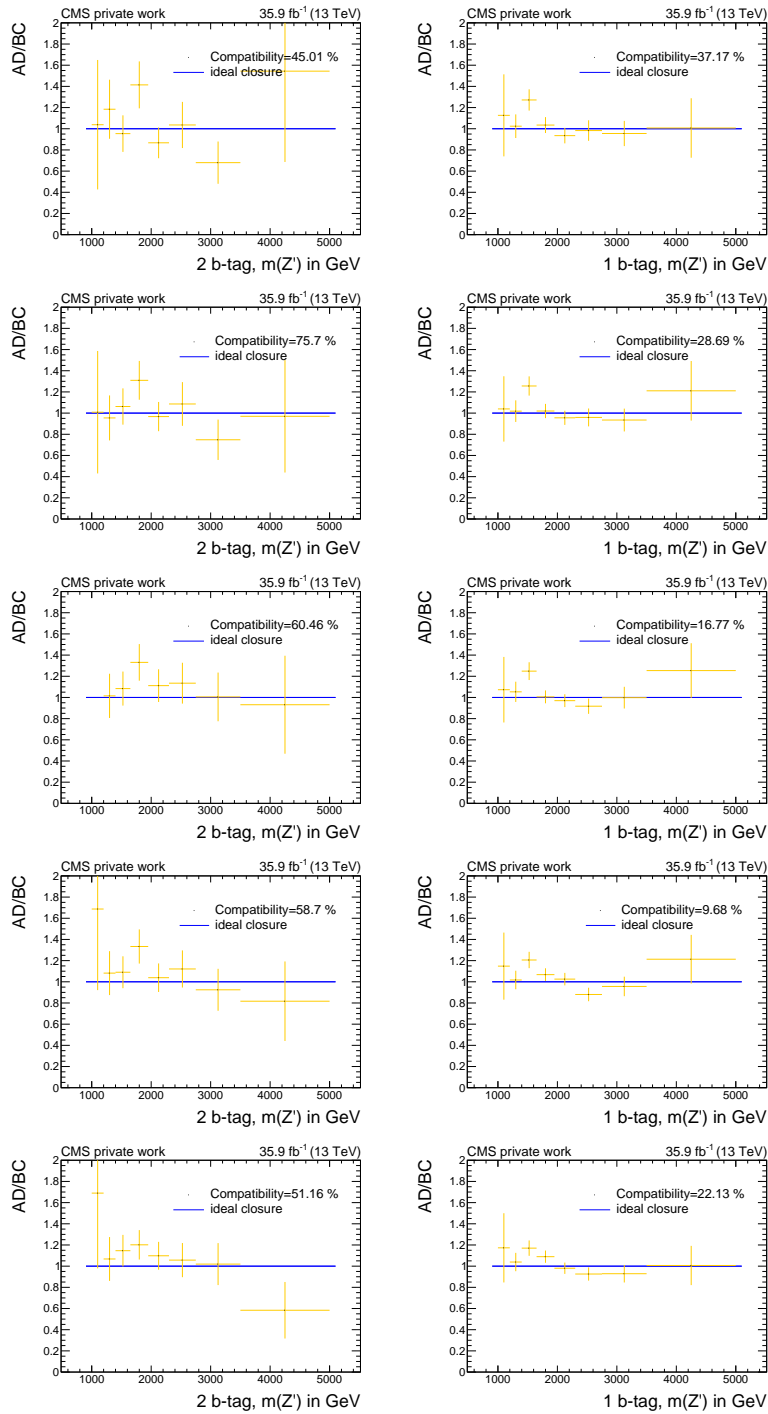
Figure A.2: Compatibility of τ_{21}-varied closure tests with ideal closure. Left: 2 b-tag category, Right: 1 b-tag category. First row: τ_{21} 10 % tighter, second row: τ_{21} 5 % tighter, third row: nominal, forth row: τ_{21} 5 % looser, fifth row: τ_{21} 10 % looser
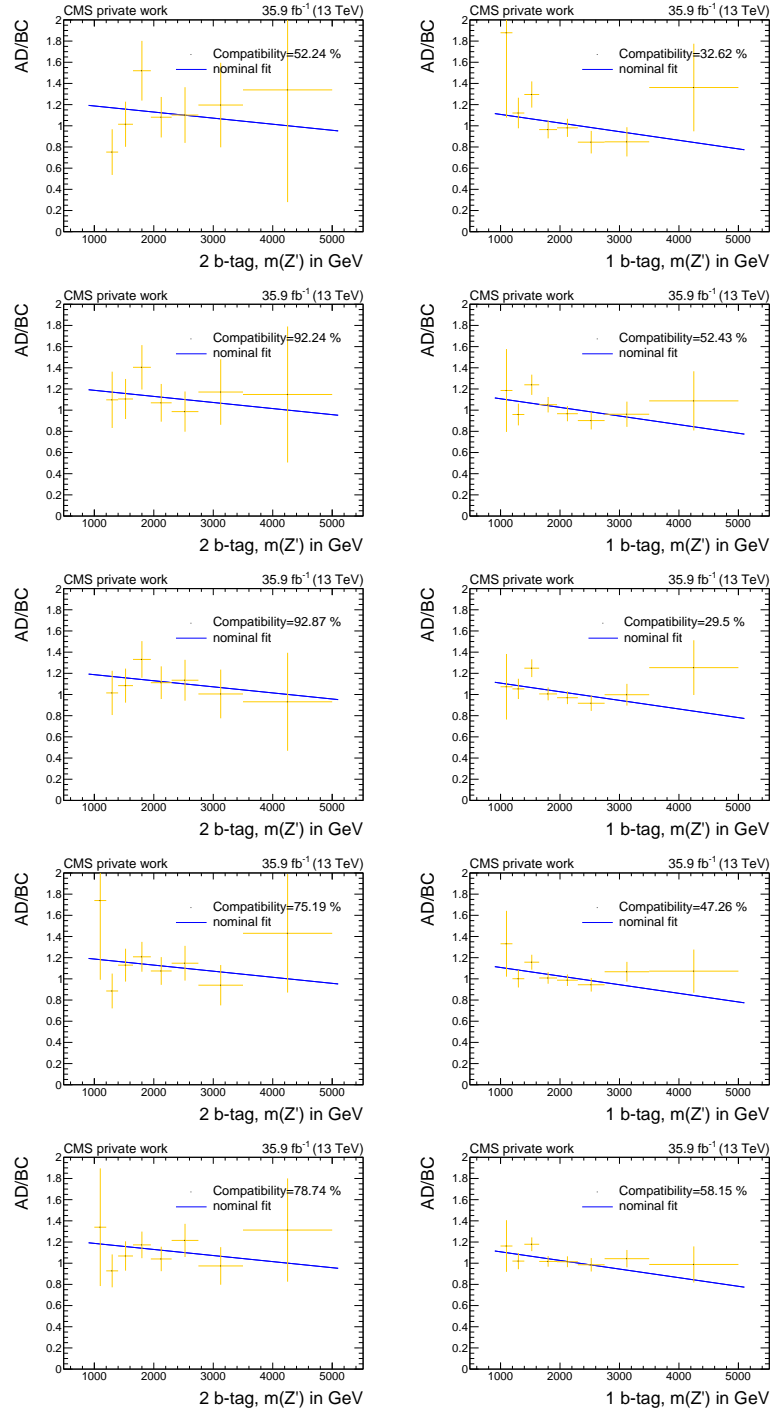
Figure A.3: Compatibility of CSV-varied closure tests with nominal fit. Left: 2 b-tag category, Right: 1 b-tag category. First row: CSV_v2 10 % tighter, second row: CSV_v2 5 % tighter, third row: nominal, forth row: CSV_v2 5 % looser, fifth row: CSV_v2 10 % looser
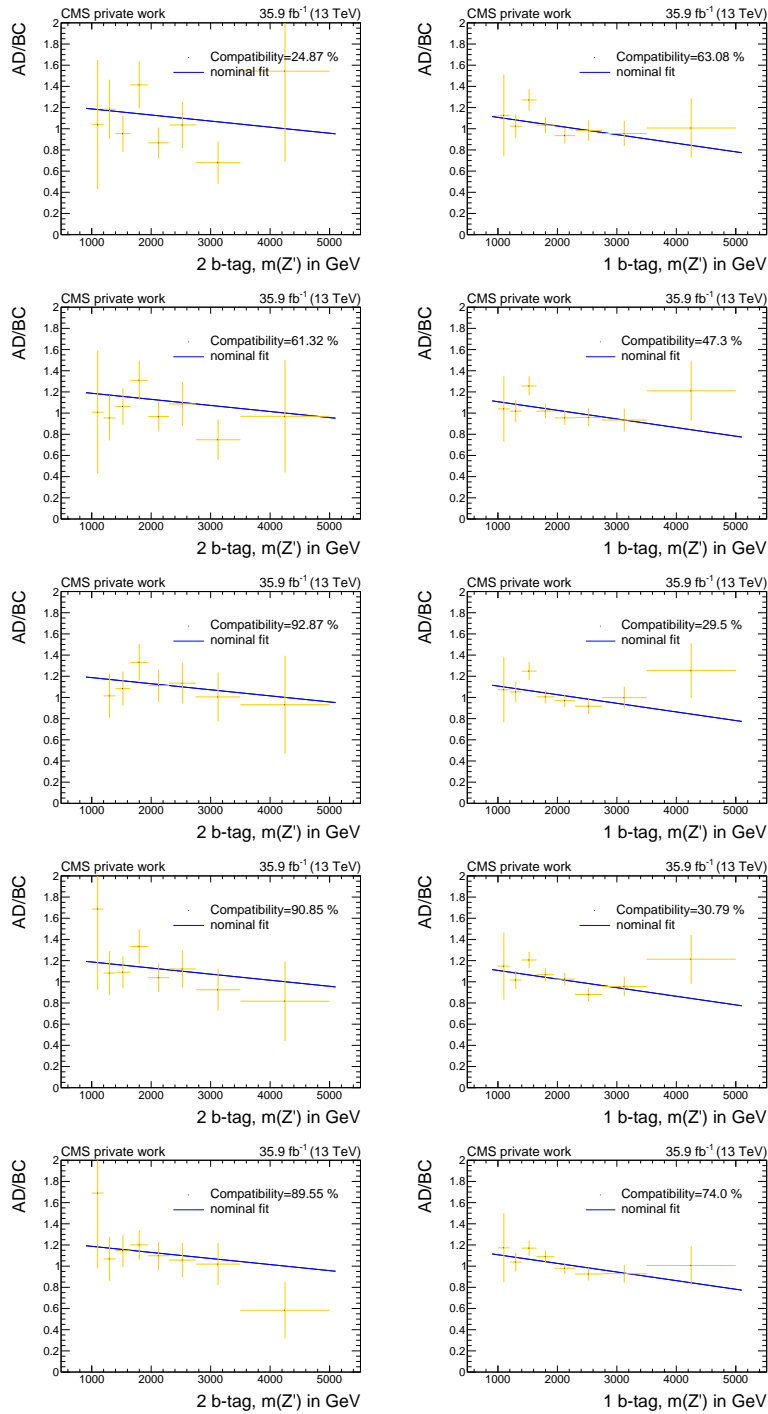
Figure A.4: Compatibility of τ_{21}-varied closure tests with nominal fit. Left: 2 b-tag category, Right: 1 b-tag category. First row: τ_{21} 10 % tighter, second row: τ_{21} 5 % tighter, third row: nominal, forth row: τ_{21} 5 % looser, fifth row: τ_{21} 10 % looser

A.3 Systematic uncertainties on Top background
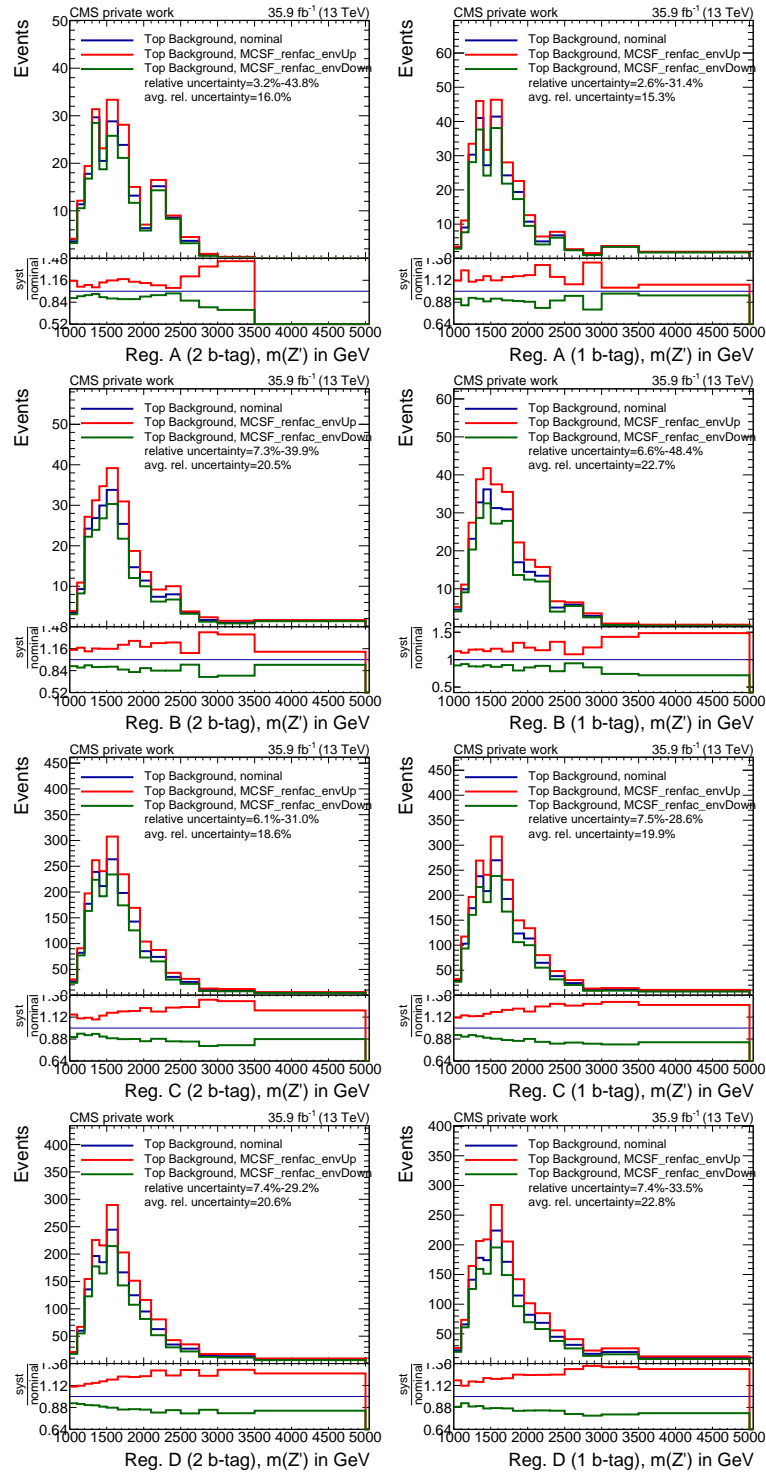
Figure A.5: Impact of the factorization and renormalization scale on the Top background. left: 2 b-tag category, right: 1 b-tag category, from top to bottom: Reg. A, Reg. B, Reg. C, Reg. D.
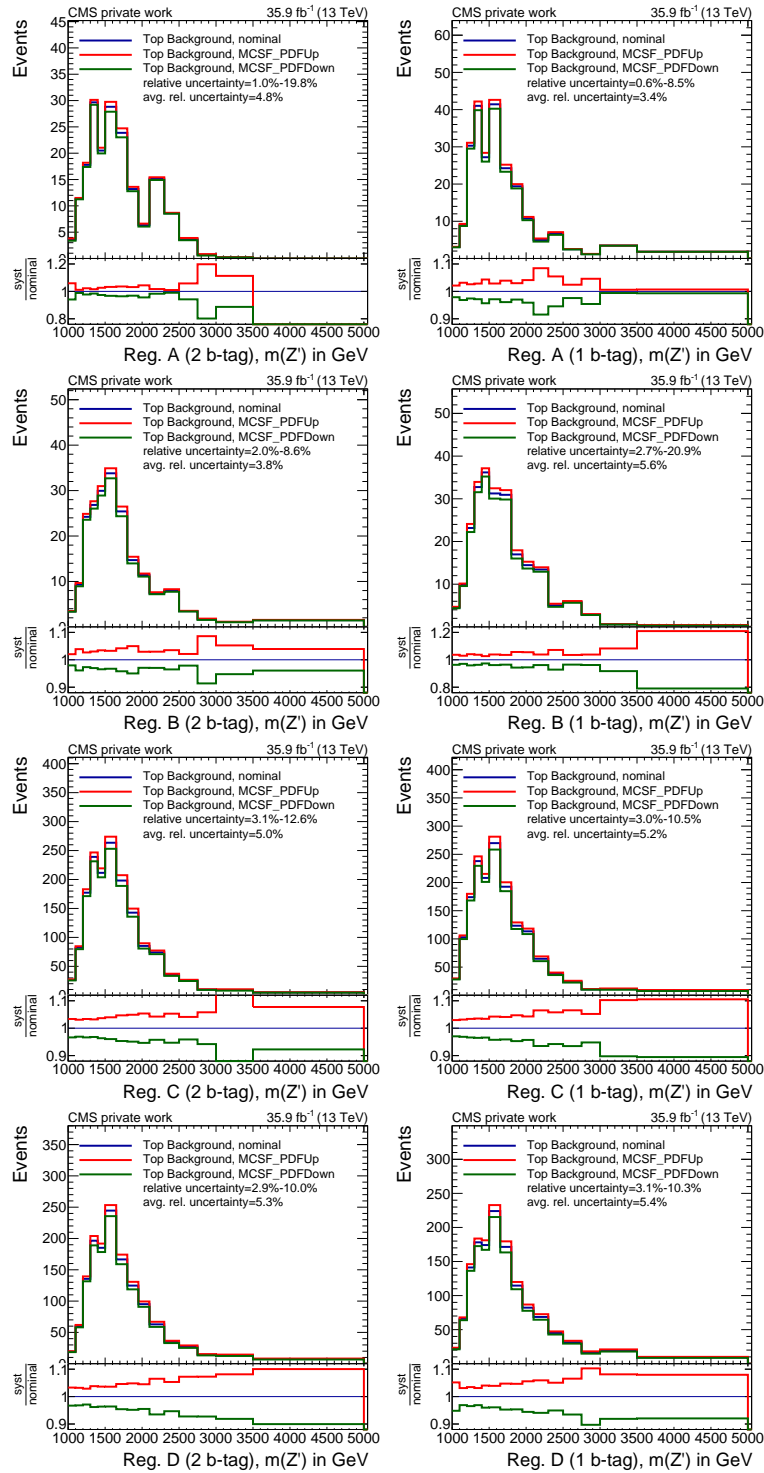
Figure A.6: Impact of PDF uncertainty on the Top background. left: 2 b-tag category, right: 1 b-tag category, from top to bottom: Reg. A, Reg. B, Reg. C, Reg. D.
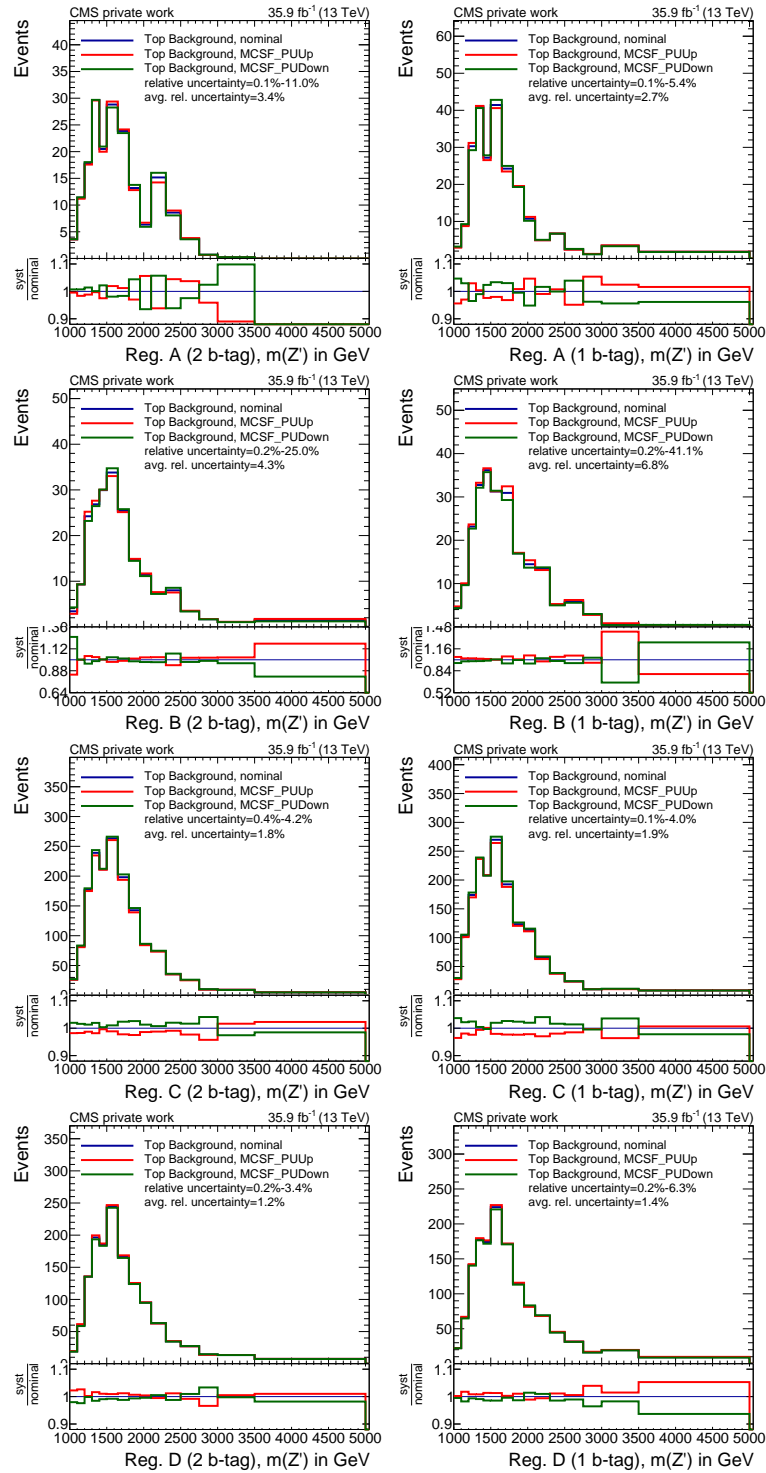
Figure A.7: Impact of pile-up uncertainty on the Top background. left: 2 b-tag category, right: 1 b-tag category, from top to bottom: Reg. A, Reg. B, Reg. C, Reg. D.
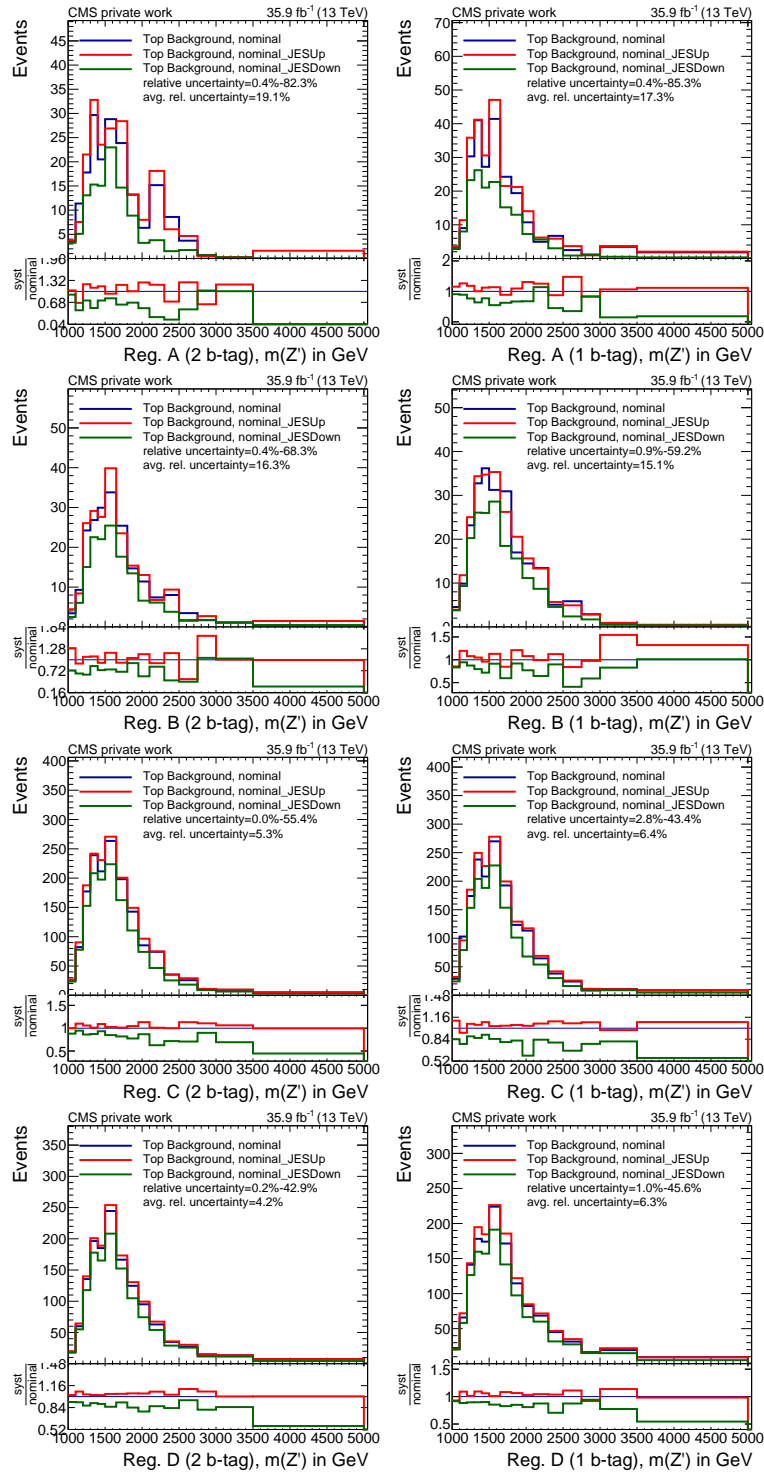
Figure A.8: Impact of JES uncertainty on the Top background. left: 2 b-tag category, right: 1 b-tag category, from top to bottom: Reg. A, Reg. B, Reg. C, Reg. D.
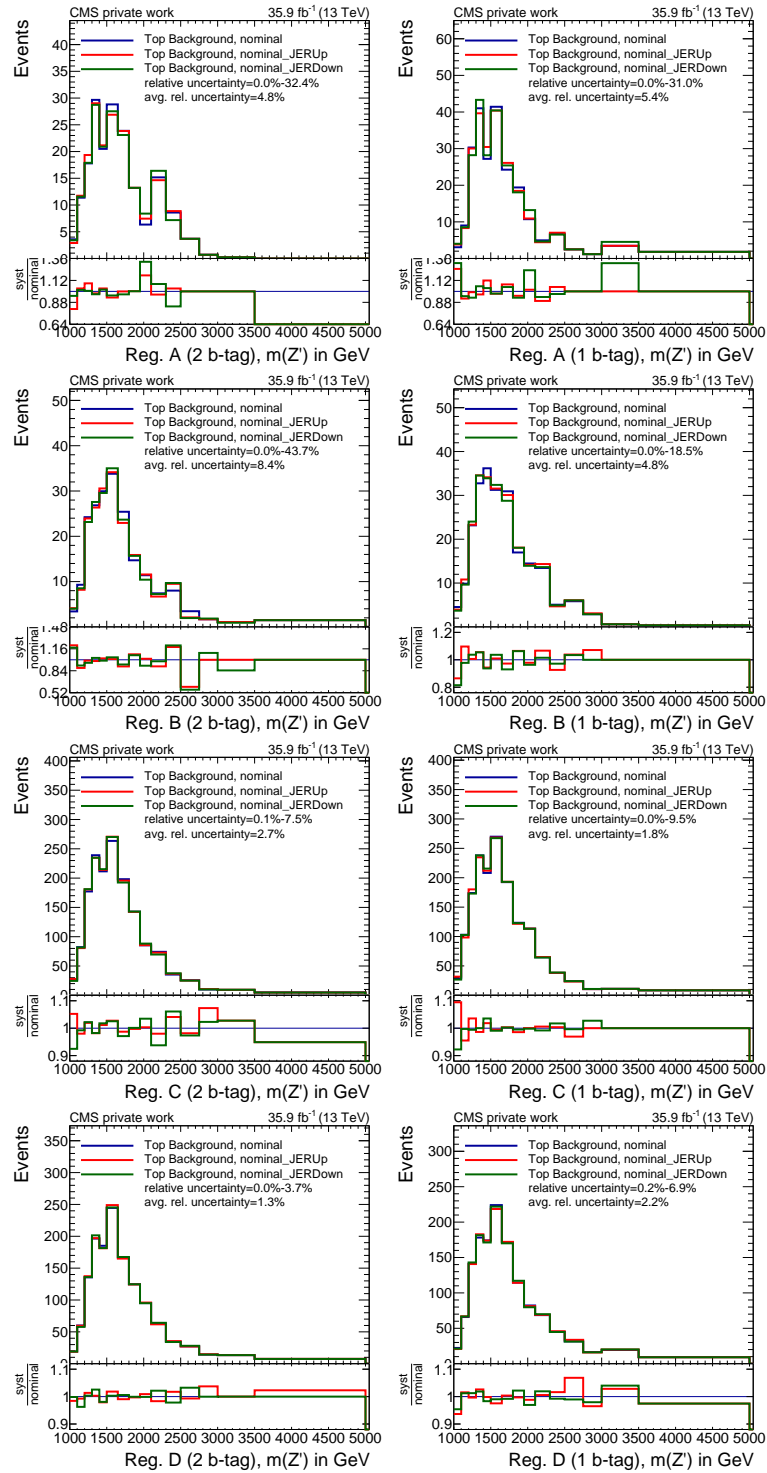
Figure A.9: Impact of JER uncertainty on the Top background. left: 2 b-tag category, right: 1 b-tag category, from top to bottom: Reg. A, Reg. B, Reg. C, Reg. D.
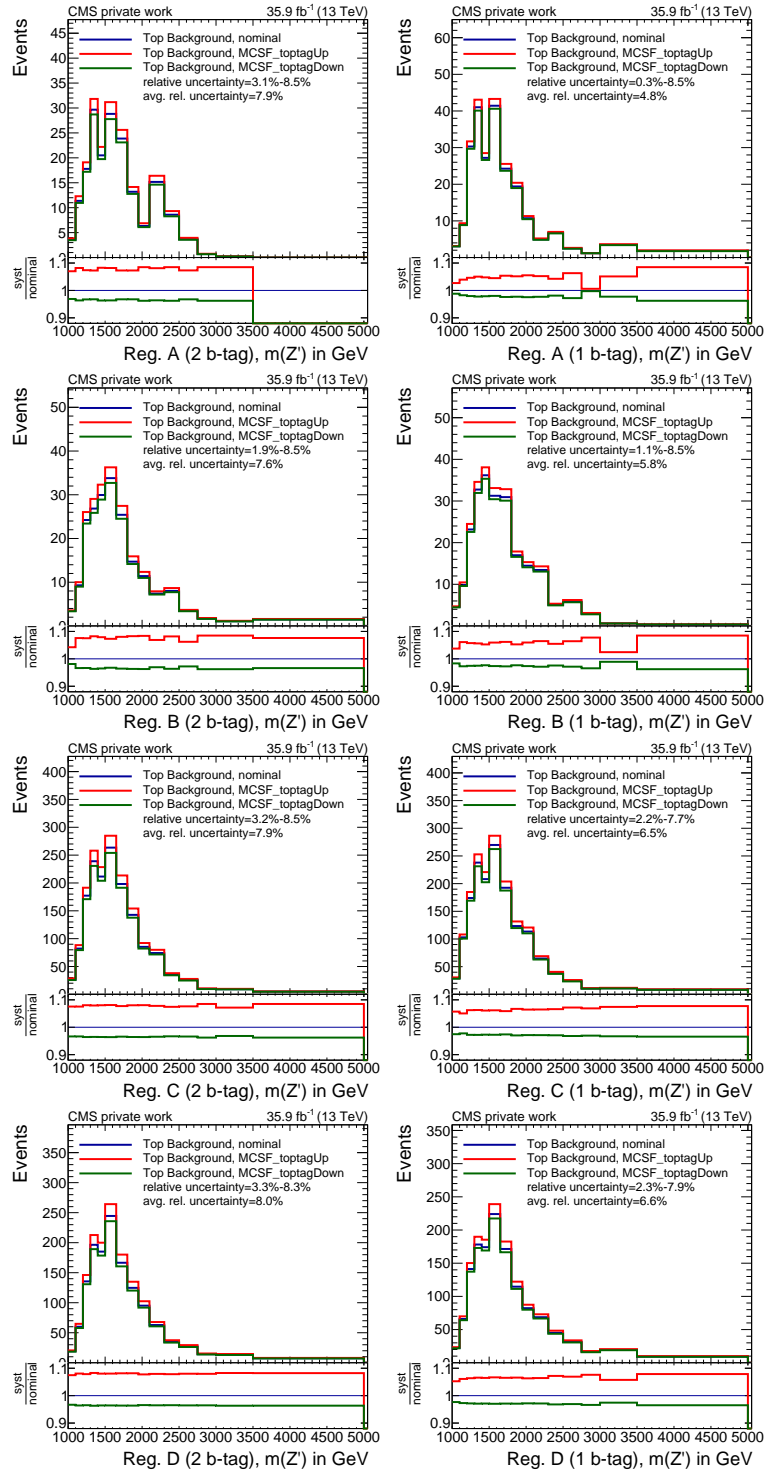
Figure A.10: Impact of t tagging uncertainty on the Top background. left: 2 b-tag category, right: 1 b-tag category, from top to bottom: Reg. A, Reg. B, Reg. C, Reg. D.
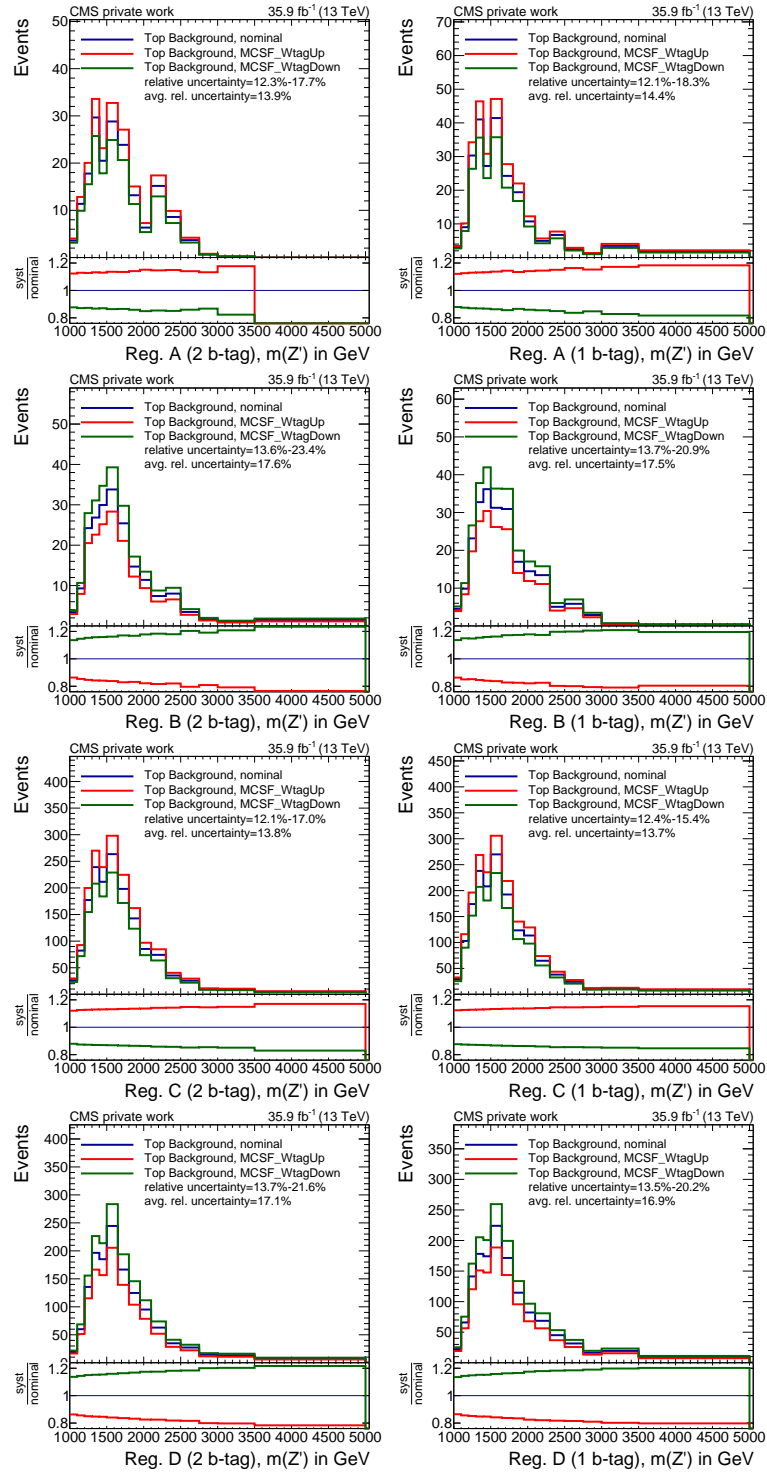
Figure A.11: Impact of W tagging uncertainty on the Top background. left: 2 b-tag category, right: 1 b-tag category, from top to bottom: Reg. A, Reg. B, Reg. C, Reg. D.
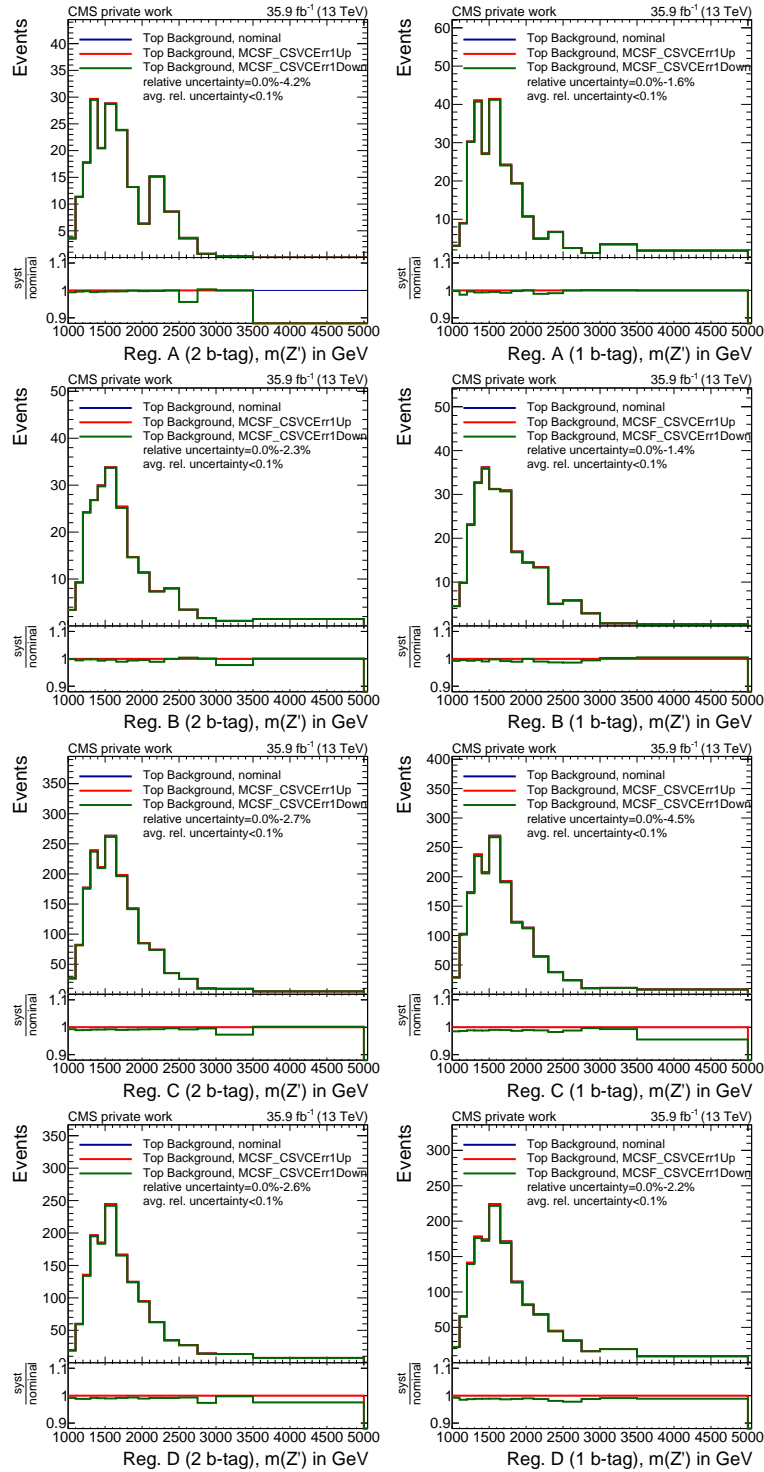
Figure A.12: Impact of b tagging uncertainty (CErr1) on the Top background. left: 2
b-tag category, right: 1 b-tag category, from top to bottom: Reg. A, Reg. B, Reg. C,
Reg. D.
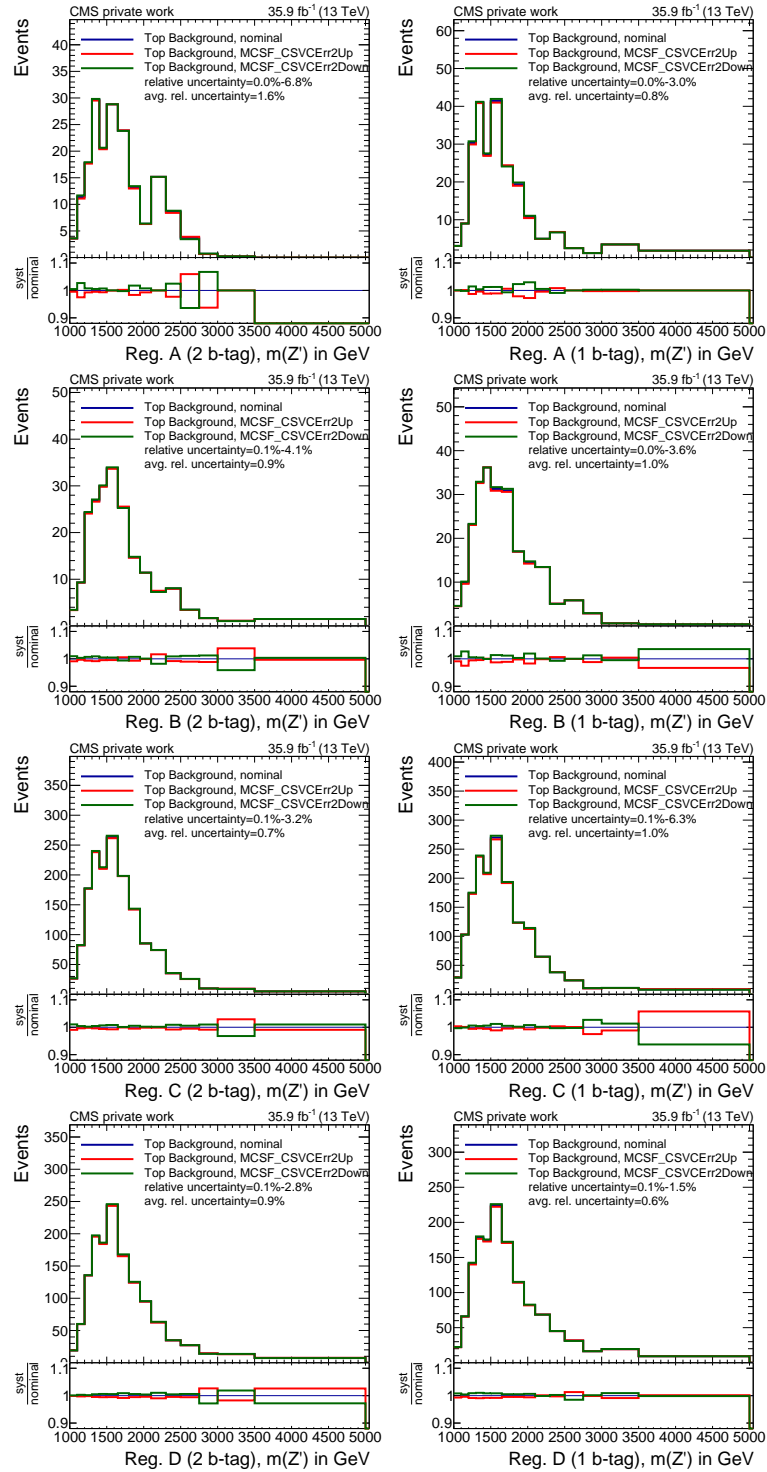
Figure A.13: Impact of b tagging uncertainty (CErr2) on the Top background. left: 2 b-tag category, right: 1 b-tag category, from top to bottom: Reg. A, Reg. B, Reg. C, Reg. D.
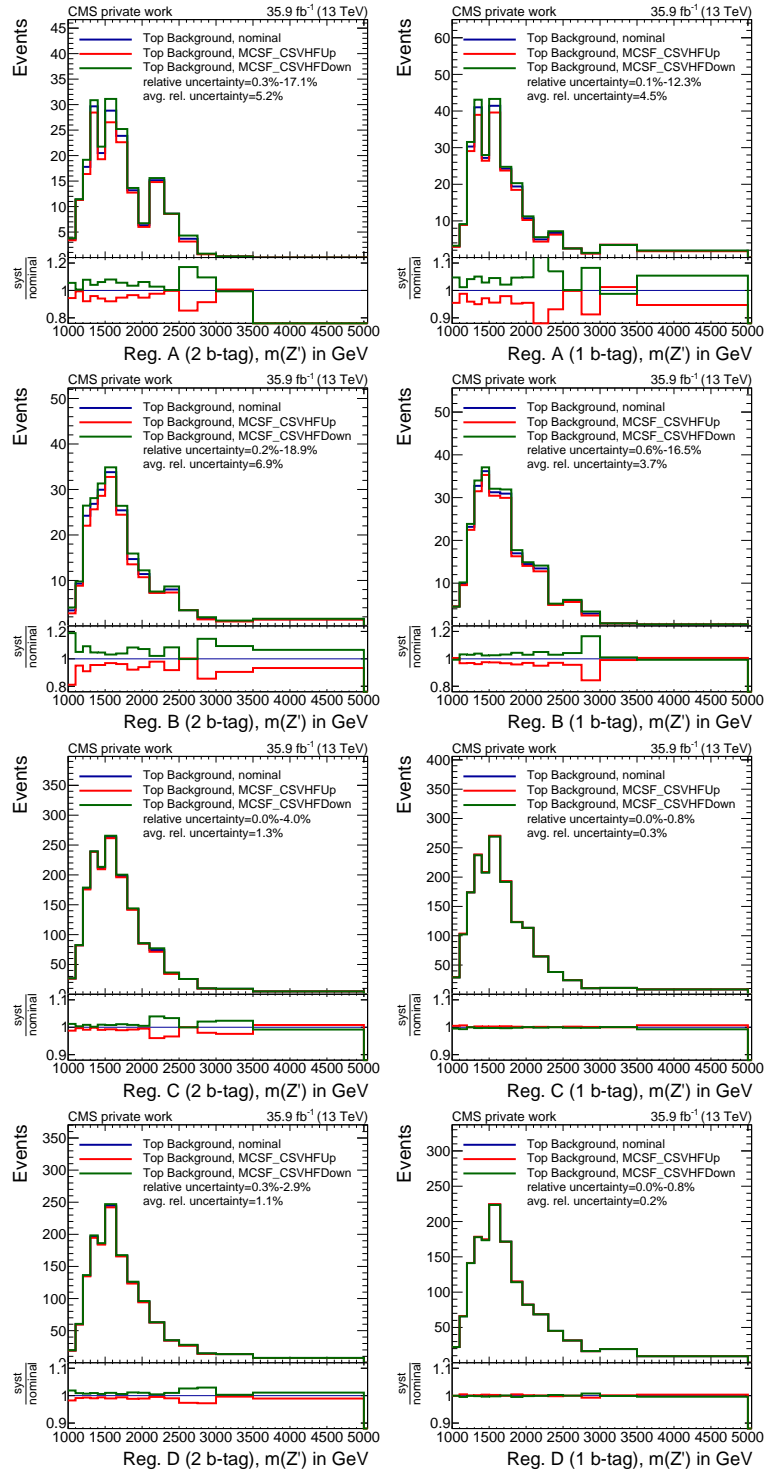
Figure A.14: Impact of b tagging uncertainty (HF) on the Top background. left: 2 b-tag category, right: 1 b-tag category, from top to bottom: Reg. A, Reg. B, Reg. C, Reg. D.
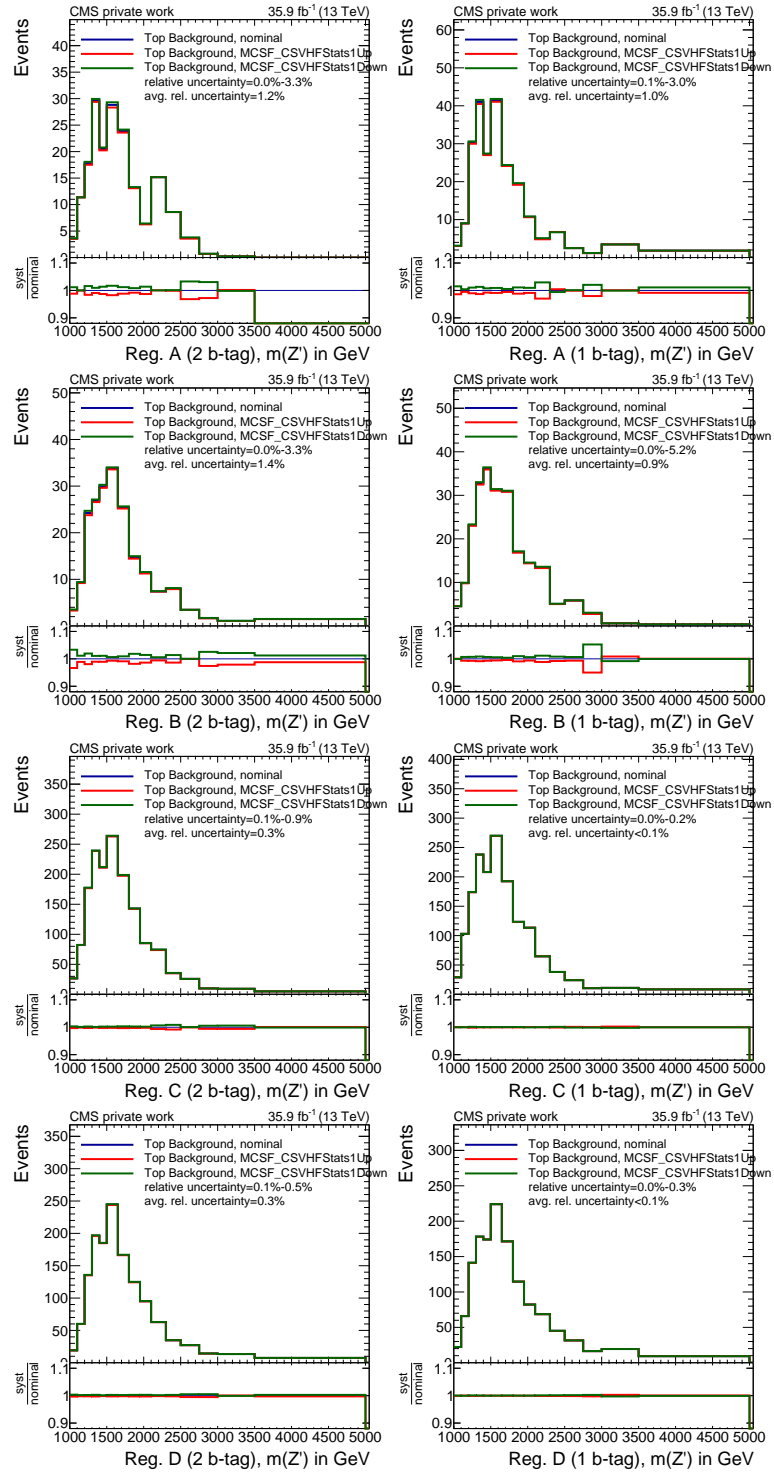
Figure A.15: Impact of b tagging uncertainty (HFStats1) on the Top background. left: 2 b-tag category, right: 1 b-tag category, from top to bottom: Reg. A, Reg. B, Reg. C, Reg. D.
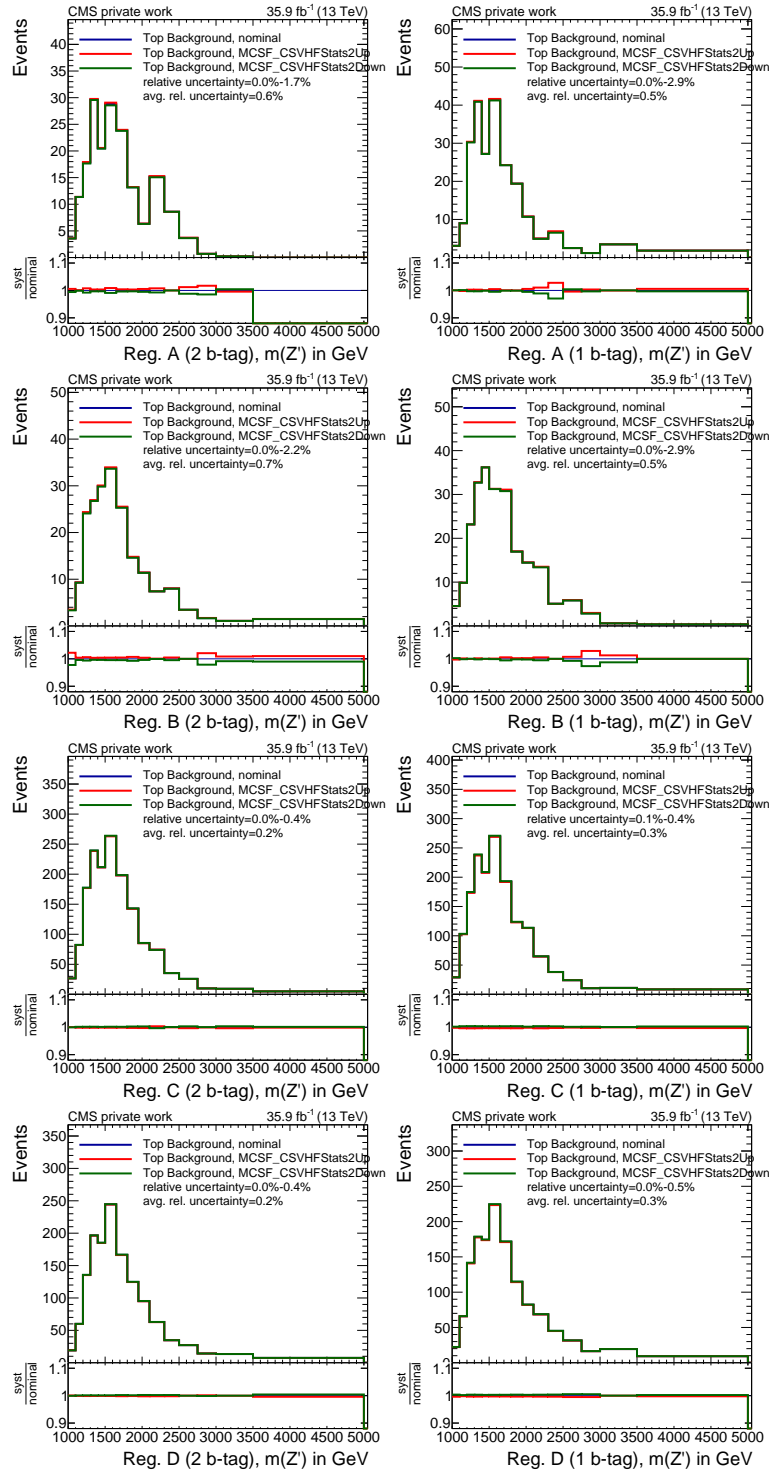
Figure A.16: Impact of b tagging uncertainty (HFStats2) on the Top background. left: 2 b-tag category, right: 1 b-tag category, from top to bottom: Reg. A, Reg. B, Reg. C, Reg. D.
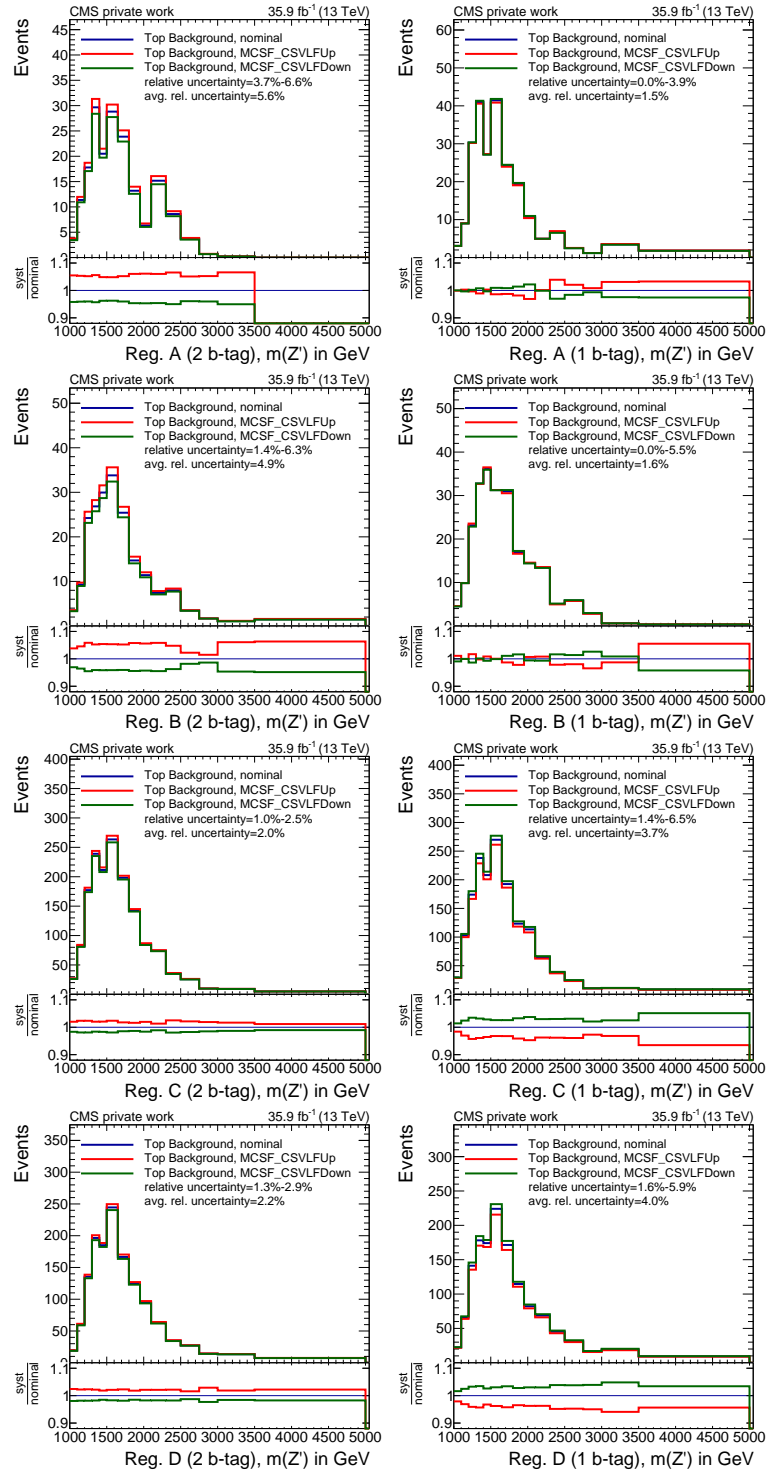
Figure A.17: Impact of b tagging uncertainty (LF) on the Top background. left: 2 b-tag category, right: 1 b-tag category, from top to bottom: Reg. A, Reg. B, Reg. C, Reg. D.
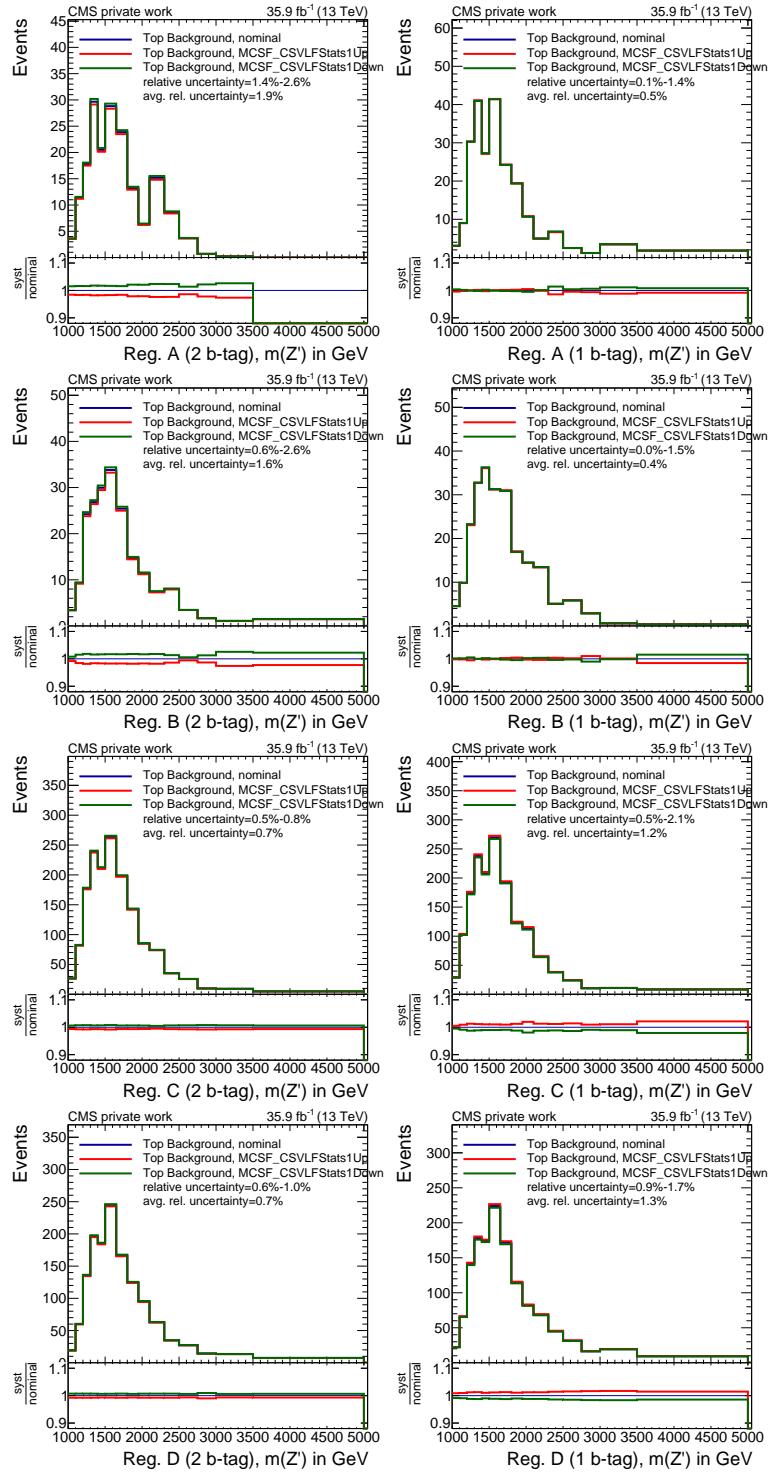
Figure A.18: Impact of b tagging uncertainty (LFStats1) on the Top background. left: 2 b-tag category, right: 1 b-tag category, from top to bottom: Reg. A, Reg. B, Reg. C, Reg. D.
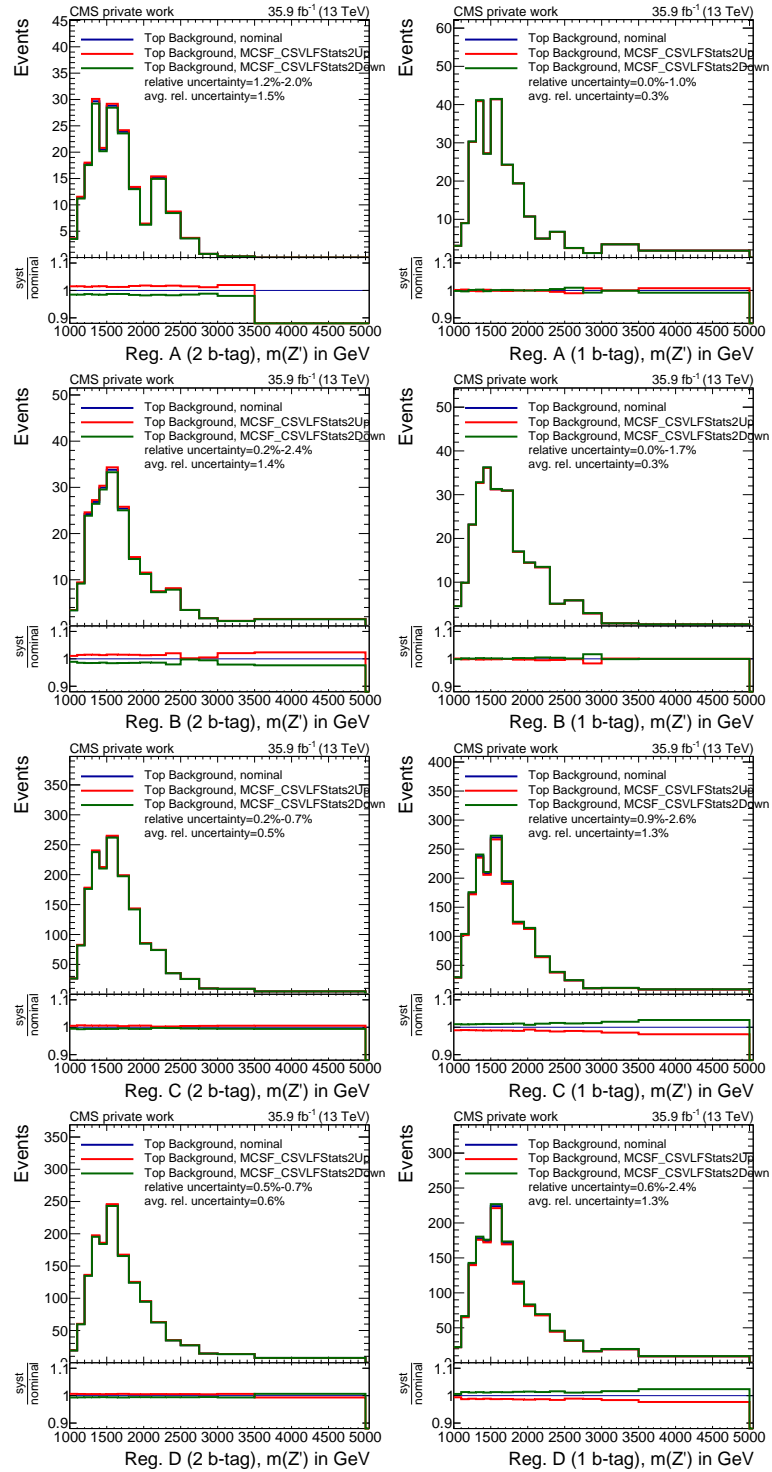
Figure A.19: Impact of b tagging uncertainty (LFStats2) on the Top background. left: 2 b-tag category, right: 1 b-tag category, from top to bottom: Reg. A, Reg. B, Reg. C, Reg. D.
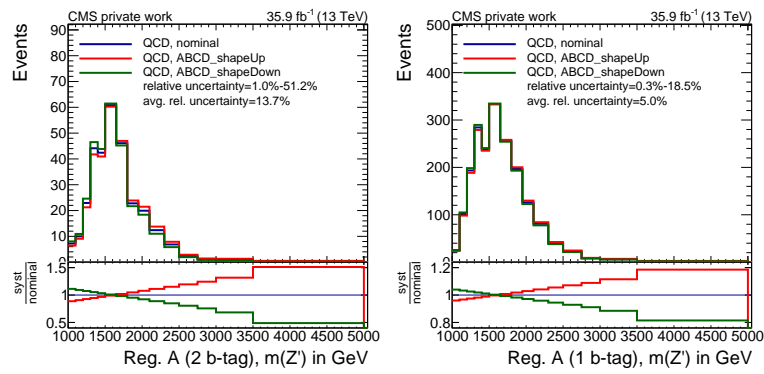
Figure A.20: Impact of ABCD shape uncertainty on QCD-multijet background. left: 2 region A in b-tag category, right: region A in 1 b-tag category. The expectation is taken from the MC QCD-multijet prediction.

A.4 Correlation matrices
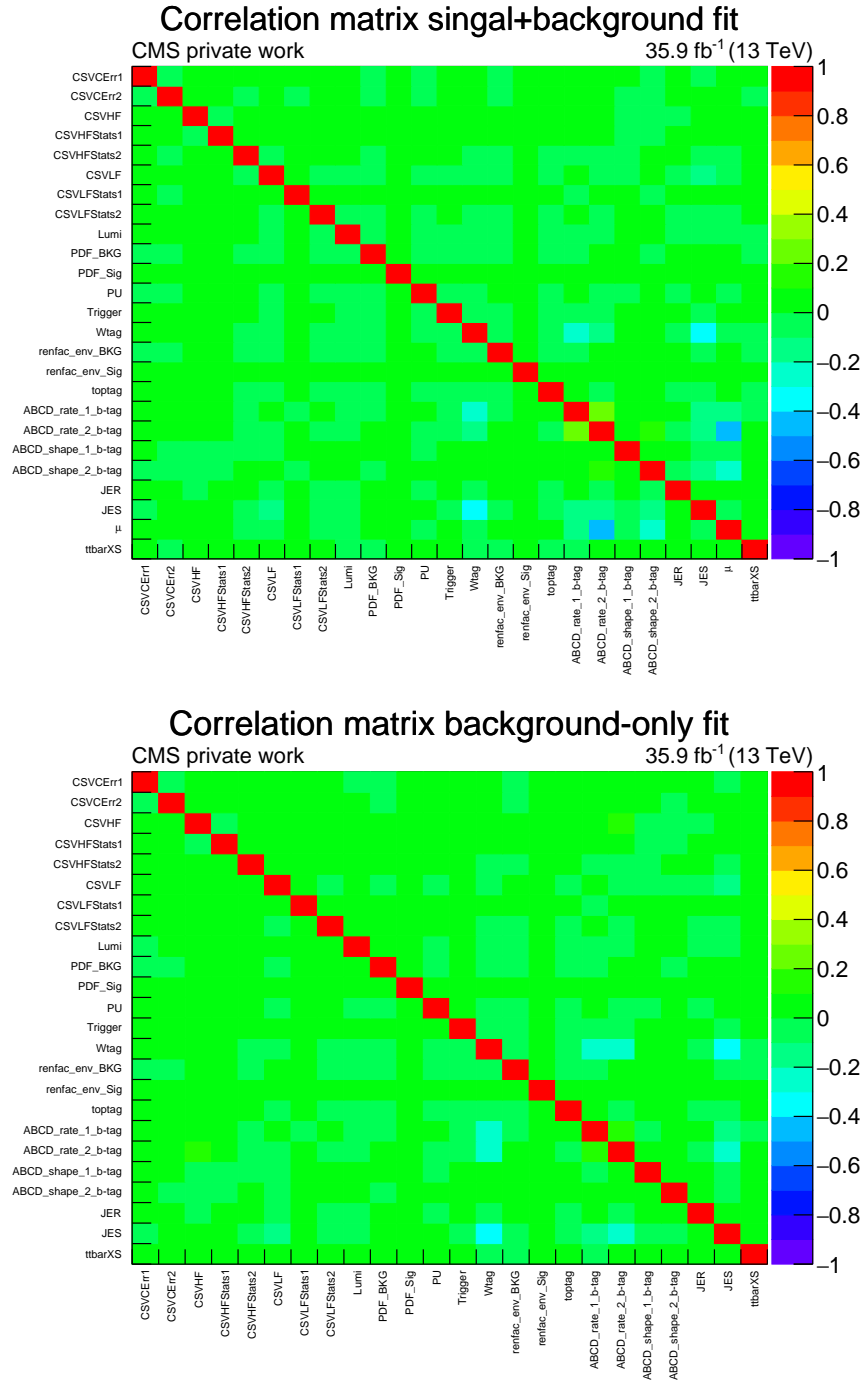
Figure A.21: Correlations for Asimov data without signal presence. Correlation matrices between the fit parameters for the Asimov data (without the presence of a signal) for the signal+background hypothesis (top) and the background only hypothesis (bottom). The fit has been performed for the signal hypothesis of: $m_{Z'} = 2000\,\text{GeV}$, $m_T = 1200\,\text{GeV}$, $\text{BR}(T \to \text{Wb}/\text{Zt}/\text{Ht}) = 50\,\%/25\,\%/25\,\%$.
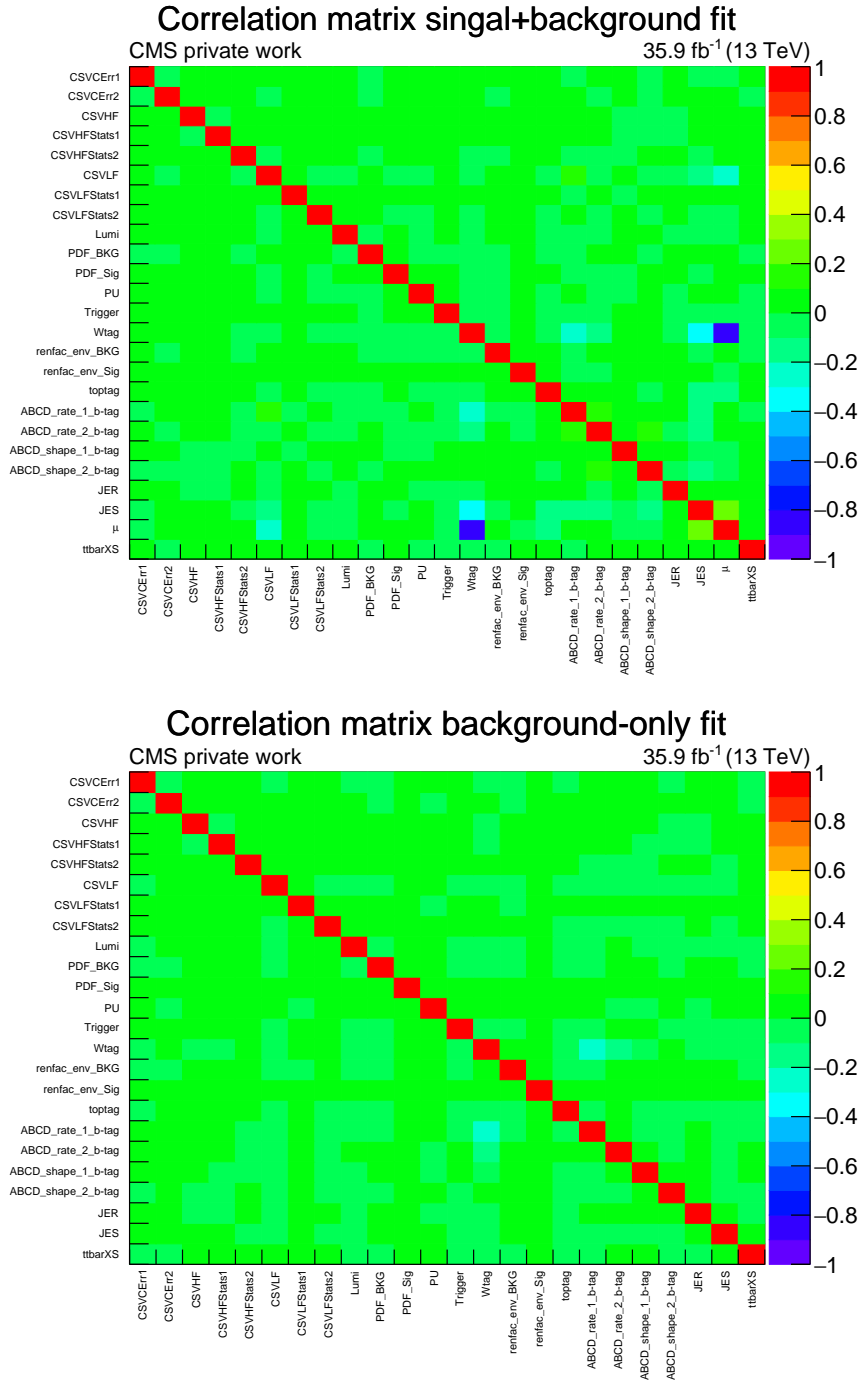
Figure A.22: Correlations for Asimov data with signal presence. Correlation matrices between the fit parameters for the Asimov data (with the presence of a signal) for the signal+background hypothesis (top) and the background only hypothesis (bottom). The fit has been performed for the signal hypothesis of: $m_{Z'} = 2000\,\text{GeV}$, $m_T = 1200\,\text{GeV}$, $\text{BR}(T \to \text{Wb/Zt/Ht}) = 50\,\%/25\,\%/25\,\%$.
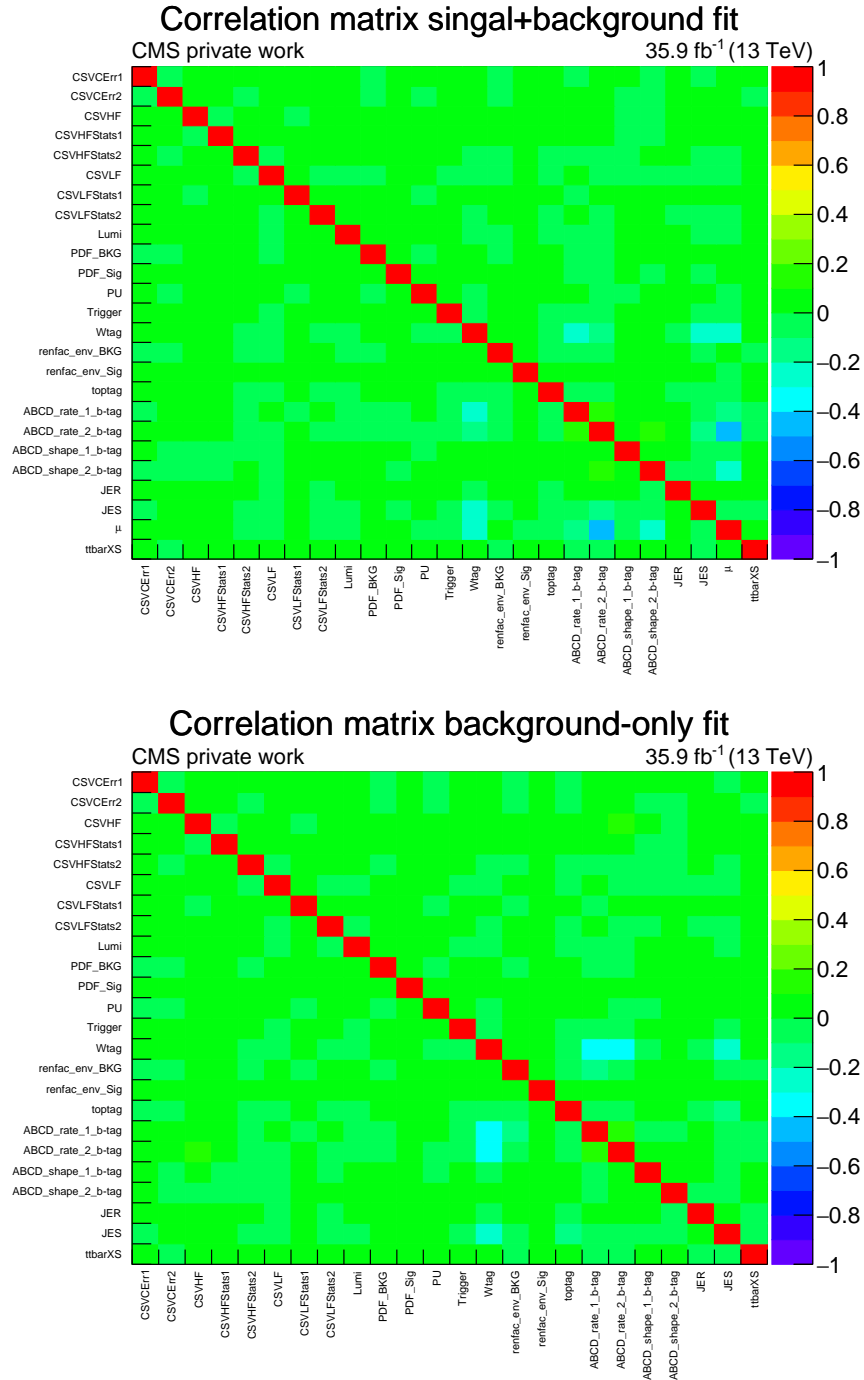
Figure A.23: Correlations for simulated background data without signal presence. Correlation matrices between the fit parameters for the simulated background data (without the presence of a signal) for the signal+background hypothesis (top) and the background only hypothesis (bottom). The fit has been performed for the signal hypothesis of: $m_{Z'} = 2000\,\text{GeV}$, $m_{T} = 1200\,\text{GeV}$, $\text{BR}(T \rightarrow \text{Wb}/\text{Zt}/\text{Ht}) = 50\,\%/25\,\%/25\,\%$.
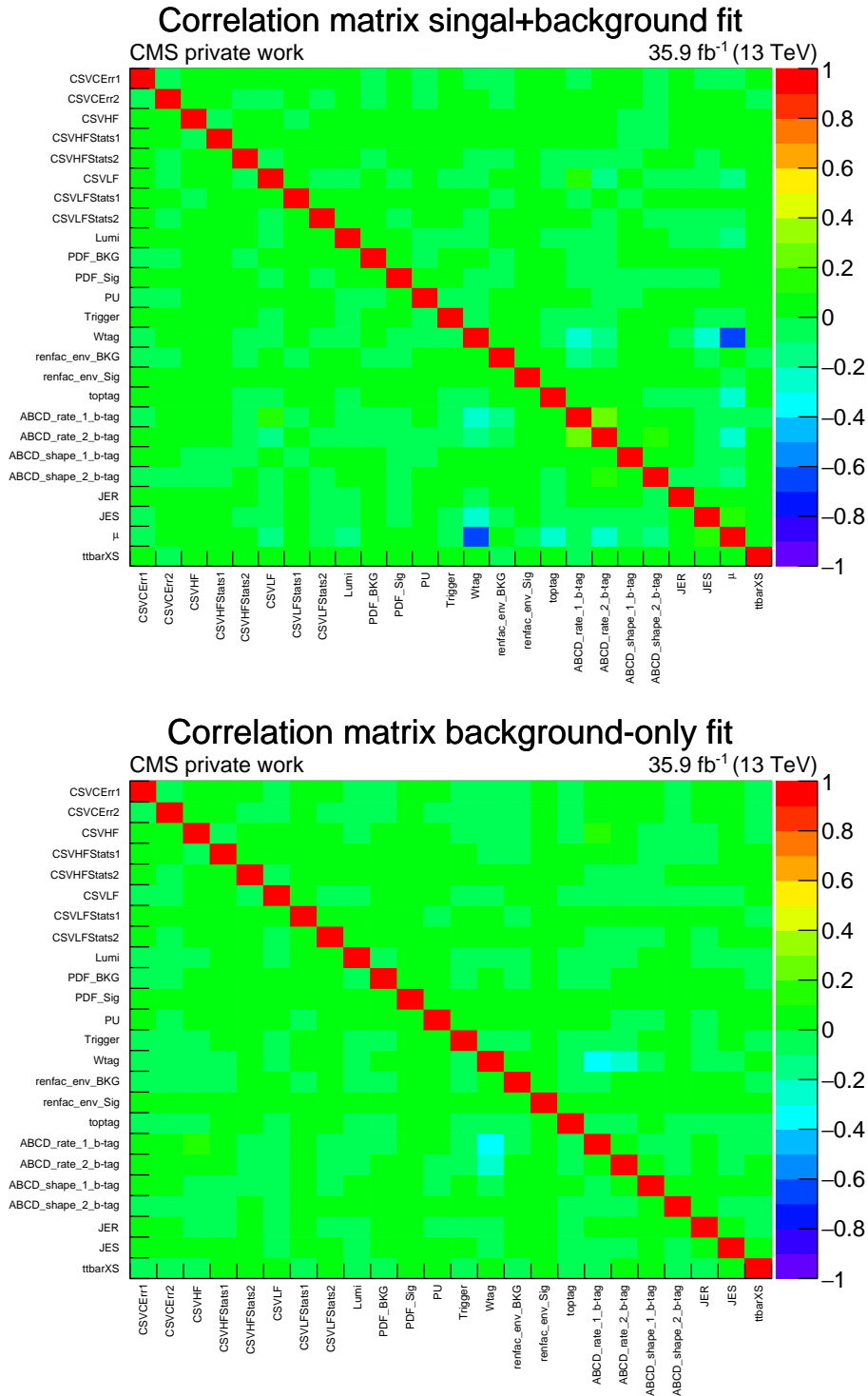
Figure A.24: Correlations for simulated background data with signal presence. Correlation matrices between the fit parameters for the simulated background data (with the presence of a signal) for the signal+background hypothesis (top) and the background only hypothesis (bottom). The fit has been performed for the signal hypothesis of: $m_{Z'} = 2000\,\mathrm{GeV}$, $m_{T} = 1200\,\mathrm{GeV}$, $\mathrm{BR}(\mathrm{T} \to \mathrm{Wb/Zt/Ht}) = 50\,\%/25\,\%/25\,\%$.
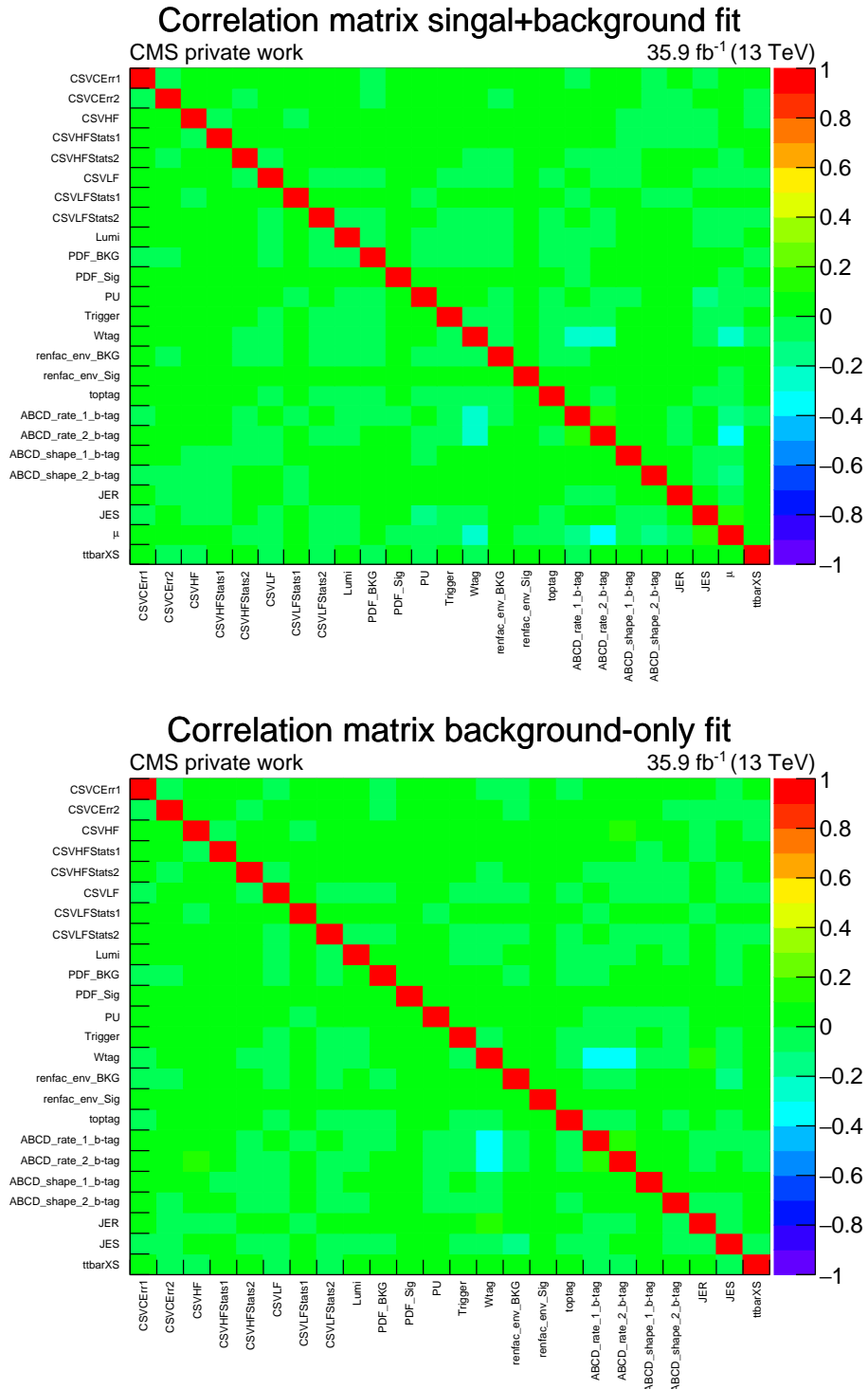
Figure A.25: Nuisance parameter correlations of data. Correlation matrices between the fit parameters of datafor the signal+background hypothesis (top) and the background only hypothesis (bottom). The fit has been performed for the signal hypothesis of: $m_{Z'} = 2000\,\text{GeV}$, $m_T = 1200\,\text{GeV}$, $\text{BR}(T \to \text{Wb/Zt/Ht}) = 50\,\%/25\,\%/25\,\%$.

A.5 Observed and expected limits

Table A.3: Upper limits using little-Higgs model signal samples. The table lists model-independent observed and expected upper cross section limits. The limits are derived using the signal samples based on the effective little-Higgs model.

$m_{Z'}$	$\Gamma_{Z'}/m_{Z'}$	m_T	decay	observed	Expected in pb				
in GeV	in %	in GeV		in pb	-2σ	-1σ	median	$+1\sigma$	$+2\sigma$
1500	1	700	T → Wb	0.23	0.09	0.12	0.18	0.26	0.39
1500	1	900	T → Wb	0.52	0.19	0.25	0.36	0.54	0.81
1500	1	1200	T → Wb	8.8	1.8	2.5	3.7	5.8	9.6
2000	1	900	T → Wb	0.11	0.042	0.056	0.081	0.12	0.18
2000	1	1200	T → Wb	0.13	0.05	0.069	0.098	0.15	0.22
2000	1	1500	T → Wb	0.77	0.28	0.38	0.56	0.84	1.3
2500	1	1200	T → Wb	0.068	0.03	0.041	0.061	0.094	0.14
2500	1	1500	T → Wb	0.044	0.034	0.047	0.068	0.1	0.15
1500	1	700	T → Zt	0.44	0.2	0.27	0.4	0.6	0.9
1500	1	900	T → Zt	0.44	0.17	0.23	0.33	0.5	0.74
1500	1	1200	T → Zt	0.86	0.37	0.51	0.74	1.1	1.8
2000	1	900	T → Zt	0.25	0.09	0.12	0.17	0.25	0.38
2000	1	1200	T → Zt	0.19	0.07	0.089	0.128	0.19	0.29
2000	1	1500	T → Zt	0.17	0.07	0.089	0.127	0.19	0.29
2500	1	1200	T → Zt	0.097	0.041	0.057	0.083	0.13	0.19
2500	1	1500	T → Zt	0.076	0.032	0.045	0.066	0.1	0.15
1500	1	700	T → Ht	0.75	0.31	0.43	0.63	1.0	1.7
1500	1	900	T → Ht	0.57	0.29	0.4	0.58	0.9	1.4
1500	1	1200	T → Ht	3.2	1.1	1.5	2.2	3.4	5.6
2000	1	900	T → Ht	0.56	0.18	0.25	0.37	0.62	1.0
2000	1	1200	T → Ht	0.54	0.19	0.26	0.38	0.64	1.1
2000	1	1500	T → Ht	0.65	0.21	0.28	0.41	0.66	1.2
2500	1	1200	T → Ht	0.23	0.1	0.15	0.21	0.28	0.36
2500	1	1500	T → Ht	0.21	0.1	0.14	0.21	0.28	0.35

Table A.4: Upper limits using warped extra dimensions model signal samples. The table lists model-independent observed and expected upper cross section limits. The limits are derived using the signal samples based on the effective warped extra dimensions model.

$m_{Z'}$ in GeV	$\Gamma_{Z'}/m_{Z'}$ in %	m_{T} in GeV	decay	observed in pb	Expected in pb				
					-2σ	-1σ	median	$+1\sigma$	$+2\sigma$
1500	1	800	T → Wb	0.23	0.09	0.12	0.18	0.27	0.4
1500	1	1000	T → Wb	1.3	0.5	0.69	1.0	1.5	2.2
1500	1	1300	T → Wb	5.8	2.2	3.1	4.6	6.8	9.6
1750	1	1300	T → Wb	1.9	0.6	0.86	1.26	1.9	2.9
2000	1	1000	T → Wb	0.093	0.034	0.046	0.068	0.1	0.15
2000	1	1300	T → Wb	0.18	0.06	0.084	0.121	0.18	0.28
2000	1	1500	T → Wb	0.6	0.22	0.3	0.44	0.65	0.98
2250	1	1300	T → Wb	0.089	0.036	0.049	0.072	0.11	0.17
2250	1	1500	T → Wb	0.096	0.05	0.073	0.107	0.17	0.25
2500	1	1300	T → Wb	0.055	0.025	0.035	0.051	0.079	0.12
2500	1	1500	T → Wb	0.059	0.036	0.047	0.065	0.097	0.14
2500	1	1800	T → Wb	0.12	0.05	0.074	0.109	0.17	0.24
2750	1	1500	T → Wb	0.024	0.017	0.024	0.036	0.054	0.081
3000	1	1500	T → Wb	0.013	0.011	0.015	0.022	0.035	0.054
3000	1	1800	T → Wb	0.016	0.013	0.018	0.028	0.043	0.067
3000	1	2100	T → Wb	0.027	0.81	0.81	0.82	0.82	0.83
3500	1	1800	T → Wb	0.018	0.008	0.011	0.016	0.025	0.037
3500	1	2100	T → Wb	0.022	0.009	0.012	0.018	0.027	0.04
3500	1	2500	T → Wb	0.031	0.013	0.017	0.025	0.037	0.052
4000	1	2100	T → Wb	0.013	0.006	0.0078	0.0105	0.015	0.021
4000	1	2500	T → Wb	0.013	0.006	0.0078	0.0105	0.016	0.022
4000	1	3000	T → Wb	0.016	0.007	0.0095	0.0129	0.018	0.026
1500	1	800	T → Zt	0.27	0.17	0.23	0.34	0.51	0.77
1500	1	1000	T → Zt	0.4	0.2	0.27	0.39	0.6	0.91
1500	1	1300	T → Zt	3.3	1.1	1.5	2.2	3.3	4.8
1750	1	1300	T → Zt	0.31	0.11	0.15	0.21	0.31	0.46
2000	1	1000	T → Zt	0.21	0.08	0.1	0.15	0.22	0.33

$m_{Z'}$ in GeV	$\Gamma_{Z'}/m_{Z'}$ in %	m_T in GeV	decay	observed in pb		Expected in pb			
					-2σ	-1σ	median	$+1\sigma$	$+2\sigma$
2000	1	1300	$T \to Zt$	0.19	0.06	0.085	0.129	0.21	0.34
2000	1	1500	$T \to Zt$	0.17	0.07	0.091	0.131	0.2	0.29
2250	1	1300	$T \to Zt$	0.15	0.044	0.06	0.088	0.13	0.2
2250	1	1500	$T \to Zt$	0.13	0.038	0.053	0.076	0.11	0.17
2500	1	1300	$T \to Zt$	0.079	0.037	0.051	0.075	0.12	0.17
2500	1	1500	$T \to Zt$	0.067	0.032	0.044	0.065	0.1	0.15
2500	1	1800	$T \to Zt$	0.063	0.031	0.042	0.062	0.095	0.14
2750	1	1500	$T \to Zt$	0.039	0.022	0.03	0.045	0.069	0.1
3000	1	1500	$T \to Zt$	0.02	0.015	0.022	0.032	0.049	0.074
3000	1	1800	$T \to Zt$	0.016	0.013	0.017	0.026	0.04	0.061
3000	1	2100	$T \to Zt$	0.015	0.016	0.019	0.027	0.039	0.058
3500	1	1800	$T \to Zt$	0.013	0.006	0.0087	0.0137	0.022	0.034
3500	1	2100	$T \to Zt$	0.011	0.005	0.0072	0.0113	0.019	0.029
3500	1	2500	$T \to Zt$	0.017	0.006	0.0087	0.0168	0.034	0.051
4000	1	2100	$T \to Zt$	0.0098	0.0048	0.0061	0.009	0.013	0.019
4000	1	2500	$T \to Zt$	0.0088	0.0042	0.0054	0.0074	0.012	0.016
4000	1	3000	$T \to Zt$	0.0092	0.0044	0.0058	0.0082	0.012	0.016
1500	1	800	$T \to Ht$	0.32	0.22	0.31	0.45	0.7	1.1
1500	1	1000	$T \to Ht$	0.78	0.36	0.49	0.72	1.1	1.9
1500	1	1300	$T \to Ht$	6.0	2.4	3.4	5.0	7.8	12.5
1750	1	1300	$T \to Ht$	0.67	0.23	0.32	0.47	0.72	1.2
2000	1	1000	$T \to Ht$	0.45	0.15	0.2	0.3	0.48	0.9
2000	1	1300	$T \to Ht$	0.8	0.26	0.35	0.52	0.84	1.6
2000	1	1500	$T \to Ht$	0.47	0.14	0.19	0.28	0.43	0.72
2250	1	1300	$T \to Ht$	0.27	0.1	0.14	0.21	0.34	0.56
2250	1	1500	$T \to Ht$	0.26	0.1	0.13	0.2	0.32	0.56
2500	1	1300	$T \to Ht$	0.22	0.09	0.12	0.19	0.25	0.33
2500	1	1500	$T \to Ht$	0.16	0.08	0.11	0.16	0.23	0.3
2500	1	1800	$T \to Ht$	0.18	0.08	0.11	0.16	0.24	0.31
2750	1	1500	$T \to Ht$	0.15	0.06	0.082	0.125	0.18	0.23

$m_{Z'}$ in GeV	$\Gamma_{Z'}/m_{Z'}$ in %	m_{T} in GeV	decay	observed in pb	Expected in pb				
					-2σ	-1σ	median	$+1\sigma$	$+2\sigma$
3000	1	1500	T → Ht	0.062	0.037	0.052	0.078	0.11	0.15
3000	1	1800	T → Ht	0.058	0.037	0.05	0.075	0.11	0.15
3000	1	2100	T → Ht	0.05	0.034	0.047	0.07	0.11	0.15
3500	1	1800	T → Ht	0.028	0.014	0.02	0.03	0.042	0.057
3500	1	2100	T → Ht	0.026	0.014	0.019	0.029	0.04	0.055
3500	1	2500	T → Ht	0.025	0.013	0.018	0.028	0.04	0.054
4000	1	2100	T → Ht	0.021	0.01	0.013	0.018	0.026	0.036
4000	1	2500	T → Ht	0.02	0.01	0.013	0.018	0.025	0.034
4000	1	3000	T → Ht	0.02	0.01	0.013	0.018	0.025	0.035
1500	30	800	T → Wb	0.43	0.13	0.18	0.27	0.4	0.61
1500	30	1000	T → Wb	0.5	0.19	0.25	0.37	0.56	0.85
1500	30	1300	T → Wb	0.46	0.21	0.28	0.41	0.63	0.96
2000	30	1000	T → Wb	0.17	0.06	0.083	0.122	0.19	0.28
2000	30	1300	T → Wb	0.14	0.07	0.1	0.15	0.23	0.35
2000	30	1500	T → Wb	0.15	0.09	0.13	0.18	0.28	0.43
2500	30	1300	T → Wb	0.05	0.033	0.045	0.067	0.1	0.16
2500	30	1500	T → Wb	0.053	0.036	0.049	0.072	0.11	0.17
2500	30	1800	T → Wb	0.049	0.035	0.05	0.074	0.12	0.18
3000	30	1500	T → Wb	0.027	0.016	0.022	0.034	0.054	0.084
3000	30	1800	T → Wb	0.028	0.016	0.023	0.035	0.055	0.084
3000	30	2100	T → Wb	0.038	0.017	0.024	0.037	0.057	0.083
3500	30	1800	T → Wb	0.039	0.03	0.038	0.057	0.1	0.17
3500	30	2100	T → Wb	0.026	0.011	0.015	0.021	0.032	0.047
3500	30	2500	T → Wb	0.024	0.011	0.014	0.02	0.029	0.042
4000	30	2100	T → Wb	0.019	0.009	0.011	0.016	0.023	0.033
4000	30	2500	T → Wb	0.017	0.007	0.01	0.014	0.02	0.029
4000	30	3000	T → Wb	0.018	0.008	0.01	0.015	0.022	0.031
1500	30	800	T → Zt	0.62	0.26	0.36	0.52	0.78	0.88
1500	30	1000	T → Zt	0.65	0.22	0.3	0.44	0.66	1.0
1500	30	1300	T → Zt	0.49	0.15	0.2	0.3	0.45	0.69

$m_{Z'}$ in GeV	$\Gamma_{Z'}/m_{Z'}$ in %	m_T in GeV	decay	observed in pb		Expected in pb			
					-2σ	-1σ	median	$+1\sigma$	$+2\sigma$
2000	30	1000	$T \to Zt$	0.33	0.12	0.17	0.25	0.38	0.59
2000	30	1300	$T \to Zt$	0.19	0.08	0.11	0.16	0.24	0.37
2000	30	1500	$T \to Zt$	0.18	0.06	0.087	0.126	0.19	0.29
2500	30	1300	$T \to Zt$	0.079	0.043	0.059	0.087	0.13	0.2
2500	30	1500	$T \to Zt$	0.057	0.037	0.051	0.075	0.12	0.18
2500	30	1800	$T \to Zt$	0.044	0.029	0.039	0.058	0.089	0.14
3000	30	1500	$T \to Zt$	0.03	0.02	0.028	0.043	0.067	0.1
3000	30	1800	$T \to Zt$	0.022	0.015	0.02	0.03	0.047	0.072
3000	30	2100	$T \to Zt$	0.017	0.01	0.015	0.023	0.036	0.055
3500	30	1800	$T \to Zt$	0.02	0.009	0.013	0.021	0.032	0.049
3500	30	2100	$T \to Zt$	0.016	0.007	0.01	0.015	0.024	0.036
3500	30	2500	$T \to Zt$	0.015	0.006	0.0087	0.0137	0.021	0.031
4000	30	2100	$T \to Zt$	0.014	0.006	0.009	0.0129	0.019	0.028
4000	30	2500	$T \to Zt$	0.01	0.0048	0.0061	0.009	0.013	0.019
4000	30	3000	$T \to Zt$	0.0081	0.0037	0.0048	0.0066	0.01	0.014
1500	30	800	$T \to Ht$	0.92	0.39	0.54	0.8	1.2	2.0
1500	30	1000	$T \to Ht$	0.97	0.37	0.51	0.75	1.2	1.8
1500	30	1300	$T \to Ht$	1.1	0.29	0.4	0.59	0.91	1.4
2000	30	1000	$T \to Ht$	0.61	0.22	0.3	0.46	0.75	1.3
2000	30	1300	$T \to Ht$	0.45	0.16	0.22	0.33	0.53	0.89
2000	30	1500	$T \to Ht$	0.34	0.15	0.2	0.3	0.49	0.77
2500	30	1300	$T \to Ht$	0.21	0.1	0.14	0.21	0.31	0.42
2500	30	1500	$T \to Ht$	0.16	0.09	0.12	0.18	0.27	0.36
2500	30	1800	$T \to Ht$	0.12	0.07	0.096	0.145	0.23	0.31
3000	30	1500	$T \to Ht$	0.074	0.046	0.064	0.098	0.15	0.2
3000	30	1800	$T \to Ht$	0.064	0.037	0.053	0.079	0.11	0.15
3000	30	2100	$T \to Ht$	0.045	0.025	0.036	0.055	0.084	0.12
3500	30	1800	$T \to Ht$	0.043	0.021	0.03	0.045	0.064	0.087
3500	30	2100	$T \to Ht$	0.039	0.018	0.025	0.037	0.054	0.073
3500	30	2500	$T \to Ht$	0.033	0.014	0.02	0.029	0.043	0.059

$m_{Z'}$ in GeV	$\Gamma_{Z'}/m_{Z'}$ in %	m_{T} in GeV	decay	observed in pb	-2σ	-1σ	Expected in pb median	+1σ	+2σ
4000	30	2100	T $\rightarrow$ Ht	0.027	0.013	0.018	0.025	0.036	0.05
4000	30	2500	T $\rightarrow$ Ht	0.023	0.011	0.015	0.02	0.028	0.04
4000	30	3000	T $\rightarrow$ Ht	0.016	0.009	0.011	0.014	0.02	0.029

List of Acronyms

ADC Analog-Digital Converter
ALICE A Large Ion Collider Experiment
APD Avalanche Photo Diode
ASIC Application-Specific Integrated Circuit
ATLAS A Toroidal LHC ApparatuS

BCB Benzocyclobutene
BDT boosted decision tree
BGA Ball Grid Array
BPIX Barrel Pixel Detector

C4 Controlled Collapse Chip Connection
CA Cambridge-Aachen
CC charged current
CDF Collider Detector at Fermilab
CERN Conseil Européen pour la Recherche Nucléaire
CFRP Carbon-Fiber Reinforced Plastic
CHS Charged Hadron Substraction
CIS CiS Forschungsinstitut für Mikrosensorik GmbH
CKM Cabibbo-Kobayashi-Maskawa
CMOS Complementary Metal-Oxide-Semiconductor
CMS Compact Muon Solenoid
CMSSW Compact Muon Solenoid Software
CNC Computerized Numerical Control
CSC Cathode Strip Chamber
CSV Combined Secondary Vertex
CL confidence level
CT cleaning tray
CPU Central Processing Unit

DCol Double Column
DAC Digital-to-Analogue Converter
DAQ Data Acquisition
DT Drift Tube
DESY Deutsches Elektronen-Synchrotron
DM Dark Matter
DNN deep neural network
DTB Digital Test Board

ECAL Electromagnetic Calorimeter
ED extra dimension
EDX energy-dispersive X-ray
ENEPIG electroless nickel electroless palladium immersion gold
ESD electrostatic discharge
ETH Eidgenössische Technische Hochschule Zürich
ETP Institute of Experimental Particle Physics

EYETS Extended Year End Technical Shutdown

FCNC flavor changing neutral current
FODO Focussing, nOthing, Defocussing, nOthing
FPGA Field-Programmable Gate Array
FIFO First In First Out
FPIX Forward Pixel Detector

GEM Gaseous Electron Multiplier
GPU Graphics Processing Unit
GR General Relativity
GUI graphical user interface
GUT Grand Unified Theory

HB Hadron Barrel
HBR heavy bosonic resonance
HCAL Hadronic Calorimeter
HDI High Density Interconnect
HEP high-energy physics
HE Hadron Endcap
HF Hadron Forward
HGC High Granularity Calorimeter
HLT high-level trigger
HL-LHC High-Luminosity LHC
HPD Hybrid Photo Diode
HPK Hamamatsu Hotonikusu Kabushiki kaisha
HO Hadron Outer

IBM International Business Machines Corporation
IEKP Institut für Experimentelle Kernphysik
IP impact parameter
IPE Institute for Data Processing and Electronics
IVF inclusive vertex finder

JEC jet energy correction
JER jet energy resolution

KK Kaluza-Klein
KIT Karlsruhe Institute of Technology

L1 level 1
LEP Large Electron-Positron Collider
LEIR Low Energy Ion Ring
LHC Large Hadron Collider
LHCb Large Hadron Collider beauty
LHCf Large Hadron Collider forward
LINAC linear accelerator
LS1 Long Shutdown 1

LS2 Long Shutdown 2

ME matrix element
MET Missing Transverse Energy
MIP minimum ionizing particle
MLE maximum likelihood estimation
mMDT modified mass-drop tagger
MoEDAL Monopole and Exotics Detector at the LHC
MC Monte Carlo

Nd-YAG Neodymium-doped Yttrium Aluminum Garnet
NN neural network
NNLO next-to-next-to leading order

PCB printed circuit board
PDF Parton Density Function
PF Particle Flow
PMNS Pontecorvo-Maki-Nakagawa-Sakata
POM Polyoxymethylen
PS Proton Synchrotron
PSB Proton Synchrotron Booster
PSI Paul Scherrer Institute
PSR pseudo signal region
PTFE Polytetrafluoroethylene
PU pileup
PUC Pixel Unit Cell
PUPPI Pileup Per Particle Identification
pXar pixel Xpert analysis & readout

QCD Quantum Chromodynamics

RAM Random Access Memory
RC random cone
RFQ Radio Frequency Quadrupole
RMS Root Mean Square
ROC readout chip
RPC Resistive Plate Chamber
RTI Research Triangle Institute
RWTH Rheinisch-Westfälische Technische Hochschule Aachen

SEM scanning electron microscopy
SEU single event upset
SF Scale Factor
SiPM Silicon Photomultiplier
SM Standard Model of Particle Physics
SMD surface mount device
SNR signal-to-noise Ratio
SPS Super Proton Synchrotron

SUSY Super-symmetry

TBM Token Bit Manager
TEC Tracker EndCap
TIB Tracker Inner Barrel
TID Tracker Inner Disk
TOB Tracker Outer Barrel
TOTEM Total Elastic and Diffractive Cross Section Measurement
TPG Thermal Pyrolytic Graphite

UBM Under Bump Metallization
UE Underlying Event
UHH University of Hamburg
USG ultrasonic generator

VLQ vector-like quark
VPT Vacuum Phototriode
VRT Vacuum Release Tray

WLCG Worldwide LHC Computing Grid

List of Figures

List of Tables

Bibliography

[3M00]   3M. *Flourinert Electronic Liquid FC-72*. May 2000. URL: http://multimedia.
             3m.com/mws/media/648920/fluorinert-electronic-liquid-fc-72.pdf
             (cited on p. 140).

[Abb11]   D. Abbaneo. *Upgrade of the CMS Tracker with tracking trigger*. In: Journal of
             Instrumentation 6.12 (Dec. 2011), p. C12065. DOI: 10.1088/1748-0221/6/
             12/c12065 (cited on p. 41).

[ACG01]   N. Arkani-Hamed, A. G. Cohen, and H. Georgi. *Electroweak symmetry breaking
             from dimensional deconstruction*. In: Physics Letters B 513.1-2 (July 2001),
             pp. 232–240. DOI: 10.1016/S0370-2693(01)00741-9 (cited on p. 14).

[AD09]   P. W. Atkins and J. De Paula. *Atkins' Physical Chemistry*. Oxford University
             Press, 2009. ISBN: 9780199543373 (cited on p. 155).

[ADM16]   A. Angelescu, A. Djouadi, and G. Moreau. *Vector-like top/bottom-quark
             partners and Higgs physics at the LHC*. In: The European Physical Journal C
             76.2 (Feb. 2016), p. 99. DOI: 10.1140/epjc/s10052-016-3950-y (cited on
             p. 12).

[Aga+08]   K. Agashe et al. *CERN LHC signals from warped extra dimensions*. In: Phys.
             Rev. D 77 (1 Jan. 2008), p. 015003. DOI: 10.1103/PhysRevD.77.015003
             (cited in pp. 18 sq.).

[Agg+17]   R. Aggleton et al. *An FPGA based track finder for the L1 trigger of the CMS
             experiment at the High Luminosity LHC*. In: Journal of Instrumentation 12.12
             (Dec. 2017), P12019. DOI: 10.1088/1748-0221/12/12/P12019 (cited on
             p. 41).

[Ago+03]   S. Agostinelli et al. *Geant4 – a simulation toolkit*. In: Nuclear Instruments
             and Methods in Physics Research Section A: Accelerators, Spectrometers,
             Detectors and Associated Equipment 506.3 (July 2003), pp. 250–303. DOI:
             10.1016/S0168-9002(03)01368-8 (cited on p. 62).

[Agu+13]   J. A. Aguilar-Saavedra et al. *Handbook of vectorlike quarks: Mixing and single
             production*. In: Physical Review D 88.9 (Nov. 2013). DOI: 10.1103/physrevd.
             88.094010 (cited in pp. 12, 14, 20).

[Agu+15]   O. de Aguiar Francisco et al. *Evaporative CO_2 microchannel cooling for the
             LHCb VELO pixel upgrade*. In: Journal of Instrumentation 10.05 (May 13,
             2015), p. C05014. DOI: 10.1088/1748-0221/10/05/c05014 (cited on p. 141).

[Aha+06]   F. Aharonian et al. *HESS Observations of the Galactic Center Region and
             Their Possible Dark Matter Interpretation*. In: Physical Review Letters 97.22
             (Nov. 2006). DOI: 10.1103/PhysRevLett.97.221102 (cited on p. 10).

[Ahm+02]   Q. R. Ahmad et al. *Direct Evidence for Neutrino Flavor Transformation from
             Neutral-Current Interactions in the Sudbury Neutrino Observatory*. In: Physical
             Review Letters 89.1 (June 2002). DOI: 10.1103/PhysRevLett.89.011301
             (cited on p. 11).

[Air18]   Airex AG. *AIREX Structural foam cores*. Feb. 18, 2018. URL: http://www.
             airexbaltekbanova.com/airex-foam.html (cited on p. 140).

[Ali+10]   S. Alioli et al. *A general framework for implementing NLO calculations in shower Monte Carlo programs: the POWHEG BOX*. In: Journal of High Energy Physics 2010.6 (June 2010). DOI: 10.1007/jhep06(2010)043 (cited on p. 65).

[Ali+11]   M. Aliev et al. *HATHOR: HAdronic Top and Heavy quarks crOss section calculatoR*. In: Computer Physics Communications 182.4 (Apr. 2011), pp. 1034–1046. DOI: 10.1016/j.cpc.2010.12.040 (cited on p. 65).

[ALI08]   ALICE Collaboration. *The ALICE experiment at the CERN LHC*. In: Journal of Instrumentation 3.08 (Nov. 14, 2008), S08002. DOI: 10.1088/1748-0221/3/08/S08002 (cited on p. 26).

[Alw+11]   J. Alwall et al. *MadGraph 5: going beyond*. In: Journal of High Energy Physics 2011.6 (June 2011). DOI: 10.1007/JHEP06(2011)128 (cited on p. 60).

[Alw+14]   J. Alwall et al. *The automated computation of tree-level and next-to-leading order differential cross sections, and their matching to parton shower simulations*. In: Journal of High Energy Physics 2014.7 (July 2014). DOI: 10.1007/jhep07(2014)079 (cited on p. 65).

[Aly17]   M. Alyari. *Construction of the Phase 1 Upgrade of the CMS Pixel Detector*. Aug. 1, 2017. URL: https://indico.fnal.gov/event/11999/session/11/contribution/256/material/slides/0.pdf (cited on p. 140).

[And+83]   B. Andersson et al. *Parton fragmentation and string dynamics*. In: Physics Reports 97.2-3 (July 1983), pp. 31–145. DOI: 10.1016/0370-1573(83)90080-7 (cited on p. 60).

[Ang+08]   J. Angle et al. *First Results from the XENON10 Dark Matter Experiment at the Gran Sasso National Laboratory*. In: Physical Review Letters 100.2 (Jan. 2008). DOI: 10.1103/PhysRevLett.100.021303 (cited on p. 10).

[APS04]   T. Appelquist, M. Piai, and R. Shrock. *Fermion masses and mixing in extended technicolor models*. In: Physical Review D 69.1 (Jan. 2004). DOI: 10.1103/PhysRevD.69.015002 (cited on p. 14).

[Ark+02]   N. Arkani-Hamed et al. *The Littlest Higgs*. In: Journal of High Energy Physics 2002.07 (July 2002), pp. 034–034. DOI: 10.1088/1126-6708/2002/07/034 (cited on p. 14).

[Art+13]   P. Artoisenet et al. *Automatic spin-entangled decays of heavy resonances in Monte Carlo simulations*. In: Journal of High Energy Physics 2013.3 (Mar. 2013). DOI: 10.1007/jhep03(2013)015 (cited on p. 65).

[AST74]   D. Ambrose, C. Sprake, and R. Townsend. *Thermodynamic properties of organic oxygen compounds XXXIII. The vapour pressure of acetone*. In: The Journal of Chemical Thermodynamics 6.7 (July 1974), pp. 693–700. DOI: 10.1016/0021-9614(74)90119-0 (cited on p. 159).

[ATL08]   ATLAS Collaboration. *The ATLAS Experiment at the CERN Large Hadron Collider*. In: Journal of Instrumentation 3.08 (Aug. 14, 2008), S08003. DOI: 10.1088/1748-0221/3/08/s08003 (cited on p. 26).

[ATL11]   ATLAS Collaboration and CMS Collaboration. *Procedure for the LHC Higgs boson search combination in Summer 2011*. Tech. rep. CMS-NOTE-2011-005. ATL-PHYS-PUB-2011-11. Geneva: CERN, Aug. 2011. URL: https://cds.cern.ch/record/1379837 (cited on p. 91).

[ATL12]   ATLAS Collaboration. *Observation of a new particle in the search for the Standard Model Higgs boson with the ATLAS detector at the LHC.* In: Physics Letters B 716.1 (Sept. 2012), pp. 1–29. DOI: `10.1016/j.physletb.2012.08.020` (cited on p. 5).

[ATL16a]   ATLAS Collaboration. *Measurement of the Inelastic Proton-Proton Cross Section at s=13 TeV with the ATLAS Detector at the LHC.* In: Physical Review Letters 117.18 (2016). DOI: `10.1103/PhysRevLett.117.182002` (cited on p. 24).

[ATL16b]   ATLAS Collaboration. *Performance of b-jet identification in the ATLAS experiment.* In: Journal of Instrumentation 11.04 (Apr. 2016), P04008. DOI: `10.1088/1748-0221/11/04/P04008` (cited on p. 53).

[ATL18]   ATLAS Collaboration. *Public Results – Exotic Physics Searches.* Mar. 1, 2018. URL: `https://twiki.cern.ch/twiki/bin/view/AtlasPublic/ExoticsPublicResults` (cited on p. 63).

[ATV18]   ATV Technologie. *SRO-700 table top IR vacuum reflow system.* Feb. 6, 2018. URL: `https://www.atv-tech.com/sro-700` (cited in pp. 174 sq.).

[Bal+15]   R. D. Ball et al. *Parton distributions for the LHC run II.* In: Journal of High Energy Physics 2015.4 (Apr. 2015). DOI: `10.1007/jhep04(2015)040` (cited on p. 88).

[Bal18]   A. Ball. *Pixel Tracker DC-DC converters - update.* Jan. 25, 2018. URL: `https://indico.cern.ch/event/698738/contributions/2868595/attachments/1589751/2515236/TIP_intro_25Jan18_AB.pdf` (cited on p. 197).

[Bar15]   N. Bartosik. *Associated Top-Quark-Pair and b-Jet Production in the Dilepton Channel at $\sqrt{s}$ = 8 TeV as Test of QCD and Background to $t\bar{t}$+Higgs Production.* Presented 03 Jul 2015. PhD thesis. University of Hamburg, Aug. 2015. URL: `https://cds.cern.ch/record/2047049` (cited on p. 61).

[Bar93]   R. J. Barlow. *Statistics: A Guide to the Use of Statistical Methods in the Physical Sciences.* Wiley, 1993. ISBN: 978-0-471-92295-7 (cited on p. 87).

[BB48]   J. Bardeen and W. H. Brattain. *The Transistor, A Semi-Conductor Triode.* In: Physical Review 74.2 (2 July 1948), pp. 230–231. DOI: `https://doi.org/10.1103/PhysRev.74.230` (cited on p. 117).

[BCL07]   M. Bigas, E. Cabruja, and M. Lozano. *Bonding techniques for hybrid active pixel sensors (HAPS).* In: Nuclear Instruments and Methods in Physics Research Section A: Accelerators, Spectrometers, Detectors and Associated Equipment 574.2 (May 2007), pp. 392–400. ISSN: 0168-9002. DOI: `10.1016/j.nima.2007.01.176` (cited in pp. 132 sq.).

[BCV12]   C. Bini, R. Contino, and N. Vignaroli. *Heavy-light decay topologies as a new strategy to discover a heavy gluon.* In: Journal of High Energy Physics 2012.1 (Jan. 2012). DOI: `10.1007/jhep01(2012)157` (cited in pp. 18 sq., 21 sq., 106).

[Bel+14]   A. Belyaev et al. *Technicolor Higgs boson in the light of LHC data.* In: Physical Review D 90.3 (Aug. 2014). DOI: `10.1103/PhysRevD.90.035012` (cited on p. 14).

[Ben18]   A. Benecke. *Search for Z' decaying into tT' in the lepton jets final state.* May 8, 2018. URL: `http://cms.cern.ch/iCMS/jsp/db_notes/noteInfo.jsp?cmsnoteid=CMS%20AN-2017/103` (cited in pp. 64, 66, 69, 74, 81, 110).

[Ber+17]   R. Bernabei et al. *DAMA/LIBRA results and perspectives*. In: EPJ Web of Conferences 136 (2017). Ed. by A. Morselli, A. Capone, and G. R. Fernandez, p. 05001. DOI: 10.1051/epjconf/201713605001 (cited on p. 10).

[Bet46]   R. A. Beth. *Strong focusing of high energy particles in a synchrotron storage ring*. US3303426A. Mar. 11, 1946 (cited on p. 25).

[Bir+14]   I. Bird et al. *Update of the Computing Models of the WLCG and the LHC Experiments*. Tech. rep. CERN-LHCC-2014-014. LCG-TDR-002. CERN, Apr. 2014. URL: http://cds.cern.ch/record/1695401 (cited on p. 39).

[Bjo+50]   R. Bjorklund et al. *High Energy Photons from Proton-Nucleon Collisions*. In: Physical Review 77.2 (Jan. 1950), pp. 213–218. DOI: 10.1103/physrev.77.213 (cited on p. 14).

[BJR18]   A. Ballantyne, T. Jones, and K. Ryder. *ENIPIG Surface Finishes for Electronics*. Feb. 12, 2018. URL: http://www.macfest-project.co.uk/images/R2i%5C%20poster%5C%20MACFEST.pdf (cited on p. 152).

[Bla+15]   T. Blank et al. *Novel module production methods for the CMS pixel detector, upgrade phase I*. In: Journal of Instrumentation 10.02 (Feb. 2015), p. C02021. DOI: 10.1088/1748-0221/10/02/c02021 (cited on p. 132).

[Blu+84]   G. R. Blumenthal et al. *Formation of galaxies and large-scale structure with cold dark matter*. In: Nature 311.5986 (Oct. 1984), pp. 517–525. DOI: 10.1038/311517a0 (cited on p. 10).

[BM14]   R. Bartek and M. Masciovecchio. *HDI Testing Procedure for the Digital HDI using LabJack*. Tech. rep. CERN, Aug. 28, 2014. URL: https://cds.cern.ch/record/1952337 (cited on p. 191).

[BN90]   B. M. Barbashov and V. Nesterenko. *Introduction to the Relativistic String*. World Scientific Publishing Company, 1990. ISBN: 9789971506872 (cited on p. 10).

[Bra+08]   M. Bradac et al. *Revealing the Properties of Dark Matter in the Merging Cluster MACS J0025.4-1222*. In: The Astrophysical Journal 687.2 (Nov. 2008), pp. 959–967. DOI: 10.1086/591246 (cited on p. 10).

[Bro+06]   C. Broennimann et al. *Development of an Indium bump bond process for silicon pixel detectors at PSI*. In: Nuclear Instruments and Methods in Physics Research Section A: Accelerators, Spectrometers, Detectors and Associated Equipment 565.1 (Sept. 2006), pp. 303–308. ISSN: 0168-9002. DOI: 10.1016/j.nima.2006.05.011 (cited in pp. 132, 165).

[Brü+04]   O. S. Brüning et al. *LHC Design Report*. CERN Yellow Reports: Monographs. Geneva: CERN, 2004. URL: http://cds.cern.ch/record/782076 (cited in pp. 23 sq., 26).

[Bru18]   Bruker Corporation. *High-resolution micro-CT*. Feb. 26, 2018. URL: https://www.bruker.com/products/microtomography/micro-ct-for-sample-scanning/skyscan-1272/overview.html (cited on p. 166).

[Buc+15]   A. Buckley et al. *LHAPDF6: parton density access in the LHC precision era*. In: Eur. Phys. J. C75 (2015), p. 132. DOI: 10.1140/epjc/s10052-015-3318-8. arXiv: 1412.7420 [hep-ph] (cited on p. 88).

[Bur+90]   D. Burdeaux et al. *Benzocyclobutene (BCB) dielectrics for the fabrication of high density, thin film multichip modules*. In: Journal of Electronic Materials 19.12 (Dec. 1990), pp. 1357–1366. DOI: 10.1007/BF02662825 (cited on p. 157).

[But+08]   J. M. Butterworth et al. *Jet Substructure as a New Higgs-Search Channel at the Large Hadron Collider*. In: Physical Review Letters 100.24 (June 2008). DOI: 10.1103/physrevlett.100.242001 (cited in pp. 57, 59).

[But18]   J. Butler. *CMS Weekly General Meeting 349*. Mar. 8, 2018. URL: https://indico.cern.ch/event/710662/contributions/2919550/attachments/1613932/2563872/WGM349_SPteam_Status_report_R1.pdf (cited on p. 197).

[Cas+16]   M. Caselle et al. *Low-cost bump-bonding processes for high energy physics pixel detectors*. In: Journal of Instrumentation 11.01 (Jan. 2016), p. C01050. DOI: 10.1088/1748-0221/11/01/c01050 (cited on p. 132).

[Cas17]   R. Caspart. *Confining the Higgs sector via the investigation of di-tau final states with LHC Run II data*. PhD thesis. Karlsruher Institut für Technologie (KIT), Oct. 27, 2017, DOI: 10.5445/IR/1000076416 (cited on p. 38).

[Cat+93]   S. Catani et al. *Longitudinally-invariant $k_\perp$-clustering algorithms for hadron-hadron collisions*. In: Nuclear Physics B 406.1-2 (Sept. 1993), pp. 187–224. DOI: 10.1016/0550-3213(93)90166-m (cited in pp. 50, 58).

[CC74]   J. R. Chelikowsky and M. L. Cohen. *Electronic structure of silicon*. In: Physical Review B 10.12 (July 1, 1974), pp. 5095–5107. DOI: 10.1103/physrevb.10.5095 (cited on p. 120).

[CFM13]   M. Czakon, P. Fiedler, and A. Mitov. *Total Top-Quark Pair-Production Cross Section at Hadron Colliders Through $O(\alpha S4)$*. In: Physical Review Letters 110.25 (June 2013). DOI: 10.1103/physrevlett.110.252004 (cited on p. 65).

[Che+08]   L. Cheng et al. *New prediction methods for CO_2 evaporation inside tubes: Part I – A two-phase flow pattern map and a flow pattern based phenomenological model for two-phase flow frictional pressure drops*. In: International Journal of Heat and Mass Transfer 51.1-2 (Jan. 2008), pp. 111–124. DOI: 10.1016/j.ijheatmasstransfer.2007.04.002 (cited on p. 141).

[Chi13]   A. Chilingarov. *Generation current temperature scaling*. Tech. rep. Lancaster University, UK, Jan. 30, 2013. URL: https://cds.cern.ch/record/1511886 (cited on p. 193).

[Cie+17]   D. Cieri et al. *An FPGA-based track finder for the L1 trigger of the CMS experiment at the HL-LHC*. In: PoS TWEPP-17 (2017), 131. 5 p. DOI: 10.22323/1.313.0131 (cited on p. 41).

[Clo+06]   D. Clowe et al. *A Direct Empirical Proof of the Existence of Dark Matter*. In: The Astrophysical Journal 648.2 (Aug. 2006), pp. L109–L113. DOI: 10.1086/508162 (cited on p. 10).

[CM14]   M. Czakon and A. Mitov. *Top++: A program for the calculation of the top-pair cross-section at hadron colliders*. In: Computer Physics Communications 185.11 (Nov. 2014), pp. 2930–2938. DOI: 10.1016/j.cpc.2014.06.021 (cited on p. 65).

[CMS06]   CMS Collaboration. *CMS Physics: Technical Design Report Volume 1: Detector Performance and Software*. Technical Design Report CMS. There is an error on cover due to a technical problem for some items. Geneva: CERN, 2006. ISBN: 9290832681. URL: http://cds.cern.ch/record/922757 (cited on p. 50).

[CMS08]   CMS Collaboration. *The CMS experiment at the CERN LHC*. In: Journal of Instrumentation 3.08 (Aug. 14, 2008), S08004. DOI: 10.1088/1748-0221/3/08/S08004 (cited in pp. 26, 31, 35, 37).

[CMS09]   CMS Collaboration. *A Cambridge-Aachen (C-A) based Jet Algorithm for boosted top-jet tagging*. Tech. rep. CMS-PAS-JME-09-001. Geneva: CERN, July 2009. URL: http://cds.cern.ch/record/1194489 (cited on p. 59).

[CMS11]   CMS Collaboration. *Technical proposal for the upgrade of the CMS detector through 2020*. Tech. rep. CERN-LHCC-2011-006. LHCC-P-004. CERN, June 2011. URL: https://cds.cern.ch/record/1355706 (cited on p. 40).

[CMS12a]   CMS Collaboration. *CMS Technical Design Report for the Pixel Detector Upgrade*. Tech. rep. CERN-LHCC-2012-016. CMS-TDR-11. CERN, Sept. 2012. URL: https://cds.cern.ch/record/1481838 (cited in pp. 36, 40, 128, 136–142, 148, 153).

[CMS12b]   CMS Collaboration. *Observation of a new boson at a mass of 125 GeV with the CMS experiment at the LHC*. In: Physics Letters B 716.1 (Sept. 2012), pp. 30–61. DOI: 10.1016/j.physletb.2012.08.021 (cited on p. 5).

[CMS12c]   CMS Collaboration. *Performance of CMS muon reconstruction in pp collision events at $\sqrt{s} = 7 TeV$*. In: Journal of Instrumentation 7.10 (Oct. 2012), P10002. DOI: 10.1088/1748-0221/7/10/p10002 (cited on p. 49).

[CMS13a]   CMS Collaboration. *Identification of b-quark jets with the CMS experiment*. In: Journal of Instrumentation 8.04 (Apr. 2013), P04013. DOI: 10.1088/1748-0221/8/04/p04013 (cited on p. 53).

[CMS13b]   CMS Collaboration. *Identifying Hadronically Decaying Vector Bosons Merged into a Single Jet*. Tech. rep. CMS-PAS-JME-13-006. Geneva: CERN, 2013. URL: http://cds.cern.ch/record/1577417 (cited in pp. 58, 89).

[CMS13c]   CMS Collaboration. *The performance of the CMS muon detector in proton-proton collisions at $\sqrt{s} = 7$ TeV at the LHC*. In: Journal of Instrumentation 8.11 (Nov. 2013), P11002. DOI: 10.1088/1748-0221/8/11/p11002 (cited on p. 34).

[CMS14a]   CMS Collaboration. *Boosted Top Jet Tagging at CMS*. Tech. rep. CMS-PAS-JME-13-007. Geneva: CERN, 2014. URL: https://cds.cern.ch/record/1647419 (cited on p. 59).

[CMS14b]   CMS Collaboration. *Description and performance of track and primary-vertex reconstruction with the CMS tracker*. In: Journal of Instrumentation 9.10 (Oct. 2014), P10009. DOI: 10.1088/1748-0221/9/10/P10009 (cited in pp. 135 sq.).

[CMS14c]   CMS Collaboration. *Pileup Removal Algorithms*. Tech. rep. CMS-PAS-JME-14-001. Geneva: CERN, 2014. URL: https://cds.cern.ch/record/1751454 (cited on p. 52).

[CMS14d]   CMS Collaboration. *Underlying Event Tunes and Double Parton Scattering*. Tech. rep. CMS-PAS-GEN-14-001. Geneva: CERN, 2014. URL: http://cds.cern.ch/record/1697700 (cited on p. 65).

[CMS15]   CMS Collaboration. *Performance of photon reconstruction and identification with the CMS detector in proton-proton collisions at $\sqrt{s} = 8$ TeV*. In: Journal of Instrumentation 10.08 (Aug. 2015), P08010. DOI: 10.1088/1748-0221/10/08/p08010 (cited on p. 50).

[CMS16a] CMS Collaboration. *CMS Detector Slice*. Jan. 12, 2016. URL: https://cds.cern.ch/record/2120661 (cited on p. 32).

[CMS16b] CMS Collaboration. *Identification of b quark jets at the CMS Experiment in the LHC Run 2*. Tech. rep. CMS-PAS-BTV-15-001. Geneva: CERN, 2016. URL: https://cds.cern.ch/record/2138504 (cited on p. 54).

[CMS16c] CMS Collaboration. *Measurements of the Higgs boson production and decay rates and constraints on its couplings from a combined ATLAS and CMS analysis of the LHC pp collision data at $\sqrt{s} = 7$ and 8 TeV*. In: Journal of High Energy Physics 2016.8 (Aug. 2016). DOI: 10.1007/JHEP08(2016)045 (cited in pp. 10, 12).

[CMS16d] CMS Collaboration. *Top Tagging with New Approaches*. Tech. rep. CMS-PAS-JME-15-002. CERN, 2016. URL: http://inspirehep.net/record/1416681/files/JME-15-002-pas.pdf (cited on p. 59).

[CMS17a] CMS Collaboration. *CMS Luminosity Measurements for the 2016 Data Taking Period*. Tech. rep. CMS-PAS-LUM-17-001. Geneva: CERN, 2017. URL: https://cds.cern.ch/record/2257069 (cited on p. 89).

[CMS17b] CMS Collaboration. *CMS Tracking POG Performance Plots For 2017 with PhaseI pixel detector*. May 2, 2017. URL: https://twiki.cern.ch/twiki/bin/view/CMSPublic/TrackingPOGPerformance2017MC (cited on p. 138).

[CMS17c] CMS Collaboration. *CMS TriDAS project: Technical Design Report, Volume 1: The Trigger Systems*. Technical Design Report CMS. July 26, 2017. URL: http://cds.cern.ch/record/706847 (cited on p. 37).

[CMS17d] CMS Collaboration. *Heavy flavor identification at CMS with deep neural networks*. In: CMS Performance Note (Mar. 13, 2017). URL: http://cds.cern.ch/record/2255736?ln=en (cited in pp. 54, 137).

[CMS17e] CMS Collaboration. *Jet algorithms performance in 13 TeV data*. Tech. rep. CMS-PAS-JME-16-003. Geneva: CERN, 2017. URL: https://cds.cern.ch/record/2256875 (cited on p. 58).

[CMS17f] CMS Collaboration. *Jet energy scale and resolution in the CMS experiment in pp collisions at 8 TeV*. In: Journal of Instrumentation 12.02 (Feb. 2017), P02014. DOI: 10.1088/1748-0221/12/02/P02014 (cited in pp. 50, 52).

[CMS17g] CMS Collaboration. *Jet energy scale and resolution in the CMS experiment in pp collisions at 8 TeV*. In: Journal of Instrumentation 12.02 (Feb. 2017), P02014–P02014. DOI: 10.1088/1748-0221/12/02/P02014 (cited on p. 89).

[CMS17h] CMS Collaboration. *Particle-flow reconstruction and global event description with the CMS detector*. In: Journal of Instrumentation 12.10 (Oct. 2017), P10003. DOI: 10.1088/1748-0221/12/10/P10003 (cited in pp. 47 sq., 51).

[CMS17i] CMS Collaboration. *Public CMS Luminosity Information*. Dec. 4, 2017. URL: https://twiki.cern.ch/twiki/bin/view/CMSPublic/LumiPublicResults (cited in pp. 24, 135).

[CMS17j] CMS Collaboration. *Run II Pixel Performance plots for data and simulation*. 2017. URL: https://twiki.cern.ch/twiki/bin/view/CMSPublic/PixelOfflinePlots2016 (cited in pp. 135 sq.).

[CMS17k] CMS Collaboration. *Search for a heavy resonance decaying to a top quark and a vector-like top quark at $\sqrt{s} = 13$ TeV*. In: Journal of High Energy Physics 2017.9 (Sept. 2017). DOI: 10.1007/JHEP09(2017)053 (cited in pp. 63 sq.).

[CMS17l]   CMS Collaboration. *Search for pair production of vector-like T and B quarks in single-lepton final states using boosted jet substructure in proton-proton collisions at $\sqrt{13} = 13$ TeV*. In: Journal of High Energy Physics 2017.11 (Nov. 2017). DOI: 10.1007/JHEP11(2017)085 (cited on p. 13).

[CMS17m]   CMS Collaboration. *Search for single production of a heavy vector-like T quark decaying to a Higgs boson and a top quark with a lepton and jets in the final state*. In: Physics Letters B 771 (Aug. 2017), pp. 80–105. DOI: 10.1016/j.physletb.2017.05.019 (cited on p. 13).

[CMS17n]   CMS Collaboration. *Search for single production of vector-like quarks decaying to a Z boson and a top or a bottom quark in proton-proton collisions at $\sqrt{s} = 13$ TeV*. In: Journal of High Energy Physics 2017.5 (May 2017). DOI: 10.1007/JHEP05(2017)029 (cited on p. 13).

[CMS17o]   CMS Collaboration. *Search for top quark partners with charge 5/3 in the single-lepton final state at $\sqrt{s} = 13$ TeV*. Tech. rep. CMS-PAS-B2G-17-008. CERN, 2017. URL: http://inspirehep.net/record/1599659/files/B2G-17-008-pas.pdf (cited on p. 13).

[CMS17p]   CMS Collaboration. *The Phase-2 Upgrade of the CMS Tracker*. Tech. rep. CERN-LHCC-2017-009. CMS-TDR-014. Geneva: CERN, June 2017. URL: https://cds.cern.ch/record/2272264 (cited on p. 39).

[CMS18a]   CMS Collaboration. *Baseline muon selections for Run-II*. Apr. 5, 2018. URL: https://twiki.cern.ch/twiki/bin/viewauth/CMS/SWGuideMuonIdRun2#Medium_Muon (cited on p. 49).

[CMS18b]   CMS Collaboration. *Beyond 2 Generations Publications*. Mar. 1, 2018. URL: http://cms-results.web.cern.ch/cms-results/public-results/publications/B2G/index.html (cited on p. 63).

[CMS18c]   CMS Collaboration. *Boosted Top Jet Tagging*. Mar. 26, 2018. URL: https://twiki.cern.ch/twiki/bin/viewauth/CMS/JetTopTagging (cited in pp. 57, 89).

[CMS18d]   CMS Collaboration. *CMS detector design*. Feb. 26, 2018. URL: http://cms.web.cern.ch/news/cms-detector-design (cited on p. 32).

[CMS18e]   CMS Collaboration. *Documentation of the RooStats -based statistics tools for Higgs PAG*. Mar. 19, 2018. URL: https://twiki.cern.ch/twiki/bin/view/CMS/SWGuideHiggsAnalysisCombinedLimit (cited on p. 91).

[CMS18f]   CMS Collaboration. *Identification of heavy-flavour jets with the CMS detector in pp collisions at 13 TeV*. In: Journal of Instrumentation 13.05 (May 2018), P05011–P05011. DOI: 10.1088/1748-0221/13/05/p05011. arXiv: 1712.07158 [physics.ins-det] (cited in pp. 54 sq., 90).

[CMS18g]   CMS Collaboration. *Jet Energy Resolution*. Mar. 26, 2018. URL: https://twiki.cern.ch/twiki/bin/view/CMS/JetResolution#JER_Scaling_factors_and_Uncertai (cited on p. 89).

[CMS18h]   CMS Collaboration. *Jet energy scale uncertainty sources*. Mar. 26, 2018. URL: https://twiki.cern.ch/twiki/bin/view/CMS/JECUncertaintySources (cited in pp. 53, 89).

[CMS18i]   CMS Collaboration. *Jet Identification for the 13 TeV data Run2016*. Apr. 30, 2018. URL: https://twiki.cern.ch/twiki/bin/view/CMS/JetID13TeVRun2016 (cited on p. 52).

[CMS18j]   CMS Collaboration. *Multivariate Electron Identification for Run2*. Apr. 5, 2018. URL: https://twiki.cern.ch/twiki/bin/view/CMS/MultivariateElectronIdentificat Recommended_MVA_recipes_for_2016 (cited on p. 50).

[CMS18k]   CMS Collaboration. *NNLO+NNLL top-quark-pair cross sections*. Mar. 26, 2018. URL: https://twiki.cern.ch/twiki/bin/view/LHCPhysics/ TtbarNNLO?rev=16#Top_quark_pair_cross_sections_at (cited in pp. 65, 89).

[CMS18l]   CMS Collaboration. *Observation of $t\bar{t}H$ production*. Tech. rep. CERN, 2018. arXiv: 1804.02610 [hep-ex]. URL: https://arxiv.org/abs/1804.02610 (cited in pp. 7, 74).

[CMS18m]   CMS Collaboration. *Search for pair production of vector-like quarks in the bWbW channel from proton-proton collisions at $\sqrt{s} = 13$ TeV*. In: Physics Letters B 779 (Apr. 2018), pp. 82–106. DOI: 10.1016/j.physletb.2018.01. 077 (cited on p. 13).

[CMS18n]   CMS Collaboration. *Single Top Cross sections*. May 23, 2018. URL: https: //twiki.cern.ch/twiki/bin/viewauth/CMS/SingleTopSigma?rev=12 (cited on p. 65).

[CMS18o]   CMS Collaboration. *The Performance plots for Phase 1 Pixel Detector 2017*. Apr. 27, 2018. URL: https://twiki.cern.ch/twiki/bin/view/CMSPublic/ PixelOfflinePlots2017 (cited on p. 198).

[CMS18p]   CMS Collaboration. *Utilities for Accessing Pileup Information for Data*. May 23, 2018. URL: https://twiki.cern.ch/twiki/bin/view/CMS/ PileupJSONFileforData#Pileup_JSON_Files_For_Run_II (cited on p. 89).

[CMS18q]   CMS Collaboration. *W/Z-tagging of Jets*. Apr. 5, 2018. URL: https://twiki. cern.ch/twiki/bin/viewauth/CMS/JetWtagging (cited on p. 56).

[CMS18r]   CMS Collaboration. *W/Z-tagging of Jets*. Mar. 26, 2018. URL: https://twiki. cern.ch/twiki/bin/viewauth/CMS/JetWtagging#Recommendation_for_ 13_TeV_data_a (cited on p. 89).

[CMS97a]   CMS Collaboration. *The CMS electromagnetic calorimeter project: Technical Design Report*. Technical Design Report CMS. Geneva: CERN, 1997. URL: http://cds.cern.ch/record/349375 (cited on p. 35).

[CMS97b]   CMS Collaboration. *The CMS hadron calorimeter project: Technical Design Report*. Technical Design Report CMS. CERN, 1997. URL: http://cds.cern. ch/record/357153 (cited in pp. 34 sq.).

[Col16]   F. Colombo. *Packaging and assembly technologies for the pixel detector upgrade and measurement of $\tau\tau$ final states with the CMS experiment at the LHC*. PhD thesis. Karlsruher Institut für Technologie (KIT), July 1, 2016. URL: https: //ekp-invenio.physik.uni-karlsruhe.de/record/48804/files/EKP- 2016-00016.pdf (cited in pp. 145, 158, 180 sqq., 189).

[Con+15]   D. Contardo et al. *Technical Proposal for the Phase-II Upgrade of the CMS Detector*. Tech. rep. CERN-LHCC-2015-010. LHCC-P-008. CMS-TDR-15-02. Geneva: CERN, June 2015. URL: https://cds.cern.ch/record/2020886 (cited in pp. 40 sq.).

[Cos18]   Costruzioni Apparecchiature Elettroniche Nucleari S.p.A. *Dual/Quad Digital Multi Channel Analyzer*. Jan. 11, 2018. URL: http://www.caen.it/jsp/ Template2/CaenProd.jsp?parent=64&idmod=922 (cited on p. 129).

[Cow+11]   G. Cowan et al. *Asymptotic formulae for likelihood-based tests of new physics*. In: The European Physical Journal C 71.2 (Feb. 2011), pp. 1–19. DOI: 10. 1140/epjc/s10052-011-1554-0 (cited on p. 92).

[CS06]   N. D. Christensen and R. Shrock. *Extended technicolor models with two extended technicolor groups*. In: Physical Review D 74.1 (July 2006). DOI: 10.1103/PhysRevD.74.015004 (cited on p. 14).

[CST06]   E. J. Copeland, M. Sami, and S. Tsujikawa. *Dynamics of dark energy*. In: International Journal of Modern Physics D 15.11 (Nov. 2006), pp. 1753–1935. DOI: 10.1142/S021827180600942X (cited on p. 11).

[Dag+15]   J. Daguin et al. *Evaporative CO_2 cooling system for the upgrade of the CMS pixel detector at CERN*. In: IEEE Intersociety Conference on Thermal and Thermomechanical Phenomena in Electronic Systems (ITherm) (2012-07-15). DOI: 10.1109/ITHERM.2012.6231499 (cited on p. 141).

[DF00]   M. Doets and M. Ferro-Luzzi. *Preliminary studies for the LHCb vertex detector cooling system*. Tech. rep. LHCb-99-046. Geneva: CERN, Apr. 2000. URL: http://cds.cern.ch/record/691534 (cited on p. 140).

[Dir26]   P. A. M. Dirac. *On the Theory of Quantum Mechanics*. In: Proceedings of the Royal Society A: Mathematical, Physical and Engineering Sciences 112.762 (1926), pp. 661–677. DOI: 10.1098/rspa.1926.0133 (cited on p. 118).

[Djo08]   A. Djouadi. *The anatomy of electroweak symmetry breaking: Tome I: The Higgs boson in the Standard Model*. In: Physics Reports 457.1-4 (Feb. 2008), pp. 1–216. DOI: 10.1016/j.physrep.2007.10.004 (cited on p. 8).

[DK03]   M. Dine and A. Kusenko. *Origin of the matter-antimatter asymmetry*. In: Reviews of Modern Physics 76.1 (Dec. 2003), pp. 1–30. DOI: 10.1103/RevModPhys.76.1 (cited on p. 11).

[Dok+97]   Y. Dokshitzer et al. *Better jet clustering algorithms*. In: Journal of High Energy Physics 1997.08 (Aug. 1997), p. 001. DOI: 10.1088/1126-6708/1997/08/001 (cited on p. 50).

[Dru00]   P. Drude. *Zur Elektronentheorie der Metalle*. In: Annalen der Physik 306.3 (1900), pp. 566–613. DOI: 10.1002/andp.19003060312 (cited on p. 117).

[DS79]   S. Dimopoulos and L. Susskind. *Mass without scalars*. In: Nuclear Physics B 155.1 (Aug. 1979), pp. 237–252. DOI: 10.1016/0550-3213(79)90364-X (cited on p. 14).

[EB08]   L. Evans and P. Bryant. *LHC Machine*. In: Journal of Instrumentation 3.08 (2008), S08001. DOI: 10.1088/1748-0221/3/08/s08001 (cited on p. 26).

[EB64]   F. Englert and R. Brout. *Broken Symmetry and the Mass of Gauge Vector Mesons*. In: Physical Review Letters 13.9 (Aug. 1964), pp. 321–323. DOI: 10.1103/PhysRevLett.13.321 (cited on p. 8).

[Ebe13]   R. Eber. *Untersuchung neuartiger Sensorkonzepte und Entwicklung eines effektiven Modells der Strahlenschädigung für die Simulation hochbestrahlter Silizium-Teilchendetektoren*. PhD thesis. Karlsruher Institut für Technologie (KIT), Nov. 29, 2013. URL: https://publikationen.bibliothek.kit.edu/1000038403 (cited on p. 128).

[EL80]   E. Eichten and K. Lane. *Dynamical breaking of weak interaction symmetries*. In: Physics Letters B 90.1-2 (Feb. 1980), pp. 125–130. DOI: 10.1016/0370-2693(80)90065-9 (cited on p. 14).

[Ele18]   Electrical4u. *Forward and Reverse Bias of P N Junction*. May 23, 2018. URL: https://www.electrical4u.com/pn-junction/ (cited on p. 122).

[Erd+10]   W. Erdmann et al. *Upgrade plans for the CMS pixel barrel detector*. In: Nuclear Instruments and Methods in Physics Research Section A: Accelerators, Spectrometers, Detectors and Associated Equipment 617.1-3 (May 2010), pp. 534–537. DOI: 10.1016/j.nima.2009.10.029 (cited in pp. 136, 144).

[Erd00]   W. Erdmann. *The CMS pixel detector*. In: Nuclear Instruments and Methods in Physics Research Section A: Accelerators, Spectrometers, Detectors and Associated Equipment 447.1-2 (June 2000), pp. 178–183. DOI: 10.1016/s0168-9002(00)00186-8 (cited on p. 37).

[Erd15]   W. Erdmann. *Status of the Pixel Barrel*. Nov. 30, 2015. URL: https://indico.cern.ch/event/462092/contributions/1978820/attachments/1190335/1738684/2015-11-30-bpix.pdf (cited in pp. 140, 143).

[EVW09]   S. D. Ellis, C. K. Vermilion, and J. R. Walsh. *Techniques for improved heavy particle searches with jet substructure*. In: Physical Review D 80.5 (Sept. 2009). DOI: 10.1103/physrevd.80.051501 (cited on p. 56).

[EVW10]   S. D. Ellis, C. K. Vermilion, and J. R. Walsh. *Recombination algorithms and jet substructure: Pruning as a tool for heavy particle searches*. In: Physical Review D 81.9 (May 2010). DOI: 10.1103/physrevd.81.094023 (cited on p. 56).

[Fel+11]   L. Feld et al. *CO_2 cooling for the CMS tracker at SLHC*. In: Journal of Instrumentation 6.01 (2011), p. C01091. DOI: 10.1088/1748-0221/6/01/C01091 (cited on p. 141).

[Fel17]   L. Feld. *Abschätzung des QCD-Multijet-Untergrunds mit der ABCD-Methode für die Suche nach schweren bosonischen Resonanzen mit dem CMS-Experiment*. Bachelor thesis. Karlsruher Institut für Technologie (KIT), Aug. 4, 2017. URL: https://ekp-invenio.physik.uni-karlsruhe.de/record/48927/files/EKP-2017-00054.pdf (cited in pp. 76, 79).

[Fer+15]   E. Ferri et al. *The Status of the MARE Experiment with ^{187}Re and $^{163}HoIsotopes$*. In: Physics Procedia 61 (2015), pp. 227–231. DOI: 10.1016/j.phpro.2014.12.037 (cited on p. 11).

[Fer26]   E. Fermi. *Zur Quantelung des idealen einatomigen Gases*. In: Zeitschrift für Physik 36.11-12 (1926), pp. 902–912. DOI: 10.1007/bf01400221 (cited on p. 118).

[Fin17]   Finetech GmbH & Co. KG. *FINEPLACER®femto 2*. Feb. 7, 2017. URL: http://www.finetech.de/micro-assembly/products/fineplacerr-femto-2.html (cited on p. 172).

[Fox+12]   P. J. Fox et al. *Missing energy signatures of dark matter at the LHC*. In: Physical Review D 85.5 (Mar. 2012). DOI: 10.1103/PhysRevD.85.056011 (cited on p. 10).

[Fre15]   B. Freund. *Module Production and Qualification for the Phase I Upgrade of the CMS Pixel Detector*. Tech. rep. CMS-CR-2015-228. Geneva: CERN, Oct. 2015. URL: https://cds.cern.ch/record/2062928 (cited on p. 192).

[Fre17]   B. Freund. *Modulproduktion für den CMS-Phase-I-Pixeldetektor und Unter-suchung der erwarteten Leistungsfähigkeit über dessen Betriebsdauer.* PhD thesis. Karlsruher Institut für Technologie (KIT), July 28, 2017. URL: `https://ekp-invenio.physik.uni-karlsruhe.de/record/48919/files/EKP-2017-00046.pdf` (cited in pp. 131, 137, 146, 150, 153, 167 sq., 170, 186 sqq., 192, 196).

[FS81]   E. Farhi and L. Susskind. *Technicolour.* In: Physics Reports 74.3 (Aug. 1981), pp. 277–321. DOI: `10.1016/0370-1573(81)90173-3` (cited on p. 14).

[Fuk+98]   Y. Fukuda et al. *Evidence for Oscillation of Atmospheric Neutrinos.* In: Physical Review Letters 81.8 (Aug. 1998), pp. 1562–1567. DOI: `10.1103/PhysRevLett.81.1562` (cited on p. 11).

[GA96]   L. Goenka and A. Achari. *Void formation in flip chip solder bumps. II.* In: *Nineteenth IEEE/CPMT International Electronics Manufacturing Technology Symposium.* IEEE, Oct. 14, 1996. DOI: `10.1109/iemt.1996.559783` (cited on p. 181).

[Gas+17]   L. Gastaldo et al. *The electron capture in 163Ho experiment ECHo.* In: The European Physical Journal Special Topics 226.8 (June 2017), pp. 1623–1694. DOI: `10.1140/epjst/e2017-70071-y` (cited on p. 11).

[GBC16]   I. Goodfellow, Y. Bengio, and A. Courville. *Deep Learning (Adaptive Computation and Machine Learning series).* The MIT Press, 2016. ISBN: 978-0262035613 (cited on p. 165).

[GHK64]   G. S. Guralnik, C. R. Hagen, and T. W. B. Kibble. *Global Conservation Laws and Massless Particles.* In: Physical Review Letters 13.20 (Nov. 1964), pp. 585–587. DOI: `10.1103/PhysRevLett.13.585` (cited on p. 8).

[Giu08]   G. F. Giudice. *Naturally Speaking: The Naturalness Criterion and Physics at the LHC.* June 2008. DOI: `10.1142/9789812779762_0010` (cited on p. 11).

[GL14]   D. Greco and D. Liu. *Hunting composite vector resonances at the LHC: naturalness facing data.* In: Journal of High Energy Physics 2014.12 (Dec. 2014). DOI: `10.1007/JHEP12(2014)126` (cited in pp. 15 sq.).

[GM12]   R. Gross and A. Marx. *Festkörperphysik.* Gruyter, Walter de GmbH, Nov. 20, 2012. ISBN: 9783486714869 (cited on p. 118).

[Goe14]   M. Goerner. *Differential Cross Sections for Top-Quark-Pair Production in the e/μ+Jets Final State at $\sqrt{s} = 8$ TeV in CMS.* PhD thesis. University of Hamburg, 2014. URL: `https://cds.cern.ch/record/1754332` (cited on p. 61).

[Gol61]   J. Goldstone. *Field theories with « Superconductor » solutions.* In: Il Nuovo Cimento 19.1 (Jan. 1961), pp. 154–164. DOI: `10.1007/BF02812722` (cited on p. 8).

[Gos08]   W. S. Gosset. *The Probable Error of a Mean.* In: Biometrika 6.1 (1908), p. 1. DOI: `10.2307/2331554` (cited on p. 179).

[GP75]   H. Georgi and A. Pais. *Vacuum symmetry and the pseudo-Goldstone phenomenon.* In: Physical Review D 12.2 (July 1975), pp. 508–512. DOI: `10.1103/PhysRevD.12.508` (cited on p. 14).

[GSW62]   J. Goldstone, A. Salam, and S. Weinberg. *Broken Symmetries.* In: Physical Review 127.3 (Aug. 1962), pp. 965–970. DOI: `10.1103/PhysRev.127.965` (cited on p. 8).

[Han13]   K. Hanke. *PAST AND PRESENT OPERATION OF THE CERN PS BOOSTER.* In: International Journal of Modern Physics A 28.13 (2013), p. 1330019. DOI: 10.1142/s0217751x13300196 (cited on p. 25).

[Har17]   F. Hartmann. *Evolution of Silicon Sensor Technology in Particle Physics.* 2nd ed. Springer, Nov. 3, 2017. ISBN: 978-3-319-64434-9. DOI: 10.1007/978-3-319-64436-3 (cited on p. 126).

[Hei12]   S. Heitz. *Bump-Bonding-Technologie für das Upgrade des CMS-Pixeldetektors.* Master thesis. Karlsruher Institut für Technologie (KIT), Oct. 5, 2012. URL: http://ekp-invenio.physik.uni-karlsruhe.de/record/48178/files/iekp-ka2012-16.pdf (cited on p. 132).

[Hei16]   S. M. Heindl. *Production and Quality Assurance of Modules and Study of optimized Pixel Sensor Designs for the Upgrade of the CMS Pixel Detector.* PhD thesis. Karlsruher Institut für Technologie (KIT), Dec. 2, 2016. URL: http://ekp-invenio.physik.uni-karlsruhe.de/record/48899 (cited in pp. 153 sq., 190 sq., 195).

[Hig64a]   P. W. Higgs. *Broken symmetries, massless particles and gauge fields.* In: Physics Letters 12.2 (Sept. 1964), pp. 132–133. DOI: 10.1016/0031-9163(64)91136-9 (cited on p. 8).

[Hig64b]   P. W. Higgs. *Broken Symmetries and the Masses of Gauge Bosons.* In: Physical Review Letters 13.16 (Oct. 1964), pp. 508–509. DOI: 10.1103/PhysRevLett.13.508 (cited on p. 8).

[Hig66]   P. W. Higgs. *Spontaneous Symmetry Breakdown without Massless Bosons.* In: Physical Review 145.4 (May 1966), pp. 1156–1163. DOI: 10.1103/PhysRev.145.1156 (cited on p. 8).

[Hit15]   B. Hiti. *Probe Station for Functionality Tests of Bare Modules for the Phase I Upgrade of the CMS Pixel Detector.* Master thesis. Karlsruher Institut für Technologie (KIT), Sept. 3, 2015. URL: http://ekp-invenio.physik.uni-karlsruhe.de/record/48731 (cited in pp. 161, 167, 170 sq.).

[HL06]   A. Höcker and Z. Ligeti. *CP Violation and the CKM Matrix.* In: Annual Review of Nuclear and Particle Science 56.1 (Nov. 2006), pp. 501–567. DOI: 10.1146/annurev.nucl.56.080805.140456 (cited in pp. 7, 11).

[Höc15]   S. Höche. *Introduction to parton-shower event generators.* In: *Proceedings, Theoretical Advanced Study Institute in Elementary Particle Physics: Journeys Through the Precision Frontier: Amplitudes for Colliders (TASI 2014): Boulder, Colorado, June 2-27, 2014.* 2015, pp. 235–295. DOI: 10.1142/9789814678766_0005. arXiv: 1411.4085 [hep-ph] (cited on p. 30).

[HS15]   D. Hits and A. Starodumov. *The CMS Pixel Readout Chip for the Phase 1 Upgrade.* In: Journal of Instrumentation 10.05 (May 2015), pp. C05029–C05029. DOI: 10.1088/1748-0221/10/05/c05029 (cited on p. 146).

[Hu01]   W. Hu. *Mapping the Dark Matter through the Cosmic Microwave Background Damping Tail.* In: The Astrophysical Journal 557.2 (Aug. 2001), pp. L79–L83. DOI: 10.1086/323253 (cited on p. 10).

[Huf+03]   A. Huffman et al. *Fine-pitch wafer bumping and assembly for high density detector systems.* In: *2003 IEEE Nuclear Science Symposium. Conference Record (IEEE Cat. No.03CH37515).* Vol. 5. IEEE, 2003, pp. 3522–3526. DOI: 10.1109/nssmic.2003.1352670 (cited in pp. 133, 155, 157, 166).

[IPC12]   IPC – Association Connecting Electronics Industries. *Specification for Electroless Nickel / Electroless Palladium / Immersion Gold (ENEPIG) Plating for Printed Circuit Boards.* July 2012. URL: http://www.ipc.org/committee/drafts/4-14_d_IPC-4556_FinalDraft_7-30-2012.pdf (cited on p. 153).

[Jor03]   J. Jordan. *Gold stud bump in flip-chip applications.* In: *27th Annual IEEE/SEMI International Electronics Manufacturing Technology Symposium.* Vol. 46. IEEE, 2003, p86. DOI: 10.1109/iemt.2002.1032735 (cited on p. 133).

[Jun14]   A. Jung. *Scanning electron microscope pictures, recorded at the Institute for Technical Physics (ITEP).* 2014 (cited on p. 133).

[Jun18]   T. Junk. *Staistical Methods for Experimental Particle Physics.* May 18, 2018. URL: https://www-cdf.fnal.gov/~trj/trjethstatsday4.pdf (cited on p. 76).

[Kal21]   T. Kaluza. *Zum Unitätsproblem der Physik.* In: Sitzungsber. Preuss. Akad. Wiss. Berlin (Math. Phys.) 1921 (1921), pp. 966–972. arXiv: 1803.08616 [physics.hist-ph] (cited on p. 16).

[Kal60]   R. Kalman. *A New Approach to Linear Filtering and Prediction Problems.* In: Journal of Basic Engineering 82.1 (Jan. 1960), pp. 35–45. DOI: 10.1115/1.3662552 (cited on p. 47).

[Kan+15]   P. Kant et al. *HatHor for single top-quark production: Updated predictions and uncertainty estimates for single top-quark production in hadronic collisions.* In: Computer Physics Communications 191 (June 2015), pp. 74–89. DOI: 10.1016/j.cpc.2015.02.001 (cited on p. 65).

[Kar+97]   V. Karimäki et al. *The CMS tracker system project: Technical Design Report.* Technical Design Report CMS. Geneva: CERN, 1997. URL: http://cds.cern.ch/record/368412 (cited on p. 35).

[Käs+06]   H. C. Kästli et al. *Design and performance of the CMS pixel detector readout chip.* In: Nuclear Instruments and Methods in Physics Research Section A: Accelerators, Spectrometers, Detectors and Associated Equipment 565.1 (Sept. 2006), pp. 188–194. DOI: 10.1016/j.nima.2006.05.038 (cited on p. 146).

[Kas+15]   G. Kasieczka et al. *Resonance Searches with an Updated Top Tagger.* In: JHEP 06 (2015), p. 203. DOI: 10.1007/JHEP06(2015)203. arXiv: 1503.05921 [hep-ph] (cited on p. 59).

[Käs13]   H. C. Kästli. *Frontend electronics development for the CMS pixel detector upgrade.* In: Nuclear Instruments and Methods in Physics Research Section A: Accelerators, Spectrometers, Detectors and Associated Equipment 731 (Dec. 11, 2013), pp. 88–91. DOI: 10.1016/j.nima.2013.05.056 (cited in pp. 136, 146).

[Kei17]   Keithley. *Series 2400 SourceMeter Line.* Feb. 5, 2017. URL: https://docs-emea.rs-online.com/webdocs/10eb/0900766b810eb7d7.pdf (cited on p. 168).

[Ken87]   S. M. Kent. *Dark matter in spiral galaxies. II - Galaxies with H I rotation curves.* In: The Astronomical Journal 93 (Apr. 1987), p. 816. DOI: 10.1086/114366 (cited on p. 10).

[KEY18]   KEYENCE CORPORATION. *Digital Microscope – VHX-5000 series.* Mar. 26, 2018. URL: https://www.keyence.com/products/microscope/digital-microscope/vhx-5000/index.jsp (cited on p. 154).

[KHP14]   KHP Kunststofftechnik e.K. *Datasheet: POM-ESL*. Last downloaded 22.05.2014. 2014. URL: http://www.khp-kunststoffe.de/Downloads/Konstruktionskunststoffe/Datenblatt_21_POM_ELS.pdf (cited on p. 159).

[Kib67]   T. W. B. Kibble. *Symmetry Breaking in Non-Abelian Gauge Theories*. In: Physical Review 155.5 (Mar. 1967), pp. 1554–1561. DOI: 10.1103/PhysRev.155.1554 (cited on p. 8).

[Kid10]   N. Kidonakis. *Two-loop soft anomalous dimensions for single top quark associated production with aW-orH-*. In: Physical Review D 82.5 (Sept. 2010). DOI: 10.1103/physrevd.82.054018 (cited on p. 65).

[Kit04]   C. Kittel. *Introduction to Solid State Physics 8th Edition*. John Wiley and Sons Ltd, Oct. 28, 2004. 704 pp. ISBN: 047141526X (cited on p. 118).

[Kle17]   K. Klein. *The Phase-1 upgrade of the CMS pixel detector*. In: Nuclear Instruments and Methods in Physics Research Section A: Accelerators, Spectrometers, Detectors and Associated Equipment 845 (Feb. 2017), pp. 101–105. DOI: 10.1016/j.nima.2016.06.039 (cited in pp. 142, 149).

[Kle26]   O. Klein. *Quantentheorie und fünfdimensionale Relativitätstheorie*. In: Zeitschrift für Physik 37.12 (Dec. 1926), pp. 895–906. DOI: 10.1007/BF01397481 (cited on p. 16).

[Kro+14]   D. Krohn et al. *Jet cleansing: Separating data from secondary collision induced radiation at high luminosity*. In: Physical Review D 90.6 (Sept. 2014). DOI: 10.1103/physrevd.90.065020 (cited on p. 52).

[Kud14]   S. Kudella. *Gold-stud bump bonding interconnection technology for the CMS experiment*. Master thesis. Karlsruher Institut für Technologie (KIT), May 28, 2014. URL: http://ekp-invenio.physik.uni-karlsruhe.de/record/48571 (cited in pp. 132 sq., 142, 158, 160, 165 sq., 173).

[Kud17]   S. Kudella. *Qualification of barrel pixel detector modules for the Phase 1 Upgrade of the CMS vertex detector*. In: PoS Vertex2016 (2017), p. 068. URL: http://inspirehep.net/record/1615377/?ln=de (cited in pp. 171, 192, 194).

[Lai+97]   H. L. Lai et al. *Improved parton distributions from global analysis of recent deep inelastic scattering and inclusive jet data*. In: Physical Review D 55.3 (Feb. 1997), pp. 1280–1296. DOI: 10.1103/physrevd.55.1280 (cited on p. 27).

[Lan44]   L. Landau. *On the energy loss of fast particles by ionization*. In: J. Phys.(USSR) (1944) (cited on p. 124).

[Lar+14]   A. J. Larkoski et al. *Soft drop*. In: Journal of High Energy Physics 2014.5 (May 2014). DOI: 10.1007/jhep05(2014)146 (cited in pp. 56 sq.).

[Le 90]   L. Le Cam. *Maximum Likelihood: An Introduction*. In: International Statistical Review / Revue Internationale de Statistique 58.2 (Aug. 1990), p. 153. DOI: 10.2307/1403464 (cited on p. 91).

[LHC08a]   LHCb Collaboration. *The LHCb Detector at the LHC*. In: Journal of Instrumentation 3.08 (Aug. 14, 2008), S08005. DOI: 10.1088/1748-0221/3/08/S08005 (cited on p. 26).

[LHC08b]   LHCf Collaboration. *The LHCf detector at the CERN Large Hadron Collider*. In: Journal of Instrumentation 3.08 (2008), S08006. DOI: 10.1088/1748-0221/3/08/S08006 (cited on p. 26).

[Lim04]   J. A. S. Lima. *Alternative dark energy models: an overview*. In: Brazilian Journal of Physics 34.1a (Mar. 2004), pp. 194–200. DOI: 10.1590/S0103-97332004000200009 (cited on p. 11).

[LP17]   K. Lane and L. Pritchett. *The light composite Higgs boson in strong extended technicolor*. In: JHEP 06 (2017), p. 140. DOI: 10.1007/JHEP06(2017)140. arXiv: 1604.07085 [hep-ph] (cited on p. 14).

[LP70]   P. Leiderer and F. Pobell. *Mutual friction and the thermal conductivity of superfluid helium near T?* In: Journal of Low Temperature Physics 3.6 (1970), pp. 577–588. DOI: 10.1007/bf00628335 (cited on p. 26).

[LTF01]   T. Y. Lee, K. N. Tu, and D. R. Frear. *Electromigration of eutectic SnPb and SnAg3.8Cu0.7 flip chip solder bumps and under-bump metallization*. In: Journal of Applied Physics 90.9 (Nov. 2001), pp. 4502–4508. DOI: 10.1063/1.1400096 (cited on p. 132).

[Lut07]   G. Lutz. *Semiconductor Radiation Detectors*. ISBN: 978-3-540-71678-5 (Print) 978-3-540-71679-2 (Online). Springer, 2007. DOI: 10.1007/978-3-540-71679-2 (cited in pp. 119, 121, 123).

[Maj17]   D. Majumder. *Private communication*. 2017 (cited on p. 71).

[Man+07]   M. L. Mangano et al. *Matching matrix elements and shower evolution for top-pair production in hadronic collisions*. In: Journal of High Energy Physics 2007.01 (Jan. 2007), pp. 013–013. DOI: 10.1088/1126-6708/2007/01/013 (cited on p. 60).

[Man+12]   J. Mans et al. *CMS Technical Design Report for the Phase 1 Upgrade of the Hadron Calorimeter*. Tech. rep. CERN-LHCC-2012-015. CMS-TDR-10. CERN, Sept. 2012. URL: https://cds.cern.ch/record/1481837 (cited on p. 40).

[Mil69]   L. F. Miller. *Controlled Collapse Reflow Chip Joining*. In: IBM Journal of Research and Development 13.3 (May 1969), pp. 239–250. DOI: 10.1147/rd.133.0239 (cited on p. 132).

[Min08]   H. Minkowski. *Die Grundgleichungen für die elektromagnetischen Vorgänge in bewegten Körpern*. In: Nachrichten von der Gesellschaft der Wissenschaften zu Göttingen, Mathematisch-Physikalische Klasse 1908 (1908), pp. 53–111. URL: http://eudml.org/doc/58707 (cited on p. 7).

[Mit17]   V. A. Mitsou. *The MoEDAL experiment at the LHC: status and results*. In: Journal of Physics: Conference Series 873 (2017), p. 012010. DOI: 10.1088/1742-6596/873/1/012010 (cited on p. 27).

[Mob16]   E. Mobs. *The CERN accelerator complex. Complexe des accélérateurs du CERN*. July 8, 2016. URL: http://cds.cern.ch/record/2197559/files/?docname=CCC-v2017&version=all&ln=de (cited on p. 25).

[Mor15]   K. E. Morabit. *A study of the multivariate analysis of Higgs boson production in association with a top quark-antiquark pair in the boosted regime at the CMS experiment*. Master thesis. Karlsruhe Institute of Technology, Oct. 22, 2015. URL: http://ekp-invenio.physik.uni-karlsruhe.de/record/48864 (cited on p. 92).

[Moy16]   M. M. Moya. *CMS pixel upgrade for the phase I: Module production and qualification.* In: Nuclear Instruments and Methods in Physics Research Section A: Accelerators, Spectrometers, Detectors and Associated Equipment 831 (Sept. 2016), pp. 137–139. DOI: 10.1016/j.nima.2016.03.030 (cited on p. 192).

[Nam60]   Y. Nambu. *Quasi-Particles and Gauge Invariance in the Theory of Superconductivity.* In: Physical Review 117.3 (Feb. 1960), pp. 648–663. DOI: 10.1103/PhysRev.117.648 (cited on p. 8).

[Nat17a]   National Instruments Corp. *LabWindows/CVI (C for Virtual Instrumentation) Development Environment.* Feb. 5, 2017. URL: http://www.ni.com/lwcvi/ (cited in pp. 161, 169).

[Nat17b]   National Instruments Corp. *NI Vision Software.* May 2, 2017. URL: http://www.ni.com/vision/software/ (cited in pp. 161, 169).

[NB82]   G. C. Nelson and J. A. Borders. *Surface composition of a tin–lead alloy.* In: Journal of Vacuum Science and Technology 20.4 (Apr. 1982), pp. 939–942. DOI: 10.1116/1.571647 (cited on p. 181).

[Nie18]   M. Nielsen. *Neural Networks and Deep Learning.* Feb. 12, 2018. URL: http://neuralnetworksanddeeplearning.com/ (cited on p. 165).

[Nor18]   Nordson DAGE. *4000 Multipurpose Bondtester.* Feb. 12, 2018. URL: http://www.nordson.com/en/divisions/dage/products/bondtesters/4000-multipurpose-bondtester (cited on p. 166).

[NP33]   J. Neyman and E. S. Pearson. *On the Problem of the Most Efficient Tests of Statistical Hypotheses.* In: Philosophical Transactions of the Royal Society A: Mathematical, Physical and Engineering Sciences 231.694-706 (Jan. 1933), pp. 289–337. DOI: 10.1098/rsta.1933.0009 (cited on p. 91).

[Nür14]   A. Nürnberg. *Studien an bestrahlten Siliziumsensoren für den CMS Spurdetektor am HL-LHC.* PhD thesis. Karlsruher Institut für Technologie (KIT), July 30, 2014. URL: http://ekp-invenio.physik.uni-karlsruhe.de/record/48576 (cited on p. 127).

[Pan+06]   J. Pan et al. *The effect of reflow profile on SnPb and SnAgCu solder joint shear strength.* In: Soldering & Surface Mount Technology 18.4 (Oct. 2006), pp. 48–56. DOI: 10.1108/09540910610717901 (cited on p. 182).

[Par12]   Particle Data Group. *Review of Particle Physics.* In: Physical Review D 86.1 (July 2012). DOI: 10.1103/PhysRevD.86.010001 (cited in pp. 119, 123 sqq.).

[Par16]   Particle Data Group. *Review of Particle Physics.* In: Chinese Physics C 40.10 (Oct. 2016), p. 100001. DOI: 10.1088/1674-1137/40/10/100001 (cited in pp. 7, 20).

[Pea00]   K. Pearson. *X. On the criterion that a given system of deviations from the probable in the case of a correlated system of variables is such that it can be reasonably supposed to have arisen from random sampling.* In: The London, Edinburgh, and Dublin Philosophical Magazine and Journal of Science 50.302 (July 1900), pp. 157–175. DOI: 10.1080/14786440009463897 (cited on p. 83).

[Pea95]   K. Pearson. *Note on regression and inheritance in the case of two parents.* In: Proceedings of the Royal Society of London 58.-1 (Jan. 1895), pp. 240–242. DOI: 10.1098/rspl.1895.0041 (cited on p. 79).

[Per+15] I. Perić et al. *Overview of HVCMOS pixel sensors.* In: Journal of Instrumentation 10.05 (May 2015), p. C05021. DOI: 10.1088/1748-0221/10/05/c05021 (cited on p. 130).

[Per+97] S. Perlmutter et al. *Measurements of the cosmological parameters Omega and Lambda from the first 7 supernovae at z ≥ 0.35.* In: Astrophys. J. 483 (1997), p. 565. DOI: 10.1086/304265. arXiv: astro-ph/9608192 [astro-ph] (cited on p. 10).

[Per07] M. Perelstein. *Little Higgs models and their phenomenology.* In: Progress in Particle and Nuclear Physics 58.1 (Jan. 2007), pp. 247–291. DOI: 10.1016/j.ppnp.2006.04.001 (cited on p. 15).

[Pes15] M. Peskin. *An Introduction To Quantum Field Theory, Student Economy Edition (Frontiers in Physics).* CRC Press, 2015. ISBN: 9780813350196 (cited on p. 7).

[Poc15] A. Pocar. *Searching for neutrino-less double beta decay with EXO-200 and nEXO.* In: Nuclear and Particle Physics Proceedings 265-266 (Aug. 2015), pp. 42–44. DOI: 10.1016/j.nuclphysbps.2015.06.011 (cited on p. 11).

[PS12] T. Plehn and M. Spannowsky. *Top tagging.* In: Journal of Physics G: Nuclear and Particle Physics 39.8 (May 2012), p. 083001. DOI: 10.1088/0954-3899/39/8/083001 (cited on p. 59).

[PSS10] T. Plehn, G. P. Salam, and M. Spannowsky. *Fat Jets for a Light Higgs Boson.* In: Physical Review Letters 104.11 (Mar. 2010). DOI: 10.1103/physrevlett.104.111801 (cited on p. 58).

[Ram39] S. Ramo. *Currents Induced by Electron Motion.* In: Proceedings of the IRE 27.9 (Sept. 1939), pp. 584–585. DOI: 10.1109/jrproc.1939.228757 (cited on p. 127).

[Ren17] J. Renner. *Planning and validation of the thermal mock-up for the CMS Pixel Detector.* Master thesis. Karlsruher Institut für Technologie (KIT), Apr. 6, 2017. URL: https://ekp-invenio.physik.uni-karlsruhe.de/record/48898/files/EKP-2017-00025.pdf (cited on p. 141).

[Rie17] F. Riese. *Boosted-Jet Reconstruction Methods in a Search for Higgs-Boson Production in Association with a Top-Quark-Antiquark Pair at the CMS Experiment.* Master thesis. Karlsruhe Institute of Technology, Jan. 31, 2017. URL: https://ekp-invenio.physik.uni-karlsruhe.de/record/48891 (cited on p. 60).

[Rob12] L. Robertson. *Computing Services for LHC: From Clusters to Grids.* Ed. by R. Brun, F. Carminati, and G. Galli Carminati. Berlin, Heidelberg: Springer Berlin Heidelberg, 2012, pp. 69–89. ISBN: 978-3-642-23157-5. DOI: 10.1007/978-3-642-23157-5_3 (cited on p. 39).

[Roh+11] T. Rohe et al. *Planar sensors for the upgrade of the CMS pixel detector.* In: Nuclear Instruments and Methods in Physics Research Section A: Accelerators, Spectrometers, Detectors and Associated Equipment 650.1 (Sept. 11, 2011), pp. 136–139. DOI: 10.1016/j.nima.2010.11.156 (cited on p. 146).

[Ros+06] L. Rossi et al. *Pixel Detectors.* ISBN: 978-3-540-28333-1. Springer-Verlag, 2006. DOI: 10.1007/3-540-28333-1 (cited in pp. 130, 132, 145).

[Ros98] K. Rose. *Deterministic annealing for clustering, compression, classification, regression, and related optimization problems*. In: Proceedings of the IEEE 86.11 (1998), pp. 2210–2239. DOI: 10.1109/5.726788 (cited on p. 49).

[Rov11] C. Rovelli. *Loop quantum gravity: the first 25 years*. In: Classical and Quantum Gravity 28.15 (June 2011), p. 153002. DOI: 10.1088/0264-9381/28/15/153002 (cited on p. 10).

[RS99a] L. Randall and R. Sundrum. *An Alternative to Compactification*. In: Physical Review Letters 83.23 (Dec. 1999), pp. 4690–4693. DOI: 10.1103/physrevlett.83.4690 (cited in pp. 17 sq.).

[RS99b] L. Randall and R. Sundrum. *Large Mass Hierarchy from a Small Extra Dimension*. In: Physical Review Letters 83.17 (Oct. 1999), pp. 3370–3373. DOI: 10.1103/PhysRevLett.83.3370 (cited in pp. 17 sq.).

[RSS16] L. Rossi, S. Stavrev, and A. Szeberenyi. *3rd Periodic HiLumi LHC Report: Deliverable D1.13*. Tech. rep. CERN, Jan. 2016. URL: http://cds.cern.ch/record/2121246 (cited in pp. 39 sq.).

[Sak98] A. D. Sakharov. *Violation of CP-invariance, C-asymmetry, and baryon asymmetry of the universe*. In: Soviet Physics Uspekhi 34.5 (Nov. 1998), pp. 84–87. DOI: 10.1070/PU1991v034n05ABEH002497 (cited on p. 11).

[SBM17] A. Starodumov, P. Berger, and M. Meinhard. *High rate capability and radiation tolerance of the PROC600 readout chip for the CMS pixel detector*. In: Journal of Instrumentation 12.01 (Jan. 2017), p. C01078. DOI: 10.1088/1748-0221/12/01/c01078 (cited on p. 142).

[Sch15] D. Schell. *Evaluation of Sensor Materials and Technologies for the Innermost Layer of the CMS Pixel Detector at the HL-LHC*. Master thesis. Karlsruher Institut für Technologie (KIT), Aug. 19, 2015. URL: http://ekp-invenio.physik.uni-karlsruhe.de/record/48732 (visited on 01/08/2018) (cited on p. 131).

[SCR14] P. Skands, S. Carrazza, and J. Rojo. *Tuning PYTHIA 8.1: the Monash 2013 tune*. In: The European Physical Journal C 74.8 (Aug. 2014). DOI: 10.1140/epjc/s10052-014-3024-y (cited on p. 65).

[Sha98] A. Sharma. *Properties of some gas mixtures used in tracking detectors*. In: SLAC-J-ICFA-16-3, SLAC-JOURNAL-ICFA-16-3 (1998) (cited on p. 123).

[Sho38] W. Shockley. *Currents to Conductors Induced by a Moving Point Charge*. In: Journal of Applied Physics 9.10 (Oct. 1938), pp. 635–636. DOI: 10.1063/1.1710367 (cited on p. 127).

[Sim+13] A. D. Simone et al. *A first top partner hunter's guide*. In: Journal of High Energy Physics 2013.4 (Apr. 2013). DOI: 10.1007/JHEP04(2013)004 (cited on p. 12).

[Sjö+15] T. Sjöstrand et al. *An introduction to PYTHIA 8.2*. In: Computer Physics Communications 191 (June 2015), pp. 159–177. DOI: 10.1016/j.cpc.2015.01.024 (cited on p. 65).

[Ske46] J. Skellam. *The Frequency Distribution of the Difference Between Two Poisson Variates Belonging to Different Populations*. In: Journal of the Royal Statistical Society 109.3 (1946), p. 296. DOI: 10.2307/2981372 (cited on p. 92).

[SMP15]   S. Spannagel, B. Meier, and H. C. Perrey. *The pxarCore Library - Technical Documentation, Reference Manual, and Sample Applications*. Tech. rep. CMS-NOTE-2016-001. CERN-CMS-NOTE-2016-001. Geneva: CERN, Oct. 16, 2015. URL: http://cds.cern.ch/record/2137512 (cited in pp. 168 sq.).

[Son17]   J. M. Sonneveld. *Commissioning and first results from the CMS phase-1 upgrade pixel detector*. Tech. rep. CMS-CR-2017-425. Geneva: CERN, Nov. 2017. URL: https://cds.cern.ch/record/2297549 (cited on p. 197).

[Spa16]   S. Spannagel. *Top quark mass measurements with the CMS experiment at the LHC*. In: PoS DIS2016 (2016), p. 150. arXiv: 1607.04972 [hep-ex]. URL: https://inspirehep.net/search?p=find+eprint+1607.04972 (cited on p. 7).

[Spe+03]   D. N. Spergel et al. *First-Year Wilkinson Microwave Anisotropy Probe(WMAP) Observations: Determination of Cosmological Parameters*. In: The Astrophysical Journal Supplement Series 148.1 (Sept. 2003), pp. 175–194. DOI: 10.1086/377226 (cited on p. 10).

[Spe04]   C. Spearman. *The Proof and Measurement of Association between Two Things*. In: The American Journal of Psychology 15.1 (Jan. 1904), p. 72. DOI: 10.2307/1412159 (cited on p. 79).

[Spi05]   H. Spieler. *Semiconductor Detector Systems*. OXFORD UNIV PR, Oct. 11, 2005. 489 pp. ISBN: 9780198527848 (cited in pp. 128 sq.).

[SS11]   D. E. Soper and M. Spannowsky. *Finding physics signals with shower deconstruction*. In: Physical Review D 84.7 (Oct. 2011). DOI: 10.1103/physrevd.84.074002 (cited on p. 58).

[ST05]   M. Schmaltz and D. Tucker-Smith. *Little Higgs theories*. In: Annual Review of Nuclear and Particle Science 55.1 (Dec. 2005), pp. 229–270. DOI: 10.1146/annurev.nucl.55.090704.151502 (cited on p. 14).

[Sti18]   J. Stirling. *PARTON LUMINOSITY AND CROSS SECTION PLOTS*. Feb. 26, 2018. URL: http://www.hep.ph.ic.ac.uk/~wstirlin/plots/plots.html (cited on p. 29).

[Str11]   S. Streuli. *Barrel module assembly manual*. June 8, 2011. URL: https://cms-docdb.cern.ch/cgi-bin/DocDB/ShowDocument?docid=%204899 (cited on p. 191).

[Str18]   Struers. *Grinding and Polishing*. Feb. 12, 2018. URL: https://www.struers.com/en/Products/Grinding-and-Polishing (cited on p. 166).

[TA13]   A. Tapper and D. Acosta. *CMS Technical Design Report for the Level-1 Trigger Upgrade*. Tech. rep. CERN-LHCC-2013-011. CMS-TDR-12. CERN, June 2013. URL: https://cds.cern.ch/record/1556311 (cited on p. 40).

[The18]   The Dow Chemical Company. *CYCLOTENE Advanced Electronics Resins - Photosensitive Resins*. Feb. 12, 2018. URL: https://www.dow.com/cyclotene/prod/photo.htm (cited on p. 157).

[Tin11]   G. Tinti. *Study of the readout chip and silicon sensor degradation for the CMS pixel upgrade*. In: *Particles and fields. Proceedings, Meeting of the Division of the American Physical Society, DPF 2011, Providence, USA, August 9-13, 2011*. 2011. arXiv: 1110.1173 [physics.ins-det]. URL: http://inspirehep.net/record/930849/files/arXiv:1110.1173.pdf (cited on p. 127).

[TOT08]   TOTEM Collaboration. *The TOTEM Experiment at the CERN Large Hadron Collider*. In: Journal of Instrumentation 3.08 (2008), S08007. DOI: 10.1088/1748-0221/3/08/S08007 (cited on p. 26).

[Tri+10]   S. M. Tripathi et al. *Gold-stud bump bonding for HEP applications*. In: Journal of Instrumentation 5.08 (Aug. 2010), p. C08005. DOI: 10.1088/1748-0221/5/08/c08005 (cited on p. 133).

[TT11]   J. Thaler and K. V. Tilburg. *Identifying boosted objects with N-subjettiness*. In: Journal of High Energy Physics 2011.3 (Mar. 2011). DOI: 10.1007/jhep03(2011)015 (cited on p. 57).

[TT12a]   J. Thaler and K. V. Tilburg. *Maximizing boosted top identification by minimizing N-subjettiness*. In: Journal of High Energy Physics 2012.2 (Feb. 2012). DOI: 10.1007/jhep02(2012)093 (cited on p. 57).

[TT12b]   J. Thaler and K. V. Tilburg. *Maximizing boosted top identification by minimizing N-subjettiness*. In: Journal of High Energy Physics 2012.2 (Feb. 2012). DOI: 10.1007/jhep02(2012)093 (cited on p. 58).

[Tu07]   K.-N. Tu. *Solder Joint Technology: Materials, Properties, and Reliability (Springer Series in Materials Science)*. Springer, 2007. ISBN: 9780387388908 (cited on p. 180).

[UA183a]   UA1 Collaboration. *Experimental observation of isolated large transverse energy electrons with associated missing energy at*. In: Physics Letters B 122.1 (Feb. 1983), pp. 103–116. DOI: 10.1016/0370-2693(83)91177-2 (cited on p. 8).

[UA183b]   UA1 Collaboration. *Experimental observation of lepton pairs of invariant mass around 95 GeV/c^2 at the CERN SPS collider*. In: Physics Letters B 126.5 (July 1983), pp. 398–410. DOI: 10.1016/0370-2693(83)90188-0 (cited on p. 8).

[UA283a]   UA2 Collaboration. *Evidence for Z0→ee- at the CERN p collider*. In: Physics Letters B 129.1-2 (Sept. 1983), pp. 130–140. DOI: 10.1016/0370-2693(83)90744-X (cited on p. 8).

[UA283b]   UA2 Collaboration. *Observation of single isolated electrons of high transverse momentum in events with missing transverse energy at the CERN p collider*. In: Physics Letters B 122.5-6 (Mar. 1983), pp. 476–485. DOI: 10.1016/0370-2693(83)91605-2 (cited on p. 8).

[Uni14]   University of California, Davis – Facility for Interconnect Technology. *General Bonding Procedure*. Last downloaded 22.05.2014. Apr. 24, 2014. URL: http://fit.physics.ucdavis.edu/doku.php?id=shared:finetech (cited on p. 131).

[Uni18]   United States National Library of Medicine. *Hazardous Substances Data Bank – Acetone*. Feb. 12, 2018. URL: https://toxnet.nlm.nih.gov/cgi-bin/sis/search2/f?./temp/~HkZt9C:1 (cited on p. 159).

[US 91]   US Department of Defense. *Test Method Standard Microcircuits - MIL-STD-883E*. Dec. 31, 1991. URL: http://scipp.ucsc.edu/groups/fermi/electronics/mil-std-883.pdf (cited in pp. 165, 191).

[Usa17]   E. Usai. *Searches for heavy resonances in all-jet final states with top quarks using jet substructure techniques with the CMS Experiment.* PhD thesis. University of Hamburg, July 27, 2017. URL: https://cds.cern.ch/record/2294585/files/TS2017_026_2.pdf (cited in pp. 17, 64 sqq., 71, 76, 97, 106, 109).

[Ves17]   V. Veszpremi. *Performance verification of the CMS Phase-1 Upgrade Pixel detector.* In: Journal of Instrumentation 12.12 (Dec. 2017), p. C12010. DOI: 10.1088/1748-0221/12/12/C12010 (cited on p. 197).

[WFV07]   W. Waltenberger, R. Frühwirth, and P. Vanlaer. *Adaptive vertex fitting.* In: Journal of Physics G: Nuclear and Particle Physics 34.12 (Nov. 2007), N343–N356. DOI: 10.1088/0954-3899/34/12/n01 (cited on p. 49).

[Whi16]   L. Whitehead. *Neutrino oscillations with MINOS and MINOS.* In: Nuclear Physics B 908 (July 2016), pp. 130–150. DOI: 10.1016/j.nuclphysb.2016.03.004 (cited on p. 11).

[Wik18]   Wikipedia. *Standard Model of Elementary Particles.* Apr. 8, 2018. URL: https://en.wikipedia.org/wiki/Standard_Model#/media/File:Standard_Model_of_Elementary_Particles.svg (cited on p. 6).

[Wil16]   S. D. Williamson. *Search for Higgs-Boson Production in Association with a Top-Quark Pair in the Boosted Regime with the CMS Experiment.* PhD thesis. Karlsruhe Institute of Technology, Nov. 11, 2016. DOI: 10.5445/IR/1000068213 (cited in pp. 60, 74).

[Woe+02]   A. A. Woering et al. *Thermal Modeling Issues Concerning the Mechanically Pumped Two-Phase CO_2 Cooling for the AMS-2 Tracker.* In: *SAE Technical Paper Series.* SAE International, July 2002. DOI: 10.4271/2002-01-2466 (cited on p. 141).

[Woz17]   S. Wozniewski. *Entwicklung multivariater Analysemethoden zur Steigerung der Sensitivität auf supersymmetrische Higgs-Bosonen im $H \to \tau\tau$ Zerfallskanal.* Master thesis. Karlsruher Institut für Technologie (KIT), May 30, 2017. URL: http://ekp-%20invenio.physik.uni-karlsruhe.de/record/48913. (cited on p. 9).

[XZ13]   Z.-z. Xing and Y.-L. Zhou. *MajoranaCP-violating phases in neutrino-antineutrino oscillations and other lepton-number-violating processes.* In: Physical Review D 88.3 (Aug. 2013). DOI: 10.1103/PhysRevD.88.033002 (cited on p. 11).

[Zie17]   K. Ziehl. *Fake rate-based multi-jet QCD background estimation technique for a heavy gauge-boson search at the CMS experiment.* bachelorthesis. Karlsruher Institut für Technologie (KIT), Sept. 19, 2017. URL: https://ekp-invenio.physik.uni-karlsruhe.de/record/48933/files/EKP-2017-00060.pdf (cited on p. 76).

Acknowledgements